

# **STRUCTURAL ANALYSIS DRIVEN SHOULDER ARTHROPLASTY**

by

**Gulshan Baldev Sharma**

B.E., University of Mumbai, India, 2002

M.S., University of Pittsburgh, Pittsburgh, PA, 2004

Submitted to the Graduate Faculty of  
School of Engineering in partial fulfillment  
of the requirements for the degree of  
Doctor of Philosophy

University of Pittsburgh

2007

UNIVERSITY OF PITTSBURGH

SCHOOL OF ENGINEERING

This dissertation was presented

by

Gulshan Baldev Sharma

It was defended on

March 26, 2007

and approved by

Richard E. Debski, PhD, Assistant Professor, Departments of Orthopaedic Surgery and  
Bioengineering

Lars G. Gilbertson, Ph.D., Director, Spine Institute, Cleveland Clinic, Cleveland, Ohio

Patrick J. McMahon, M.D., Assistant Professor, Department of Orthopaedic Surgery

Patrick J. Smolinski, Ph.D., Associate Professor, Department of Mechanical Engineering

George D. Stetten, M.D., Ph.D., Associate Professor, Department of Bioengineering

Douglas D. Robertson, M.D., Ph.D., Associate Professor, Departments of Orthopaedic Surgery  
and Bioengineering  
Dissertation Director

Copyright © by Gulshan Baldev Sharma

2007

# **STRUCTURAL ANALYSIS DRIVEN SHOULDER ARTHROPLASTY**

Gulshan Baldev Sharma, PhD

University of Pittsburgh, 2007

Shoulder arthroplasty, the most common treatment option for patients diagnosed with end-stage glenohumeral osteoarthritis, is able to provide pain relief and restore some functionality. However, this highly advanced surgical procedure often suffers from a major complication of glenoid prosthesis loosening. The problem is magnified during repeat surgeries mainly due to the minimal quantity of bone in the glenoid vault. The goals of this dissertation were to perform structural analysis of normal and osteoarthritic glenoid, evaluate glenoid design variable effects on restoring long-lasting functionality to damaged shoulders, and create a finite element model (FEM)-based simulation process for computing subject-specific internal glenoid bone remodeling.

3D computer models of normal and osteoarthritic scapulae were created using high-resolution volumetric computed tomography images. The computer models were used for glenoid structural analyses. The morphological measurements were comparable to prior studies. The glenoid was found to be approximated by geometric analogs. The osteoarthritic scapula was highly retroverted compared to the normal, and had relatively higher glenoid bone density. Internal glenoid morphology was quantified for the first time.

Two and three dimensional stress analysis was used to compare glenoid prosthesis design variables. A custom program assigned location-specific material properties to the bone elements, based on the computed tomography data, making the FEMs similar to the actual scapula. Cemented or uncemented polyethylene pegs, compared to metal, gave stresses comparable to intact scapula.

Two dimensional FEM based simulation process for normal glenoid bone remodeling was successfully created and validated. The “element” approach better predicted the actual specimen bone density distribution than the “node”. Some of the findings agreed with past studies that is, obtaining “checkerboard” pattern in the “element” approach. The various combinations of multiple loads had minimal effect on the predicted bone density distribution.

The computer modeling, numerical stress analysis, and the simulated bone remodeling allowed successful glenoid structural analysis. The approach adopted improved our understanding of the glenoid prosthesis and successful shoulder arthroplasty.

## TABLE OF CONTENTS

<b>PREFACE</b> .....	<b>xix</b>
<b>ACRONYMS</b> .....	<b>xx</b>
<b>1.0 INTRODUCTION</b> .....	<b>1</b>
<b>2.0 BACKGROUND</b> .....	<b>4</b>
2.1 HUMAN SHOULDER .....	4
2.2 SCAPULA BONE ANATOMY .....	5
2.3 GLENOHUMERAL ARTICULATION .....	9
2.4 GLENOID.....	10
2.5 GLENOID PROSTHETIC REPLACEMENT .....	13
2.6 STRESS ANALYSIS.....	16
2.7 BONE REMODELING .....	18
2.8 SHOULDER ARTHRITIS .....	19
2.9 LIMITATIONS OF PRIOR STUDIES .....	20
2.10 SIGNIFICANCE AND HEALTH RELEVANCE .....	21
2.11 UNIQUENESS OF STUDY .....	23
<b>3.0 GLENOID STRUCTURAL ANALYSES</b> .....	<b>24</b>
3.1 INTRODUCTION .....	24
3.2 MATERIALS AND METHODS.....	25
3.3 RESULTS .....	31
3.4 DISCUSSION.....	45
<b>4.0 2D STRESS ANALYSES OF GLENOID BONE</b> .....	<b>52</b>
4.1 INTRODUCTION .....	52
4.2 MATERIALS AND METHODS.....	54
4.3 RESULTS .....	61

4.4	DISCUSSION .....	69
<b>5.0</b>	<b>3D STRESS ANALYSES OF SCAPULA .....</b>	<b>75</b>
5.1	INTRODUCTION .....	75
5.2	MATERIALS AND METHODS.....	76
5.3	RESULTS .....	83
5.4	DISCUSSION.....	89
<b>6.0</b>	<b>GLENOID BONE REMODELING: NUMERICAL SIMULATION AND VALIDATION.....</b>	<b>93</b>
6.1	INTRODUCTION .....	93
6.2	MATERIALS AND METHODS.....	94
6.3	RESULTS .....	100
6.4	DISSCUSION.....	108
<b>7.0</b>	<b>CONCLUSION AND FUTURE DIRECTIONS.....</b>	<b>114</b>
7.1	CONCLUSION.....	114
7.2	FUTURE DIRECTIONS .....	116
<b>APPENDIX A .....</b>	<b>117</b>	
	GLENOID MORPHOLOGY MEASUREMENT VALUES .....	117
<b>APPENDIX B .....</b>	<b>129</b>	
	MATLAB® PROGRAM FOR BONE ELEMENTS MATERIAL PROPERTIES .....	129
<b>APPENDIX C .....</b>	<b>141</b>	
	VON MISES STRESS PLOTS FOR 2D FEA OF GLENOID PROSTHESES.....	141
<b>APPENDIX D .....</b>	<b>145</b>	
	ANSYS® PROGRAM FOR FEM-BASED GLENOID BONE REMODELING .....	145
<b>APPENDIX E .....</b>	<b>179</b>	
	GLENOID BONE REMODELING SIMULATION AND VALIDATION RESULTS.....	179
<b>BIBLIOGRAPHY.....</b>	<b>188</b>	

## LIST OF TABLES

Table 1.	The p-values for the male-female and right-left difference for select internal glenoid morphology parameters in the normal scapulae specimen (*: Slice 1, #: Slice 2, §: Slice 3).....	34
Table 2.	The mean, standard deviation, and range of the difference between the actual specimen and computer model (accuracy), and the repeated and original computer model (reliability) measurements of the scapulae morphology parameters. ....	38
Table 3.	The mean and standard deviation of the bone density in the various regions of interest in the three selected axial slices of the osteoarthritic scapulae specimen ( <i>NA: Not Applicable for axial slice 3</i> ). ....	40
Table 4.	The comparison between select glenoid morphology parameter values in this study with prior investigations. ....	46
Table 5.	The finite element models created in the current study, along with their abbreviations. ....	56
Table 6.	Approximate cancellous bone von Mises stress (kPa) in intact bone model, and percent change from intact (positive number means increase, and negative number means decrease) for the twelve glenoid prosthesis-bone models for the center, anterior offset, and posterior offset loading conditions in the five regions of interest: 3 proximal (center(cen), posterior(pos), and anterior(ant) ), middle center (Mid cen), and distal center (Dist cen). Gray shaded values are percent differences beyond the design selection criteria (increase by more than 200% of intact or decrease by more than 50% of intact). ....	61
Table 7.	Approximate cortical bone von Mises stress (kPa) in intact bone model, and percent change from intact (positive number means increase, and negative number means decrease) for the twelve prostheses-bone models for the center, anterior offset, and posterior offset loading conditions in the two regions of interest: mid posterior (Post), and proximal to mid anterior (Ant). Gray shaded values are percent differences beyond the design	



	selection criteria (increase by more than 200% of intact or decrease by more than 50% of intact).....	64
Table 8.	The maximum von Mises stress values in the bone, prosthesis, and the cement region in the finite element models of the scapula specimen from the male donor and the same implanted with the all-polyethylene Depuy Anchor Peg® Glenoid Prosthesis, the Stryker Solar® Glenoid Prosthesis, and the one glenoid prosthesis design variable model (NA: regions not applicable to the finite element model).....	88
Table 9.	The element and node count for the five axial and three coronal plane glenoid bone finite element models created for the remodeling simulations. ....	96
Table 10.	The six different combinations of multiple loads applied to the axial and the coronal plane glenoid finite element models during the remodeling process.....	97
Table 11.	The linear regression analysis results for the predicted bone apparent density value in kg/m <sup>3</sup> at the end of the iterative remodeling process using the “element” (E) and “node” (N) based approach for all the glenoid FEMs with the 6 different load combinations (Load 1:ACP/CIS, Load 2:APC/CSI, Load 3:CAP/ICS, Load 4:CPA/ISC, Load 5:PAC/SCI, Load 6:PCA/SIC) versus that in the corresponding actual specimen (equation of line (y: predicted, x: specimen), correlation coefficient (r), and root mean square error (rmse) value).....	107
Table 12.	The mean, standard deviation, range, p-value for male-female difference, and p-value for right-left difference for the glenoid external morphology parameters in lateral view. ....	117
Table 13.	The mean, standard deviation, range, p-value for male-female difference, and p-value for right-left difference for the glenoid external morphology parameters in the anterior and posterior views. ....	118
Table 14.	The mean, standard deviation, and range values for the internal morphology parameters in the selected axial slices of the scapulae specimens (NR# = Not required. <i>These measurements not required for axial slices 1, and 2 geometry</i> ). ....	119
Table 15.	The descriptive values of the selected variables, the p-value of the test of homogeneity of variances, and the one-way ANOVA analysis results. ....	120
Table 16.	The Post Hoc Tukey's honestly significant difference (HSD) procedure (*: <i>The mean difference is significant at the 0.05 level</i> ). ....	122

Table 17.	The homogenous subsets using Tukey's HSD ( <i>Means for groups in homogenous subsets are displayed. Harmonic Mean sample size = 40</i> ) .....123
Table 18.	The mean*, and standard deviation of the bone density values in the various regions of interest in the three axial slices (*: <i>These values are not clinically equivalent, #NR = Not required. ROC 5 not present in axial slice 3</i> ). .....123
Table 19.	The correlation coefficients (r) and p-values (in parentheses) from linear regression analysis of selected external and internal bone morphological parameters. ....124
Table 20.	The mean and standard deviation of the glenoid external morphology parameters in the normal, and osteoarthritic (OA) scapulae specimen lateral view.....127
Table 21.	The mean, and standard deviation for the internal morphology parameters in the selected axial slices of the normal (N) and the osteoarthritic (OA) scapulae specimen (NR# = Not required. <i>These measurements not required for the concerned axial slices</i> ). .....128

## LIST OF FIGURES

Figure 1.	An illustration of the bony structures of the shoulder and the four articulations (illustration by author).....	5
Figure 2.	An illustration to show that the scapulae form the posterior part of the shoulder girdle (illustration by author). ....	6
Figure 3.	The ventral surface of the human scapula showing the various parts (figure by author).....	6
Figure 4.	The dorsal surface of the human scapula showing the various parts (figure by author).....	7
Figure 5.	The lateral view of the human scapula showing the various parts (figure by author).....	9
Figure 6.	The two-dimensional orientation of the articular surface of the humerus with respect to the bicondylar axis [1, 44] (figure by author). ....	10
Figure 7.	The lateral view of human scapula showing the glenoid labrum (figure by author).....	11
Figure 8.	The process used to create 3D scapula computer model from computed tomography images (figure by author). ....	25
Figure 9.	The glenoid external morphology measurements on the 3D scapula computer model (figure by author).....	27
Figure 10.	The internal glenoid morphology measurements in the three selected axial slices (figure by author). ....	28
Figure 11.	The glenoid vault depth calculated at multiple locations in the three selected axial slices (figure by author).....	28
Figure 12.	The glenoid regional bone density in the three selected axial slices recalibrated as L=relatively low density, M=relatively medium density, and H=relatively high density (figure by author). ....	29

Figure 13.	The glenoid external morphology measurement values in normal scapulae specimen for select parameters (*: p<0.05) (figure by author).....	32
Figure 14.	The glenoid internal morphology measurement values in normal scapulae specimen for select parameters (figure by author).....	33
Figure 15.	The mean glenoid version (a°) in the three selected axial slices of the normal scapulae specimen (figure by author).....	36
Figure 16.	The mean and standard deviation of normal glenoid vault depth values at multiple locations in the selected axial slices of the normal scapulae specimen (*: p<0.05) (figure by author).....	36
Figure 17.	The three dimensional computer models of the three osteoarthritic (OA) scapulae specimen showing the various measurements in the lateral view (figure by author).....	39
Figure 18.	The internal morphology measurements for each of the osteoarthritic (OA) scapulae specimen three selected axial slices (figure by author).....	39
Figure 19.	The bone density in the various regions of interest in the three axial slices of the osteoarthritic scapulae specimen calibrated as H:relatively high, M:relatively medium, and L:relatively low (figure by author).....	40
Figure 20.	The glenoid external morphology parameter values comparison between the normal and osteoarthritic (OA) scapulae specimen (*: p<0.05) (figure by author).....	42
Figure 21.	The glenoid internal morphology and vault depth measurement values comparison between the normal and osteoarthritic (OA) scapulae specimen (figure by author).....	44
Figure 22.	The sequence of steps used for the 2D stress analyses of the glenoid bone (illustration by author). .....	54
Figure 23.	(A) Axial CT slice of right scapula selected for finite element modeling and analysis, (B) axial slice CT numbers (Hounsfield Units or HU) shown using a color mapped range, (C) finite element model (FEM) of the intact bone with the assigned element CT numbers (HU), and (D) FEM of intact bone showing the location-specific Young's modulus values in GPa (illustration by author). .....	55
Figure 24.	The finite element models of the twelve glenoid prostheses showing the location-specific Young's modulus values in GPa. Rows show the material variations for the glenoid prostheses backing and the fixations (PE: all-PE,	

PB: Partial Metal Backing with PE fixations, MB: Metal Backing with PE fixations and MM: Metal Backing with Metal fixations). Columns indicate the fixation type (C: straight center long, P: angled posterior-long anterior-short, and A: angled anterior-long posterior-short) (illustration by author). .....57

Figure 25. The center, anterior-offset, and posterior-offset point loads in the intact bone and the glenoid prosthesis-bone finite element models, along with the regions of interest for stress comparison (illustration by author). .....60

Figure 26. von Mises stress (Pa), for the center loading case, in the cancellous bone of the intact, and the twelve glenoid prostheses. Rows show the various prostheses backing and fixation materials (PE: all-PE, PB: Partial Metal Backing with PE fixations, MB: Metal Backing with PE fixations and MM: Metal Backing with Metal fixations) and columns indicate the fixation type (C: straight center long, P: angled posterior-long anterior-short, and A: angled anterior-long posterior-short) (figure by author). .....62

Figure 27. von Mises stress (Pa), for the center loading case, in the cortical bone of the intact, and the twelve glenoid prostheses. Rows show the various prostheses backing and the fixation materials (PE: all-PE, PB: Partial Metal Backing with PE fixations, MB: Metal Backing with PE fixations and MM: Metal Backing with Metal fixations) and columns indicate the peg type (C: straight center long, P: angled posterior-long anterior-short, and A: angled anterior-long posterior-short) (figure by author). .....65

Figure 28. von Mises stress (Pa), for the posterior loading case, in the cancellous bone of the intact, and the all-PE (PE) and metal-backed (MB) posterior-long anterior short glenoid prostheses (figure by author). .....67

Figure 29. von Mises stress (Pa), for the posterior loading case, in the cortical bone of the intact, and the all-PE (PE) and metal-backed (MB) posterior-long anterior short glenoid prosthesis prostheses (figure by author). .....68

Figure 30. The process used for creating the 3D finite element model of scapula (illustration by author). .....77

Figure 31. The simulation of the surgical implantation of 3D CAD model of the glenoid prosthesis in the 3D scapula computer model using the SolidWorks® (SolidWorks Corporation, Concord, MA, USA) software (illustration by author). .....78

Figure 32. The finite element models of intact scapula specimen from an 82 year old female donor, and the same implanted with the all-polyethylene Stryker Solar® Glenoid Prosthesis, and two partial-metal backed glenoid

	prosthesis having same geometry, but metal and polyethylene angled fixations (illustration by author).....	79
Figure 33.	The finite element models of intact scapula specimen from a 55 year old male donor, and the same implanted with the all-polyethylene Depuy Anchor Peg® Glenoid Prosthesis, Stryker Solar® Glenoid Prosthesis, and the one glenoid prosthesis variable model (illustration by author).....	80
Figure 34.	The load of one bodyweight, 800N, and the boundary condition of fixed nodes at the medial border for the finite element models of the scapula specimen from the female donor, and the same implanted with the Stryker Solar® Glenoid Prosthesis, and the two partial-metal backed glenoid prosthesis having the same geometry but metal, and polyethylene angled fixations respectively (illustration by author).....	81
Figure 35.	The load of one bodyweight, 800N, and the boundary condition of fixed nodes at the medial border for the finite element models of the scapula specimen from the male donor, and the same implanted with the all-polyethylene Depuy Anchor Peg® Glenoid Prosthesis, the Stryker Solar® Glenoid Prosthesis, and the one glenoid prosthesis variable model (illustration by author).....	82
Figure 36.	The frequency distribution plots of the CT number and the Young's modulus values of the bone elements of the intact scapula specimen from the male donor (graphs by author).....	83
Figure 37.	The von Mises stress (Pa) in the axial plane at multiple locations for the first case of the finite element analysis using the scapula specimen from the female donor (figure by author).....	84
Figure 38.	The von Mises stress (Pa) in the coronal plane at multiple locations for the first case of the finite element analysis using the scapula specimen from the female donor (figure by author).....	84
Figure 39.	The von Mises stress (Pa) plots of the finite element models of the scapula specimen from the male donor, and the same implanted with the all-polyethylene Depuy Anchor Peg® Glenoid Prosthesis, the Stryker Solar® Glenoid Prosthesis, and the one glenoid prosthesis variable model (figure by author).....	86
Figure 40.	The von Mises stress (Pa) plots of the finite element models of the all-polyethylene Depuy Anchor Peg® Glenoid Prosthesis, the Stryker Solar® Glenoid Prosthesis, and the one glenoid prosthesis variable model and the corresponding bone cement layer (figure by author).....	87

Figure 41.	The five axial and three coronal plane glenoid bone finite element models created using three cadaver scapula specimens obtained from donors, a 55 year-old male (specimen 1), an 82 year-old female (specimen 2), and a 42 year-old female (specimen 3), in the Midwestern United States (illustration by author). .....	95
Figure 42.	The center, anterior-offset, posterior-offset, superior-offset, and inferior-offset loads and the fixed medial edge boundary condition applied to the axial and coronal plane cross-section glenoid finite element models (illustration by author). .....	97
Figure 43.	The glenoid bone “element” based remodeling algorithm adapted from Weinans, Huiskes et al [36] (illustration by author). .....	99
Figure 44.	The bone apparent density plots at the end of the iterative “element” and “node” based remodeling process for all the glenoid finite element models simulated using the load combination 4 (CPA/ISC). Also shown for comparison is the bone apparent density plot for all the actual specimens (figure by author). .....	103
Figure 45.	The absolute value of the location-specific difference of the predicted and the actual specimen bone apparent density images of the glenoid finite element models at the end of the “element” and the “node” based bone remodeling simulations with the load combination 4, CPA/ISC (figure by author). .....	104
Figure 46.	The mean and standard deviation of the location-specific absolute difference between the predicted and the corresponding actual specimen bone apparent density value in $\text{kg/m}^3$ computed at the end of the simulations over all the elements and the nodes depending upon the “element” (E) or the “node” (N) based remodeling process for all the glenoid finite element models using the six different multiple load combinations (Load 1:ACP/CIS, Load 2:APC/CSI, Load 3:CAP/ICS, Load 4:CPA/ISC, Load 5:PAC/SCI, Load 6:PCA/SIC) (figure by author). .....	105
Figure 47.	The frequency distribution of the absolute difference between the predicted and the actual specimen bone apparent density in the Axial 1 and Coronal 3 glenoid FEM for the “element” and “node” based simulations using the load combination 4 (figure by author). .....	106
Figure 48.	The linear approximation of the predicted bone apparent density value with respect to that in the actual specimen in the Specimen 1: Axial 1 and Specimen 3: Coronal 3 glenoid FEMs at the end of the “element” and	

	“node” based remodeling process using the load combination 4:CPA/ISC (figure by author).....	108
Figure 49.	The error bar plot showing equal variance between the selected parameters $L_{1h}$ , $L_{2h}$ , $L_{3h}$ , $L_{4h}$ , $C/3$ , and $D/2$ (y-axis unit is “mm”) (figure by author).....	121
Figure 50.	Linear regression between C and D ( $p = 0.0$ , $r = 0.80$ , $D = 1.8653 + 0.6514C$ ) (figure by author).....	124
Figure 51.	Linear regression between C and $L_1$ ( $p = 0.0$ , $r = 0.79$ , $L_1 = -2.2369 + 0.8526C$ ) (figure by author).....	125
Figure 52.	Linear regression between C and $L_3$ ( $p = 0.0$ , $r = 0.78$ , $L_3 = 2.2699 + 0.7276C$ ) (figure by author).....	125
Figure 53.	Linear regression between D and $L_2$ ( $p = 0.0$ , $r = 0.92$ , $L_2 = 0.6817 + 0.9799D$ ) (figure by author).....	126
Figure 54.	Linear regression between D and $L_4$ ( $p = 0.0$ , $r = 0.93$ , $L_4 = 2.2829 + 0.9108D$ ) (figure by author).....	126
Figure 55.	von Mises stress (Pa), for the anterior offset loading case, in the cancellous bone of the intact, and the twelve glenoid prostheses. Rows show the various prostheses backing and the pegs materials (PE: all-PE, PB: Partial Metal Backing with PE pegs, MB: Metal Backing with PE pegs and MM: Metal Backing with Metal pegs). Columns indicate the peg type (C: straight center long, P: angled posterior-long anterior-short, and A: angled anterior-long posterior-short) (figure by author).....	141
Figure 56.	von Mises stress (Pa), for the anterior offset loading case, in the cortical bone of the intact, and the twelve glenoid prostheses. Rows show the various prostheses backing and the pegs materials (PE: all-PE, PB: Partial Metal Backing with PE pegs, MB: Metal Backing with PE pegs and MM: Metal Backing with Metal pegs). Columns indicate the peg type (C: straight center long, P: angled posterior-long anterior-short, and A: angled anterior-long posterior-short) (figure by author).....	142
Figure 57.	von Mises stress (Pa), for the posterior offset loading case, in the cancellous bone of the intact, and the twelve glenoid prostheses. Rows show the various prostheses backing and the pegs materials (PE: all-PE, PB: Partial Metal Backing with PE pegs, MB: Metal Backing with PE pegs and MM: Metal Backing with Metal pegs). Columns indicate the peg type (C: straight center long, P: angled posterior-long anterior-short, and A: angled anterior-long posterior-short) (figure by author).....	143



Figure 58.	von Mises stress (Pa), for the posterior offset loading case, in the cortical bone of the intact, and the twelve glenoid prostheses. Rows show the various prostheses backing and the pegs materials (PE: all-PE, PB: Partial Metal Backing with PE pegs, MB: Metal Backing with PE pegs and MM: Metal Backing with Metal pegs). Columns indicate the peg type (C: straight center long, P: angled posterior-long anterior-short, and A: angled anterior-long posterior-short) (figure by author). .....	144
Figure 59.	The bone apparent density plots at the end of the iterative “element” based remodeling process for all the glenoid finite element models simulated using the six different load combinations (Load 1: ACP/CIS, Load 2: APC/CSI, Load 3: CAP/ICS, Load 4: CPA/ISC, Load 5: PAC/SCI, Load 6: PCA/SIC). Also shown for comparison is the bone apparent density plot for all the actual specimens (figure by author). .....	180
Figure 60.	The bone apparent density plots at the end of the iterative “node” based remodeling process for all the glenoid finite element models simulated using the six different load combinations (Load 1: ACP/CIS, Load 2: APC/CSI, Load 3: CAP/ICS, Load 4: CPA/ISC, Load 5: PAC/SCI, Load 6: PCA/SIC). Also shown for comparison is the bone apparent density plot for all the actual specimens (figure by author). .....	181
Figure 61.	The mean of the difference between the predicted and the actual specimens bone apparent density value computed on a location specific basis in each of the iterations over all the elements or nodes depending upon the “element” or the “node” based remodeling process, represented by the subscript ‘E’ and ‘N’ in the legend respectively, used for all the glenoid FEMs with the six different load combinations (Load 1: ACP/CIS, Load 2: APC/CSI, Load 3: CAP/ICS, Load 4: CPA/ISC, Load 5: PAC/SCI, Load 6: PCA/SIC) (figure by author). .....	182
Figure 62.	The correlation coefficient value between the predicted and the actual specimen bone apparent density value in each of the iterations for all the glenoid bone FEMs “element” and “node” based remodeling simulations, represented by subscript ‘E’ and ‘N’ respectively in the legend, with the six different load combinations (Load 1: ACP/CIS, Load 2: APC/CSI, Load 3: CAP/ICS, Load 4: CPA/ISC, Load 5: PAC/SCI, Load 6: PCA/SIC) (figure by author).....	183
Figure 63.	The absolute bone apparent density difference images of the glenoid finite element models at the end of the “element” based bone remodeling simulations using the various load combinations (Load 1: ACP/CIS, Load 2: APC/CSI, Load 3: CAP/ICS, Load 4: CPA/ISC, Load 5: PAC/SCI,	

	Load 6: PCA/SIC) and the actual specimen computed on a location-specific basis (figure by author).....	184
Figure 64.	The absolute bone apparent density difference images of the glenoid finite element models at the end of the “node” based bone remodeling simulations using the various load combinations (Load 1: ACP/CIS, Load 2: APC/CSI, Load 3: CAP/ICS, Load 4: CPA/ISC, Load 5: PAC/SCI, Load 6: PCA/SIC) and the actual specimen computed on a location-specific basis (figure by author).....	185
Figure 65.	The linear approximation of the predicted bone apparent density value in terms of that in the corresponding specimen for all the glenoid FEMs at the end of “element” based remodeling process for all the load combinations (Load 1: ACP/CIS, Load 2: APC/CSI, Load 3: CAP/ICS, Load 4: CPA/ISC, Load 5: PAC/SCI, Load 6: PCA/SIC) using regression analysis in Matlab® software (figure by author).....	186
Figure 66.	The linear approximation of the predicted bone apparent density value in terms of that in the corresponding specimen for all the glenoid FEMs at the end of “node” based remodeling process for all the load combinations (Load 1: ACP/CIS, Load 2: APC/CSI, Load 3: CAP/ICS, Load 4: CPA/ISC, Load 5: PAC/SCI, Load 6: PCA/SIC) using regression analysis in Matlab® software (figure by author).....	187

## PREFACE

Life in Pittsburgh over the past years has been an *interesting* experience. All I can say that it was destiny, fate, and karma. Firstly, I would like to thank the Chairman, Dr. Harvey Borovetz, and the admissions committee for accepting my application for the prestigious BioEngineering graduate program at the University of Pittsburgh, and my advisor Dr. Doug Robertson for giving me opportunity to perform research in his esteemed Musculoskeletal Imaging and Biomechanics Laboratory. Dr. Robertson is one of the nicest and most understanding persons I have met in my life. He has always patiently given me excellent guidance not only in the realm of research work and academics but also at a personal level.

Many thanks to rest of the dissertation committee for invaluable suggestions to improve this research work. I am honored to have been guided by elite professors and surgeons, Drs. Richard Debski, Lars Gilbertson, Patrick McMahon, Patrick Smolinski, and George Stetten.

Thanks to the BioEngineering faculty for their well-structured and exceptionally taught courses that created an atmosphere conducive for in-depth learning. Furthermore, I would like to thank the administration personnel for their kind help whenever it was needed. Everyone in the Pitt BioEngineering department was willing to help for which I am truly grateful.

Thanks to my parents, family, and friends for their support. And thanks to the *Malik* for everything.

“Nothing belongs to us, except time.” Baltasar Gracian, Mystic 17<sup>th</sup> century.

## ACRONYMS

CAD	Computer Aided Design
CT	Computed Tomography
FEA	Finite Element Analysis
FEM	Finite Element Model
HU	Hounsfield Units
IGES	Initial Graphics Exchange Specification
MRI	Magnetic Resonance Imaging
NURBS	Non-Uniform Rational B-Spline
OA	Osteoarthritis
PE	Polyethylene
PMMA	Polymethylmethacrylate
UHMWPE	Ultra High Molecular Weight Polyethylene

## 1.0 INTRODUCTION

The shoulder is one of the most actively used joints in the human body, having a higher range of motion relative to other joints [1-4]. End-stage glenohumeral arthritis causes loss of shoulders full function [5-12]. When severe enough, shoulder arthroplasty is necessary, providing pain relief and restoring shoulder function [5, 9, 12-15]. Although highly advanced, shoulder arthroplasty is not always as effective and durable as it can be. Problems with the glenoid prosthesis [16-21] are not uncommon, with loosening [13, 15, 22-30] being one of the major complications.

In order to improve the glenoid prosthesis design, an understanding of the scapular structure is required, especially of the glenoid morphology and the bone density distribution. Current market glenoid prostheses are of two kinds, namely, all polyethylene, and metal-backed with polyethylene insert for the articulating surface. In each of these prostheses types the fixations may be either keeled or pegged or screwed, and may be implanted with or without polymethylmethacrylate (PMMA or bone cement) [17, 31]. The choice and the overall stability of any glenoid prosthesis is dependent on numerous factors, such as quality and quantity of the glenoid bone, soft tissue balance, implantation surgical technique, presence of functioning rotator cuff, post-operative care, and the design of the prosthesis and its fixation [32, 33]. Present glenoid prostheses have been unable to fulfill the longevity requirement due to numerous reasons

such as fixation breakage, high cement stresses, and polyethylene deformations to name a few, therefore novel fixations are needed to address this issue [13, 34].

Natural bone is known to modify its shape and internal structure in response to mechanical loads, as explained by Wolff's law of adaptive bone remodeling [35-37]. It is also known that the stresses in the bone implanted with a prosthesis change compared to intact, resulting in remodeling of the bone around the prosthesis fixations and possibly causing loosening [28, 29, 38]. Recently, it has been shown that changes in the trabeculae architecture of the glenoid is related to the applied loads corresponding to functional shoulder activities [39]. To investigate bone remodeling behavior in animals or humans for an improved glenoid prosthesis design would be difficult due to numerous reasons like cost to success ratio, ethics and large amount of time requirement [37].

Therefore, the goals of this dissertation were to (i) perform structural analysis of normal and osteoarthritic glenoid, (ii) evaluate glenoid design variables effects on restoring long-lasting functionality to damaged shoulders, and (iii) create a finite element model (FEM)-based simulation process for computing subject-specific internal glenoid bone remodeling. The methodology adopted was to first understand the structure of the normal as well as the osteoarthritic glenoid, second, to evaluate improved fixations and glenoid prosthesis design variables using finite element analysis, and lastly create a finite element method to simulate the bone remodeling process.

In the next chapter, background information on the human shoulder, scapula bone anatomy, glenohumeral articulation, glenoid, glenoid prosthetic replacement, stress analyses, bone remodeling, shoulder arthritis, limitations of prior studies, significance and health relevance, and uniqueness of study are described. Chapter 3 includes a description of the glenoid

structural analyses with relevance to shoulder arthroplasty that comprised of the external and internal glenoid morphology measurements, glenoid version determination, glenoid bone density distribution, and glenoid vault depth calculation. 2D stress analyses of glenoid bone with various glenoid prosthesis design variables, and 3D stress analyses of scapula implanted with glenoid prostheses demonstrating various design variables are explained in chapters 4, and 5 respectively. Chapter 6 describes the 2D FEM-based glenoid bone remodeling simulation and validation. The conclusion and future directions are given in chapter 7.

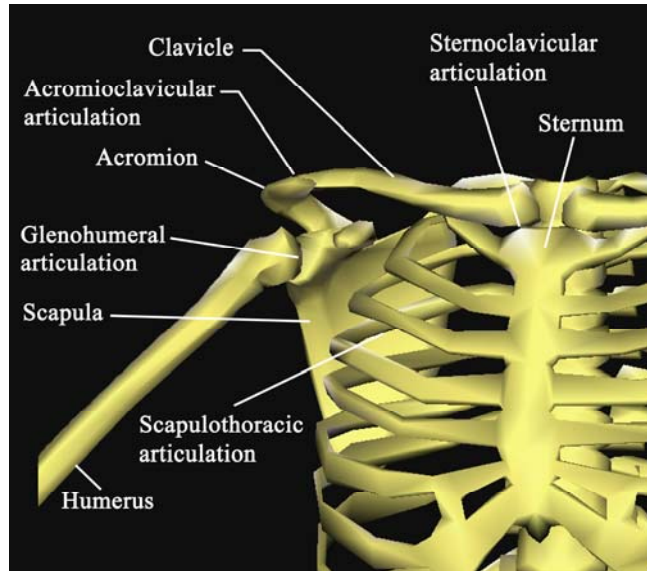
## **2.0 BACKGROUND**

### **2.1 HUMAN SHOULDER**

The shoulder is one of the most important, highly complex, and dynamic joints of the human body. It connects the upper extremity to the trunk (Figure 1). With the aid of the elbow joint and spine movement, the shoulder is able to place the hands in space and allow us to perform daily living activities. The wide range of motion of the shoulder is due to the absence of bony constraints [1-3, 40, 41].

The shoulder consists of four articulations, namely, glenohumeral, acromioclavicular, sternoclavicular, and scapulothoracic (Figure 1). The musculature and ligamentous structures acting on these various articulations provide stability to the shoulder. All the four articulations are vital for normal functioning of the shoulder. However, the major role is played by the glenohumeral joint.





**Figure 1.** An illustration of the bony structures of the shoulder and the four articulations (illustration by author).

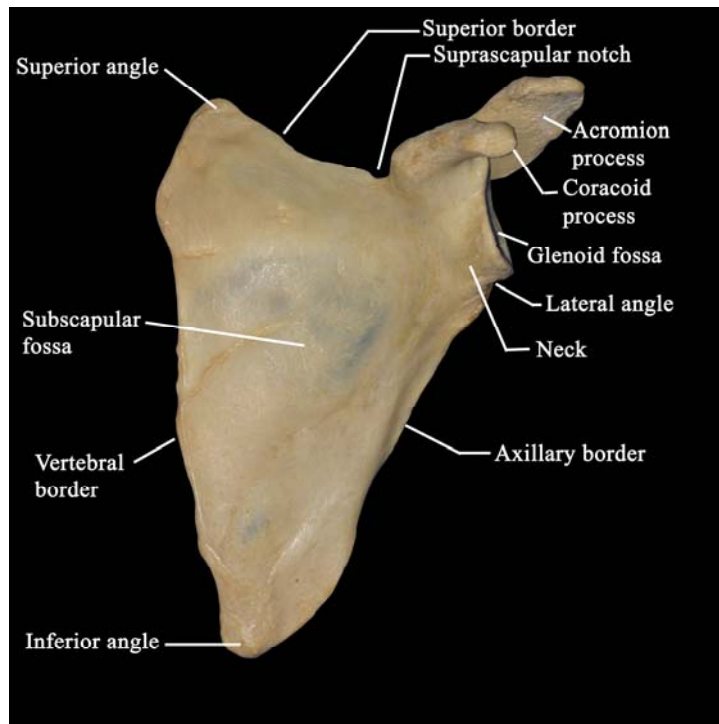
## **2.2 SCAPULA BONE ANATOMY**

The human scapula is a flat, approximately triangular bone, with two surfaces, three borders, and three angles [42]. It forms the posterior part of the shoulder girdle as illustrated in Figure 2. Other parts of the scapula are the spine, the acromion process, and the coracoid process.

Figure 3 shows the various parts of the scapula in the anterior view. The ventral surface has the concave subscapular fossa which has several lateral-superior oblique ridges providing attachment for tendinous insertions and fibers of the subscapularis muscle (Figure 3). The bone region at the medial and inferior angles attaches the serratus anterior muscle [42].

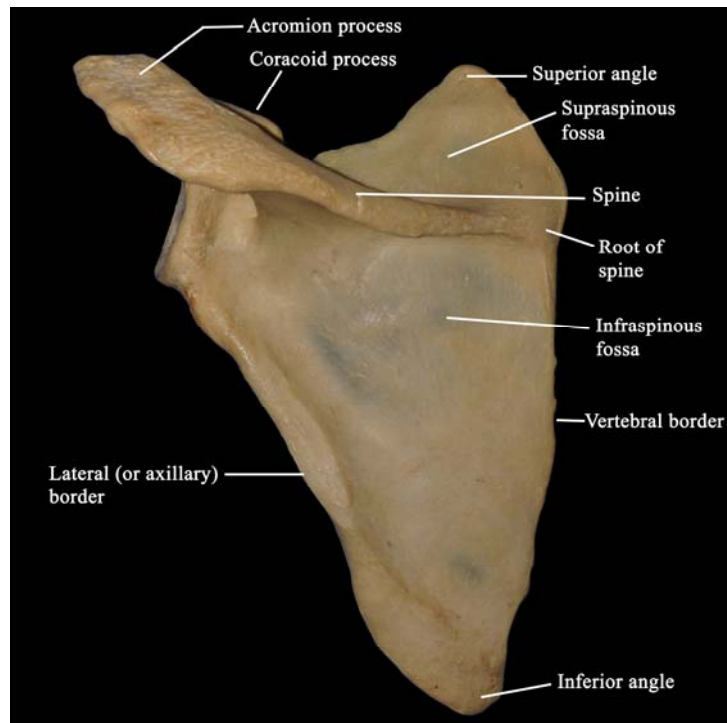


**Figure 2.** An illustration to show that the scapulae form the posterior part of the shoulder girdle (illustration by author).



**Figure 3.** The ventral surface of the human scapula showing the various parts (figure by author).

Figure 4 shows the posterior view of the scapula. The vertical medial border is parallel to the vertebral column, hence, also called the vertebral border. It meets the lateral or axillary border at the inferior angle. The axillary border extends superolaterally to the lateral angle and flares out into a short neck that flattens into the shallow glenoid fossa. The superior border meets the vertebral border at the superior angle, is indented by the suprascapular notch, and bears the coracoid process (Figure 4).

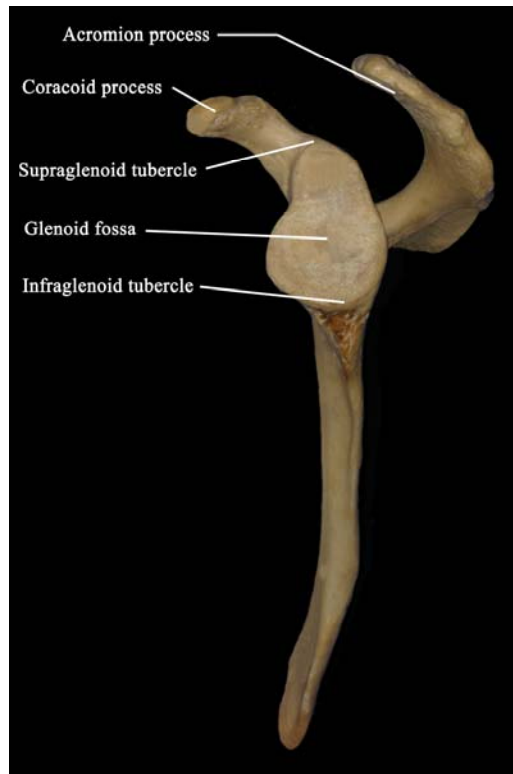


**Figure 4.** The dorsal surface of the human scapula showing the various parts (figure by author).

The dorsal surface is arched and unequally divided into two parts by the spine of the scapula. The portion above the spine is called the supraspinous fossa and that below it the infraspinous fossa (Figure 4). The supraspinatus muscle attaches at the supraspinous fossa, while the infraspinatus muscle attaches at the infraspinous fossa. The thickened lateral border provides attachment for both the teres minor and the teres major muscles. The levator scapulae, the rhomboideus minor, and the rhomboideus major muscles are attached at the vertebral border.

The spine of the scapula which starts from the vertebral border, widens as it rises laterally, extending behind the neck of the scapula and the glenoid fossa, and ending in the broad flat acromion process. This arrangement and shape of the scapula spine strengthens the thin body of the scapula and provides increased area of attachment for the deltoid and the trapezius muscles [42].

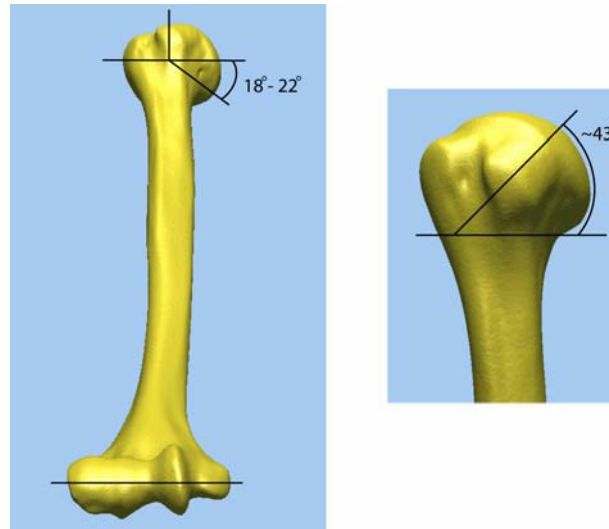
The acromion process forms the summit of the shoulder. Its superior surface is convex, and rough, while its inferior surface is concave, and smooth. Its anterior margin presents the articular facet for the lateral end of the clavicle [43]. The coracoid process is directed superiorly from the superior border, twisting sharply laterally and anteriorly like a bent hook or beak. It is the point of attachment for the several muscles that extend upward from the chest wall and the arm (Figure 5).



**Figure 5.** The lateral view of the human scapula showing the various parts (figure by author).

### **2.3 GLENOHUMERAL ARTICULATION**

The glenohumeral joint consists of the humeral head and the glenoid both of which are covered by hyaline cartilage. The articular surface of the proximal humerus forms a  $120^\circ$  arc [1]. The humeral head is retroverted approximately  $20^\circ$  with respect to the intercondylar plane of the distal humerus and has a medial inclination of approximately  $43^\circ$  giving the humerus a more anterior and lateral orientation [16, 44] (Figure 6). The proximal humerus articulates with the glenoid fossa which contains approximately one-third of the diameter of the humeral head.

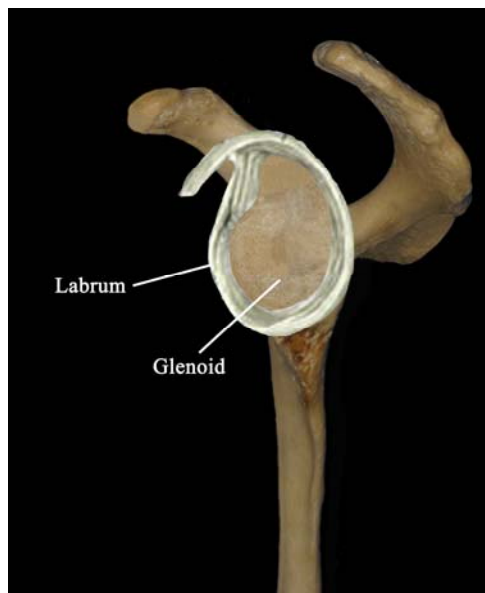


**Figure 6. The two-dimensional orientation of the articular surface of the humerus with respect to the bicondylar axis [1, 44] (figure by author).**

## 2.4 GLENOID

The glenoid is the part of the scapula forming the glenohumeral joint with the humeral head (Figure 1). The articulating surface of the glenoid is concave in curvature and surrounded by the glenoid labrum which is a fibrocartilaginous structure having a triangular cross-section that helps to increase the depth of the glenohumeral joint by approximately 50% [45] (Figure 7). The glenoid labrum attachment is firm on the inferior part of the glenoid. However it is variable and loose on the superior and anterosuperior portions. Due to the absence of bony restrictions, the stability of the glenohumeral joint is mainly provided by the musculature and ligaments surrounding it [3, 4, 46].

The size and shape of the extra-articular glenoid has been measured extensively [47-56]. The glenoid has been reported to be pear-like, oval, or inverted comma like, in shape, broader in the inferior glenoid than the superior [31, 57]. However, none of the previous studies mathematically defined the glenoid shape or any of its bony landmarks. Prior studies measured distances from the glenoid bare-spot to the inferior, anterior, and posterior boundaries, and indicated that the inferior glenoid can be fit by a circle [58, 59], but did not mathematically define the glenoid center.



**Figure 7. The lateral view of human scapula showing the glenoid labrum (figure by author).**

The glenoid version, that is, the orientation of the glenoid surface in the axial plane has been measured in numerous ways using radiographs, computer tomography (CT), or magnetic resonance (MR) images [8, 9, 46, 60, 61]. Majority of the earlier studies reported the glenoid

version for a single axial slice through the glenoid. A couple of studies had measured the glenoid version at various locations in the inferior-superior direction using different techniques [61, 62]. In these studies the glenoid version was found to become increasingly retroverted in the superior direction. Increased glenoid retroversion can cause instability of the shoulder joint, and arthritis [6, 8, 10, 46]. Prior to implanting the glenoid prosthesis surgeons try to correct the retroverted glenoid close to neutral version [5, 13, 63]. In fact, the success of the current surgical procedure is based on the surgeon's judgment and experience [13, 64-66].

The density and architecture of the glenoid cancellous bone have been found to vary with location [39, 67-71]. Some studies have used experimental methods to determine the bone strength and mechanical properties [22, 23]. Previous studies have reported relatively high density or high strength bone in the middle posterior and deep within the glenoid vault, while lower density bone has been found in the superior and central glenoid [23, 67, 70]. Knowledge of the glenoid bone-density distribution is needed not only to design fixations at structurally sound locations and orientations, but also to assign location specific material properties to the bone elements in the finite element analyses of scapula implanted with glenoid prosthesis.



## 2.5 GLENOID PROSTHETIC REPLACEMENT

Most of the current market prostheses are made of ultra high molecular weight polyethylene (UHMWPE), and are fixed using polymethylmethacrylate (PMMA) or bone cement [13, 31, 72]. “Conformity” of the glenoid prosthesis is defined as the ratio of the humeral head and glenoid prosthesis radius of curvature, while “constraint” is defined as the slope of the glenoid prosthesis articular surface at the rim [73]. The conforming glenoid prosthesis, in which the radius of curvature of the glenoid component articular surface equals that of the humeral, has shown high rates of loosening due to increased loading of the rim, and frictional torque [24, 74, 75]. On the other hand, the non-conforming glenoid prosthesis, which has the radius of curvature of the glenoid component articular surface greater than the corresponding humeral head component by 4-6mm, showed lower translational forces that may prevent the glenoid prosthesis from mechanical loosening [24, 72, 76, 77]. The all-polyethylene glenoid prostheses can be divided based on their fixations into keel and peg types [31, 72].

Radiographic studies have found radiolucent lines at the cement-bone interface in up to 30% to 95% of the glenoid prostheses [13-15, 72, 78-81]. On the other hand, symptomatic component loosening requiring revision surgery has been reported in only 2% to 6% of the glenoid prostheses [14, 15]. Also, no definite correlation has been reported between glenoid radiolucent lines and clinical loosening [14, 15, 78, 80, 82-84]. This wide range in the findings has been attributed to the variations in the radiographic technique and to the lack of standardized methods of measurements [24, 80, 83]. The radiographic findings of glenoid rotation greater than 10° from neutral [83], and radiolucent lines  $\geq 2$ mm in width [83, 85] are associated with glenoid prosthesis failure. Previous studies have reported greater incidence of radiolucent lines in glenoid prostheses with keels as compared to those with pegs [78, 80, 86]. Reduced radiolucent lines

were observed when the radius of curvature of the glenoid prosthesis articular surface was less than that in the humeral component by 6-10mm [87], and also when specially designed instruments, new glenoid prosthesis designs and modern cementing techniques were employed [13, 14, 17, 78]. The exothermic curing reaction of PMMA can cause thermal necrosis of the bone and may lead to glenoid component loosening [88].

The above findings has led groups of researchers to develop uncemented glenoid prostheses [31, 81, 82, 89, 90]. These prostheses have two parts: a metal backing for fixation and a polyethylene insert for the articulating surface [13, 31, 72]. The metal backing is usually porous coated to allow bone in-growth for long-term fixation and frequently supplemented by screws [13, 31, 72, 81].

Reduced radiolucent lines were reported in uncemented glenoid prostheses compared to the cemented [14, 82, 90-92]. Pain relief, range of motion and function for the uncemented glenoid prostheses have been reported to be comparable to cemented, however their rate of early post-surgery complications is higher [81, 91, 93]. Increased rate of polyethylene wear, dissociation of polyethylene insert from metal-backing and screw breakage has reduced enthusiasm for their use [81, 94-97]. Polyethylene wear particles can cause macrophage mediated biologic response leading to osteolysis of periprosthetic bone and loosening [96, 98, 99].

Numerous parameters need to be considered when designing glenoid prosthetic replacements. These include the glenoid shape and size, intra-articular morphology, glenoid vault depth, bone-density distribution, glenohumeral conformity, fixation type (keel or pegs), fixation location and orientation, prosthesis thickness, cemented or uncemented, and biomaterials [13, 17, 31]. The success of total shoulder arthroplasty depends not only on the prostheses design but also

on its accurate placement, restoration of soft-tissue balance, correction of glenoid version to neutral, and the biomechanics of the shoulder post-surgery [16-18, 25, 57, 99-101].

Previous studies have reported normal biomechanics and function post-surgery in patients implanted with non-conforming prostheses and having good musculature, soft-tissue balance and intact rotator-cuff [5, 31, 76, 99, 102]. Increased shoulder instability following arthroplasty has been attributed to soft-tissue imbalance, deficient rotator-cuff, incorrect glenoid and humeral prostheses placement, and excessive glenoid retroversion [16, 17, 63, 103-105].

The choice of glenoid prosthesis is based on the pathology with total shoulder replacement giving better pain relief and kinematics in patients with intact rotator-cuff than without [13, 20, 106, 107].

Humeral hemiarthroplasty, a surgical procedure in which only the humeral prosthesis is implanted, and performed in rheumatoid arthritis patients with lower density of glenoid bone and rotator-cuff deficiency has been reported to restore function comparable to total shoulder arthroplasty [106, 108-112], but lower pain relief and range of motion [17, 109, 110, 113].

Surface replacement arthroplasty introduced in the 1980s is performed to replace only the humeral head in shoulder arthritis patients providing pain relief and range of motion comparable to stemmed humerus arthroplasty [114-118]. Some of the advantages of the surface replacement prostheses compared to the stemmed are minimal bone removal, bone preservation, recreating patient's humeral head anatomy, reduced risk of humeral shaft fractures, and no need for sophisticated instruments to measure humeral head version, inclination and offset [114, 117-120].

Reverse total shoulder arthroplasty is a treatment option for severe glenohumeral arthritis patients with an irreparable rotator cuff [121-128]. Recent studies have reported promising

results in terms of pain relief and increased range of motion using the current market reverse shoulder prostheses designs [121, 122, 124-126, 128, 129] but concerns about the higher revision rates, component wear, and loosening need to be addressed for their long-term success [121, 124-126, 130-132].

## 2.6 STRESS ANALYSIS

Numerical simulation and biomechanical testing allows researchers to compare the stresses in the intact scapula [26, 27, 33, 38, 133-137], and the glenoid implanted with the various cemented all-polyethylene [25-30, 32, 136, 137], cemented metal-backed [27, 135, 138] and uncemented metal-backed prostheses designs [26, 33, 38]. The following is a brief summary of key findings of some of the prior studies.

(i) Stress distribution in the glenoid implanted with the cemented all-polyethylene prosthesis was closer to intact compared to the other prostheses designs [26]. Further more the glenoid bone stresses with the cemented all-polyethylene pegged glenoid prosthesis better approximated the intact bone stresses than the keeled type [28, 139]. Anatomic placement of the keel fixation resulted in a more natural stress distribution compared to the central keel design [32, 33].

(ii) Glenoid bone stresses increased with greater cement layer thickness [26, 29, 30] and were minimum when the cement layer thickness was between 1-1.5mm [30]. Cement layer stresses increased with reducing cement layer thickness [30] and were lower in all-polyethylene

prostheses compared to the metal-backed [27]. Failure stress levels were reported in the cement layer of cemented metal-backed prostheses. On the other hand, the stresses at the metal-bone interface of uncemented metal-backed prostheses were lower than the bone failure stress [38].

(iii) Compared to intact, greater reduction in the glenoid bone stress was found with the metal-backed prostheses than the all-polyethylene designs, causing possible stress shielding of the proximal trabecular bone, and probably resulting in glenoid prostheses loosening [26, 27, 38, 135]. Lower stresses were reported in the polyethylene insert of metal-backed prostheses compared to the all-polyethylene designs [38]. Higher polyethylene insert-metal interface stresses were found for metal-backed prostheses which could result in their dissociation [38].

(iv) Higher glenoid bone and cement layer stresses, strains and humeral head translations were found for the low conforming prostheses compared to the high conforming designs [29, 102, 135, 136, 140]. However, in the high conforming prostheses there was greater glenoid rim loading which could cause increased tensile stresses resulting in the rocking horse effect, polyethylene deformation, wear and loosening [102, 135-137, 141].

(v) Eccentric loading of the glenoid implanted with the all-polyethylene prostheses resulted in higher stresses and strains in the bone and the cement layer, and increased the tendency for posterior bending of the prostheses as compared to the metal-backed prostheses designs [25, 29, 102, 137].

(vi) Glenoid prostheses with a curved-backing, and rough fixation surface or threaded pegs resulted in lower prosthesis displacements and greater prosthesis distraction forces compared to the flat-backed, and smoother fixations thereby reducing the rocking horse effect and loosening [139, 141, 142]. All-metal keeled glenoid prostheses implanted with

supplementary screws and cement provided better fixation compared to uncemented designs [143].

## **2.7 BONE REMODELING**

The human bone is known to constantly remodel that is change in external morphology and internal structure based on the mechanical load it experiences throughout a lifetime. In other words, increased mechanical load above a certain threshold would cause bone apposition and reduced mechanical load below a certain threshold would result in bone resorption. This phenomenon is known as Wolff's Law of adaptive bone remodeling. It is important to understand this behavior of bone to decrease glenoid prosthesis loosening, and increase prosthesis longevity [35-37].

Previous investigators have explained the bone external and internal remodeling behavior using stress and strain related numerical theories [36, 37, 144] and obtained satisfactory results. These remodeling theories have been successfully used to understand some of the effects of prosthesis on the bone density distribution in the femur and the tibia bone using the finite element analysis method [35, 37]. For the femur models with surface prosthesis, increased bone resorption was observed around the peg compared to the metal cap and metal cap with loosened edges [35]. In another study the density changes around the femur implant stem in an animal

model were found to compare well with those of the computer simulation [36]. Also, increased density was obtained near the tip of the femur prosthesis stem compared to the non-operated femur. To the best of the author's knowledge there have been no prior subject-specific studies to simulate the normal glenoid bone remodeling or remodeling in response to implanted glenoid prostheses. A recent study developed formulae to predict the orientation of the glenoid trabeculae architecture and studied its changes due to various loads corresponding to some functional activities [39, 145].

Despite the sophistication of the remodeling computer simulations much still needs to be accomplished in terms of the values of the various constants, and the appropriate load and boundary conditions for subject-specific remodeling. Once successful, the remodeling process could be an invaluable tool for engineers to design and test optimized glenoid prostheses in a cost effective manner [37].

## **2.8 SHOULDER ARTHRITIS**

Arthritis is the leading cause of disability in the population of the United States [146]. In 2002, 43 million American adults reported physician-diagnosed arthritis and another 23 million people reported chronic joint symptoms including pain, aching, stiffness and swelling [147]. These numbers are expected to rise as the population ages [148]. The annual estimated costs for arthritis medical care are more than \$150 billion [149]. Osteoarthritis is the most common form of arthritis and is estimated to affect 21 million adults [150]. Various risk factors have been

associated with osteoarthritis including age, gender, ethnicity, bone density, nutrition, obesity, articular cartilage loading, joint trauma, occupation, sports participation, and physical disability [146, 147, 151].

Primary osteoarthritis of the shoulder includes glenohumeral joint stiffness, joint space reduction, osteophytes, rotator cuff with minimal lesions, and increased retroversion [8-11]. Glenohumeral arthritis causes pain and shoulder dysfunction and is treated by shoulder arthroplasty consisting of total shoulder arthroplasty, hemiarthroplasty, surface replacement, or reverse shoulder arthroplasty [12]. The procedure choice is dependent on the underlying pathology and extent of rotator cuff tear [13, 17]. In the year 2002, the total number of shoulder replacement procedures performed in United States were 23,000 which included 7000 total shoulder arthroplasties and 16,000 hemiarthroplasties [152]. Another 17,000 procedures were performed for shoulder repair or revision arthroplasty [152]. Although, shoulder arthroplasty provides immediate pain relief and function post-surgery, there is limited long-term success with revisions required in 2%-10% of the patients after on average 5 years [14, 15, 153].

## **2.9 LIMITATIONS OF PRIOR STUDIES**

The extra-articular glenoid morphology has been measured and reported to be pear-like, oval or inverted-comma in shape [31, 48-57]. Also, the inferior glenoid region has been shown to be fitted by a circle, and measurements have been made from the glenoid bare spot to the inferior, anterior, and posterior margins [58, 59]. However, none of the studies have mathematically



defined the shape of the glenoid and the location of key bony landmarks including the glenoid center.

Glenoid version [6, 8-10, 46, 60-62] and bone-density distribution [22, 23, 67-71] has been measured extensively, but there are no studies quantifying the intra-articular morphology and modeling the glenoid vault depth at multiple locations using CT images.

Numerous studies have performed finite element stress analyses [25-30, 32, 33, 38, 133-135, 154, 155] and biomechanical testing [102, 136, 137, 139-143, 156-158] of intact scapula and existing prostheses, and suggested criteria for prostheses design however none has designed or tested improved glenoid prostheses based on the glenoid size, extra- and intra-articular shape, bone depth and bone-density distribution.

Although prior finite element analysis studies of the shoulder use location-specific bone material properties, physiologic joint reaction and muscle loads, and realistic boundary conditions, none have incorporated Wolff's Law to simulate normal glenoid bone remodeling or remodeling in response to implanted glenoid prostheses.

## **2.10 SIGNIFICANCE AND HEALTH RELEVANCE**

Osteoarthritis is one of the most prevalent and leading cause of disability affecting about 21 million people in the United States [146, 147, 150]. It is estimated that the number of people aged 65 years and over diagnosed with arthritis will increase more than two fold by the year 2030 [148]. Osteoarthritis affects the quality of life and the total annual expenses for its

treatment have been estimated to be in excess of \$150 billion [149, 159]. In the year 2000, more than 12 million physician visits have been attributed to shoulder problems [160]. Glenohumeral arthritis causes pain and shoulder dysfunction and decreases the ability of people to perform activities of daily living [6, 8-12]. Numerous treatments for arthritis are: (i) physical therapy to reduce pain, improve strength, and range-of-motion of the joint, (ii) pharmaceutical medications to reduce pain and inflammation, (iii) joint resurfacing which may be achieved in two ways, firstly, using biologic medium containing growth factors to restore the cartilage or if the cartilage is completely worn-out then artificial surfaces are used (total shoulder arthroplasty for glenohumeral arthritis), and (iv) surgical techniques for bone debriment, and cartilage repair. This dissertation concentrated on the glenoid resurfacing with prosthesis. Furthermore, the focus was on the biomechanics of the glenoid prosthesis using numerical analysis. Shoulder arthroplasty, a highly advanced surgical procedure [5, 9, 13], is able to provide pain relief and function in arthritic shoulders, but long-term success is low with revision required in 2%-10% of the patients [12, 14, 15, 153]. The most common post-shoulder arthroplasty problem has been glenoid prosthesis loosening [13, 15, 22-30, 157]. Previous studies have indicated that prosthesis loosening depends not only on its design, but also on the underlying pathology, rotator cuff tear, glenoid version, prosthesis placement and fit, and cement layer thickness [13, 16-19, 30, 32, 33, 48, 52, 133, 135, 154]. By designing improved glenoid prostheses based on the complete glenoid structure including the bone-density distribution, along with the relevant surgical instruments the objective of restoring long-lasting functionality to damaged shoulders can be expected to be fulfilled.

## 2.11 UNIQUENESS OF STUDY

The research study was innovative and unique in the sense of the approach adopted. The designing and testing of the glenoid prosthesis began with an extensive analysis of the normal and osteoarthritic glenoid structure giving mathematical relationships between key bony landmarks on the glenoid. This gave an understanding of the glenoid external and internal morphology, bone density distribution and bone depth, allowing for the evaluation of glenoid prostheses with fixations at appropriate locations and orientations that capture the high density bone and help reduce loosening. The well documented non-destructive methods of computer modeling and finite element analysis were then used to compare the stresses in the intact scapula, to that of scapula implanted with prostheses with various design features. To the best of the author's knowledge no previous investigation had incorporated the Wolff's law of adaptive bone remodeling in their analysis of the shoulder. In this study the finite element based bone remodeling process was simulated and validated for the first time in the normal glenoid. The strain-energy based remodeling theory explained in the literature was adapted for the glenoid. The tools and techniques developed were generic and can be used for any human joint or bone.

### **3.0 GLENOID STRUCTURAL ANALYSES**

#### **3.1 INTRODUCTION**

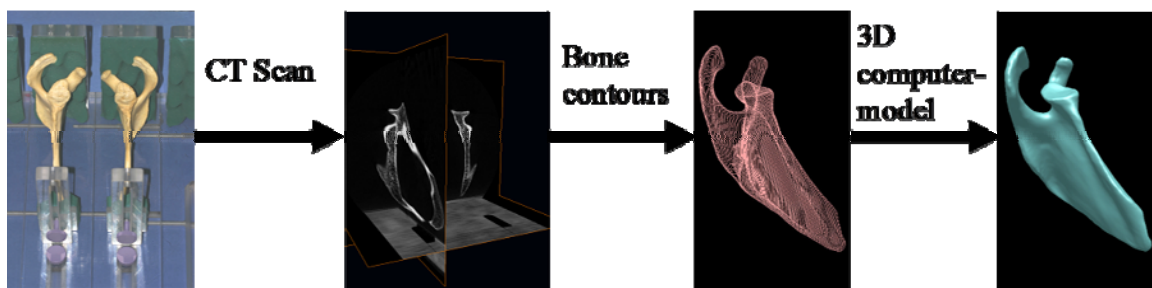
The most common complication of total shoulder arthroplasty is prosthesis loosening mainly due to the quantity, and orientation of bone available for fixation [13, 48, 51, 70]. Current glenoid prostheses, although highly advanced, lack longevity. Increasing glenoid prosthesis longevity requires an understanding of the scapular structure, especially the glenoid morphology and bone density distribution. Also, majority of the glenoid prosthesis designs are based on the normal scapula, however they are implanted mostly in patients diagnosed with osteoarthritis of the shoulder.

Previous investigators have used radiographs, CT, MRI or cadaver measurements to study the external bone morphology of the scapula [8, 48, 49, 51, 53, 58, 61, 161-163], with none quantifying the internal glenoid bone morphology. The purpose of this study was to employ modern computer modeling techniques to quantify external and internal glenoid morphology and bone density distribution in both the normal and osteoarthritic scapulae specimen, and relate these findings to improve arthroplasty.

### 3.2 MATERIALS AND METHODS

20 pairs of normal scapulae cadavers, 11 male ( $50.2 \pm 11.8$  years), and 9 female ( $60 \pm 20.5$  years), were obtained from donors in the Midwestern United States. None of the scapulae had any pathology except negligible osteoarthritis. Each scapula pair was radiographed and then underwent volumetric high-resolution axial computed tomography (CT) imaging using a custom designed stand. Also, 3 scapulae, 2 male (74, and 64 years) and 1 female (59 years), diagnosed clinically with severe OA underwent volumetric high-resolution axial CT imaging.

The CT images were electronically transferred and imported into 3D visualization and modeling software Amira® 3.0 (TGS, Inc., San Diego, CA, USA). Bone segmentation was performed using threshold and region growing. The resultant axial bone contours were converted to tessellated surfaces in Amira®.



**Figure 8.** The process used to create 3D scapula computer model from computed tomography images (figure by author).

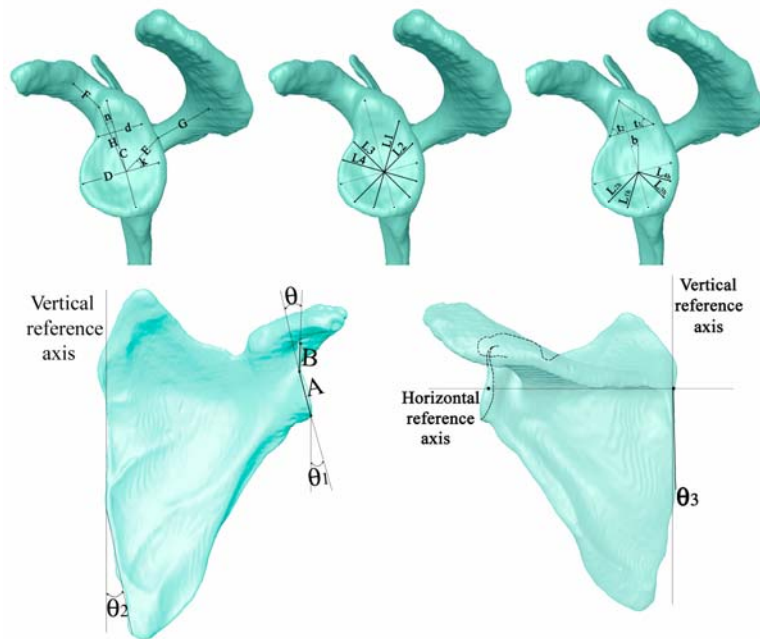
The external morphological measurements performed were (Figure 9):-

- (1) C: superior-inferior glenoid length between the supra- and infra-glenoid tubercle.
- (2) D: anterior-posterior width of the glenoid. Diameter D was perpendicular to segment C and their intersection point was considered as the centre of the glenoid articulating surface.
- (3) d: anterior-posterior width in the superior portion of the glenoid measured between the notch on the anterior boundary and the point on the posterior boundary ( $d \perp C$ ).
- (4) F and G: minimum distance of the coracoid and the acromion process from the glenoid boundary respectively.
- (5) E, H,  $k^\circ$ , and  $n^\circ$ : located two reference points on the glenoid boundary closest to the acromion and the coracoid processes respectively.
- (6)  $L_1$ ,  $L_2$ ,  $L_3$ , and  $L_4$ : gave the overall morphology of the glenoid.
- (7)  $t_1^\circ$ ,  $t_2^\circ$ , and  $\Delta ht$ : base angles and height of the approximate superior triangle.
- (8)  $L_{1h}$ ,  $L_{2h}$ ,  $L_{3h}$ , and  $L_{4h}$ : radial lengths in inferior glenoid region.

Anterior and posterior view measurements were made only for the normal scapulae specimen to compare with prior studies (Figure 9).

For the internal bone morphological analysis, three axial slices of each of the scapulae specimen were considered. The axial slices were taken at three different locations as shown in Figure 10. The approximate geometries fitted on axial slices 1, 2, and 3 of scapula are shown in Figure 10. The subchondral bone glenoid version ( $a^\circ$ ) and the glenoid version ( $m^\circ$ ) were measured with respect to the horizontal reference axis. The segments D', U, V, W, X, and Y (in slice 3 only) were kept within the outer boundary of cortical bone. The anterior and posterior

margin angles  $r^\circ$  and  $s^\circ$  were measured in all the three axial slices whereas angles  $p^\circ$  and  $q^\circ$  were measured only in slice 3.



**Figure 9.** The glenoid external morphology measurements on the 3D scapula computer model (figure by author).

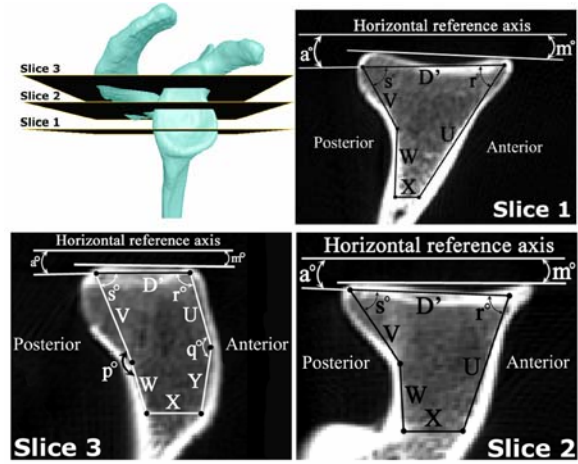


Figure 10. The internal glenoid morphology measurements in the three selected axial slices (figure by author).

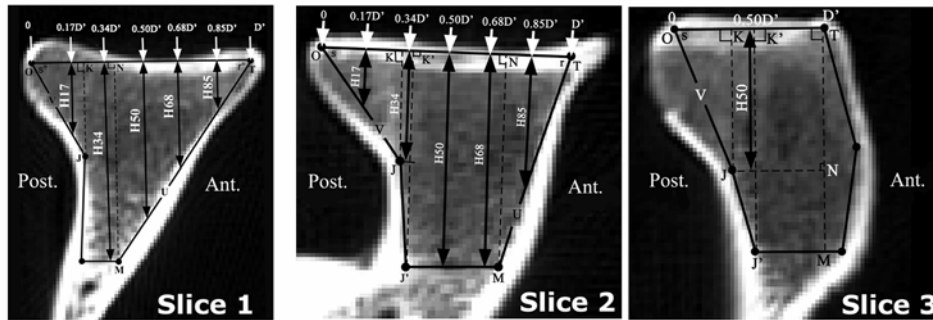
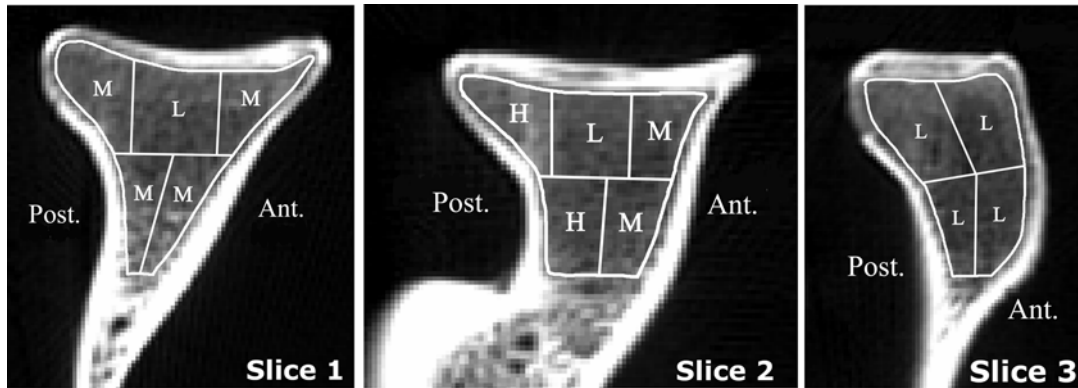


Figure 11. The glenoid vault depth calculated at multiple locations in the three selected axial slices (figure by author).





**Figure 12.** The glenoid regional bone density in the three selected axial slices recalibrated as L=relatively low density, M=relatively medium density, and H=relatively high density (figure by author).

The glenoid vault depth was calculated from the approximate geometrical shape fitted in axial slices 1, 2, and 3 (Figure 11). Trigonometric relations were used to calculate the bone depth perpendicular to segment  $D'$  at distances equal to 17% ( $0.17D'$ ), 34% ( $0.34D'$ ), 50% ( $0.50D'$ ), 68% ( $0.68D'$ ), and 85% ( $0.85D'$ ) of its length, from posterior to anterior, for axial slices 1, and 2. In axial slice 3 the bone depth was calculated only at  $0.50D'$ .

For the regional bone density measurements, the axial slices 1, and 2 were divided into five regions of interest, whereas the axial slice 3 was divided into four regions of interest. All the measurements were done in Amira® (Figure 12).

The mean and standard deviation of all the parameters were computed for both, the normal and the osteoarthritic scapulae specimen. For the normal scapulae specimen, two-tailed paired t-test was used to determine the difference between right and left scapulae while two-tailed independent samples t-test was used to determine difference between scapulae from male and female donors. Similar tests were used to determine the difference between right and left, and male and female scapulae specimen with regard to (i) length of segment  $D'$ , and (ii) value of

angles  $a^\circ$ ,  $m^\circ$ ,  $r^\circ$ , and  $s^\circ$ , for each of the three axial slices. One way ANOVA was used to check if the inferior glenoid region can be approximated by a circle. Linear regression analysis was performed for the following morphological parameters: length of segments D, d,  $\Delta ht$ , E, F, G, H,  $L_1$ ,  $L_2$ ,  $L_3$ ,  $L_4$ ,  $L_{1h}$ ,  $L_{2h}$ ,  $L_{3h}$ ,  $L_{4h}$ , A, B, and D', and value of angles b, k, n,  $t_1$ ,  $t_2$ , and  $\theta$ .

For the normal and the osteoarthritic scapulae the mean and standard deviation of the bone density values in each of the three axial slices were computed. The obtained mean values were calibrated into a three-point scale of “High”, “Medium”, and “Low”. Also, the mean and standard deviation of the glenoid vault depth at the different locations were calculated for each of the three axial slices.

To test for accuracy, and reliability the length of segments C, and D, and the value of angles  $b^\circ$  and  $\theta^\circ$ , were re-measured for twenty randomly selected normal scapulae. Measurements were made on the actual scapulae specimen using precision calipers and on the computer models of the scapulae specimen using the software Amira®. Accuracy was defined as the average difference between the caliper measurement and the original computer model measurement of the same scapula. Reliability was defined as the difference between repeated and original computer model measurements. Repeatability was the measure of reliability relative to the variation among specimens.

The mean for various parameters in the external and internal morphology measurements were compared between the normal and the osteoarthritic scapulae specimen. All the statistical analyses were carried out using SPSS software (SPSS Inc.), with level of significance set at 0.05.

### 3.3 RESULTS

#### *Normal Scapulae Specimen:*

Figure 13 shows select glenoid external morphology measurements graphically (the mean, standard deviation, range, p-value for male-female difference, and right-left difference for the glenoid external morphology parameters are given in Table 12 and Table 13, see Appendix A).

The superior-inferior glenoid length (C) and the anterior-posterior glenoid width (D) were greater in males (C:35±2mm, D:26±2mm) than females (C:33±2mm, D:22±2mm, p=0.004) and equal in right and left scapulae specimen (C:34±3mm, D:24±3mm, p>0.05). The anterior-posterior glenoid width at the anterior notch (d) was equal between male and female, and right and left scapulae specimen (~18±2mm, p>0.05). The radial length measurements ( $L_{1h}$ - $L_{4h}$ ) were greater in males (mean±SD:11.9±1mm) than females (10.3±1mm) (p<0.05). The inferior glenoid boundary was found to be approximated by a circle (mean radius:11.1±1mm). The glenoid tilt ( $b^\circ$ ) and the base angles ( $t_1^\circ$ ,  $t_2^\circ$ ) of the superior approximate triangle were found to be equal in male (14°±3°, 48°±3°, 56°±4°) and female (15°±3°, 47°±4°, 54°±4°) scapulae specimen respectively (p>0.05). The height of the approximate superior triangle ( $\Delta ht$ ) and segment A were found to be greater in males (12±2mm, 22±2mm) than females (11±1mm, 18±2mm) respectively. Angles  $k^\circ$  (56°±6°), and  $n^\circ$  (11°±2°) were found to be equal in the scapulae specimen respectively.

### Glenoid External Morphology Measurements

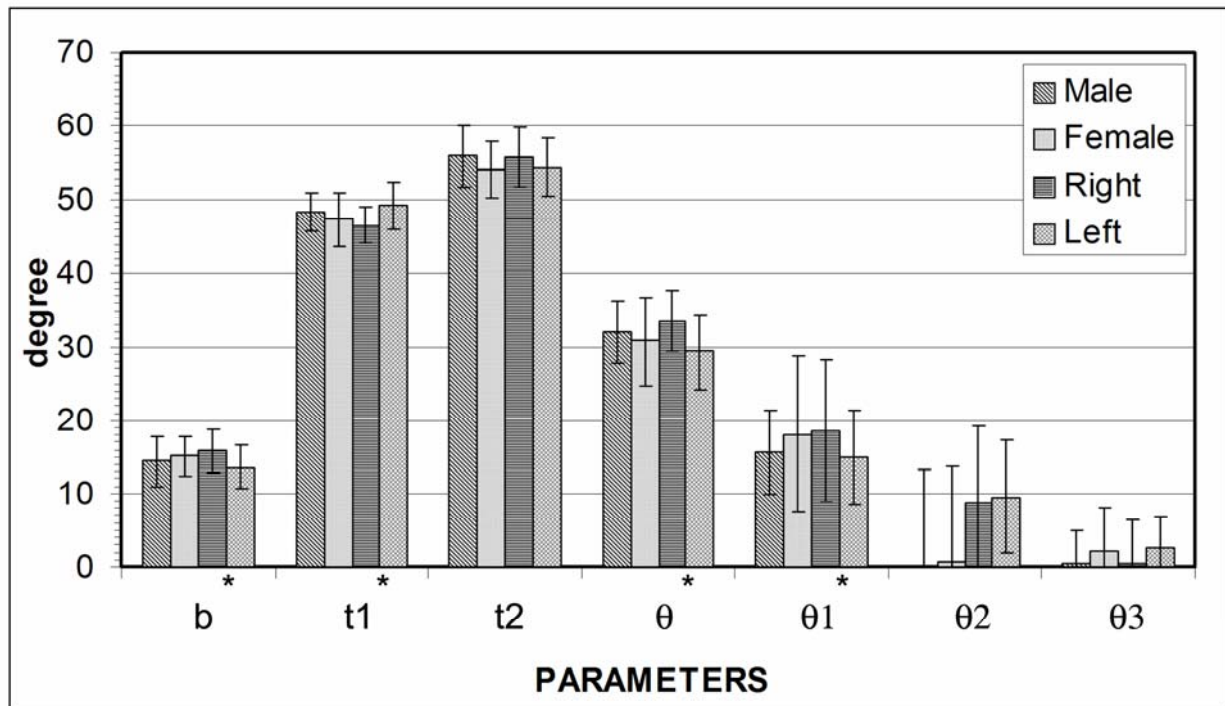
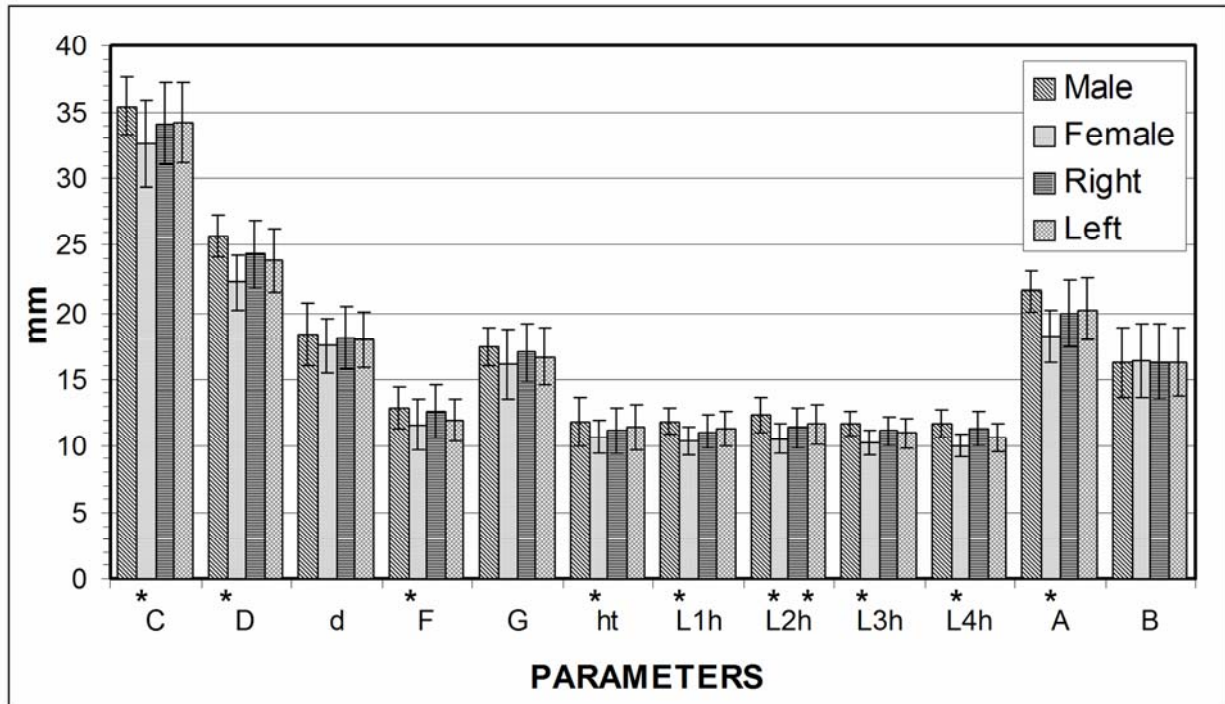


Figure 13. The glenoid external morphology measurement values in normal scapulae specimen for select parameters (\*: p<0.05) (figure by author).

## Glenoid Internal Morphology Measurements

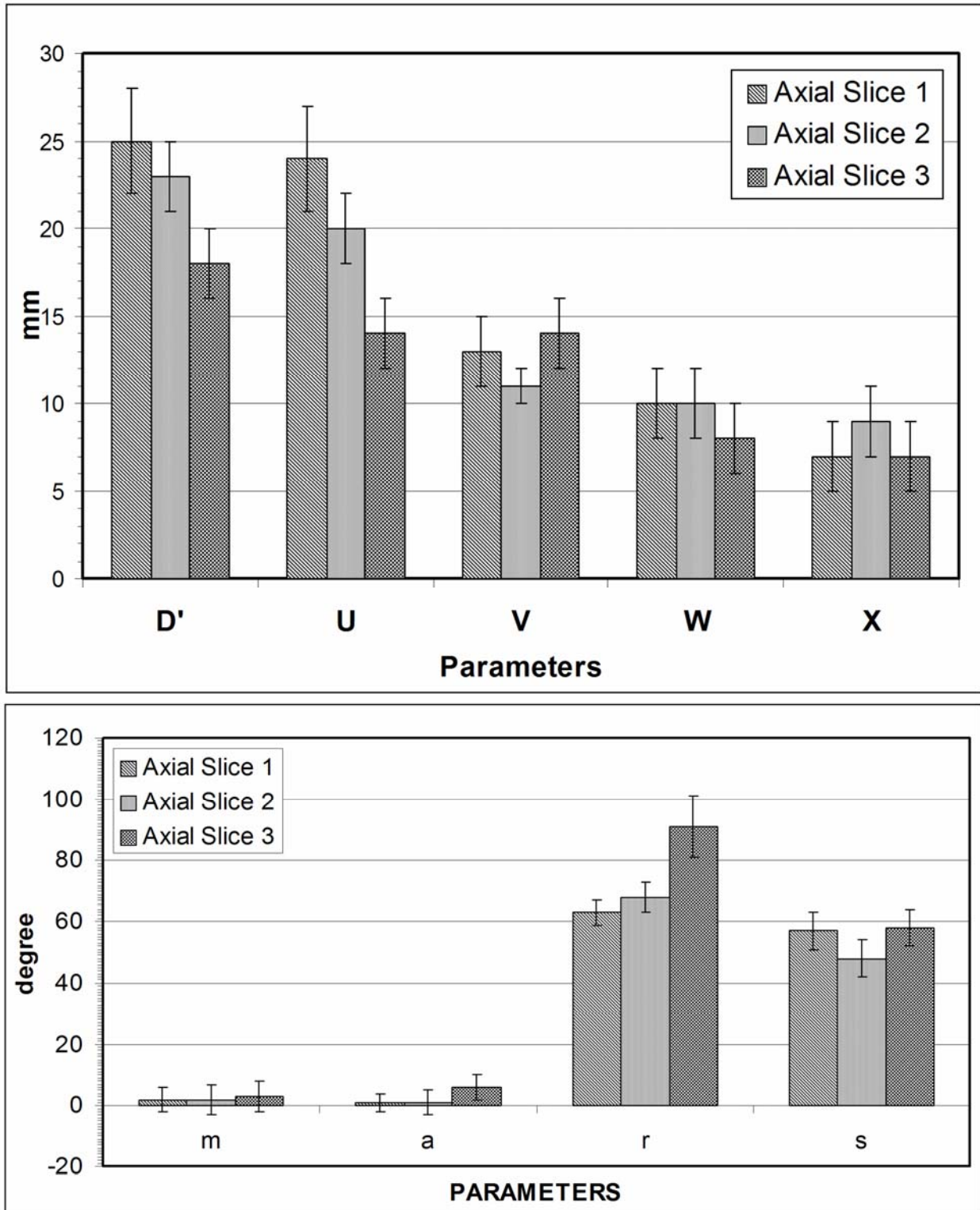


Figure 14. The glenoid internal morphology measurement values in normal scapulae specimen for select parameters (figure by author).

**Table 1. The p-values for the male-female and right-left difference for select internal glenoid morphology parameters in the normal scapulae specimen (\*: Slice 1, #: Slice 2, §: Slice 3).**

<b>Internal Glenoid Morphology Parameters</b>	<b>P value for Male-Female Difference</b>	<b>P value for Right-Left Difference</b>
<b>D' (mm)</b>	0.000 *	0.235 *
	0.008 #	0.002 #
	0.109 §	0.000 §
<b>a (degree)</b>	0.845 *	0.603 *
	0.926 #	0.892 #
	0.694 §	0.227 §
<b>m (degree)</b>	0.022 *	0.951 *
	0.010 #	0.953 #
	0.159 §	0.326 §
<b>r (degree)</b>	0.271 *	0.189 *
	0.029 #	0.079 #
	0.330 §	0.406 §
<b>s (degree)</b>	0.176 *	0.334 *
	0.784 #	0.726 #
	0.058 §	0.146 §

Figure 14 shows the internal morphology measurement values for select parameters graphically (the mean, standard deviation, and range for the glenoid internal morphology parameters are given in Table 14, see Appendix A). Table 1 gives the p-values for the male-female and right-left difference for select internal glenoid morphology parameters in the axial slices 1, 2, and 3.

Lengths D', and U decreased from slice 1 to slice 3, V was minimum in slice 2, whereas length X was maximum in slice 2, and W was approximately equal in slices 1, and 2 and slightly reduced in slice 3. D' value in slices 1 and 2 was greater in males ( $26\pm 1\text{mm}$ ,  $24\pm 1\text{mm}$ ) than females ( $23\pm 3\text{mm}$ ,  $22\pm 2\text{mm}$ ,  $p < 0.05$ ) respectively, and equal in slice 3 ( $p = 0.108$ ). While D'

value in slices 2 and 3 was greater in rights ( $24\pm 2\text{mm}$ ,  $19\pm 2\text{mm}$ ) than lefts ( $22\pm 2\text{mm}$ ,  $17\pm 2\text{mm}$ ,  $p<0.05$ ) respectively. The anterior margin angle ( $r^\circ$ ) increased from slice 1 to slice 3, while the posterior margin angle ( $s^\circ$ ) was minimum for slice 2, and approximately equal for slices 1, and 3.

The glenoid version ( $m^\circ$ ), and the subchondral glenoid bone version ( $a^\circ$ ) were more retroverted in superior glenoid (negative values signify retroversion). Glenoid version in the three selected axial slices 1, 2, and 3 was more retroverted in males ( $-2.86^\circ\pm 4.22^\circ$ ;  $-3.2^\circ\pm 3.93^\circ$ ;  $-4.17^\circ\pm 4.02^\circ$ ) than females ( $0.24^\circ\pm 3.92^\circ$ ;  $0.4^\circ\pm 4.42^\circ$ ;  $-2.07^\circ\pm 5.23^\circ$ ) respectively, and approximately equal between right and left scapulae specimen ( $p>0.05$ , Figure 15).

The maximum glenoid vault depth ( $H50=20\pm 0.1\text{mm}$ ) was at the glenoid center in slice 1, while the minimum depth ( $H17=4.4\pm 0.5\text{mm}$ ) was found on the posterior side in slice 2 (Figure 16). The male specimens had greater glenoid vault depth in most of the locations than female (Figure 16). The mean, and standard deviation of the various regions of interest in the three selected axial slices were not clinically equivalent since the cadaver specimen were dried and CT scanned in air (Table 18, see Appendix A). Hence the values obtained were calibrated into relatively Low ( $L\leq -360\text{HU}$ ), Medium ( $-360\text{HU}<M<-200\text{HU}$ ), and High ( $H\geq -200\text{HU}$ ) density regions. The maximum regional bone density was found in the posterior part of slice 2, whereas lower density bone was found in the central and superior glenoid regions (Figure 12).

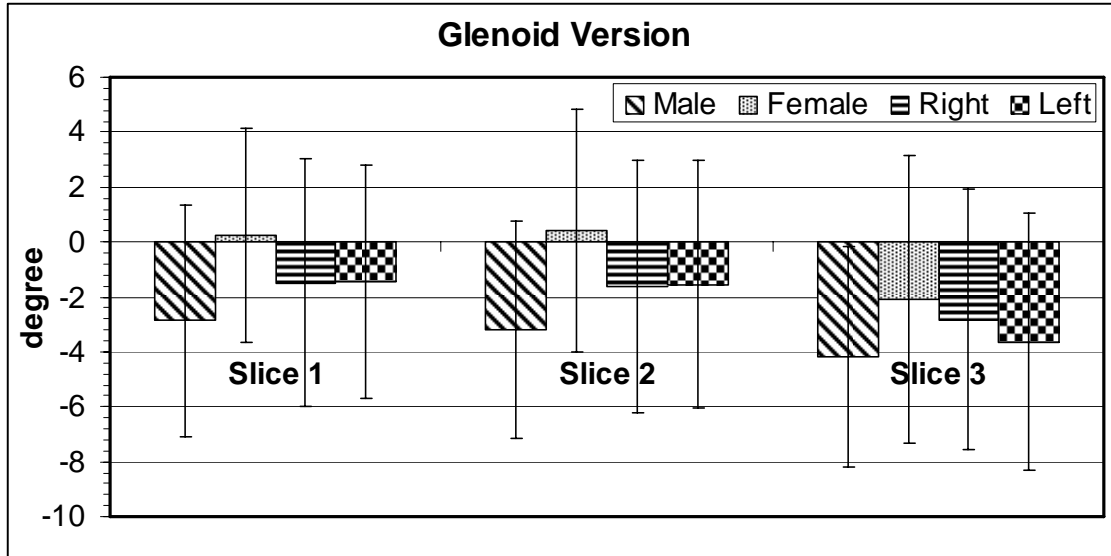


Figure 15. The mean glenoid version ( $a^\circ$ ) in the three selected axial slices of the normal scapulae specimen (figure by author).

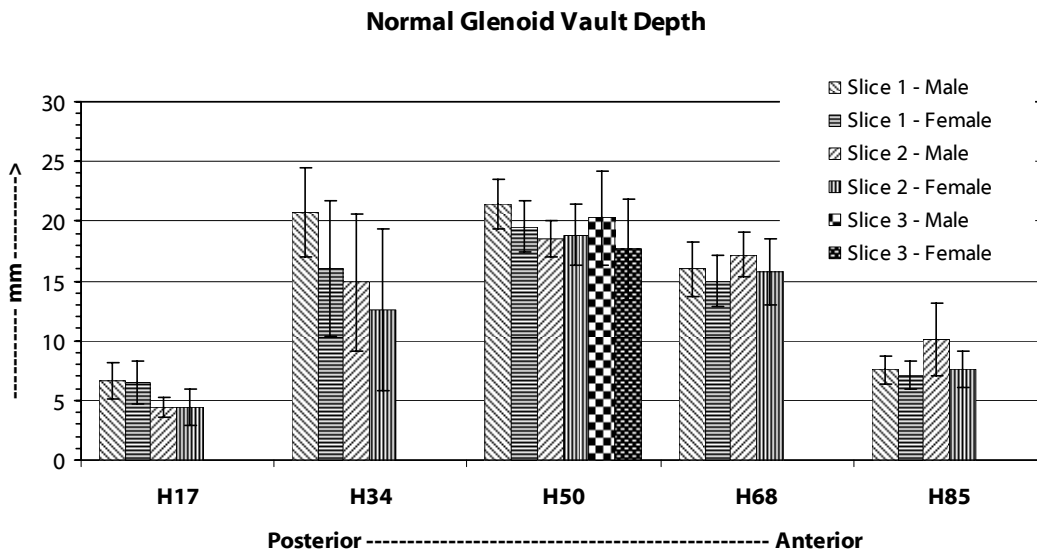


Figure 16. The mean and standard deviation of normal glenoid vault depth values at multiple locations in the selected axial slices of the normal scapulae specimen (\*:  $p < 0.05$ ) (figure by author).



Segment C was very highly correlated with segment H ( $r=0.92$ ). Also, segment D was very highly correlated with segments  $L_2$  ( $r=0.92$ ) and  $L_4$  ( $r=0.93$ ). Medium correlation was obtained between segments C and D ( $r = 0.8$ ),  $L_1$  ( $r=0.79$ ), and  $L_3$  ( $r=0.78$ ). In Appendix A, Table 19, Figure 51, Figure 52, Figure 53, and Figure 54 give the correlation coefficients and the linear regression analysis of select external and internal bone morphological parameters.

Table 2 gives, for parameters C, D,  $b^\circ$ , and  $\theta^\circ$ , the mean, standard deviation, and range of the difference between the repeated and the original measurements made on the scapulae computer models, and the actual scapulae specimen and the corresponding computer models. In both these cases, the mean difference in the length measurements were less than or equal to 0.5mm with a standard deviation of less than 1mm and that in the angular were less than  $2^\circ$  with a standard deviation of less than or equal to  $4.4^\circ$ . The repeatability of the measurements was high, with the difference between the original and repeat measurements representing 0.5%, and 2% of measurement variation for lengths C, and D respectively, and 9%, and 6% of measurement variation for angles  $b^\circ$  and  $\theta^\circ$  respectively, among the scapulae specimen.

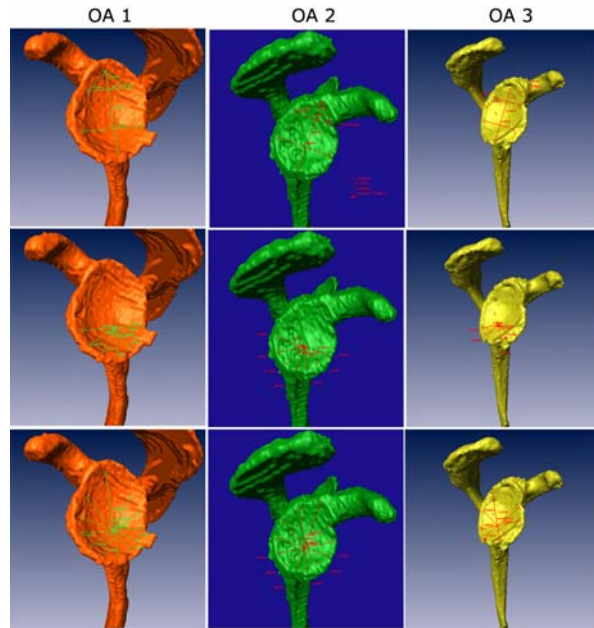
**Table 2. The mean, standard deviation, and range of the difference between the actual specimen and computer model (accuracy), and the repeated and original computer model (reliability) measurements of the scapulae morphology parameters.**

<b>Parameter</b>	<b>Mean Difference (Physical – Model) ± S.D. (Range)</b>	<b>Mean Difference (model) (Repeated – Original) ± S.D. (Range)</b>
<b>C (mm)</b>	0.4 ± 0.9 (-1.5-2.2)	-0.2 ± 0.6 (-1.8-0.9)
<b>D (mm)</b>	0.3 ± 0.8 (-1.2-2.0)	0.5 ± 0.7 (-0.5-1.5)
<b>b (degree)</b>	1.2 ± 2.7 (-3.3-4.1)	1.3 ± 4.4 (-7.6-12.0)
<b>θ (degree)</b>	0.3 ± 2.9 (-3.7-4.1)	-1.9 ± 3.5 (-6.8-5.1)

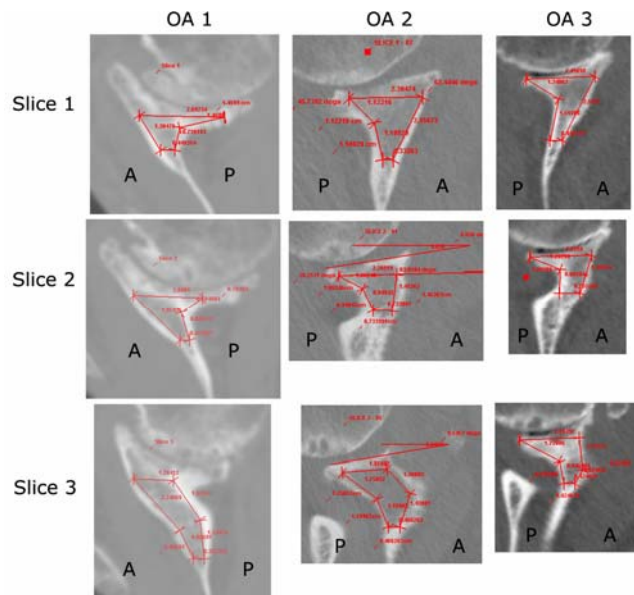
*Osteoarthritic Scapulae Specimen:*

Figure 17 shows the 3D computer models for the three osteoarthritic scapulae specimen in the lateral view along with the measurements (see Table 20 in Appendix A for the mean and standard deviation of all the external morphology parameters measured in the lateral view). It can be observed that the arthritis has resulted in a change in the glenoid boundary compared to the normal specimen. Therefore during surgery excess bone on the glenoid boundary is removed. Hence the measurements were made by not considering the arthritic growth.

Figure 18 gives the axial cross-sections showing the internal morphology measurements for the three osteoarthritic scapulae specimen (see Table 21 in Appendix A for the mean and standard deviation values). Similar to the measurement technique used for the external morphology, the approximate polygon was fitted in the glenoid vault to account for the shape after the completion of glenoid surface preparation.



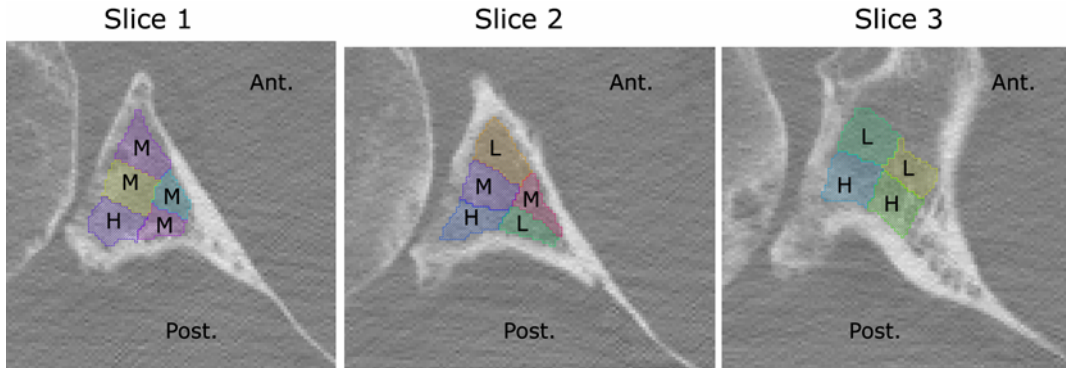
**Figure 17.** The three dimensional computer models of the three osteoarthritic (OA) scapulae specimen showing the various measurements in the lateral view (figure by author).



**Figure 18.** The internal morphology measurements for each of the osteoarthritic (OA) scapulae specimen three selected axial slices (figure by author).

**Table 3. The mean and standard deviation of the bone density in the various regions of interest in the three selected axial slices of the osteoarthritic scapulae specimen (NA: Not Applicable for axial slice 3).**

Axial Cross-section	Mean ± S.D. (HU)				
	ROI 1 (Proximal-Posterior)	ROI 2 (Proximal-Center)	ROI 3 (Proximal-Anterior)	ROI 4 (Distal-Posterior)	ROI 5 (Distal-Anterior)
Slice 1	580 ± 119	382 ± 108	385 ± 106	418 ± 37	484 ± 226
Slice 2	625 ± 175	409 ± 24	349 ± 97	318 ± 137	442 ± 200
Slice 3	548 ± 330	NA	314 ± 251	526 ± 167	261 ± 54



**Figure 19. The bone density in the various regions of interest in the three axial slices of the osteoarthritic scapulae specimen calibrated as H:relatively high, M:relatively medium, and L:relatively low (figure by author).**

Table 3 gives the mean and standard deviation of the bone density measurement for the various regions of interest in the three axial slices of the osteoarthritic scapulae specimen. For better understanding the values obtained were calibrated into relatively high (H:CT number in HU>500), medium (M:350≤CT number in HU≤500), and low density (L:CT number in

HU<350), as shown in Figure 19. Relatively high density was found in the posterior glenoid, medium density in the center, and low density in the anterior-superior region.

*Comparing Normal and Osteoarthritic Scapulae Specimen:*

Figure 20 shows graphically the glenoid external morphology measurement values in the normal and osteoarthritic scapulae specimen (the mean and standard deviation are listed in Table 20, see Appendix A). All the length measurements, except the triangle height ( $\Delta ht$ ) in superior glenoid, were greater in the osteoarthritic scapulae specimen than the normal. However it can be observed that the trends in the length measurements were approximately equal.  $L_{2h}$  was greatest, while  $L_{1h}$ ,  $L_{3h}$ , and  $L_{4h}$  were approximately equal among the measurements  $L_{1h}$ ,  $L_{2h}$ ,  $L_{3h}$ , and  $L_{4h}$ .  $L_2$  and  $L_4$  were less than  $L_1$  and  $L_3$  in both the normal and osteoarthritic scapulae specimen. The difference in the measurements C and D, and D and d were approximately equal between the normal (8mm, 6mm) and the osteoarthritic (9mm, 8mm) scapulae specimen respectively. The base angle  $t_2^\circ$  of the superior triangle was less than  $t_1^\circ$ , whereas the glenoid tilt ( $b^\circ$ ) was approximately equal in the normal and the osteoarthritic scapulae specimen.

### Glenoid External Morphology Measurements Normal and Osteoarthritic Scapulae Specimen Comparison

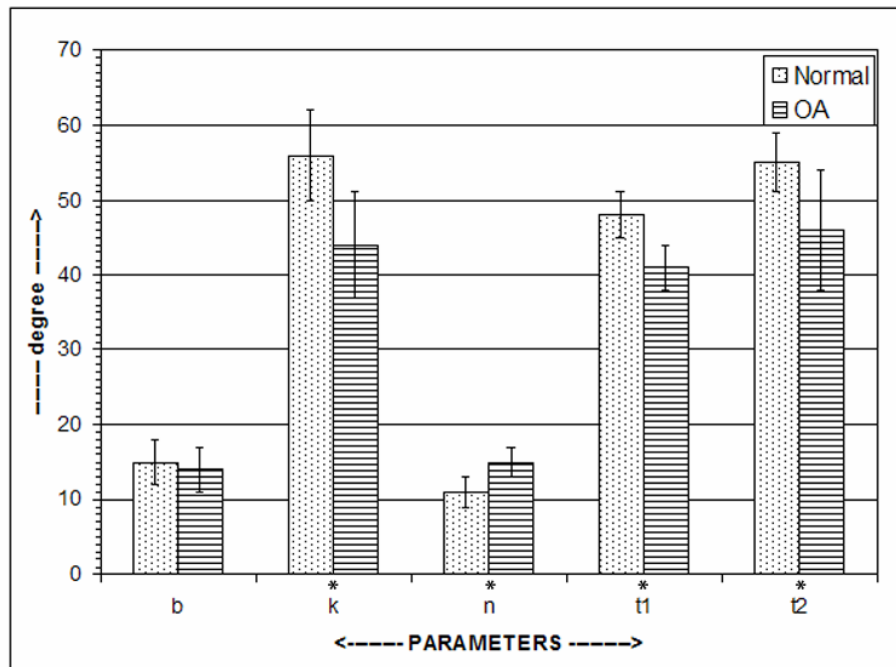
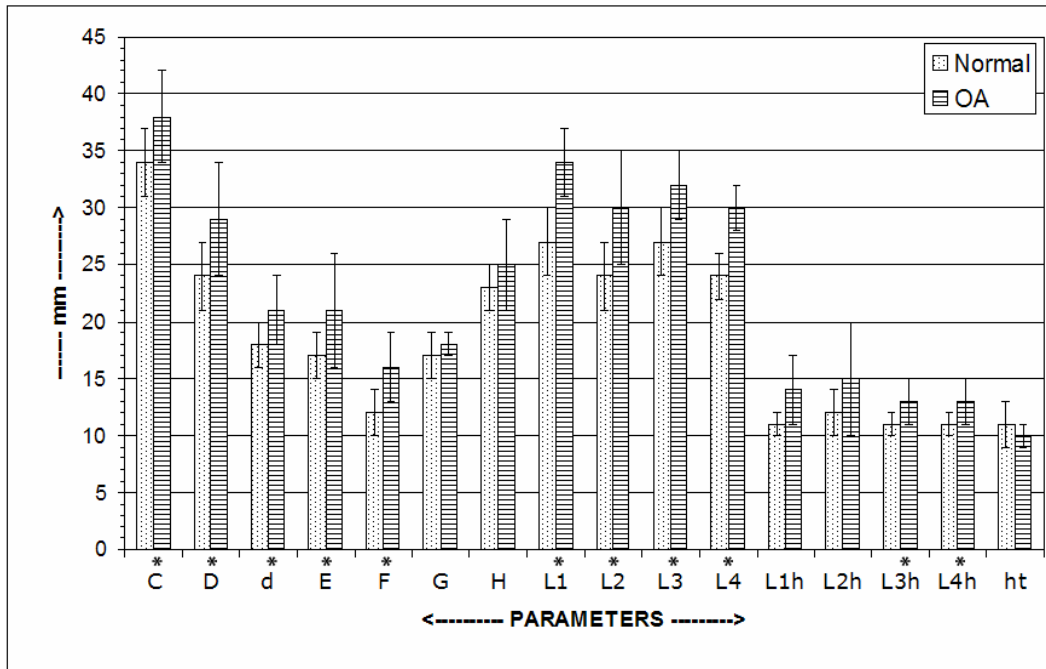


Figure 20. The glenoid external morphology parameter values comparison between the normal and osteoarthritic (OA) scapulae specimen (\*:  $p < 0.05$ ) (figure by author).

Figure 21 shows graphically the glenoid internal morphology and vault depth measurements in the normal and the osteoarthritic scapulae specimen (the mean and standard deviation values are listed in Table 21, see Appendix A). The D' measurement was found to decrease in both the normal and the osteoarthritic scapulae specimen from slice 1 to slice 3. The glenoid neck width (segment X) in the three slices was greater in the normal compared to that in the osteoarthritic scapulae specimen respectively, however a similar trend was observed in both kinds of specimen with the value being greatest in slice 2, and approximately equal in slices 1 and 3. Overall the glenoid vault depth was lower in the osteoarthritic scapulae specimen (maximum depth: slice 1, H50=14±9mm) than the normal (maximum depth: slice 1, H50=21±0mm). The glenoid was highly retroverted (negative angle signify retroversion) in the osteoarthritic scapulae specimen (mean±SD: -18°±9°) compared to the normal (mean±SD: -2°±5°), however the subchondral bone glenoid version was approximately equal (mean±SD: -2.5°±2°). The anterior margin angle r° was approximately equal and increased from slice 1 to slice 3 in both the normal and the osteoarthritic scapulae specimen.

**Glennoid Internal Morphology Measurements  
Normal and Osteoarthritic Scapulae Specimen Comparison**

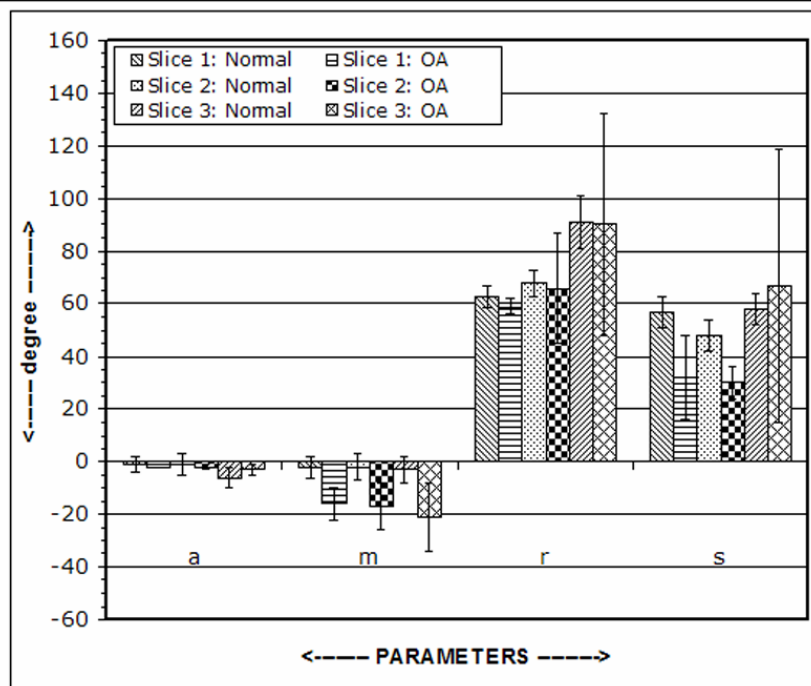
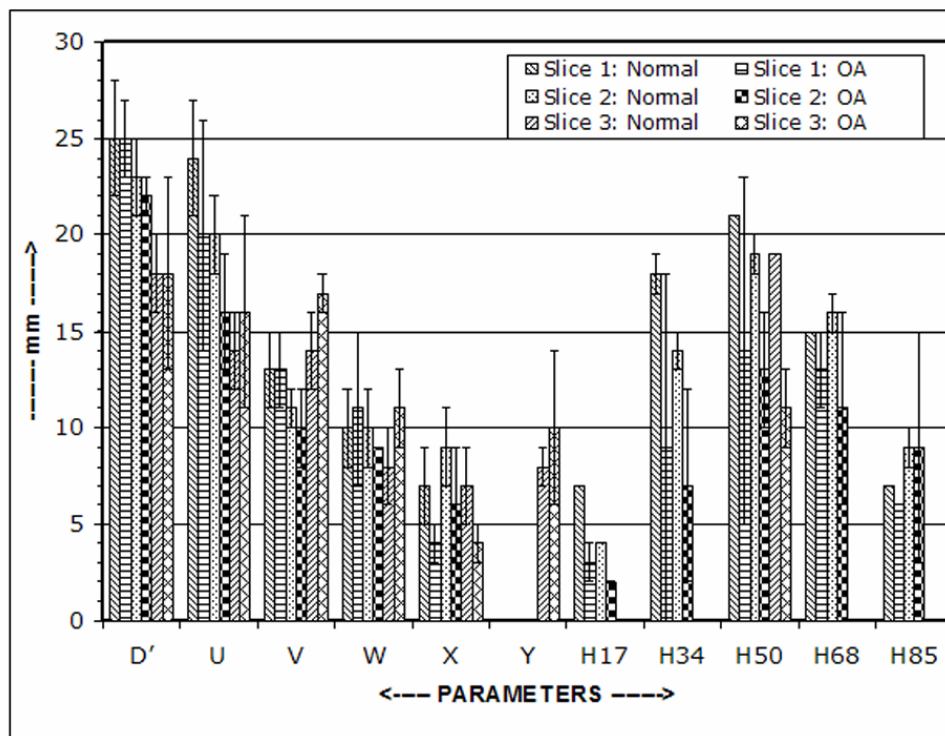


Figure 21. The glenoid internal morphology and vault depth measurement values comparison between the normal and osteoarthritic (OA) scapulae specimen (figure by author).



### 3.4 DISCUSSION

The success of total shoulder arthroplasty depends on the design of the implant as well as its positioning. To increase the longevity of the glenoid prosthesis, the first task is to understand the structure of the bone in which it is going to be fixed. The knowledge of the external morphology of the scapula helps in the positioning of the prosthesis, on the other hand the internal bone morphology influences its fixation. These two morphological considerations can be understood by the three-dimensional structural analyses of the bone. Three osteoarthritic scapulae specimen were also included for comparison with the normal case. This permitted to first determine key relationships in the normal glenoid and then verify them in the osteoarthritic scapulae specimen thereby improving the clinical relevance of the study.

The normal glenoid superior-inferior, and anterior-posterior length measurements were found to be greater ( $p < 0.05$ ) in male specimens ( $35 \pm 2$ mm) than female ( $33 \pm 3$ mm) and equal ( $p > 0.05$ ) between right and left specimens. The values obtained on the computer models over-estimated the caliper measurements on the corresponding actual specimen by a mere 0.4, and 0.3mm respectively indicating high accuracy and reliability. These measurements were comparable to those found by previous investigators [48, 51, 53, 161-163] as can be seen in Table 4.

The superior-inferior length of the glenoid value reported by Iannotti, et al [51] ( $39 \pm 3.5$ mm) approximately equaled that found in this study for the normal ( $34 \pm 3$ mm) and osteoarthritic scapulae specimen ( $38 \pm 4$ mm) . Also, the ratio of the anterior-posterior (superior) measurement to the anterior-posterior (inferior) measurement reported by Iannotti, et al, ( $1:0.8 \pm 0.01$ ) was highly comparable to that obtained in this study for the normal ( $1:0.8 \pm 0.04$ )

and approximately equal to the osteoarthritic ( $1:0.7\pm 0.1$ ) scapulae specimen. Two other ratios reported by Iannotti, et al, were the superior-inferior measurement to the anterior-posterior (inferior) measurement ( $1:0.7\pm 0.02$ ) and the superior-inferior measurement to the anterior-posterior (superior) measurement ( $1:0.6\pm 0.06$ ), which approximately equaled the normal ( $1:0.7\pm 0.01$ ,  $1:0.5\pm 0.02$ ) and the osteoarthritic ( $1:0.8\pm 0.01$ ,  $1:0.6\pm 0.08$ ) scapulae specimen respectively.

**Table 4.** The comparison between select glenoid morphology parameter values in this study with prior investigations.

Parameter	Current study Mean $\pm$ S.D. (Range)		Prior studies Mean $\pm$ S.D. (Range)
	Normal	Osteoarthritic	
<b>Superior-Inferior Length (mm)</b>	34 $\pm$ 3 (28-39)	38 $\pm$ 4 (35-43)	36 $\pm$ 2 (29-43) [48] 42 $\pm$ 3 (not given) [53] 36 $\pm$ 4 (30-43) [163] 35 $\pm$ 4 (29-44) [162] 39 $\pm$ 4 (30-48) [51] 34 $\pm$ 3 (26-39) [161]
<b>Anterior-Posterior Width (mm)</b>	24 $\pm$ 3 (21-29)	29 $\pm$ 5 (23-34)	21 $\pm$ 2 (19-33) [48] 30 $\pm$ 3 (not given) [53] 29 $\pm$ 3 (25-34) [163] 24 $\pm$ 3 (16-30) [162] 29 $\pm$ 3 (21-35) [51] 23 $\pm$ 3 (16-29) [161]
<b>Glenoid Version (degree)</b>	-2 $\pm$ 5 (-10-7)	-18 $\pm$ 9 (-21- -16)	2 $\pm$ 5 (-12-14) [8] -17 (-22-12) [67] -1 $\pm$ 4 (-11-10) [48] -1 $\pm$ 2 (not given) [61] -2 $\pm$ 4 (-12-7) [162] -2 $\pm$ 3 (-13-7) [49]
<b>Glenoid Neck Width (mm)</b>	<b>Slice 1:</b> 7 $\pm$ 2 (5-10) <b>Slice 2:</b> 9 $\pm$ 2 (5-15) <b>Slice 3:</b> 7 $\pm$ 2 (4-12)	<b>Slice 1:</b> 4 $\pm$ 1 (3-5) <b>Slice 2:</b> 6 $\pm$ 3 (3-8) <b>Slice 3:</b> 4 $\pm$ 1 (4-5)	<b>Slice 1:</b> 9 $\pm$ 2 (3-13) <b>Slice 2:</b> 13 $\pm$ 3 (8-18) <b>Slice 3:</b> 8 $\pm$ 3 (3-15) [161]

In the anterior view of the normal scapula, segment A was found greater ( $p < 0.05$ ) in male specimens ( $22 \pm 2$ mm) than female ( $18 \pm 2$ mm), and equal between right and left specimens ( $p > 0.05$ ). Segment B on the other hand was found equal not only between right and left but also between male and female specimens ( $p > 0.05$ ). This may be the reason why segment A was uncorrelated ( $r = 0$ ,  $p = 0$ ) with segment B. Hughes, et al, [50] found the glenoid inclination to be about  $91^\circ$ . The same value was not measured in this study, but on calculating the glenoid inclination (utilizing the measurements A, B,  $\theta^\circ$ , and  $\theta_1^\circ$  made in the anterior view) was found to be  $93^\circ$ , which is approximately equal to that reported by Hughes, et al. Also, Churchill, et al, [48] reported the glenoid inclination as  $5^\circ$ , which is comparable to the calculated value of  $3^\circ$  found in the current study.

The glenoid tilt ( $b^\circ$ ) was found equal ( $p > 0.05$ ) between male and female normal specimens, and greater ( $p < 0.05$ ) in rights ( $15.8^\circ \pm 2.9^\circ$ ) than lefts ( $13.6^\circ \pm 3^\circ$ ). Also, the glenoid tilt found for the osteoarthritic specimens was  $14^\circ \pm 3^\circ$ . Malon, et al, [162] had reported the glenoid tilt angle as  $12^\circ$ , which is comparable to that found in this study.

Other measurements that quantified the overall shape of the glenoid boundary included segments  $L_1$ ,  $L_2$ ,  $L_3$ , and  $L_4$ , which were found greater ( $p < 0.05$ ) in males than females and equal ( $p > 0.05$ ) in rights and lefts. The values found in the osteoarthritic specimens were greater than those in the normal, probably due to the arthritis on the glenoid boundary of the former. For the normal specimens medium correlation was seen between segments C and D ( $r = 0.8$ ,  $p = 0$ ), C and  $L_1$  ( $r = 0.79$ ,  $p = 0$ ), and C and  $L_3$  ( $r = 0.78$ ,  $p = 0$ ) and very high correlation was obtained for D and  $L_2$  ( $r = 0.92$ ,  $p = 0$ ), and D and  $L_4$  ( $r = 0.93$ ,  $p = 0$ ). Therefore by simply measuring the length of segment C, all the other parameters (D,  $L_1$ ,  $L_2$ ,  $L_3$ , and  $L_4$ ) can be approximated to obtain the overall glenoid boundary.

The superior portion of the glenoid was approximated with a triangle having base angles  $t_1$  and  $t_2$ , the values of which were lower for the osteoarthritic ( $41^\circ \pm 3^\circ$ ,  $46^\circ \pm 8^\circ$ ) specimens compared to the normal ( $48^\circ \pm 3^\circ$ ,  $55^\circ \pm 4^\circ$ ) respectively. This may be due to the increased triangle base length (segment d) in the osteoarthritic specimens ( $21 \pm 3$ mm) compared to the normal ( $18 \pm 2$ mm). In the normal specimens segment d was found equal ( $p > 0.05$ ) not only in males and females but also in rights and lefts. The height of the triangle ( $\Delta ht$ ) was found greater ( $p < 0.05$ ) in male normal specimens ( $12 \pm 2$ mm) than female ( $11 \pm 1$ mm) and equal ( $p > 0.05$ ) in rights and lefts, however it was lower for the osteoarthritic specimens ( $10 \pm 1$ mm). Burkhart, et al [58] had suggested the glenoid bare spot as the center of a circle in the inferior portion of the glenoid. The measurements of the distances from this glenoid bare spot to the anterior ( $12.1[11-15]$ mm), posterior ( $12.3[11-15]$ mm), and inferior ( $12.1[11-15]$ mm) glenoid boundary were approximately comparable to the measurements obtained in this study for the normal ( $11.4[9-13]$ mm,  $12.1[9-15]$ mm) and osteoarthritic specimens ( $12.7[12-14]$ mm,  $14.5[12-17]$ mm) respectively. In the current study as well, it was found that the inferior glenoid region can be approximated by a circle, and its center was obtained mathematically.

Previous investigators [48, 51, 161-163] had only studied the external anatomy of the scapula. The key for designing improved glenoid prosthesis is to have knowledge of both the external as well as internal glenoid morphology. The success of total shoulder arthroplasty depends on the bone density distribution of the glenoid [22, 23, 67-71, 164]. The amount of bone available for fixation of glenoid prosthesis is less compared to other parts of the body, namely, hip and knee, therefore to obtain a “good-fit” the design of the glenoid prosthesis must utilize the small volume of bone effectively.

In the internal bone morphological analysis carried out, three axial slices of the glenoid were considered. The advantage of using three-dimensional computer models was the ability to accurately choose the three appropriate axial slices of interest. The anterior-posterior width near the glenoid neck (segment X) measured in this study for normal specimens axial slices 1, 2, and 3 as  $7\pm 2\text{mm}$ ,  $9\pm 2\text{mm}$ , and  $7\pm 2\text{mm}$ , were approximately comparable to those reported by Ebraheim, et al [161] as  $9\pm 2\text{mm}$ ,  $13\pm 3\text{mm}$ , and  $8\pm 3\text{mm}$  respectively. The values for the osteoarthritic specimens were however lower ( $4\pm 1\text{mm}$ ,  $6\pm 3\text{mm}$ ,  $4\pm 1\text{mm}$ ) than those of the normal and previous investigations probably in part due to deformation of the glenoid vault.

The glenoid vault depth calculated for the normal specimens at the five different locations (posterior to anterior) in the axial slice 1 (6.5, 18.4, 20.5, 15.5, and 7.3mm), 2 (4.4, 13.7, 18.6, 16.5, and 8.8mm), and 3 (12mm) were comparable to those reported by Anglin, et al [23] that is, slice 1:  $\leq 7$ ,  $\leq 17.5$ ,  $\leq 21$ ,  $\leq 10.5$ , and  $\leq 7\text{mm}$ , slice 2:  $\leq 3.5$ ,  $\leq 17.5$ ,  $\leq 21$ ,  $\leq 14$ , and  $\leq 3.5\text{mm}$ , and slice 3:  $\leq 14\text{mm}$  respectively. Again it was found that the glenoid vault depth in the osteoarthritic specimens were lower (slice 1: 3, 9, 14, 13 and 6mm, slice 2: 2, 7, 13, 11 and 9mm, slice 3: 11mm) than the normal possibly because of the increased posterior bending.

The calibrated bone density distribution for the three normal specimen axial slices in the current study consent with the findings reported by Couteau, et al, [67], and Muller-Gerbl et al, [164], that is, high density bone on the posterior glenoid, low density central and medium density in the anterior portion. Frich, et al, [69], and Mansat, et al, [68] had found low density bone on the anterior side, and the medium density in the center of the glenoid, which agrees with that found for the osteoarthritic specimens. High density was also found in the superior-posterior region of the osteoarthritic glenoid. This may be since the glenoid showed excessive posterior bending which could have resulted in bone apposition as per Wolff's law of bone remodeling.

The glenoid version has been regarded as an important contributing factor for glenohumeral stability [8, 48, 49, 67, 162, 165]. Majority of the previous investigations [48, 49, 61, 162] had used the technique given by Friedman, et al, [8]. In the current study male normal specimens were found to be retroverted in all three axial slices whereas female specimens were found to be anteverted in slices 1, and 2 and retroverted in slice 3. The glenoid version obtained in this study (for axial slice that passed through the centre of the glenoid) was  $-2^{\circ}\pm 5^{\circ}$  (negative angle signifying retroversion), which was comparable with the values obtained by Churchill, et al ( $-1^{\circ}\pm 4^{\circ}$ ), Inui, et al ( $-1^{\circ}\pm 2^{\circ}$ ), Mallon, et al ( $-2^{\circ}\pm 4^{\circ}$ ), and Gallino, et al ( $-2^{\circ}\pm 3^{\circ}$ ). Friedman, et al ( $2^{\circ}\pm 5^{\circ}$ ), reported the glenoid version angle as a positive value signifying anteversion. Most of the previous investigators measured the glenoid version by considering only a single slice through the central portion the glenoid. Inui, et al [61] reported that the glenoid version varied from the inferior portion of the glenoid to the superior portion. In the present study the glenoid version value obtained in axial slices 1 ( $-2^{\circ}\pm 4^{\circ}$ ), 2 ( $-2^{\circ}\pm 5^{\circ}$ ), and 3 ( $-3^{\circ}\pm 5^{\circ}$ ), were approximately comparable to those reported by Inui, et al, as  $1^{\circ}\pm 3.2^{\circ}$ ,  $-1^{\circ}\pm 2^{\circ}$ , and  $-6.9^{\circ}\pm 3.7^{\circ}$  respectively. The difference between the values obtained in this study and those reported by Inui, et al might be due to the scapulae specimen differences. The osteoarthritic specimens were highly retroverted compared to the normal, and also showed increased retroversion in the superior glenoid (slice 1:  $-16^{\circ}\pm 6^{\circ}$ , slice 2:  $-17^{\circ}\pm 9^{\circ}$ , slice 3:  $-21^{\circ}\pm 13^{\circ}$ ). It must be noted here that the osteoarthritic specimen were classified as having severe OA (retroversion  $> 10^{\circ}$ ).

Previous investigations had not reported about the subchondral bone glenoid version, which is important for total shoulder arthroplasty. Friedman, et al, [8] gave a simple formula based on the glenoid version angle to determine the width of the bone graft needed to correct the version to a value of  $2^{\circ}$  anteversion which they suggested should be the surgeons goal. In the

current study the subchondral glenoid bone version (angle  $a^\circ$ ) was measured with two aims, to keep the maximum high-density bone, and to obtain the glenoid version as close to neutral prior to prosthesis implantation. The value of this angle for the normal specimens ( $-2.7^\circ \pm 3.7^\circ$ ) was approximately equal to the osteoarthritic ( $-2.3^\circ \pm 1^\circ$ ).

The computer-based modeling approach proved highly beneficial for analyzing the morphology of the scapula especially the glenoid. Using computer-based measuring tools the external morphological parameters in the various views were easily measured. Also, the internal glenoid morphology was quantified for the first time using axial cross-sections at three different locations. The methods of measurement were non-destructive, highly accurate, and reliable. The values for the various parameters measured not only confirmed with what has been reported in previous investigations, but also expanded the data available about the glenoid morphology by providing an extensive analysis of the internal bone morphology, and the available bone depth at various locations. All the information presented in the current study is important not only to design improved glenoid prosthesis, but also for selection of the appropriate prosthetic component at the time of arthroplasty. Future work involves increasing the sample size of the osteoarthritic scapulae to further improve the database for shoulder arthroplasty.

## **4.0 2D STRESS ANALYSES OF GLENOID BONE**

### **4.1 INTRODUCTION**

Total shoulder arthroplasty is a popular clinical treatment for end-stage glenohumeral arthritis [26, 80]. Glenoid component loosening is one of the major complications encountered in patients with total shoulder arthroplasty [13, 28, 29, 139, 141-143]. The stability of the glenoid component is dependent on many factors, such as quality and quantity of the glenoid bone, soft tissue balance, implantation surgical technique, presence of functioning rotator cuff, post-operative care, and the design of the prosthesis and its fixation [32, 33].

Most of the current glenoid prostheses are made from ultra high molecular weight polyethylene (UHMWPE) and implanted using polymethylmethacrylate (PMMA) or bone cement. Clinical and radiographic studies have shown progressive radiolucent lines at the cement-bone interface, and symptomatic component loosening [15, 166]. The exothermic curing reaction of PMMA can cause thermal necrosis of the bone and may lead to glenoid component loosening [88]. These findings have led groups of researchers towards the design and testing of uncemented glenoid prostheses [38].

Numerous designs of the glenoid prosthesis have been developed in an attempt to increase their fixation longevity in patients. Broadly, the anchoring designs can be classified into

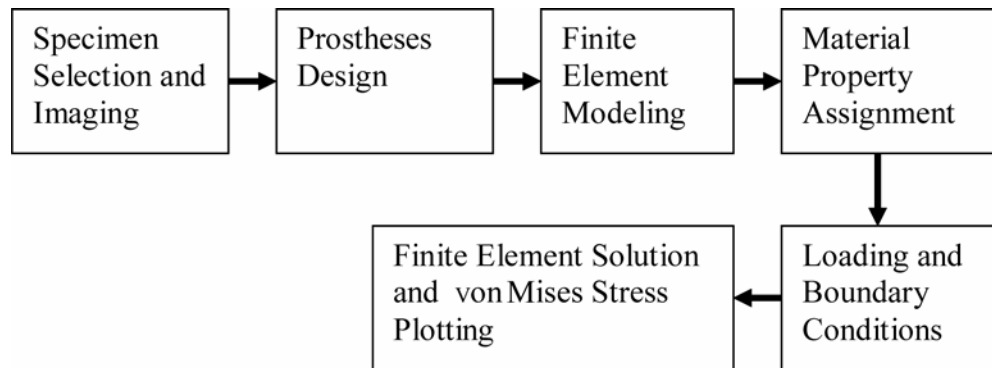


two categories: keels, and pegs. Within each of these categories there are many possible keel and peg geometries. Other design parameter that have been investigated, which are common to both keel and peg glenoid prostheses, are flat or curved backing with or without metal, conforming or non-conforming articulating surface, and constrained or non-constrained articulating surface [139].

At present there are few designs for uncemented glenoid prostheses (Kessel prosthesis with press fit design, the Cofield metal-backed design with tissue-ingrowth capability, and the Biomet's Biomodular porous-coated glenoid component), which are being used for select patients having a good bone stock. Although, pain relief, range of motion, and functional capacity for the glenoid prostheses fixed without cement have been reported to be comparable to those fixed with cement, their rate of early post-surgery complications is high [82]. The glenoid prosthesis design parameters are many, and therefore, in this study the metal backing (complete or partial), fixation orientations (straight or angled), and materials have been varied to design a total of twelve glenoid prostheses models. A comparison of the stresses in the intact bone, and the glenoid prostheses-bone models is also studied to better understand the effects of these design changes within the cortical and cancellous glenoid bone regions.

## 4.2 MATERIALS AND METHODS

Figure 22 summarizes the various steps used in the methodology of the current study. A detailed explanation of each step is given below.



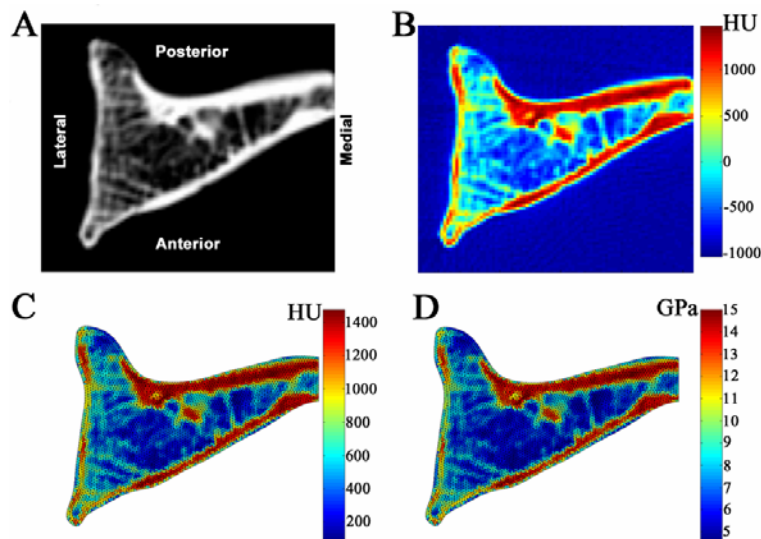
**Figure 22.** The sequence of steps used for the 2D stress analyses of the glenoid bone (illustration by author).

### **Specimen Selection and Imaging:**

A right cadaver scapula specimen was obtained from a 55-year-old male donor from Midwestern United States. The scapula specimen was approximately of average size with superior-inferior glenoid length of 37.2mm and anterior-posterior width of 27.1mm [48] having no pathology. The scapula specimen was placed in a custom designed stand depicting the lateral view. High-resolution volumetric axial computed tomography (CT) images with 1 mm slice thickness at 1 mm intervals were obtained. All the images were reconstructed using a bone algorithm.

## Prostheses Design:

The axial slices were then imported into a 3D visualization and modeling software Amira® 3.0 (TGS, Inc., San Diego, CA, USA) and the slice passing through the glenoid center (Figure 23) was selected for the two-dimensional finite element modeling and analysis. Using the Image Segmentation Tools in Amira® (threshold, region growing) the bone contours were obtained. The contours were then imported into the mechanical design software SolidWorks® (SolidWorks Corporation, Concord, MA, USA), and spline curves were fitted to obtain smooth intact bone contours.



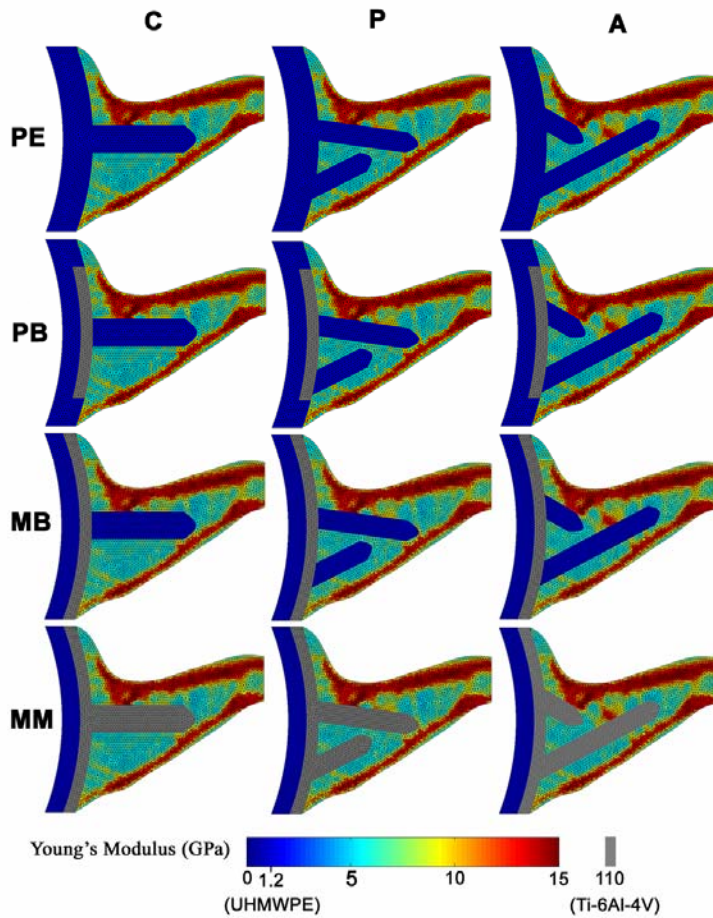
**Figure 23.** (A) Axial CT slice of right scapula selected for finite element modeling and analysis, (B) axial slice CT numbers (Hounsfield Units or HU) shown using a color mapped range, (C) finite element model (FEM) of the intact bone with the assigned element CT numbers (HU), and (D) FEM of intact bone showing the location-specific Young's modulus values in GPa (illustration by author).

**Table 5. The finite element models created in the current study, along with their abbreviations.**

Abbreviation	Finite Element Model
Int	Intact Bone
PE-C	All- <b>PE</b> , <b>C</b> enter fixation
PE-P	All- <b>PE</b> , <b>P</b> osterior-long Anterior-short angled fixations
PE-A	All- <b>PE</b> , <b>A</b> nterior-long Posterior-short angled fixations
PB-C	<b>P</b> artial Metal <b>B</b> acked, <b>PE</b> <b>C</b> enter fixation
PB-P	<b>P</b> artial Metal <b>B</b> acked, <b>PE</b> <b>P</b> osterior-long Anterior-short angled fixations
PB-A	<b>P</b> artial Metal <b>B</b> acked, <b>PE</b> <b>A</b> nterior-long Posterior-short angled fixations
MB-C	<b>M</b> etal <b>B</b> acked, <b>PE</b> <b>C</b> enter fixation
MB-P	<b>M</b> etal <b>B</b> acked, <b>PE</b> <b>P</b> osterior-long Anterior-short angled fixations
MB-A	<b>M</b> etal <b>B</b> acked, <b>PE</b> <b>A</b> nterior-long Posterior-short angled fixations
MM-C	<b>M</b> etal Backed, <b>M</b> etal <b>C</b> enter fixation
MM-P	<b>M</b> etal Backed, <b>M</b> etal <b>P</b> osterior-long Anterior-short angled fixations
MM-A	<b>M</b> etal Backed, <b>M</b> etal <b>A</b> nterior-long Posterior-short angled fixations

Four different glenoid prosthesis design variables with three types of fixations were investigated (Figure 24, Table 5). The radius of curvature (34mm) for both, the articulating and the backing edges of the glenoid prostheses were equal for all the prostheses. The total thickness for all the glenoid prostheses was kept equal to 5mm to limit the lateral shift of the shoulder joint line, which can cause significant changes in joint kinematics and kinetics [167, 168]. The four glenoid prostheses design variables were (a) the one-piece all-polyethylene, (b) the partial metal-backed (2mm thickness), polyethylene (PE) fixation, PE-fronted, (c) the metal-backed (2mm thickness), PE fixation, PE-fronted (3mm thickness), and (d) the metal-backed (2mm thickness), metal fixation, PE-fronted (3mm thickness). The thickness of the metal backing was chosen as 2mm since use of a thicker (~5mm) metal backing is known to cause excessive stress shielding in the underlying bone [38]. The three different fixation orientations were (i) the single straight central-long fixation having 4mm diameter, (ii) the posterior-long and anterior-short angled fixations with each having 3mm diameter, and (iii) the anterior-long and posterior-short angled

fixations with each having 3mm diameter. The intact bone and the glenoid prosthesis-bone models were then exported from SolidWorks® in the IGES file format. The IGES files were imported into the finite element modeling and analysis software Ansys® 8.0 (Ansys, Inc., Canonsburg, PA, USA).



**Figure 24.** The finite element models of the twelve glenoid prostheses showing the location-specific Young's modulus values in GPa. Rows show the material variations for the glenoid prostheses backing and the fixations (PE: all-PE, PB: Partial Metal Backing with PE fixations, MB: Metal Backing with PE fixations and MM: Metal Backing with Metal fixations). Columns indicate the fixation type (C: straight center long, P: angled posterior-long anterior-short, and A: angled anterior-long posterior-short) (illustration by author).

### **Finite Element Modeling:**

Finite element models were created for the intact bone, and all the glenoid prostheses (Figure 23 and Figure 24). The six-node triangular solid element was used for meshing purposes having an average edge length of 0.4mm, which was less than the in-plane resolution of the selected CT slice (pixel dimensions: 0.434×0.434mm). The smaller mesh element size was needed to achieve an accurate spatial material property assignment. The intact bone model consisted of 6852 elements. The glenoid prosthesis-bone models consisted of, on average, 4071 bone elements, and 2865 prosthesis elements. All the interfaces were assumed as fully bonded.

### **Material Properties:**

Bone material properties have been found to vary with the spatial location [22, 23, 68]. A custom program was written in Matlab® (MathWorks, Inc., Natick, MA, USA) to assign linearly elastic, isotropic, non-homogenous material properties to the bone elements of the finite element models on a location specific basis (Figure 23 and Figure 24). The algorithm for the custom program is as follows (see Appendix B for the custom program).

- (i) Read the elements, nodes, and nodal coordinates of the finite element model.
- (ii) Compute the centroid for each element.
- (iii) Find the CT pixel corresponding to the element centroid location.
- (iv) Read the Hounsfield (HU) number for the CT pixel.
- (v) Approximate the read HU number to the nearest multiple of ten, greater than or equal to the minimum HU and less than or equal to the maximum HU number in the selected axial CT slice. This helps to limit the number of materials (< 142).

(vi) Compute the bone density using the following general expression,

$$\rho = \left( \frac{0.9}{\text{max CT number}} \right) (\text{element CT number}) + 1; \text{ in } g/cc$$

(vii) Compute the Young's modulus using the expression,  $E = E_0 (\rho / \rho_0)^2$ , where

$$E_0 = 15 \text{ GPa}, \rho_0 = 1.9 \text{ g/cm}^3, \rho : \text{bone density}, [133] \text{ and}$$

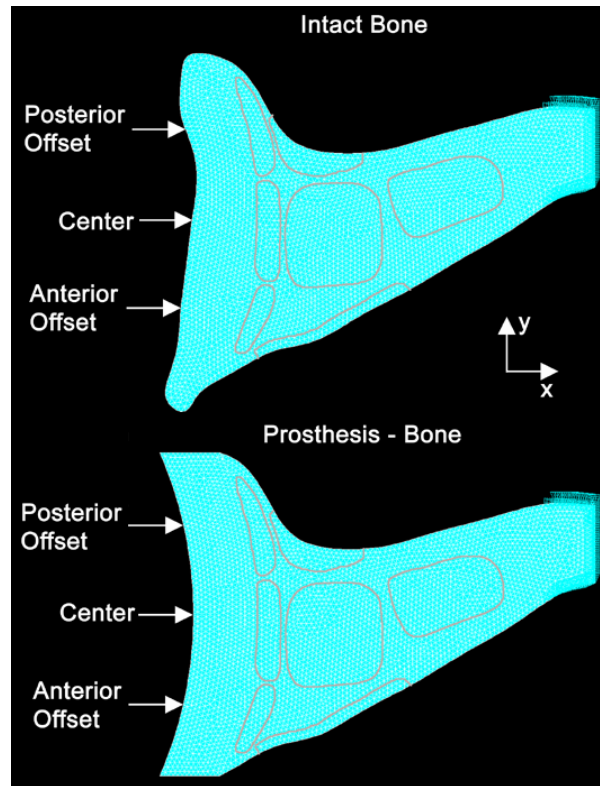
(viii) Write an Ansys® script file to assign the elemental material properties.

The Poisson's ratio for bone was taken to be 0.3 [155]. The PE component of the glenoid prostheses were assigned material properties of ultra high molecular weight polyethylene (UHMWPE) that is Young's modulus value of 1.2GPa, and Poisson's ratio of 0.46, which are approximately equal to those used by Gupta, et al (2004). The metal in the glenoid prostheses with a metal backing or metal fixations, was assumed to be made of Ti-6Al-4V alloy having the Young's modulus of 110 GPa, and the Poisson's ratio of 0.33 [26]. The UHMWPE and Ti-6Al-4V alloy were modeled as linearly elastic, homogeneous, and isotropic materials.

### **Loading and Boundary Conditions:**

Three loading cases were considered, namely, center, anterior-offset, and posterior-offset. In order to compare the stress patterns in all the prostheses with those in the intact bone, a medially directed (parallel to x-axis) point load of 800 N (one bodyweight of an 81.6 kg person) was applied. This simulated the arm being abducted to 90° [169]. The center load was applied at the midpoint of the anterior-posterior glenoid width (Figure 25). The anterior, and the posterior offset point loads were applied at a distance equal to 2/9 of the total anterior-posterior width, from the anterior, and the posterior glenoid margins respectively. The anterior, and the posterior offset loads allowed the study of the stresses in the bone during eccentric loading conditions,

which have been used to investigate the “rocking horse effect” in the glenoid prosthesis [32]. The medial portion of all the models was fixed (nodal displacements equal to zero) to avoid any rigid body motion.



**Figure 25.** The center, anterior-offset, and posterior-offset point loads in the intact bone and the glenoid prosthesis-bone finite element models, along with the regions of interest for stress comparison (illustration by author).

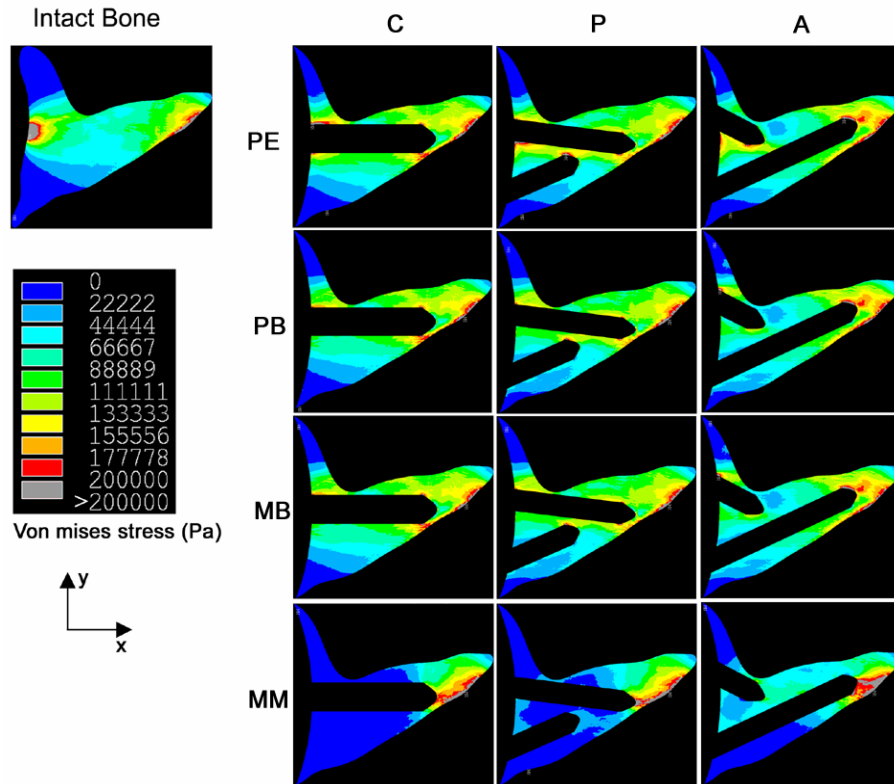


### 4.3 RESULTS

The von Mises stresses for all the prostheses and loading cases were plotted (see Appendix C). However, due to the large quantity of plots, only the stresses during center loading (Figure 26 and Figure 27), and those highlighting the key findings during the offset loadings (Figure 28 and Figure 29) are shown here. Both, Table 6 and Table 7 give the approximate average values of the von Mises stress for the intact bone finite element model (FEM), and the percent change from intact for the glenoid prosthesis-bone FEMs in the five cancellous and the two cortical bone regions of interest respectively. Comparisons were made within each of the three loading cases, and between all the design models.

**Table 6. Approximate cancellous bone von Mises stress (kPa) in intact bone model, and percent change from intact (positive number means increase, and negative number means decrease) for the twelve glenoid prosthesis-bone models for the center, anterior offset, and posterior offset loading conditions in the five regions of interest: 3 proximal (center(cen), posterior(pos), and anterior(ant) ), middle center (Mid cen), and distal center (Dist cen). Gray shaded values are percent differences beyond the design selection criteria (increase by more than 200% of intact or decrease by more than 50% of intact).**

FEM	Center Load					Anterior Offset Load					Posterior Offset Load				
	Proximal			Mid	Dist	Proximal			Mid	Dist	Proximal			Mid	Dist
	cen	pos	ant	cen	pos	cen	pos	ant	cen	cen	cen	pos	ant	cen	cen
Int(kPa)	178	11	11	67	100	17	17	266	100	300	67	250	17	50	83
PE-C	+12	+400	+400	+49	0	+388	0	-31	+17	0	-25	+20	0	0	0
PE-P	+12	+400	+200	+82	+44	+294	0	-6	+67	-39	-25	+20	0	+34	0
PE-A	+12	+400	+200	0	+170	+194	0	-6	-17	+47	-25	+20	0	+34	0
PB-C	0	+400	+400	+49	+44	+194	+194	-6	+17	-17	+24	-27	+194	0	0
PB-P	-50	-9	+400	+49	+44	+194	+194	+177	+83	-28	+24	-27	+194	+34	0
PB-A	-50	+400	+400	0	+100	+94	0	+183	-17	0	+24	-13	+194	+34	0
MB-C	-6	+400	+400	+49	+44	+194	0	-56	+17	-17	+24	-27	+194	0	0
MB-P	-50	-9	+200	+66	+44	+194	+194	-6	+83	-17	+24	-27	+194	+34	0
MB-A	-50	+400	+400	0	+100	+94	0	-6	-17	+47	+24	-13	+194	+34	0
MM-C	-94	0	0	-84	+197	+194	+194	-69	-50	0	-25	-40	0	0	0
MM-P	-81	0	0	-67	+192	0	0	-81	0	0	0	-27	0	+34	0
MM-A	-75	+200	0	+224	+204	+194	0	-81	-33	0	0	-40	0	+34	0



**Figure 26.** von Mises stress (Pa), for the center loading case, in the cancellous bone of the intact, and the twelve glenoid prostheses. Rows show the various prostheses backing and fixation materials (PE: all-PE, PB: Partial Metal Backing with PE fixations, MB: Metal Backing with PE fixations and MM: Metal Backing with Metal fixations) and columns indicate the fixation type (C: straight center long, P: angled posterior-long anterior-short, and A: angled anterior-long posterior-short) (figure by author).

### **Center Loading: Cancellous Bone (Figure 26, Table 6)**

For the all-PE models, the stress in both the proximal posterior and anterior regions increased by 2-4 times (33-55kPa) the intact bone value (11kPa). The stress in the proximal center region however, increased only by 12% (200kPa) of the intact bone value (178kPa). In the mid-cancellous bone region the all-PE, and the partial/complete metal backed prostheses with the center, and the posterior-long anterior-short angled PE fixations showed a stress increase of approximately 49% (~100kPa) of intact bone value (67kPa). However, no change was observed

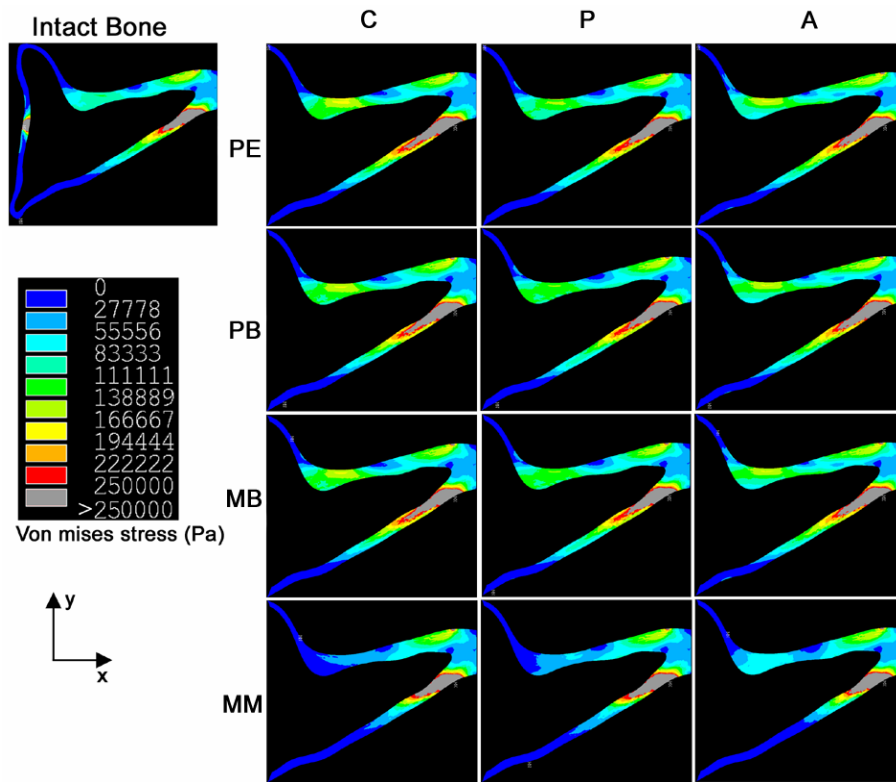
in the mid-cancellous bone region for the all-PE, and the partial/complete metal backed prostheses with the anterior-long posterior-short PE fixations. Stress in the proximal center region for the partial/complete metal backed prostheses with the angled PE fixations decreased by 50% (89kPa) of the intact bone value (178kPa). For the metal-backed metal fixation prostheses the stress in the proximal center cancellous bone decreased by 94% (11kPa) of the intact bone value (178kPa). The distal cancellous bone region stresses increased for all the prosthesis-bone models. The increase was greater for the metal fixation prostheses as compared to the PE fixation prostheses.

#### **Center Loading: Cortical Bone (Figure 27, Table 7)**

The stress in the mid-posterior region increased by 58-87% (153-181kPa) of intact (97kPa) for the all-PE and the partial/complete metal-backed prostheses with the center or the anterior-long posterior-short PE fixations. While, stress for the partial/complete metal-backed design with the posterior-long anterior-short PE screw design increased minimally by 29% (125kPa) of intact (97kPa). No change in stress was observed in the proximal to mid-anterior region for the all-PE and the metal-backed prostheses with PE fixations. The metal-backed metal fixation models stresses reduced by 28-71% (28-70kPa) of intact (97kPa) in the mid-posterior, and by 93% (1kPa) of intact (14kPa) in the proximal to mid anterior regions. The distal cortical bone stresses were found to be equal in all the prosthesis-bone and the intact bone models.

**Table 7. Approximate cortical bone von Mises stress (kPa) in intact bone model, and percent change from intact (positive number means increase, and negative number means decrease) for the twelve prostheses-bone models for the center, anterior offset, and posterior offset loading conditions in the two regions of interest: mid posterior (Post), and proximal to mid anterior (Ant). Gray shaded values are percent differences beyond the design selection criteria (increase by more than 200% of intact or decrease by more than 50% of intact).**

FEM	Center Load		Anterior Offset Load		Posterior Offset Load	
	Post	Ant	Post	Ant	Post	Ant
Int	97	14	100	150	350	50
PE-C	+87	0	0	+67	+43	0
PE-P	+39	0	0	+67	+57	0
PE-A	+58	0	0	+67	+57	0
PB-C	+72	0	0	+67	+29	0
PB-P	+29	0	0	+67	+29	0
PB-A	+58	0	0	+67	+29	0
MB-C	+72	0	0	+67	+29	0
MB-P	+29	0	0	+67	+29	0
MB-A	+58	0	0	+67	+29	0
MM-C	-71	-93	+50	-33	-29	0
MM-P	-57	-93	+50	-67	-29	0
MM-A	-28	-93	+50	-67	-29	0



**Figure 27.** von Mises stress (Pa), for the center loading case, in the cortical bone of the intact, and the twelve glenoid prostheses. Rows show the various prostheses backing and the fixation materials (PE: all-PE, PB: Partial Metal Backing with PE fixations, MB: Metal Backing with PE fixations and MM: Metal Backing with Metal fixations) and columns indicate the peg type (C: straight center long, P: angled posterior-long anterior-short, and A: angled anterior-long posterior-short) (figure by author).

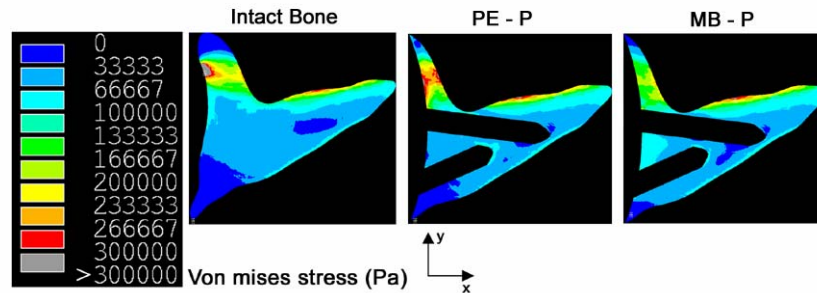
### **Anterior Offset Loading: Cancellous Bone (Table 6)**

The stress in the proximal center region for all the prostheses increased by about 2-4 times (50-83kPa) of intact (17kPa), except for the metal-backed posterior-long anterior-short metal fixation model in which the stress was approximately same as intact. No stress change was observed in the proximal posterior region for all the prostheses with the anterior-long posterior-short fixation, however the stress for the partial/complete metal-backed prostheses with the posterior-long anterior-short PE fixation increased by about 2 times (50kPa) that of intact

(17kPa). In the proximal anterior region, the stress for the partial metal-backed prostheses with angled PE fixations also increased by about 2 times that of intact (266kPa), whereas, for the complete metal-backed prostheses with the same fixation the stress decreased by 6% (250kPa) of intact (266kPa). Mid-cancellous bone stress for the partial/complete metal-backed prostheses with the posterior-long anterior-short PE fixation increased by 83% (183kPa) of intact (100kPa), while the stress decreased by 17% (83kPa) of intact (100kPa) for the all-PE and the partial/complete metal-backed prostheses with the anterior-long posterior-short PE fixation. The proximal anterior region stress for the metal-backed metal fixation prostheses decreased by 69-81% (50kPa) of intact (266kPa), however no change was observed in the distal cancellous bone region. The distal cancellous bone stresses for the all-PE and the partial/complete metal-backed prostheses with the center or the posterior-long anterior-short PE fixation remained equal or decreased by 17-39% (183-250kPa) of intact (300kPa), while the stresses for the anterior-long posterior-short fixations were equal or increased by 47% (440kPa) of intact.

#### **Anterior Offset Loading: Cortical Bone (Table 7)**

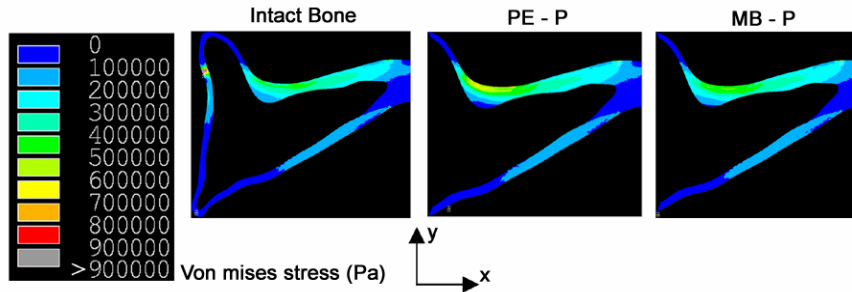
No stress change was observed in the mid-posterior region for all the prostheses. In the proximal to mid anterior region the stress increased by 67% (250kPa) of intact (150kPa) for the all-PE and the metal-backed prostheses with PE fixations, whereas for the metal-backed metal fixation prostheses the stress decreased by 33-67% (50-100kPa) of intact (150kPa).



**Figure 28.** von Mises stress (Pa), for the posterior loading case, in the cancellous bone of the intact, and the all-PE (PE) and metal-backed (MB) posterior-long anterior short glenoid prostheses (figure by author).

### **Posterior Offset Loading: Cancellous Bone (Figure 28, Table 6)**

Stress in the proximal center region increased by 24% (83kPa) of intact (67kPa) for the metal-backed PE fixation prostheses, whereas it decreased by 25% (50kPa) of intact for the all-PE prostheses. In the proximal posterior region the stress increased by 20% (300kPa) of intact (250kPa) for the all-PE prostheses, while for the metal-backed prostheses the stress decreased by 13-40% (150-217kPa) of intact bone (250kPa). In the proximal anterior region the stress in the partial/complete metal-backed prostheses with PE fixation increased by approximately 2 times (50kPa) that of intact (17kPa), however no change was observed for the all-PE and the metal-backed metal fixation prostheses. In the mid-cancellous bone region the angled fixation prostheses had stress values increased by 34% (67kPa) of intact (50kPa), but no change was found for the straight center fixation models. Also, no stress change was observed for all the prostheses in the distal cancellous bone region when compared with intact.



**Figure 29.** von Mises stress (Pa), for the posterior loading case, in the cortical bone of the intact, and the all-PE (PE) and metal-backed (MB) posterior-long anterior short glenoid prosthesis prostheses (figure by author).

### **Posterior Offset Loading: Cortical Bone (Figure 29, Table 7)**

The stress in the mid-posterior region increased by 43-57% (500-550kPa) of intact (350kPa) for the all-PE prostheses, whereas it increased by 29% (450kPa) of intact (350kPa) for the metal-backed PE fixation prostheses. Also, from Figure 29, it is observed that the stress on the inside edge of the mid-posterior region decreased by 67% (50kPa) of intact (150kPa) for the all-PE prostheses, while the decrease in the metal-backed PE fixation prostheses was limited to a smaller area compared to the all-PE prostheses. Stress in the mid-posterior region of the metal-backed metal fixation prostheses decreased by 29% (250kPa) of intact (350kPa). No stress change was observed in the proximal to mid-anterior region for all the prostheses when compared to intact.

### **Selection of design**

The design variables that caused the bone stresses to increase by more than 200% of intact or decrease by more than 50% of intact were ignored (gray shaded cells in Table 6, and Table 7). All the prostheses except the metal-backed metal fixation prostheses satisfied the



selection criteria in the cortical bone (Table 7). However, only the complete metal-backed design with the posterior-long anterior-short PE angled fixation met the selection criteria in all the cancellous bone regions of interest (Table 6). The partial metal-backed design with the posterior-long anterior-long PE angled fixation (Table 6) also satisfied the selection criteria except in the proximal anterior cancellous bone. The all-PE prostheses showed stresses beyond the selection criteria in the proximal posterior and proximal center cancellous bone regions during the center and anterior-offset loading cases respectively.

#### **4.4 DISCUSSION**

Glenoid component loosening is one of the frequently encountered complications after total shoulder arthroplasty. Majority of the current glenoid prostheses are cemented using PMMA. Past studies have found high stresses at the cement-bone interface, and increased bone temperatures due to the exothermic curing reaction of PMMA, both resulting in a high incidence of glenoid prosthesis loosening. The uncemented glenoid prostheses are presently being used in a select group of patients with good bone stock, and have shown to perform better long-term. However, fewer designs, and increased loosening rate immediately following surgery has limited its use. The purpose of this study was to evaluate glenoid prosthesis design variables including different types of backing, fixation orientations, and materials and to compare the stresses in the intact bone with those in the glenoid bone implanted with the prostheses.

When designing a glenoid prostheses one needs to consider numerous variables, a non-exhaustive list of which is backing type (flat or curve), backing material (no metal or partial metal or complete metal), total prosthesis thickness, thickness of metal backing, curvature of backing, constrained or non-constrained, conforming or non-conforming articulating surface, sizes, shapes, radius of curvature of the backing/articulating surface, fixations: type, count, locations, orientations and lengths, and the material combinations. Therefore, to simplify the evaluation twelve curve-backed glenoid prostheses were created having different metal backing length, fixation orientations, and materials. Three of the twelve prostheses were made entirely of PE, two of which had angled fixations. Although these two prostheses would be practically unfeasible to implant, they were considered for analyses in order to compare with the other angled-fixation metal-backed prostheses. The glenoid prostheses were considered to have good fixation with the bone, as no cement layer was modeled. Three different loading situations were considered, i.e., center load representing concentric loading of the glenoid, and an anterior-offset and a posterior-offset load for the eccentric loading of the glenoid. All the loads were applied as point loads to allow for comparison of the stresses between the prostheses. The bone materials were assigned element-wise based on CT data, which accounted for the spatial variation of bone density. The bone was assumed to be linearly elastic, and isotropic, however the natural bone is anisotropic. Although, the 2D finite element analysis does not take into account the out of plane forces, which are important for a complete understanding of the bone stresses in the scapula, it is useful for “fine-tuning” the glenoid prosthesis design.

The mid-cancellous bone stress in the center loading case, were increased by more than 50% of intact (67kPa) for the all-PE, and the metal-backed PE fixation prostheses. There was no change in the stress for the anterior-long posterior-short fixation design. The stresses around the

tips of the pegs were increased by approximately 100% (200kPa) of intact (100kPa). Stone, et al, [26] had found a 25% increase in the trabecular bone stress in the regions adjacent to the fixations of their cemented all-PE component. Increased level of stress around the fixations could induce bone growth and thereby reduce the chances of glenoid loosening [170]. Also, it was found that the stresses in the mid-posterior cortical bone increased by the most amount for the all-PE center fixation design (87% of intact), and the least for the metal-backed posterior-long anterior-short PE fixation design (29% of intact) compared to intact (97kPa). Orr, et al, [33] had reported a reduction in the cortical bone stresses for the all-PE triangular keel design, which contradicts the finding in this study. The reason could be that the broader keel design caused most of the load to pass through the cancellous bone, leaving the cortical bone unloaded. Whereas in this study the fixations, which are narrower, might have limited the amount of load transfer through the cancellous bone and thereby increased the cortical bone loading.

For the metal-backed metal center fixation design the stresses in the proximal cancellous bone decreased by as high as 94% of intact (178kPa). Also, in all the three loading cases, it was found that the stresses in the proximal cortical bone decreased by 93% (1kPa) of intact. This is the “stress shielding” phenomenon. Gupta, et al [38], Lacroix and Prendergast [135], Lacroix, et al [28], and Orr, et al [33] had also reported a reduction in the subchondral bone stress with metal backed glenoid components. The reason for this drastic reduction in proximal bone stress is that most of the applied load passes through the metal fixation into the distal cancellous and cortical bone. Stone, et al, [26] had reported a decrease of 20% for their uncemented metal-backed glenoid component and found the cortical bone stresses to be in the range 0-2.5MPa, while Gupta, et al, [38] found the stresses range to be 0.05-2MPa, for their uncemented metal-backed glenoid prosthesis. These ranges are comparable to the present study (0.014-2.3MPa). In the

current study, by using fixations made of PE, which has the stiffness approximately equal to the cancellous bone, and having the entire length of the fixations within the cancellous bone, i.e., not engaging the cortical bone distally as done in some of the previous studies, the stress levels in the proximal bone were found to be approximately similar to intact.

The eccentric loading cases resulted in little to no stress changes on the opposite side of the loading point, i.e., for the anterior loading case no change was found in the posterior bone and vice versa. Couteau, Mansat, et al, [29] found the anterior-posterior bending of the scapula to be a notable feature, which was accentuated with the application of eccentric (superoposterior) loading. Stone, et al, [26] had also found significantly greater bending stresses for the eccentric loading case as compared to the concentric loading case. In the current study, from the posterior offset loading case (Figure 29), it was found that the mid-posterior cortical bone stress on the outside increased by 57% of intact for the all-PE prostheses, and by 29% of intact for metal-backed PE fixation design, whereas, that on the inside decreased by 67% of intact (400kPa) for the all-PE and the metal-backed PE fixation prostheses. Also, the proximal cancellous bone stress (Figure 28) in the posterior margin of the all-PE prostheses increased by 20% of intact (250kPa), and decreased by 13-40% of intact in the metal-backed prostheses. This suggests that for the posterior offset loading case there is increased posterior bending as compared to the center, and anterior-offset loading cases. Also, the all-PE design had increased bending compared to the metal-backed prostheses, due to its low stiffness.

In the current study, it was found that the all-PE prostheses resulted in stresses close to intact for the posterior-offset load. However, the stresses due to the center loading were highly increased especially in the proximal posterior and anterior regions. The metal-backed posterior-long anterior-short PE fixation design tended to restore these high stresses close to intact.

Majority of the current market all-PE glenoid prostheses are being cemented. Lacroix and Prendergast [135] had found tensile stresses in the cement layer ranging between 7-13 MPa, indicating likelihood of failure. The advantages of using metal-backed components are three fold, firstly they allow prosthesis fixation without cement, secondly, fixation orientation can be optimized with respect to the high bone density regions, and thirdly, the fixation material can be enhanced to promote bone growth. The main reported problem of uncemented glenoid prosthesis is increased initial loosening rate post-surgery. This could be reduced with the use of newer materials for the fixations, such as porous tantalum (or trabecular metal), titanium fiber mesh, and porous-coated metal, which not only have stiffness close to cancellous bone but also allow bone ingrowth [171]. Microtexturing the metal backing and the fixations has shown increased bone growth around the prosthesis resulting in better fixation [172, 173]. Furthermore, hydroxiapatite coating of porous-coated and microtexturized fixations has also resulted in greater bone growth around the prosthesis [174, 175]

From the current study, it was found that the metal-backed metal fixation prostheses caused a reduction in the stresses within the underlying bone for all the loading cases. The cortical bone stresses in the metal-backed PE fixation prostheses were increased, but closer to those in the intact bone as compared to the all-PE prostheses. In the concentric loading case, the cancellous bone stresses for the metal-backed straight, and posterior-long anterior-short PE fixation prostheses better approximated the intact. In the eccentric loading cases, the cancellous bone stresses in the all-PE, and the metal-backed PE fixation prostheses were approximately similar to those in the intact. Increased posterior bending of bone was observed in the all-PE prostheses compared to the metal-backed prostheses for the posterior offset load. The findings of the current study indicate that the metal-backed posterior-long anterior-short PE fixation design

performed better than the others in terms of the stress levels in the cortical and cancellous bone when compared to intact. Although, the analyses were done in 2D, it has helped to consolidate, increase, and “fine tune” the knowledgebase of design possibilities and features for uncemented glenoid prosthesis.

## **5.0 3D STRESS ANALYSES OF SCAPULA**

### **5.1 INTRODUCTION**

Finite element analysis is widely used for mechanical simulations of complex shapes. Stress analysis of bone is vital for designing improved prostheses for joint arthroplasty. It is also important that the computer models accurately reflect the actual situation. Although highly effective in reducing pain and restoring functionality in end-stage glenohumeral arthritis, total shoulder arthroplasty suffers primary post-surgical complication of glenoid prosthesis loosening [27, 28]. Some of the drawbacks of two dimensional finite element analyses are the inability to consider the entire scapula, and model out-of-plane load and boundary conditions.

Hence the goals of this study were to (1) create a process for producing three-dimensional subject-specific finite element models of scapula implanted with prostheses with features and (2) perform a comparison of the stress analyses. The hypothesis was that some glenoid design variables better approximated the stresses in the intact scapula compared to the existing market glenoid prostheses.

## 5.2 MATERIALS AND METHODS

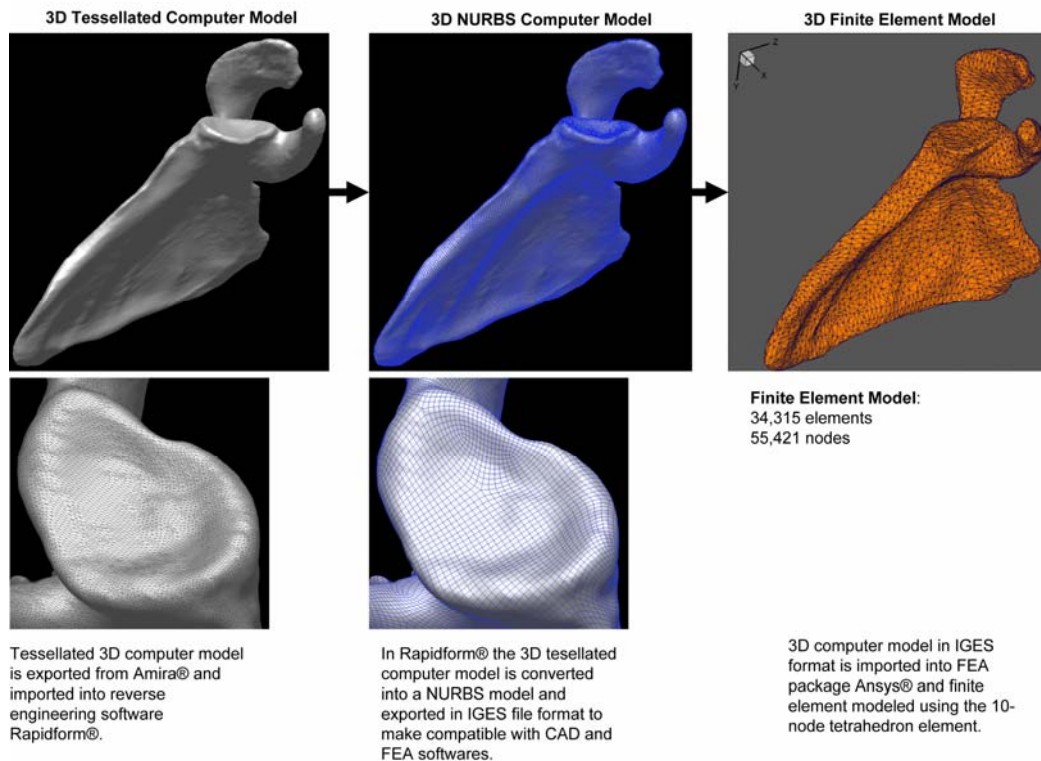
Two cadaver scapulae specimen were obtained from donors, one an 82 year-old female and the other a 55 year-old male. Both donors had no surgical procedure performed on the scapulae or humeri. Volumetric high resolution axial computed tomography (CT) imaging was performed using 1mm slice thickness and 1mm slice interval. The CT images were electronically transferred and imported into a 3D visualization and modeling software (Amira® 3.0, TGS, Inc., San Diego, CA, USA). Bone segmentation was performed using threshold and region growing. The resultant axial bone contours were converted to tessellated surfaces in Amira®. The tessellated surfaces were then converted into NURBS using reverse engineering software Rapidform® (Inus Technology Inc., San Jose, CA). The models were then imported into computer aided design (CAD) software SolidWorks® (SolidWorks Corporation, Concord, MA, USA) (Figure 30).

Two kinds of finite element analyses were performed. In the first case, two partial-metal backed glenoid prostheses (both having the same geometry but different materials for the angled fixations, metal and polyethylene respectively) were compared with the all-polyethylene Solar® Glenoid Prosthesis (Stryker Orthopaedics, Mahwah, NJ, USA). No cement layer was modeled and the 3D computer model of the scapula from the female donor was used. In the second case, three all polyethylene cemented glenoid prostheses were studied: Depuy® Anchor Peg Glenoid Prosthesis (Depuy Orthopaedics Inc., Warsaw, IN, USA), Solar® Glenoid Prosthesis (Stryker Orthopaedics, Mahwah, NJ, USA), and one glenoid prosthesis design variable model. For this case the 3D computer model of the scapula from the male donor was used. Manipulating the

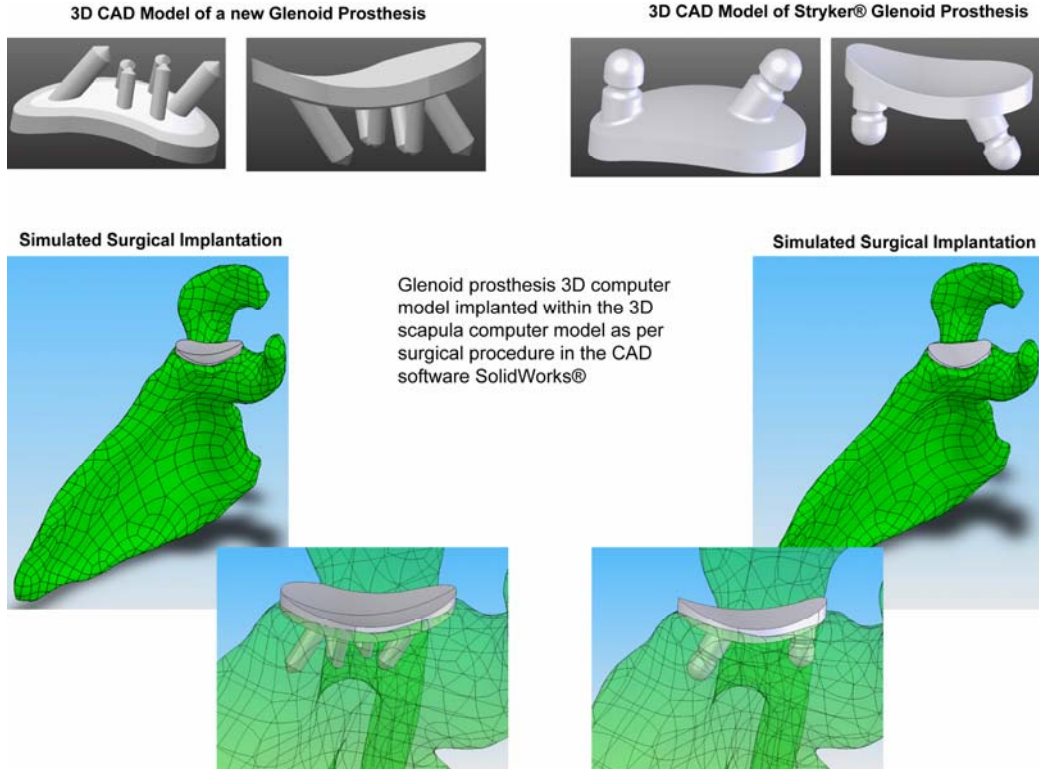


prostheses and scapula CAD models within SolidWorks®, surgical implantation of the prostheses was simulated (Figure 31).

The intact and the glenoid prosthesis-scapula CAD models were imported into Ansys Workbench® (Ansys Inc., Canonsburg, PA, USA) for creation of the finite element models. All models were meshed using 10-node tetrahedron elements. The intact scapula model of the female donor had 34,315 elements, while that of the male donor had 36,034 elements. The glenoid prosthesis-scapula models averaged 36,552 elements in the first case and 131,296 elements in the second. Ansys Classic® was used for the stress analysis.



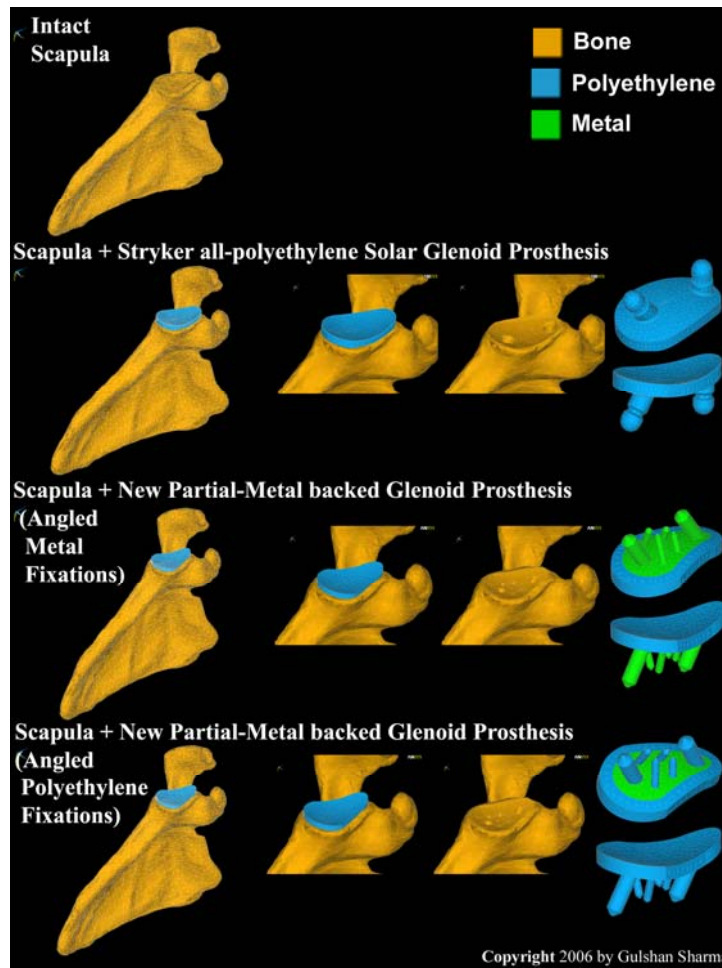
**Figure 30. The process used for creating the 3D finite element model of scapula (illustration by author).**



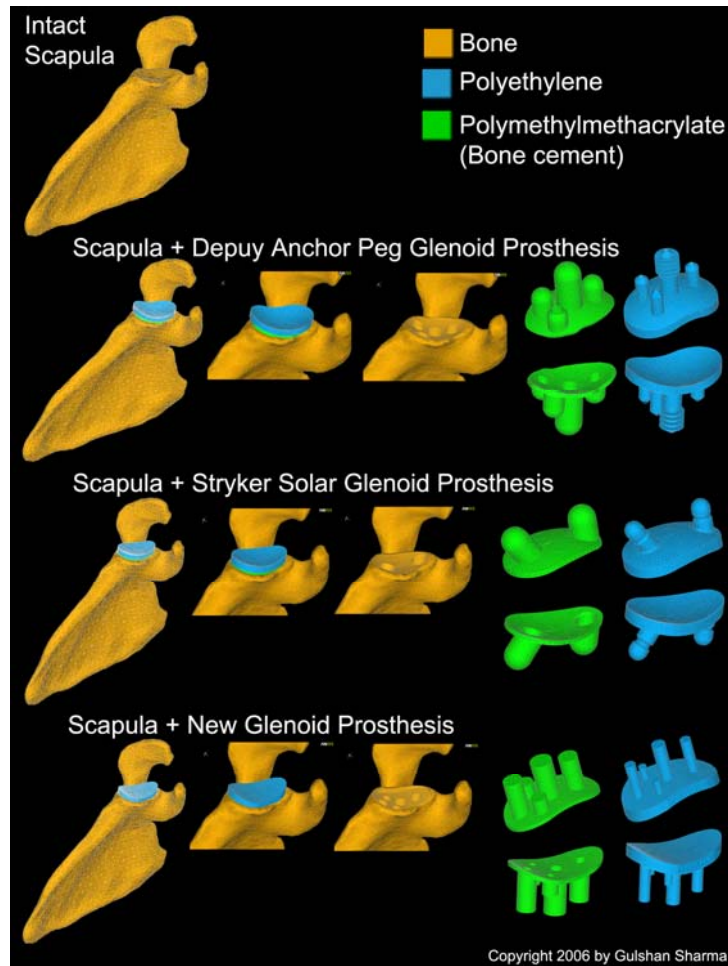
**Figure 31. The simulation of the surgical implantation of 3D CAD model of the glenoid prosthesis in the 3D scapula computer model using the SolidWorks® (SolidWorks Corporation, Concord, MA, USA) software (illustration by author).**

Figure 32 shows the finite element model (FEM) of the intact scapula from the female donor, and the FEMs of the same implanted with the Stryker all-polyethylene Solar® Glenoid Prosthesis, and the two partial-metal backed glenoid prostheses having same geometry but different material for the angled fixations that is metal and polyethylene. It also shows in close-up the FEMs of the glenoid bone, and the glenoid prostheses used. Similarly, Figure 33 shows the finite element models of the intact scapula from the male donor, and the same implanted with the all-polyethylene Depuy Anchor Peg® Glenoid Prosthesis, the Stryker Solar® Glenoid

Prosthesis, and the selected glenoid prosthesis variable model. It also shows in close-up the FEMs of the glenoid bone, bone cement layer, and the glenoid prostheses. In all of the finite element models the interfaces were considered to be fully bonded.



**Figure 32.** The finite element models of intact scapula specimen from an 82 year old female donor, and the same implanted with the all-polyethylene Stryker Solar® Glenoid Prosthesis, and two partial-metal backed glenoid prosthesis having same geometry, but metal and polyethylene angled fixations (illustration by author).



**Figure 33.** The finite element models of intact scapula specimen from a 55 year old male donor, and the same implanted with the all-polyethylene Depuy Anchor Peg® Glenoid Prosthesis, Stryker Solar® Glenoid Prosthesis, and the one glenoid prosthesis variable model (illustration by author).

The all polyethylene glenoid prostheses (Young’s modulus  $E=1.2\text{GPa}$ , Poisson’s ratio  $\nu=0.46$ ) and polymethylmethacrylate (bone cement) ( $E=2\text{GPa}$ ,  $\nu=0.23$ ) were defined as linearly elastic, isotropic, and homogeneous materials. The bone was defined as a linearly elastic, isotropic, and non-homogeneous material. Custom software was written to assign (see Appendix B), in Ansys®, bone elements material properties on a location specific basis based on the CT data of the scapula specimen. The centroid for each element was calculated and the CT number

of the voxel closest to the centroid location identified. The bone density ( $\rho$ ) for the element was

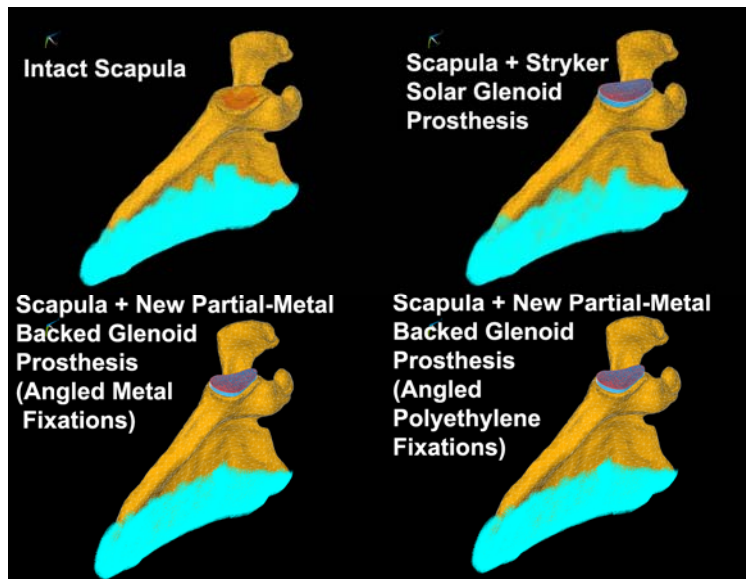
obtained using the expression  $\rho = \left(\frac{0.9}{\max CT\ number}\right)(element\ CT\ number) + 1$ ; in  $g/cc$ . The

bone density was then converted to Young's modulus, using the equation  $E = E_0(\rho/\rho_0)^2$ , where

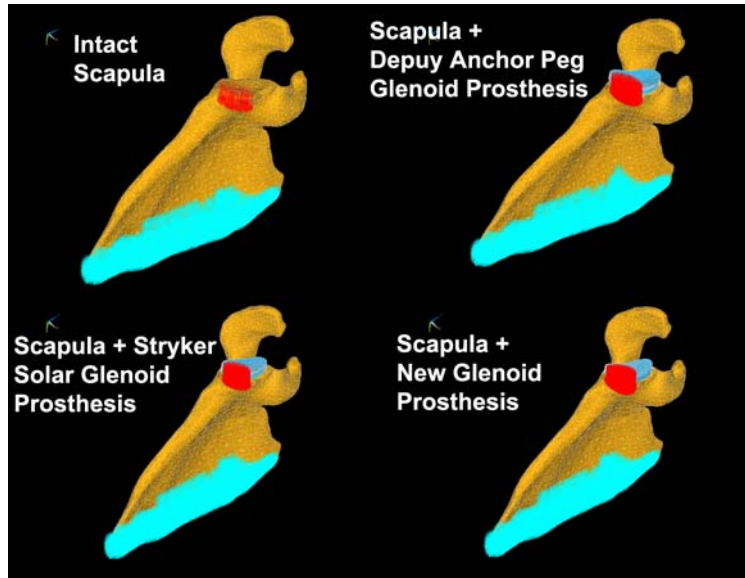
$E_0 = 15GPa$ ,  $\rho_0 = 1.9g/cc$  [133]. As a check the frequency distributions of the bone elements CT

number and the Young's modulus were plotted (Figure 36). Poisson's ratio for bone was

assigned the value 0.3.



**Figure 34.** The load of one bodyweight, 800N, and the boundary condition of fixed nodes at the medial border for the finite element models of the scapula specimen from the female donor, and the same implanted with the Stryker Solar® Glenoid Prosthesis, and the two partial-metal backed glenoid prosthesis having the same geometry but metal, and polyethylene angled fixations respectively (illustration by author).



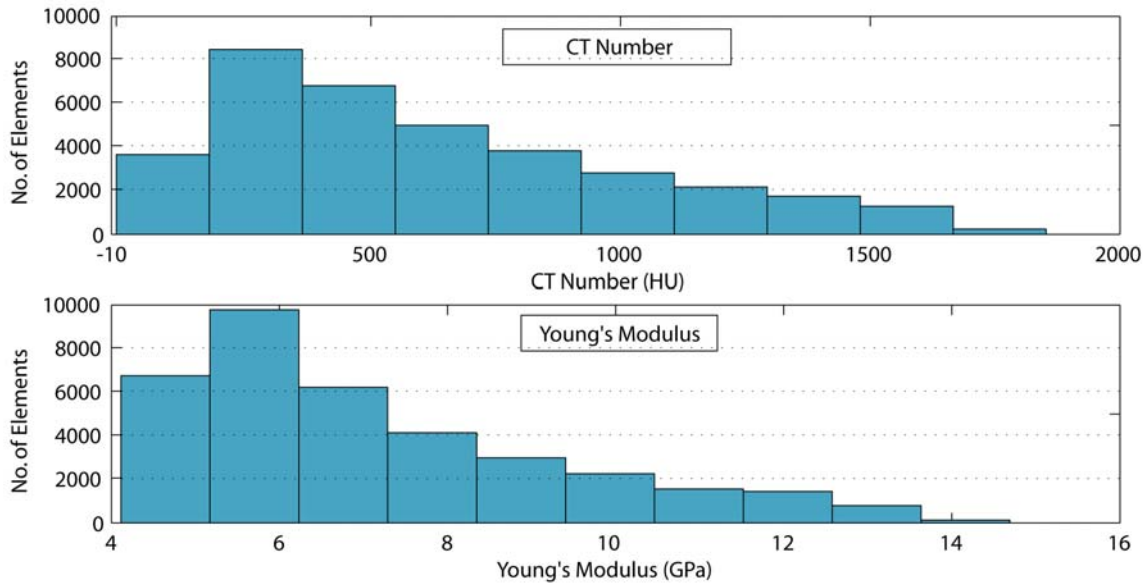
**Figure 35.** The load of one bodyweight, 800N, and the boundary condition of fixed nodes at the medial border for the finite element models of the scapula specimen from the male donor, and the same implanted with the all-polyethylene Depuy Anchor Peg® Glenoid Prosthesis, the Stryker Solar® Glenoid Prosthesis, and the one glenoid prosthesis variable model (illustration by author).

Figure 34 and Figure 35 show the load and boundary conditions for both the cases of the finite element analyses respectively. To avoid rigid body motion in the numerical simulation, the scapula FEM was fixed along the medial border. A medially directed vertical load of 800N (one bodyweight) was applied on the glenoid or the articular surface of the glenoid prostheses. This simulated the arm being abducted to 90°. For all of the FEMs the von Mises stress in the scapula bone was plotted. For the glenoid prosthesis-bone FEMs, the prosthesis and bone cement (for second case only) von Mises stresses were also plotted.



### 5.3 RESULTS

Figure 36 gives the frequency distribution of the CT number and the Young's modulus values of the bone elements of the intact scapula specimen from the male donor. It can be seen that the bone elements CT number and the Young's modulus value have approximately the same frequency distribution profile.



**Figure 36.** The frequency distribution plots of the CT number and the Young's modulus values of the bone elements of the intact scapula specimen from the male donor (graphs by author).

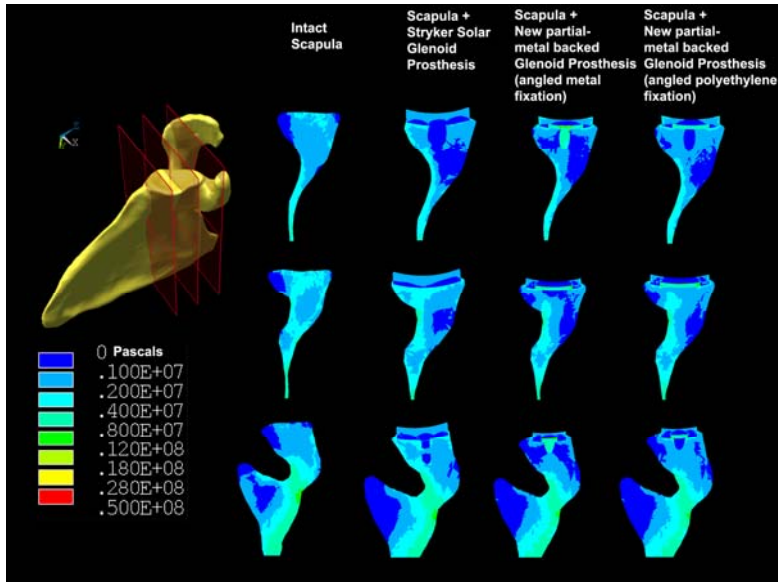


Figure 37. The von Mises stress (Pa) in the axial plane at multiple locations for the first case of the finite element analysis using the scapula specimen from the female donor (figure by author).

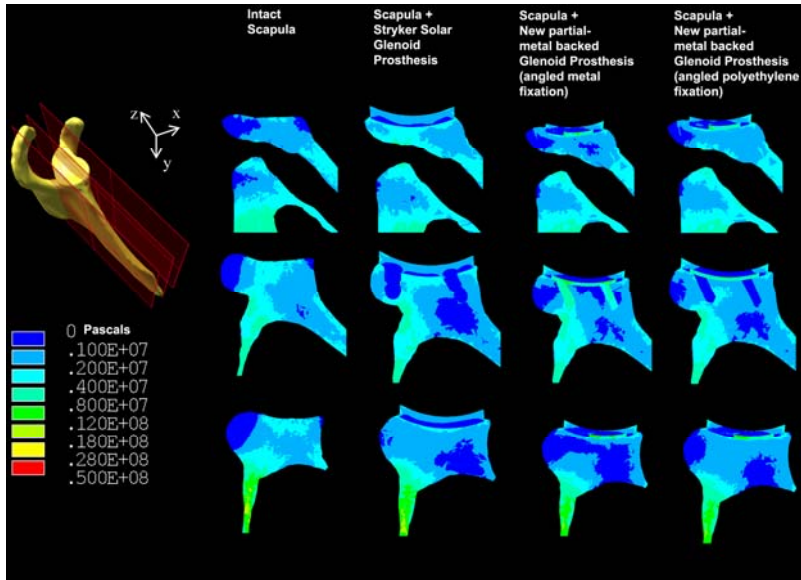


Figure 38. The von Mises stress (Pa) in the coronal plane at multiple locations for the first case of the finite element analysis using the scapula specimen from the female donor (figure by author).



The von Mises stress (Pa) in the axial and the coronal plane at various locations for the first case of the finite element analysis using the scapula specimen from the female donor are shown in Figure 37 and Figure 38 respectively. The range of von Mises stress values in the glenoid vault was approximately between 0 to 28MPa. From Figure 37 it can be seen that the von Mises stress in the anterior region of the glenoid with the various prostheses was lower (0-1MPa) than that in the intact scapula (1-2MPa). The von Mises stress in the posterior region of the glenoid bone implanted with the all-polyethylene Stryker Solar® Glenoid Prosthesis was greater (1-4MPa) than that in the intact scapula and the same implanted with the two partial-metal backed glenoid prostheses (0-2MPa). From Figure 38 it is observed that the von Mises stress in the inferior region of the glenoid bone implanted with the various glenoid prosthesis was lower (0-1MPa) than that in the intact scapula (1-4MPa). Also, the von Mises stress in the superior region of the glenoid bone implanted with the all-polyethylene Stryker Solar® Glenoid Prosthesis was greater (1-4MPa) than that in the intact scapula and the same implanted with the two partial-metal backed glenoid prosthesis (0-1MPa). In both, Figure 37 and Figure 38 it can be seen that the von Mises stress values in the proximal glenoid bone implanted with the two partial-metal backed glenoid prostheses were lower (0-2MPa), more so in the angled metal fixation than the angled polyethylene fixation, compared to that in the intact scapula and the same implanted with the Stryker Solar® Glenoid Prosthesis (1-8MPa). Whereas, the von Mises stress value in the all-polyethylene Stryker Solar® Glenoid Prosthesis was greater (1-2MPa) than that in the polyethylene articulating insert of the two partial-metal backed glenoid prostheses (0-1MPa). Also, higher von Mises stress values were observed in the metal backing of the partial-metal backed glenoid prosthesis having the angled metal fixations (4-12MPa) compared to that having the angled polyethylene fixations (2-12MPa).

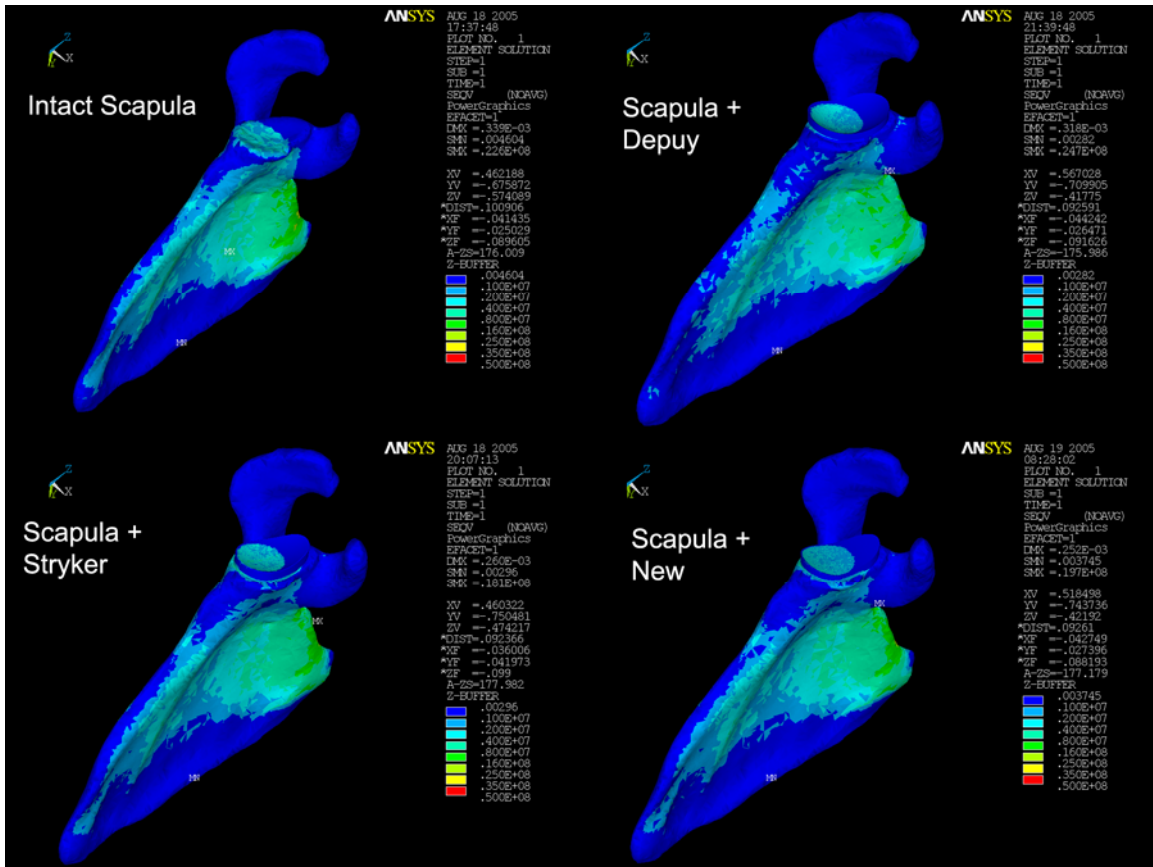


Figure 39. The von Mises stress (Pa) plots of the finite element models of the scapula specimen from the male donor, and the same implanted with the all-polyethylene Depuy Anchor Peg® Glenoid Prosthesis, the Stryker Solar® Glenoid Prosthesis, and the one glenoid prosthesis variable model (figure by author).

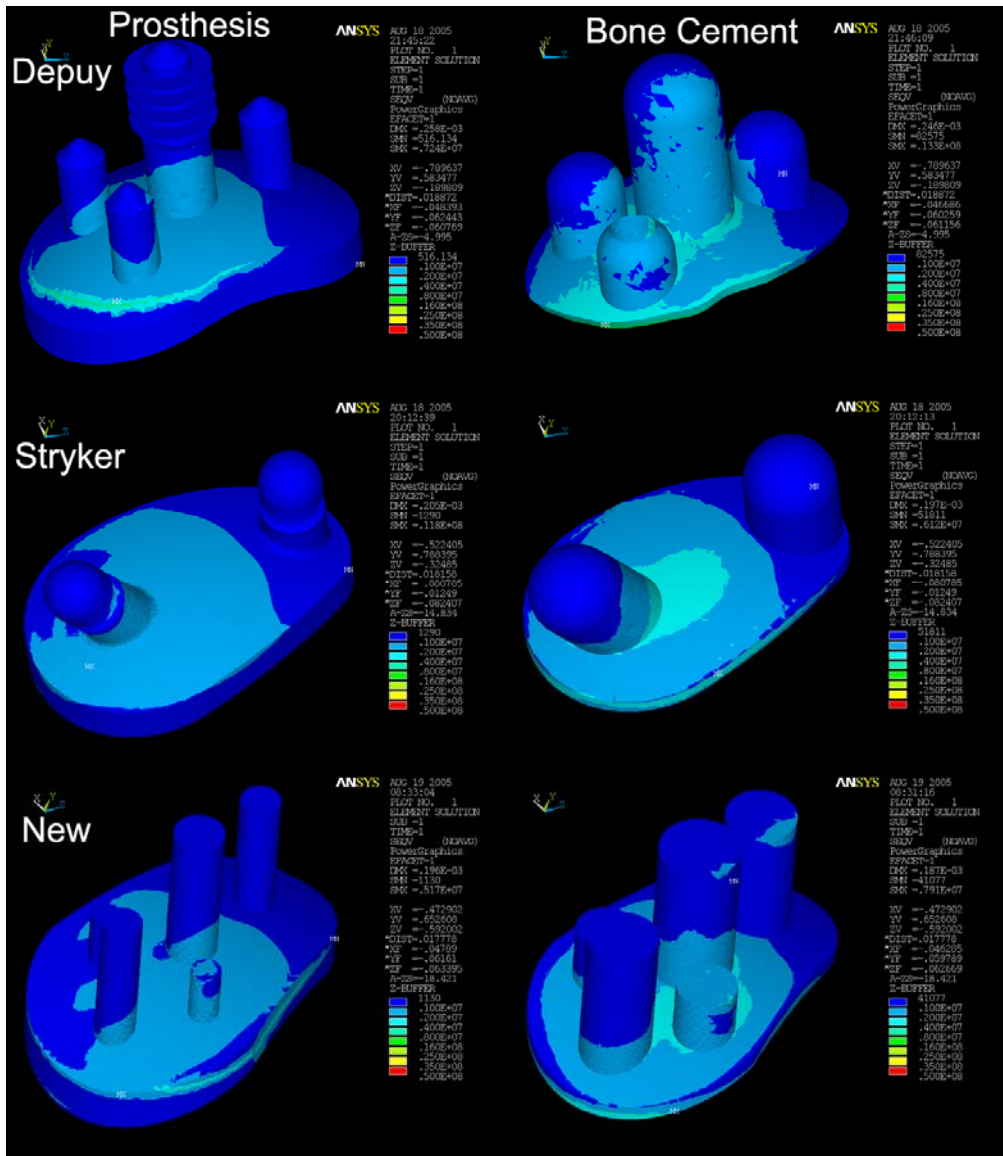


Figure 40. The von Mises stress (Pa) plots of the finite element models of the all-polyethylene Depuy Anchor Peg® Glenoid Prosthesis, the Stryker Solar® Glenoid Prosthesis, and the one glenoid prosthesis variable model and the corresponding bone cement layer (figure by author).

**Table 8. The maximum von Mises stress values in the bone, prosthesis, and the cement region in the finite element models of the scapula specimen from the male donor and the same implanted with the all-polyethylene Depuy Anchor Peg® Glenoid Prosthesis, the Stryker Solar® Glenoid Prosthesis, and the one glenoid prosthesis design variable model (NA: regions not applicable to the finite element model).**

Model	von Mises Maximum Stress (MPa)		
	Bone	Prosthesis	Cement
Intact	22.6	NA	NA
Depuy®	24.7	7.24	13.3
Stryker®	18.1	11.8	6.12
Selected	19.7	5.17	7.91

Figure 39 and Figure 40 show the von Mises stress (Pa) in the finite element models of the scapula specimen from the male donor, and the same implanted with the all-polyethylene Depuy Anchor Peg® Glenoid Prosthesis, the Stryker Solar® Glenoid Prosthesis, and the one glenoid prosthesis design variable model. Table 8 gives the maximum von Mises stress value in the bone, cement and prostheses regions of the finite element models.

The maximum von Mises stress in the bone decreased with the Stryker® (18.1MPa), and the one glenoid prosthesis design variable model (19.7MPa) compared to the intact scapula (22.6MPa), whereas it increased slightly for the Depuy® glenoid prosthesis (24.7MPa). The cement region for the Depuy® glenoid prosthesis had higher maximum von Mises stress value (13.3MPa) compared to the Stryker® (6.12MPa) and one design variable model (7.91MPa) models. These values are comparable to prior studies (~0-10MPa) [27, 135]. The cement region stresses in all the three prosthesis bone models were greater than the crack initiation value (5-7MPa) under physiologic conditions [176]. The maximum von Mises stress value in the Stryker® glenoid prosthesis (11.8MPa) was higher compared to that in the Depuy® (7.24MPa) or the one design variable model (5.17MPa).

## 5.4 DISCUSSION

The finite element method allowed comparison of the current market Depuy® Anchor Peg and Stryker® Solar Glenoid Prosthesis, and the glenoid prosthesis design variable models. Three dimensional subject-specific finite element models of the intact scapulae specimen and the same implanted with various glenoid prostheses were created successfully. The process included the simulation of the surgical method of glenoid prosthesis implantation using the computer aided design software SolidWorks®. Using a custom software program written by the author, which makes use of the computed tomography (CT) images of the scapula specimen, and the element and node data of the finite element model of the same, location specific material properties were assigned to the bone elements, thereby improving the numerical simulation's reflection of the actual situation as can be seen from the approximately similar frequency distribution plots of the bone element CT and Young's Modulus value shown in Figure 36. This captured the specificity of the material properties of the varying bone. The method developed was effectively demonstrated on the two selected scapulae specimen and can be extended to include any scapula or bone for which volumetric CT data is available.

For the first case of the finite element analysis (FEA) the scapula specimen from the 82 year old female donor was used. Two glenoid prosthesis variable models were compared to the Stryker Solar® Glenoid Prosthesis. The two glenoid prosthesis variable models were partial-metal backed with same geometry and identical angled fixations. However in one of the prostheses the angled fixations were of polyethylene while in the other they were of metal.

From the von Mises stress plots shown in Figure 37 and Figure 38 it was found that the range of the von Mises stress in the glenoid vault was approximately between 0-28MPa. This was similar to those reported in prior 3D FEA studies [27, 29, 30]. The von Mises stress in the

glenoid was found to decrease in the anterior, and increase in the posterior region of the glenoid prostheses-scapula FEMs compared to the intact scapula, signifying a tendency for the scapula implanted with the glenoid prostheses to bend posteriorly. Also, the von Mises stress in the posterior glenoid bone region of the scapula implanted with the all-polyethylene (PE) Stryker Solar® Glenoid Prosthesis was higher (2-4MPa) compared to the partial-metal backed glenoid prosthesis (0-2MPa) implying that posterior bending is greater with all-PE prosthesis than metal-backed prosthesis, probably since polyethylene is a less stiff material than metal.

The von Mises stress in the proximal glenoid decreased (0-2MPa) with the partial-metal backed prosthesis compared to the intact (1-4MPa). This is the “stress shielding” phenomenon, which means that majority of the stress passes through the denser metal into the distal cancellous bone, thereby reducing the stress in the proximal glenoid. Previous studies by Gupta et al [38], Lacroix et al [28], and Orr et al [33] had also shown lower stresses in bone proximal with metal backed glenoid prosthesis with similar stress values ranging between 0.05-2.3MPa. In this study greater reduction in the proximal glenoid von Mises stress was observed with the metal fixations compared to the polyethylene, which resulted in stress values approximately similar to the intact glenoid especially in the posterior region.

Increased von Mises stress (1-2MPa) was found in the all-PE Stryker Solar® Glenoid Prosthesis compared to the polyethylene articulating insert of the partial-metal backed prosthesis (0-1MPa), may be since most of the applied load passes through to the denser metal backing, that is, another effect of the “stress shielding” phenomenon.

In the second case of the finite element analysis, the scapula specimen from the 55 year old male donor was used. The all-PE cemented prostheses, that is, the Depuy Anchor Peg®, the Stryker Solar®, and the glenoid prosthesis variable model were compared among each other and

the intact specimen model. The range of the von Mises stress value obtained for all the FEMs (Figure 39) was between 0.001-25MPa which is approximately similar to that in previous studies by Gupta et al [27] (0-25MPa), Lacroix et al [28] (0-12MPa), and Terrier et al [30] (0-12MPa). During the surgical implantation simulation it was found that the Depuy® glenoid prosthesis did not fit well, that is, the prosthesis non-articular surface did not completely lay on the glenoid fossa of the specimen model, resulting in a portion of the prosthesis overhanging the superoanterior glenoid boundary. No such overhang was observed with the Stryker® and the glenoid prosthesis variable models.

The maximum von Mises stress value in the scapula implanted with the Stryker® (18.1MPa) and the glenoid prosthesis variable models (19.7MPa) was less than that in the intact scapula (22.6MPa). This may be due to the slight absorption of the applied load by the prosthesis and cement regions. However, the maximum von Mises stress value in the scapula implanted with the Depuy® prosthesis (24.7MPa) increased compared to intact and may be attributed to the Depuy® prosthesis overhanging the superoanterior glenoid boundary.

The poor fit of the Depuy® glenoid prosthesis may have also resulted in the maximum von Mises stress value in the cement region (13.3MPa) to be greater than that for the Stryker® (6.12MPa) and the glenoid prosthesis variable model (7.91MPa). The cement layer von Mises stress values obtained were similar to that reported by Gupta et al [27] (8.31MPa). The bone cement failure strength in tension has been reported to be 25MPa [27, 177]. Although the stress values obtained were less than the failure strength, they are higher than the crack initiation value of 5-7MPa under physiologic conditions [27, 176].

The maximum von Mises stress value found in the Stryker Solar® Glenoid Prosthesis (11.8MPa) was greater than that in the Depuy Anchor Peg® Glenoid Prosthesis (7.24MPa) and

the glenoid prosthesis variable model (5.71MPa). This may in part be due to the fewer number of pegs for fixation in the Stryker® glenoid prosthesis (2 pegs) compared to the Depuy® (4 pegs) or the glenoid prosthesis variable model (5 pegs).

Both of the above finite element analyses had certain limitations. All the interfaces in the models were assumed to be fully bonded which may not be true physiologically, perhaps possible immediately after surgery. No interface stresses were modeled. The load was applied simulating only the 90° abducted arm position and the boundary conditions did not take into account other bony articulations or muscle forces on the scapula.

However this study helped to compare different design variables to the current market Stryker Solar® and Depuy Anchor Peg® glenoid prosthesis in a non-destructive manner using subject-specific finite element models with location-specific material properties. It also demonstrated the ease with which physiologically relevant finite element models can be created.



## **6.0 GLENOID BONE REMODELING: NUMERICAL SIMULATION AND VALIDATION**

### **6.1 INTRODUCTION**

Current finite element models of the scapula with or without glenoid prostheses use location specific bone material properties, physiologic joint reaction and muscle loads, and realistic boundary conditions [27, 28, 178]. However no previous numerical model incorporated Wolff's Law [36, 37], which describes the phenomenon of bone remodeling, that is, the adaptation of bone in shape and structure to variations in the loads experienced, and have not simulated normal glenoid bone remodeling or remodeling in response to implanted glenoid prostheses. There are numerous remodeling simulation theories available in the literature [36, 37, 144, 179]. In this study, remodeling was controlled by the bone strain-energy and only the internal structure was remodeled.

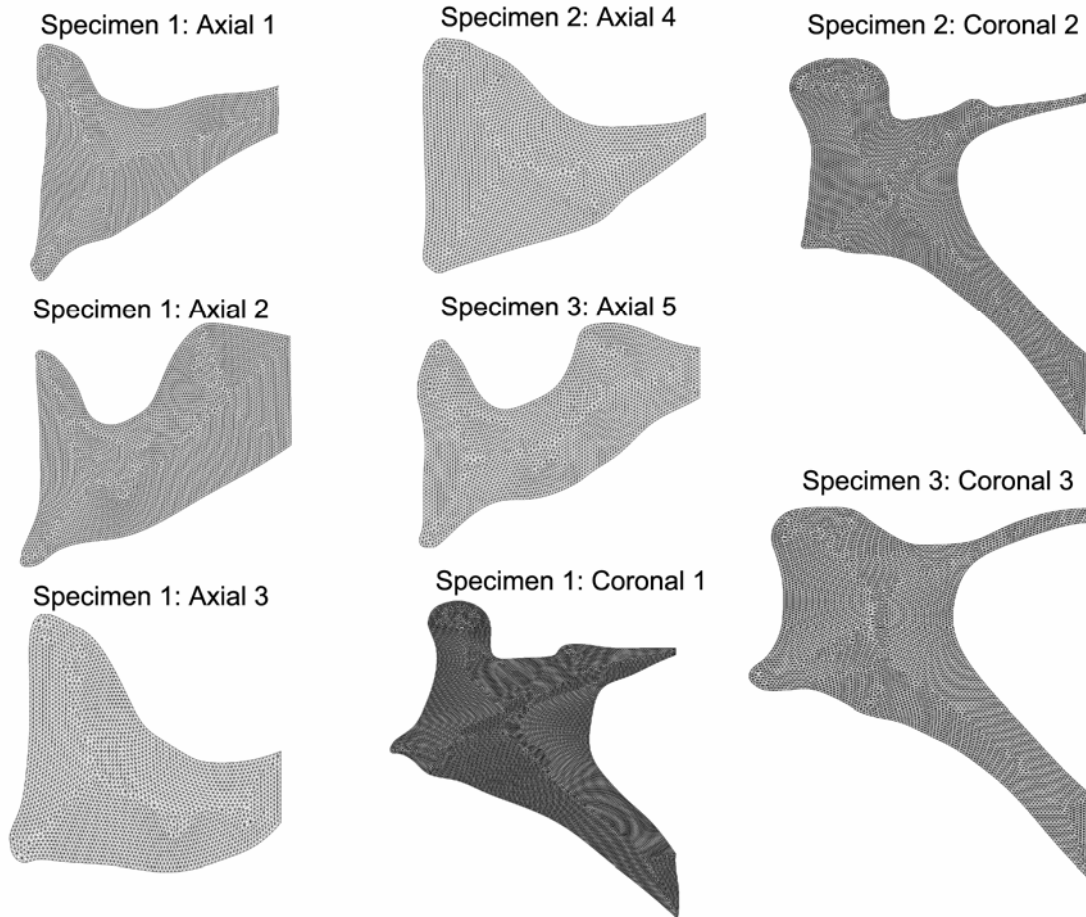
Past studies have reported the drawback of obtaining a “checkerboard” pattern, in which adjacent remodeled elements were either saturated or completely resorbed, near the region of the load application in the remodeling simulation when considering only the centroid of the elements in the finite element model, that is, the “element” based approach. Jacobs, Beaupre et al [179] had suggested a “node” based approach wherein the remodeling process operates at the nodes

rather than the element centroid and gave highly continuous results across element boundaries in the femur.

The goals of this study were to create a 2-D “element” and “node” based finite element model (FEM) process for calculating subject-specific internal bone remodeling of the glenoid using the forward-Euler method, and validate this process using actual intact glenoid initially resetting its internal material properties to be uniform and comparing the remodeling simulation results to the actual material properties. Multiple cross-sections in the axial and the coronal plane of various scapulae specimen were used for the validation.

## **6.2 MATERIALS AND METHODS**

Three cadaver scapula specimens were obtained from donors in the Midwestern United States, a 55-year-old male (specimen 1), an 82 year-old female (specimen 2), and a 42 year-old female (specimen 3). The specimens were imaged using high-resolution volumetric axial computed tomography (CT). The CT images were imported into Amira® 3.0 (TGS, Inc., CA, USA). Three axial cross-sections passing through the inferior, center, and the posterior region of the glenoid were selected from specimen 1, two axial cross-sections with each passing through the glenoid center were selected from specimens 2 and 3, and three coronal cross-sections with each passing through the glenoid were selected from all three specimens, giving a total of 8 cross-sections, 5 in the axial and 3 in the coronal plane (Figure 41). Image segmentation tools were used to contour the glenoid bone in all the 8 selected cross-sections.



**Figure 41.** The five axial and three coronal plane glenoid bone finite element models created using three cadaver scapula specimens obtained from donors, a 55 year-old male (specimen 1), an 82 year-old female (specimen 2), and a 42 year-old female (specimen 3), in the Midwestern United States (illustration by author).

The bone contours were imported into Ansys® (Ansys, Inc., PA, USA) and the 2-D finite element models (FEMs) were created using the six-node solid triangular elements with an average edge length of 0.45mm (Figure 41). Table 9 gives the element and node count for all the finite element models. On average the axial cross-section glenoid FEM had 6464 elements and 13192 nodes, whereas the coronal cross-section glenoid FEM had 14186 elements and 28887 nodes. A custom program written by the author assigned linearly elastic, isotropic, non-

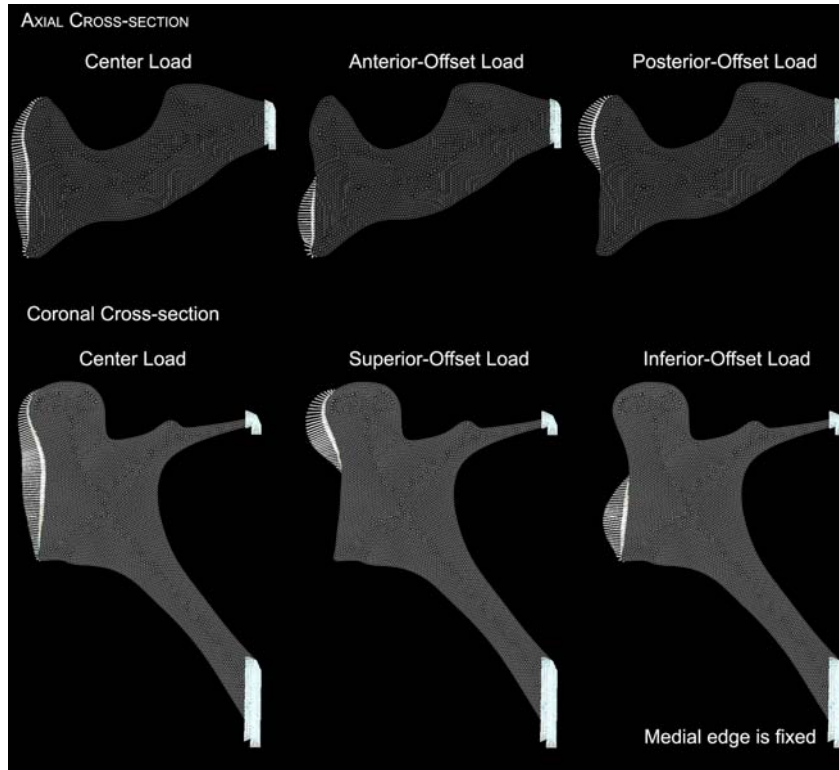
homogenous material properties to each bone element based on the CT value at that element. Poisson’s ratio for bone was assigned to be 0.3. Three kinds of load were applied to each of the 8 glenoid bone finite element models (Table 10). The center load simulated 90° of arm abduction with a total joint reaction force of 800N (1 bodyweight), while the posterior-, anterior-, inferior-, or superior-offset loads simulated extremes of the range of motion with a reaction force of 400N (0.5 bodyweight). Therefore, for each glenoid FEM, six different combinations of multiple loads were applied resulting in a total of 12 simulations, 6 for the “element” and 6 for the “node” based remodeling approach. In each simulation, the applied combination of multiple loads was repeated for 300 iterations. The medial border of the FEMs was fixed to avoid any rigid body motion.

**Table 9. The element and node count for the five axial and three coronal plane glenoid bone finite element models created for the remodeling simulations.**

<b>No.</b>	<b>Finite Element Model</b>	<b>Element Count</b>	<b>Node Count</b>
<b>1</b>	Specimen 1: Axial 1	6606	13495
<b>2</b>	Specimen 1: Axial 2	9264	18853
<b>3</b>	Specimen 1: Axial 3	5230	10687
<b>4</b>	Specimen 2: Axial 4	5415	11058
<b>5</b>	Specimen 3: Axial 5	5799	11866
<b>6</b>	Specimen 1: Coronal 1	21676	43951
<b>7</b>	Specimen 2: Coronal 2	10181	20846
<b>8</b>	Specimen 3: Coronal 3	10699	21864

**Table 10.** The six different combinations of multiple loads applied to the axial and the coronal plane glenoid finite element models during the remodeling process.

Load	Axial Cross-section	Coronal Cross-section
1	Anterior-Center-Posterior (ACP)	Center-Inferior-Superior (CIS)
2	Anterior-Posterior-Center (APC)	Center-Superior-Inferior (CSI)
3	Center-Anterior-Posterior (CAP)	Inferior-Center-Superior (ICS)
4	Center-Posterior-Anterior (CPA)	Inferior-Superior-Center (ISC)
5	Posterior-Anterior-Center (PAC)	Superior-Center-Inferior (SCI)
6	Posterior-Center-Anterior (PCA)	Superior-Inferior-Center (SIC)



**Figure 42.** The center, anterior-offset, posterior-offset, superior-offset, and inferior-offset loads and the fixed medial edge boundary condition applied to the axial and coronal plane cross-section glenoid finite element models (illustration by author).

The internal structure bone remodeling simulation was governed by the strain-energy of the element and is adapted from Weinans, Huiskes et al, [36] and Jacobs, Beaupre et al [179].

$$\frac{d\rho}{dt} = B[S - (1 \pm s)S_{ref}]S_v(\rho), \text{ if } S \geq (1 + s)S_{ref} \text{ or } S \leq (1 - s)S_{ref}, \quad (1)$$

$$= 0, \text{ otherwise},$$

Where,

$\rho$ : the bone apparent density in  $\text{kg/m}^3$ , and  $d\rho/dt$  is the rate of change of bone apparent density,

also  $\rho_{min} \leq \rho \leq \rho_{max}$ , where  $\rho_{min} = 1 \text{ kg/m}^3$ ,  $\rho_{max} = 1800 \text{ kg/m}^3$

B: the remodeling rate constant in  $(\text{kg/m}^3)^2/\text{N}\cdot\text{sec}$ ,

S: the bone remodeling stimulus in  $\text{N}\cdot\text{m}/(\text{kg/m}^3)$ , and  $S = U/\rho$ , where U: strain-energy in  $\text{N}\cdot\text{m}$ ,

$S_{ref}$ : the reference stimulus in  $\text{N}\cdot\text{m}/(\text{kg/m}^3)$ ,

s: constant determining the extent of the bone “dead zone” or “lazy zone” (remodeling stimulus range in which no bone apposition or resorption occurs), and

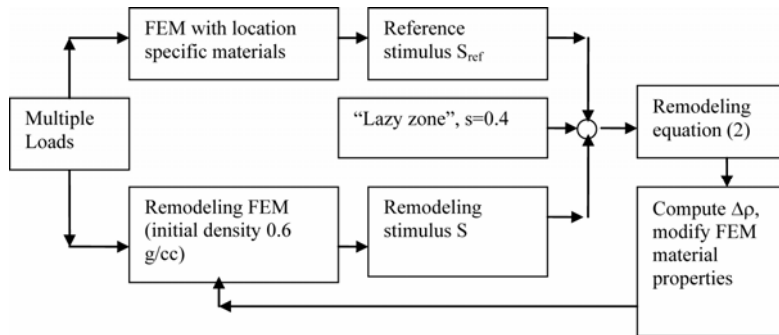
$S_v(\rho)$ : the surface area per unit volume in  $\text{m}^2/\text{m}^3$  or  $1/\text{m}$  obtained from Martin et al [180].

$$\Delta\rho = B[S - (1 \pm s)S_{ref}]S_v(\rho)\Delta t, \text{ if } S \geq (1 + s)S_{ref} \text{ or } S \leq (1 - s)S_{ref}, \quad (2)$$

$$= 0, \text{ otherwise}$$

For computational purposes the forward-Euler integration, that is,  $\rho_{n+1} = \rho_n + \Delta\rho_n$  was used, where n is the iteration number and  $\Delta\rho$  is given by expression (2) above. The bone remodeling algorithm is illustrated in Figure 43. All the glenoid FEMs with actual specimen location specific material properties were solved to obtain the reference stimulus value  $S_{ref}$  in each of the three load cases.

Validation: To test the remodeling algorithm, all glenoid bone elements were reset to a homogeneous density value of 0.6g/cc or 600kg/m<sup>3</sup>. The remodeling rate constant B was 200, “lazy zone” constant s was taken as 0.4, surface area per unit volume  $S_v(\rho)$  was obtained from literature [180], and the time increment  $\Delta t$  equaled 10 days. The predicted bone apparent density values were limited to physiologically observed range of 1-1800kg/m<sup>3</sup> [36]. During the iterative remodeling process the glenoid FEM was loaded using the multiple load combination (Table 10), remodeling stimulus S for each element computed using the remodeling expression given in equation 2, change in the element apparent density computed, and the glenoid FEM element material properties modified. The process continued for 300 iterations. For the “node based” approach additional steps in each iteration included the computation of the remodeling stimulus S at the nodes by considering the contributions from the surrounding elements, computing the change in the bone apparent density at the nodal locations, computing the element bone apparent density using the element shape functions for the 2D 6-node triangle element, and lastly modifying the glenoid FEM element material properties. A sample Ansys® script for both the “element” and “node” FEM-based glenoid bone remodeling is given in Appendix D.



**Figure 43.** The glenoid bone “element” based remodeling algorithm adapted from Weinans, Huiskes et al [36] (illustration by author).

The predicted bone apparent density values at the end of all the simulations of the glenoid FEMs were plotted along with the corresponding bone apparent density of the actual specimens. For all the “element” and “node” based remodeling simulations of the glenoid FEMs, the difference of the predicted and the actual specimen bone apparent density values computed in every iteration on a location specific-basis were averaged over all the elements or the nodes of the selected glenoid FEM respectively and plotted with respect to the iteration number. Also, for all the simulations of the glenoid FEMs, linear regression analysis was performed between the predicted and the actual specimen bone apparent density value in each of the iterations and the correlation coefficient plotted with respect to the iteration number. Finally, for all the glenoid FEMs difference images of the predicted and the actual specimen bone apparent density value at the end of the simulations were plotted. All of the above plots allowed for the validation of the developed remodeling process and understand the effects of the various combinations of multiple loads in a qualitative and quantitative manner.

### **6.3 RESULTS**

Upon examination of the large amount of data it was found that the various multiple load combinations applied during the remodeling simulations gave approximately similar results. Therefore it is sufficient to show the figures of the finite element models using the load combination 4 (CPA/ISC, Table 10) in this section. Appendix E shows the figures of the glenoid FEMs for all the load combinations.

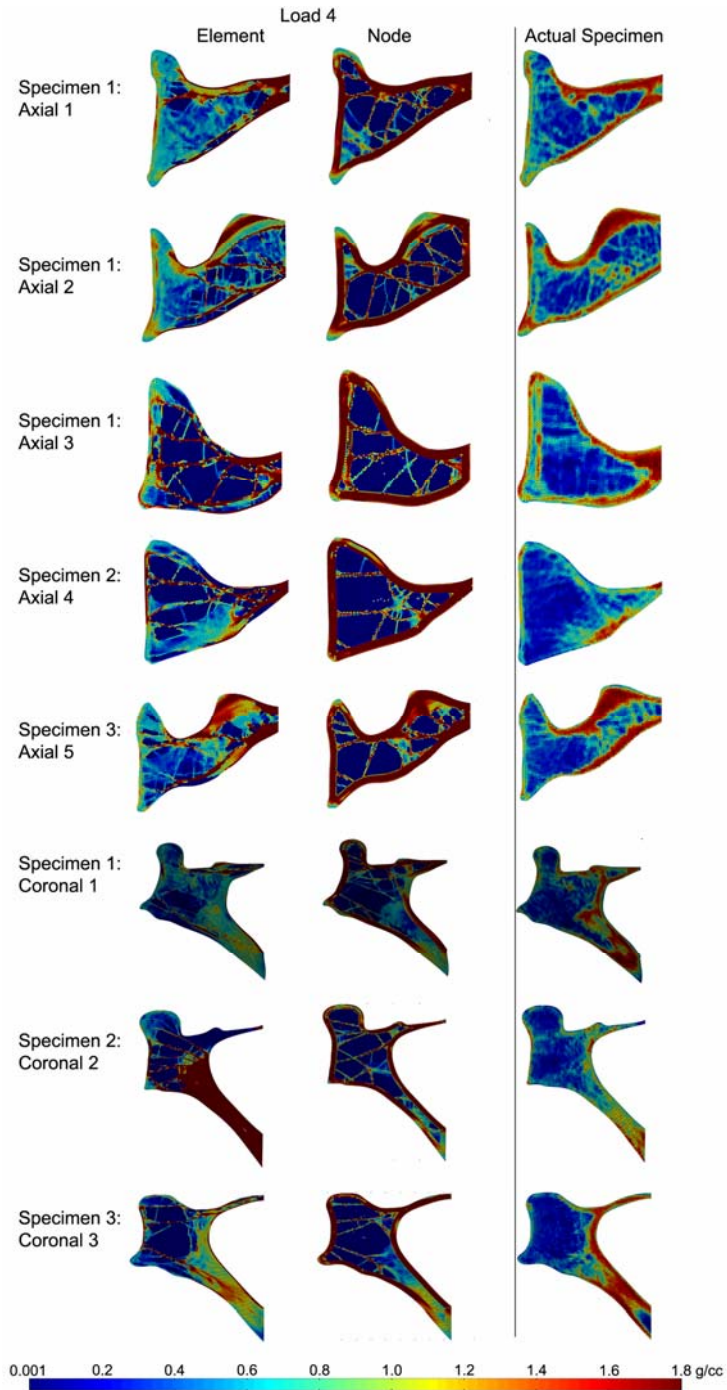


Figure 44 shows the predicted bone apparent density for all the finite element models at the end of the “element” and “node” based iterative remodeling process using load combination 4 (CPA/ISC), along with the bone apparent density plot of the actual specimens. The predicted cancellous bone apparent density for the “element” based approach was observed to better approximate that of the actual specimen. In the “node” based approach majority of the predicted cancellous bone region was found to be resorbed with only the key trabeculae distinctly visible. Also, the “element” based approach showed the “checker-board” pattern in the anterior and posterior margins cortical bone which was absent from the “node” based approach results.

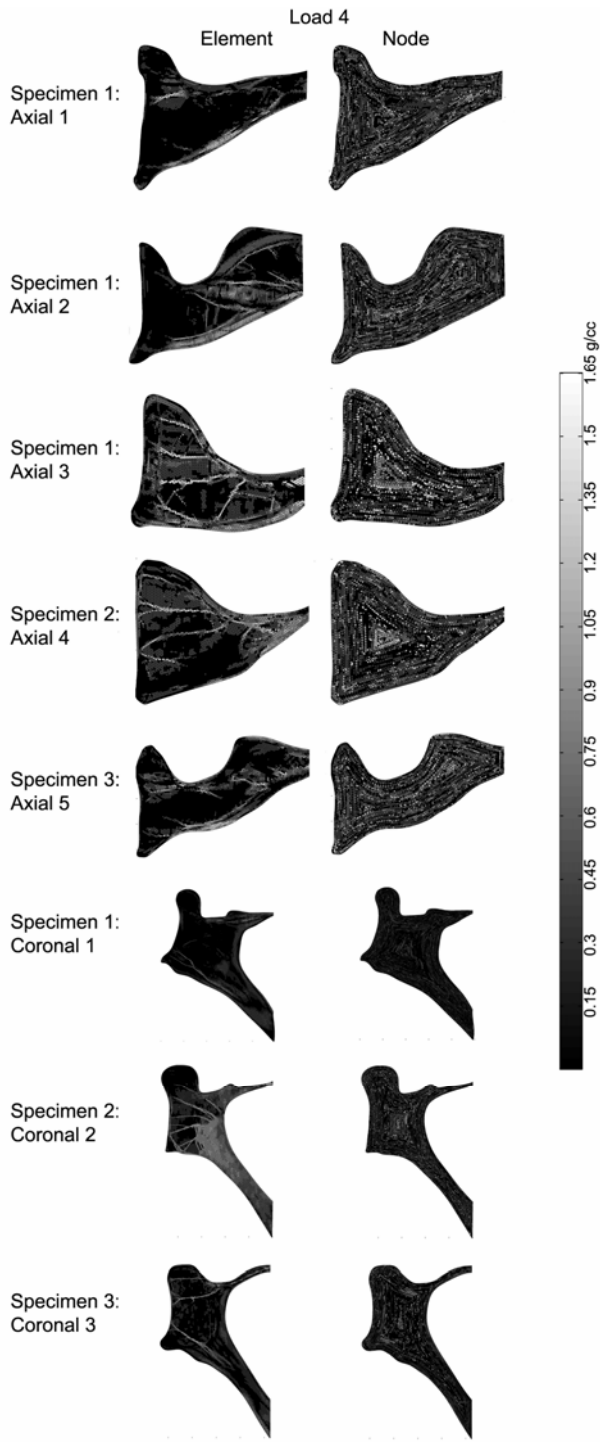
Figure 46 gives the mean and standard deviation of the location-specific absolute difference of the predicted and the actual specimen bone apparent density value in  $\text{kg/m}^3$  at the end of the remodeling simulations, computed over all the elements or the nodes of the glenoid FEM depending upon the “element” or “node” based remodeling process used. The mean of the absolute difference in the “element” based approach was lower (axial range: 280-490 $\text{kg/m}^3$ , coronal range: 350-730 $\text{kg/m}^3$ ) than that in the “node” based approach (axial range: 610-810 $\text{kg/m}^3$ , coronal range: 580-730 $\text{kg/m}^3$ ).

The absolute difference image plots of the predicted and actual specimens bone apparent density value, computed on a location-specific basis at the end of the “element” and the “node” based remodeling simulations using the load combination 4 (CPA/ISC) for the glenoid finite element models are shown in Figure 45. For the “element” based approach, the difference was less than 0.4g/cc for approximately 75% and 65% of the glenoid bone FEM in axial and coronal plane respectively, as can be seen from the frequency distribution plots in Figure 47. On the other hand, in the “node” based approach more than 50% of the axial and coronal plane glenoid bone FEM had values greater than 0.4g/cc.

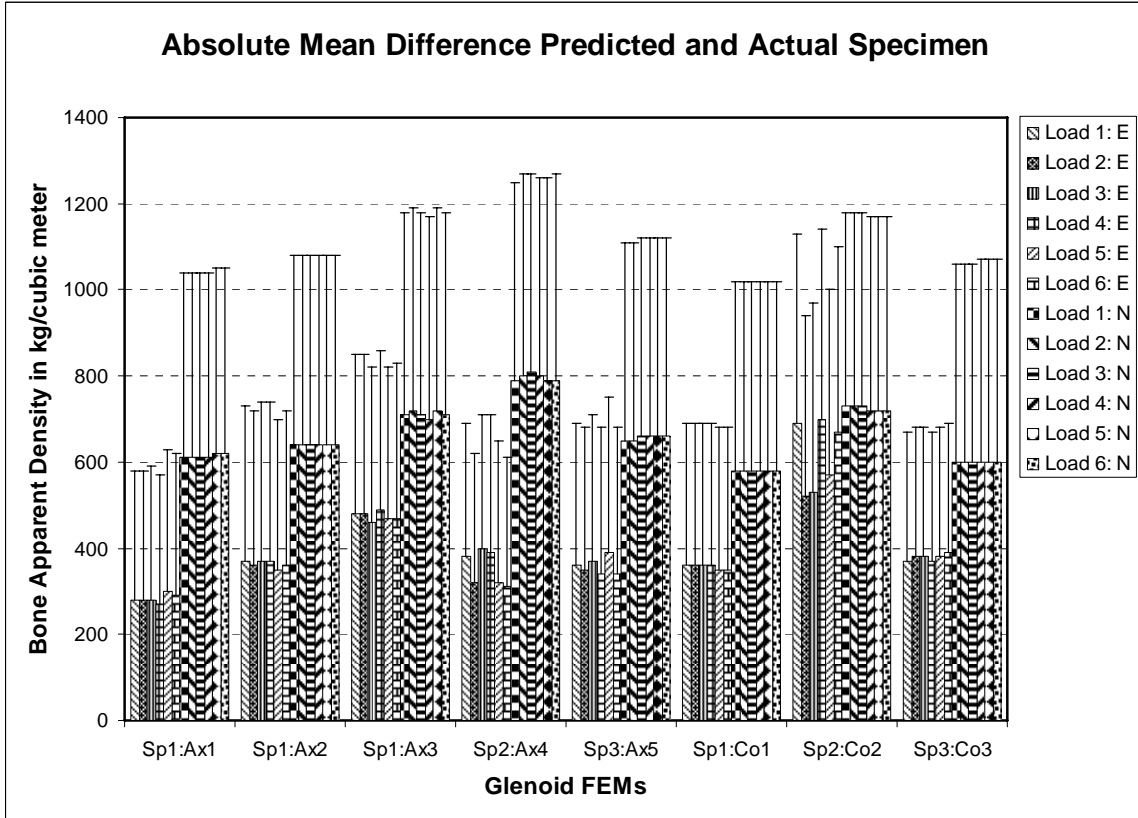
Table 11 shows the results of the linear regression analysis (equation of line, correlation coefficient, and the root mean square error) between the predicted and the actual specimen bone apparent density value at the end of the remodeling simulations for all the glenoid FEMs using the various load combinations. Medium correlation (0.51-0.69) was obtained for the “element” based approach, whereas the “node” approach had low correlation ( $<0.5$ ). Also, the root mean square error was lower for the “element” based approach ( $488\pm 87\text{kg/m}^3$ ) than the “node” ( $694\pm 44\text{kg/m}^3$ ). In Figure 48 the linear approximation of the predicted bone apparent density value with respect to that in the actual specimen for the Axial 1 and Coronal 3 glenoid FEMs was relatively better in the “element” based approach compared to the “node” based remodeling process using the load combination 4 (CPA/ISC).



**Figure 44.** The bone apparent density plots at the end of the iterative “element” and “node” based remodeling process for all the glenoid finite element models simulated using the load combination 4 (CPA/ISC). Also shown for comparison is the bone apparent density plot for all the actual specimens (figure by author).

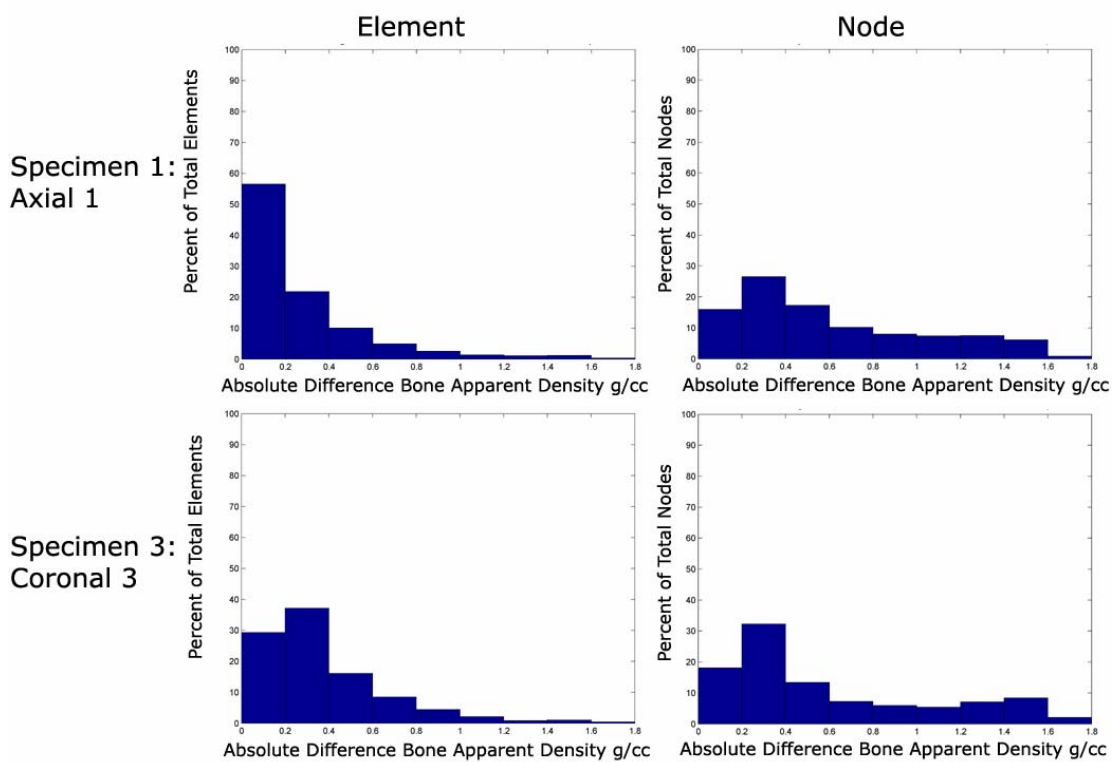


**Figure 45.** The absolute value of the location-specific difference of the predicted and the actual specimen bone apparent density images of the glenoid finite element models at the end of the “element” and the “node” based bone remodeling simulations with the load combination 4, CPA/ISC (figure by author).



**Figure 46.** The mean and standard deviation of the location-specific absolute difference between the predicted and the corresponding actual specimen bone apparent density value in  $\text{kg/m}^3$  computed at the end of the simulations over all the elements and the nodes depending upon the “element” (E) or the “node” (N) based remodeling process for all the glenoid finite element models using the six different multiple load combinations (Load 1:ACP/CIS, Load 2:APC/CSI, Load 3:CAP/ICS, Load 4:CPA/ISC, Load 5:PAC/SCI, Load 6:PCA/SIC) (figure by author).

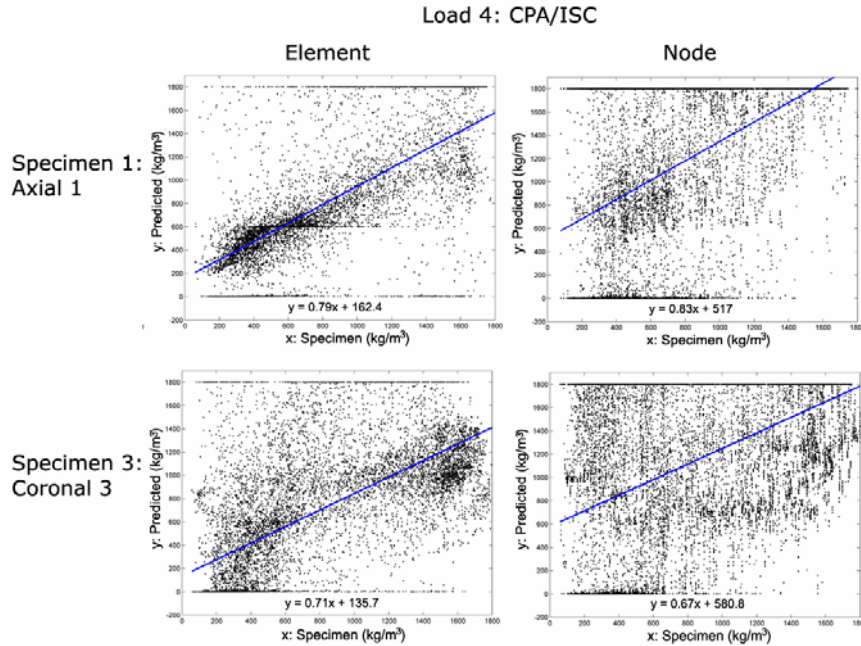
Frequency Distribution of Absolute Difference Between  
 Predicted and Actual Specimen bone apparent density  
 Load 4: CPA/ISC



**Figure 47.** The frequency distribution of the absolute difference between the predicted and the actual specimen bone apparent density in the Axial 1 and Coronal 3 glenoid FEM for the “element” and “node” based simulations using the load combination 4 (figure by author).

**Table 11. The linear regression analysis results for the predicted bone apparent density value in kg/m<sup>3</sup> at the end of the iterative remodeling process using the “element” (E) and “node” (N) based approach for all the glenoid FEMs with the 6 different load combinations (Load 1:ACP/CIS, Load 2:APC/CSI, Load 3:CAP/ICS, Load 4:CPA/ISC, Load 5:PAC/SCI, Load 6:PCA/SIC) versus that in the corresponding actual specimen (equation of line (y: predicted, x: specimen), correlation coefficient (r), and root mean square error (rmse) value).**

FEM		Load 1		Load 2		Load 3		Load 4		Load 5		Load 6	
		E	N	E	N	E	N	E	N	E	N	E	N
Ax 1	Eq. of line	y = 0.86x + 121.4	y = 0.84x + 514.1	y = 0.86x + 121.2	y = 0.84x + 515	y = 0.79x + 157.2	y = 0.83x + 515.3	y = 0.79x + 162.4	y = 0.83x + 517	y = 0.65x + 227.7	y = 0.82x + 516.4	y = 0.64x + 241.6	y = 0.82x + 513.7
	r	0.69	0.52	0.69	0.52	0.66	0.51	0.67	0.51	0.58	0.5	0.58	0.5
	rmse	405	634	406	639	406	641	396	641	414	651	409	660
Ax2	Eq. of line	y = 0.59x + 270.9	y = 0.75x + 521.3	y = 0.59x + 275.1	y = 0.75x + 528	y = 0.58x + 279.3	y = 0.75x + 522.7	y = 0.58x + 278.2	y = 0.75x + 524.4	y = 0.59x + 275.6	y = 0.74x + 528.5	y = 0.58x + 280.4	y = 0.73x + 549.4
	r	0.51	0.45	0.51	0.45	0.5	0.45	0.5	0.45	0.52	0.45	0.51	0.45
	rmse	472	699	465	695	477	698	479	700	453	698	469	692
Ax 3	Eq. of line	y = 0.74x + 92.8	y = 0.91x + 486.8	y = 0.75x + 76.1	y = 0.9x + 511.5	y = 0.77x + 90.6	y = 0.9x + 506.6	y = 0.78x + 70.8	y = 0.92x + 487.4	y = 0.84x + 33.4	y = 0.89x + 516.6	y = 0.82x + 41.2	y = 0.91x + 509.4
	r	0.49	0.49	0.5	0.48	0.51	0.48	0.5	0.49	0.55	0.48	0.54	0.49
	rmse	588	731	592	736	575	728	601	727	580	734	581	728
Ax 4	Eq. of line	y = 1.15x - 82.4	y = 1.19x + 419.7	y = 1.05x - 11.8	y = 1.15x + 454.1	y = 1.1x - 52.6	y = 1.11x + 455.3	y = 1.08x - 42.9	y = 1.12x + 443.2	y = 0.92x + 69.7	y = 1.16x + 446.7	y = 0.99x - 10.8	y = 1.12x + 473.9
	r	0.58	0.44	0.59	0.43	0.55	0.41	0.55	0.41	0.52	0.43	0.58	0.42
	rmse	489	753	438	753	504	770	509	770	458	746	426	749
Ax 5	Eq. of line	y = 0.82x + 144.8	y = 0.72x + 621	y = 0.83x + 135.5	y = 0.71x + 618.7	y = 0.82x + 141.5	y = 0.74x + 591.9	y = 0.8x + 169.3	y = 0.74x + 594	y = 0.79x + 123.7	y = 0.71x + 610.5	y = 0.76x + 160	y = 0.72x + 600.6
	r	0.64	0.45	0.65	0.45	0.63	0.46	0.64	0.46	0.6	0.44	0.62	0.45
	rmse	483	687	473	687	497	695	469	696	519	699	471	701
Co 1	Eq. of line	y = 0.41x + 331.6	y = 0.49x + 674	y = 0.41x + 332.3	y = 0.49x + 672	y = 0.41x + 331.2	y = 0.49x + 674.2	y = 0.41x + 331.4	y = 0.49x + 676.2	y = 0.41x + 332.7	y = 0.5x + 664.7	y = 0.41x + 331.6	y = 0.49x + 679.1
	r	0.43	0.36	0.43	0.34	0.43	0.34	0.43	0.34	0.43	0.34	0.43	0.34
	rmse	387	626	386	627	389	624	386	624	385	629	386	625
Co 2	Eq. of line	y = 1.19x + 268.6	y = 0.87x + 504.9	y = 1.44x + 51.7	y = 0.88x + 498.3	y = 1.38x + 121.3	y = 0.88x + 498.8	y = 1.16x + 275.6	y = 0.89x + 492.8	y = 1.42x + 98.1	y = 0.9x + 488.2	y = 1.44x + 177.9	y = 0.87x + 502.2
	r	0.44	0.34	0.6	0.34	0.58	0.34	0.43	0.34	0.57	0.35	0.55	0.34
	rmse	725	737	574	739	585	740	735	737	609	735	652	730
Co 3	Eq. of line	y = 0.75x + 133.4	y = 0.67x + 572.9	y = 0.76x + 127.7	y = 0.67x + 573.5	y = 0.73x + 132.6	y = 0.67x + 579.5	y = 0.71x + 135.7	y = 0.67x + 580.8	y = 0.72x + 137.5	y = 0.67x + 584.7	y = 0.73x + 123.2	y = 0.67x + 574.2
	r	0.65	0.46	0.65	0.46	0.64	0.46	0.64	0.46	0.64	0.46	0.64	0.46
	rmse	459	667	460	664	460	662	444	663	449	665	460	666



**Figure 48.** The linear approximation of the predicted bone apparent density value with respect to that in the actual specimen in the Specimen 1: Axial 1 and Specimen 3: Coronal 3 glenoid FEMs at the end of the “element” and “node” based remodeling process using the load combination 4:CPA/ISC (figure by author).

## 6.4 DISSCUSION

In this study, the bone remodeling theory based on Wolff’s Law was successfully simulated in the normal glenoid and validated by comparing it to the actual specimen. Two dimensional finite element models of the axial and coronal plane cross-sections of three scapulae specimen were created and had location specific material properties based on their corresponding computed tomography data, thus making them approximately similar to the real-world situation. Three kinds of loads: center, anterior- and posterior-offset (for axial cross-sections), and inferior- and



superior-offset (for coronal cross-sections) were applied in six different combinations (Table 10) to check for the effect of multiple loads on the remodeling results. The center load simulated the arm being 90° abducted whereas the offset loads simulated the extremes of the range of motion. Since the purpose of this study was to validate normal glenoid bone remodeling only the bone internal structure, that is, remodeling of the bone apparent density value was simulated based on the bone strain-energy theory adapted from Weinans, Huiskes et al [36].

The remodeling expression (2) used to guide the simulations is shown here for reference:

$$\Delta\rho = B[S - (1 \pm s)S_{ref}]S_v(\rho)\Delta t, \text{ if } S \geq (1 + s)S_{ref} \text{ or } S \leq (1 - s)S_{ref}, \quad (2)$$

$$= 0, \text{ otherwise}$$

The remodeling rate constant B as the name indicates determines the rate of change of the bone apparent density value between consecutive iterations. In some initial simulations the value of B was varied between 100 and 2000. It was found that for values greater than 300 the predicted bone apparent density was highly resorbed or saturated in certain regions of the glenoid. Whereas for values less than 200 minimal bone remodeling was observed. In this study constant B was taken as 200(kg/m<sup>3</sup>)<sup>2</sup>/N.sec. The constant “s” (s=0.4 in present study) determines the bone “dead” or “lazy” zone, which is the assumed range in which no bone apposition or resorption occurs. The remodeling stimulus value ‘S’ was computed in each iteration as the ratio of the strain-energy (U=0.5σ $\epsilon$ ×volume, units in N.m) and the bone apparent density ( $\rho$  in kg/m<sup>3</sup>). The reference stimulus value “S<sub>ref</sub>” was computed for the actual specimen. The time increment  $\Delta t$  equaled 10days, which was twice the value chosen in a prior study by Jacobs, Beaupre et al [179] for the femur. The predicted bone apparent density values were limited to the range 1-1800kg/m<sup>3</sup> approximately similar to that in previous study by Weinans, Huiskes et al [36]. The remodeling process utilized the forward-Euler integration  $\rho_{n+1}=\rho_n+\Delta\rho_n$  as done in previous studies [35, 36, 179, 181].

The remodeling simulations were executed in two methods, namely the “element” and the “node” based approach. For the “element” approach the remodeling computations were done at the element centroid whereas for the “node” approach they were performed at the nodes of the glenoid finite element models. Past studies by Jacobs, Beaupre et al [179] and Chen et al [182] had indicated that “element” approach resulted in a “checkerboard” pattern, that is, the adjacent remodeled elements were completely saturated or resorbed. In the region proximal to the load site it was attributed to the discretization of the finite element model, while in the distal regions to bone physiology. To eliminate the bone apparent density value discontinuity across elements in the proximal bone regions, Jacobs, Beaupre et al had suggested the “node” approach for the remodeling simulations. As explained in past study by Beaupre et al [181], the remodeling simulations commenced with an initial condition of homogeneous bone apparent density value (0.6 g/cc or 600 kg/m<sup>3</sup>, [179]) so that the process did not favor a particular remodeling path. Although such a homogeneous density distribution may not be physiologically relevant, it prevented biased results.

Large amounts of data ( $\sim 8 \times 14218 \times 12 \times 300 \approx 4.09 \times 10^8$  data points) were obtained in this study due to the numerous simulations. Therefore, the results given in the previous section were sufficient for the purposes of this study and are discussed here. The “element” and the “node” based remodeling results are shown in Figure 44 for all the glenoid finite element models (FEMs) using the load combination 4, CPA/ISC (for all the load combinations see Figure 59 and Figure 60 in Appendix E). The predicted bone apparent density values at the end of the simulations for all the glenoid FEMs were approximately similar to that in the corresponding actual specimen more so for the “element” approach than the “node”. The “checkerboard” pattern can be observed for all the glenoid FEMs, mainly on the anterior cortex region in the

results from the “element” approach. On the other hand, the “node” approach showed no “checkerboard” like pattern, but a high density cortex on the anterior and posterior margins of the glenoid approximately similar to that observed in the actual specimen, a finding also seen in past investigations of remodeling the femur bone [35, 179, 181]. However, the predicted high density cortex did not compare very well with the actual specimen near the load site, that is, the glenoid surface, and at the fixed support boundary condition site, that is, the medial edge.

The mean and standard deviation of the absolute difference of the predicted and the actual specimen bone apparent density value for all the glenoid FEMs and the various load combinations were given in Figure 46 (see Figure 61 in Appendix E for plot of mean difference with respect to iteration number). It was observed that for all the load combinations the mean absolute difference at the end of the “element” based simulations ranged 280-490kg/m<sup>3</sup> for the axial plane and 350-730kg/m<sup>3</sup> for the coronal plane glenoid FEMs, while that for the “node” based simulations were 610-810kg/m<sup>3</sup> and 580-730kg/m<sup>3</sup> respectively. For a more location-specific comparison, the absolute difference of the predicted and the actual specimen bone apparent density value for all the glenoid FEMs was plotted in Figure 45 for the load combination 4, CPA/ISC (for all the load combinations see Figure 63 and Figure 64 in Appendix E). The “element” approach did relatively better than the “node” which consisted of numerous randomly located high difference values. However the “element” approach did show some high difference values in certain regions of the distal and posterior glenoid, and in a few proximal trabeculae. Furthermore from the frequency distribution plots (Figure 47) it was found that the mean absolute difference for the “element” approach was less than 0.4g/cc for approximately 75% (axial) and 65% (coronal) of the total elements in the glenoid FEMs. In fact, in the axial glenoid FEM approximately 55% of the total elements had mean absolute difference value less

than 0.2g/cc. For the “node” approach more than 50% of total nodes in both the axial and the coronal glenoid FEM had mean absolute difference greater than 0.4g/cc. Therefore the “element” based remodeling approach predicted the bone apparent density distribution closer to the corresponding actual specimen than the “node” approach, despite the presence of the “checkerboard” pattern on the anterior side of the glenoid. Also, the mean absolute difference in any glenoid FEM was approximately equal among the various multiple load combinations. This indicates that the predicted bone apparent density distribution obtained was independent of the multiple load combination used for the simulation.

The linear regression analysis results between the predicted and the actual specimen bone apparent density value were given in Table 11 for all the glenoid FEMs and load combinations (see Figure 62 for plot of correlation coefficient value with respect to iteration number in Appendix E). The “element” based simulations showed medium correlation coefficient values ranging 0.5-0.69 in axial, and 0.43-0.65 in coronal cross-sections. On the other hand the “node” approach showed low correlation values ranging 0.34-0.52 in all the glenoid cross-sections. The root mean square error value ranged 385-735kg/m<sup>3</sup> (mean±SD: 488±87kg/m<sup>3</sup>), and 624-720kg/m<sup>3</sup> (mean±SD: 694±44kg/m<sup>3</sup>) for the “element”, and the “node” approach respectively. The linear approximation of the predicted bone apparent density value with respect to the actual specimen were also listed in Table 11, and graphed in Figure 65 and Figure 66 (see Appendix E for figures) for all the glenoid FEMs and load combinations. For the purpose of this discussion it was found sufficient to show the graphs (Figure 48) of an axial and a coronal glenoid FEM remodeled using the “element” and the “node” approach with load combination 4 (CPA/ISC). It can be observed that the “element” approach had relatively better linear trend than the “node”. Furthermore, in the “element” approach the higher predicted bone

apparent density values were found to be less than the actual specimen. On the other hand, in the “node” approach the lower predicted bone density values greater compared to the actual specimen.

The process to perform a FEM-based subject-specific glenoid bone remodeling was successfully created and it had solution convergence. From a glenoid of uniform bone density, the remodeling process created a bone density distribution similar to the actual specimen, with the “element” approach performing relatively better than the “node”. However, the FEM-based bone density distributions for the various glenoid models predicted by the iterative remodeling process were not identical to the corresponding actual specimen. This may, in part, be due to the load(s) applied, boundary conditions, and values of constants used. Nonetheless, this work demonstrated that numerical simulation of glenoid bone remodeling is possible and continued work warranted. If improved further, the FEM-based remodeling simulations could be a key tool for non-destructive glenoid prosthesis design and testing.

## **7.0 CONCLUSION AND FUTURE DIRECTIONS**

### **7.1 CONCLUSION**

The 3D computer models of normal and osteoarthritic scapulae specimen were successfully created using high-resolution volumetric computed tomography images of the same. The external as well as internal morphology and bone density distribution analysis resulted in key findings about the glenoid shape and reference points. The glenoid was found to be approximated by a circle in the inferior region and a triangle in the superior. The center of the inferior circle, and the points closest to the acromion and coracoid processes on the glenoid boundary would be highly useful to the surgeons for precise glenoid prosthesis placement in patients. The external morphology measurements would be useful to design glenoid prosthesis of various sizes, while the internal glenoid bone morphology would be useful in the design of improved fixations for osteoarthritic scapulae.

The finite element method was used to determine the stress in the intact glenoid as well as in that implanted with the glenoid prosthesis. A custom program was written to assign location-specific material properties to the scapula bone elements based on the corresponding computed tomography data. This accounted for the non-homogeneous bone density distribution of the subject-specific scapula specimen. In fact, the program can be modified for any bone for

which CT data is available. The angled fixations and studied glenoid design variables (metal-backed with polyethylene fixations, and all-polyethylene) resulted in stress distributions approximately identical to that in the intact specimen compared to some of the current market designs.

The finite element model-based numerical simulation incorporating the Wolff's law of adapted bone remodeling was successfully created for the first time in the normal glenoid. The method was validated by initially setting the bone density to a homogeneous value of 0.6g/cc. The remodeling process continued for 300 iterations, at the end of which the predicted bone density distribution was found to be approximately comparable to that in the actual specimen. Further improvements are warranted, that is, use of a three dimensional scapula computer model, and load and boundary conditions simulating functional shoulder activities. However, the techniques developed in this study for numerical simulation of bone remodeling could be a key tool for prosthesis designing and testing.

The knowledgebase for both the normal and osteoarthritic glenoid morphology was expanded. Also, the computer modeling, numerical stress analysis and glenoid bone remodeling helped to perform structural analysis of the glenoid that drove improvements in the glenoid prosthesis designing and testing for successful shoulder arthroplasty.

## **7.2 FUTURE DIRECTIONS**

Due to the multifaceted nature of this dissertation there are numerous possible future projects. Some of which are described below. Glenoid morphology measurements could be useful to design instruments. The glenoid vault depth and bone density distribution measurements could help in the design of glenoid prosthesis with fixations suitable for the osteoarthritic scapulae.

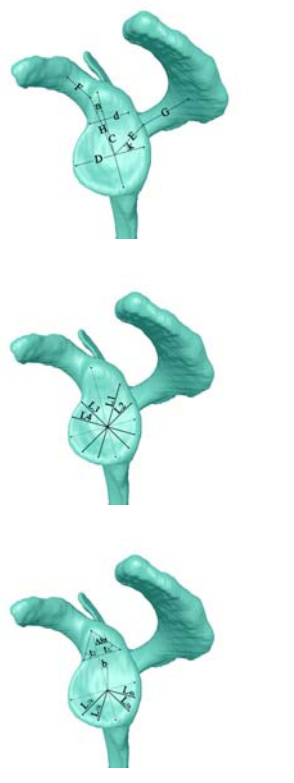
The glenoid bone remodeling simulation technique would be useful in the testing of the glenoid design variables and selecting those that would provide long term fixation within the glenoid. The generic methodology developed in this dissertation can be applied to other human joints as well.



## APPENDIX A

### GLENOID MORPHOLOGY MEASUREMENT VALUES

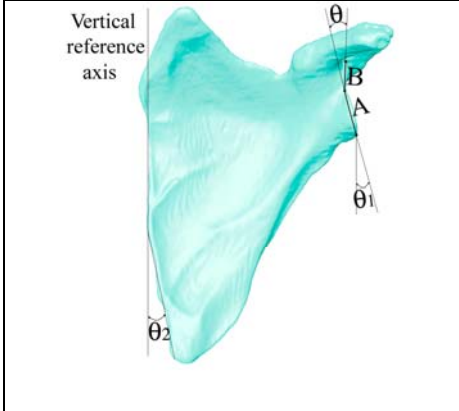
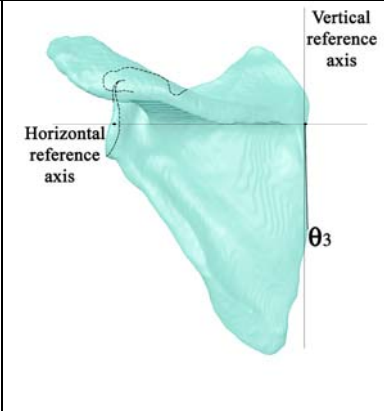
**Table 12.** The mean, standard deviation, range, p-value for male-female difference, and p-value for right-left difference for the glenoid external morphology parameters in lateral view.

	<b>Glenoid morphology parameters</b>	<b>Mean ± S.D.</b>	<b>Range</b>	<b>P value for Male-Female Difference</b>	<b>P value for Right-Left Difference</b>
	<b>C (mm)</b>	34 ± 3	28-39	0.004	0.756
	<b>D (mm)</b>	24 ± 3	21-29	0.000	0.089
	<b>d (mm)</b>	18 ± 2	15-22	0.245	0.607
	<b>E (mm)</b>	17 ± 2	15-20	0.816	0.000
	<b>F (mm)</b>	12 ± 2	10-16	0.032	0.072
	<b>G (mm)</b>	17 ± 2	14-20	0.072	0.343
	<b>H (mm)</b>	23 ± 2	18-26	0.000	0.098
	<b>k (degree)</b>	56 ± 6	47-66	0.177	0.801
	<b>n (degree)</b>	11 ± 2	7-16	0.775	0.060
	<b>L<sub>1</sub> (mm)</b>	27 ± 3	21-33	0.003	0.184
	<b>L<sub>2</sub> (mm)</b>	24 ± 3	20-30	0.000	0.211
	<b>L<sub>3</sub> (mm)</b>	27 ± 3	21-33	0.005	0.736
	<b>L<sub>4</sub> (mm)</b>	24 ± 2	20-31	0.000	0.503
	<b>L<sub>1h</sub> (mm)</b>	11 ± 1	9-14	0.000	0.601
	<b>L<sub>2h</sub> (mm)</b>	12 ± 2	10-16	0.000	0.004
	<b>L<sub>3h</sub> (mm)</b>	11 ± 1	9-14	0.000	0.314
	<b>L<sub>4h</sub> (mm)</b>	11 ± 1	9-15	0.000	0.067
	<b>Δht (mm)</b>	11 ± 2	9-15	0.035	0.186
	<b>b (degree)</b>	15 ± 3	8-25	0.425	0.031
	<b>t<sub>1</sub> (degree)</b>	48 ± 3	41-54	0.320	0.000
	<b>t<sub>2</sub> (degree)</b>	55 ± 4	47-67	0.152	0.126

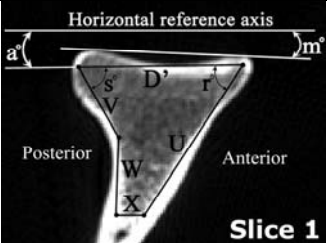
**Table 13.** The mean, standard deviation, range, p-value for male-female difference, and p-value for right-left difference for the glenoid external morphology parameters in the anterior and posterior views.

Anterior and Posterior view parameters	Mean $\pm$ S.D. (mm)	Range (mm)	P value for Male-Female Difference	P value for Right-Left Difference
<b>A (mm)</b>	20 $\pm$ 2	15-24	0.000	0.499
<b>B (mm)</b>	16 $\pm$ 3	12-22	0.894	0.976
<b><math>\theta</math> (degree)</b>	31 $\pm$ 5	20-40	0.441	0.001
<b><math>\theta_1</math> (degree)</b>	17 $\pm$ 8	2-32	0.392	0.014
<b><math>\theta_2</math> (degree)</b>	0 $\pm$ 13	-22-26	0.852	0.000
<b><math>\theta_3</math> (degree)</b>	1 $\pm$ 5	-8-9	0.337	0.153

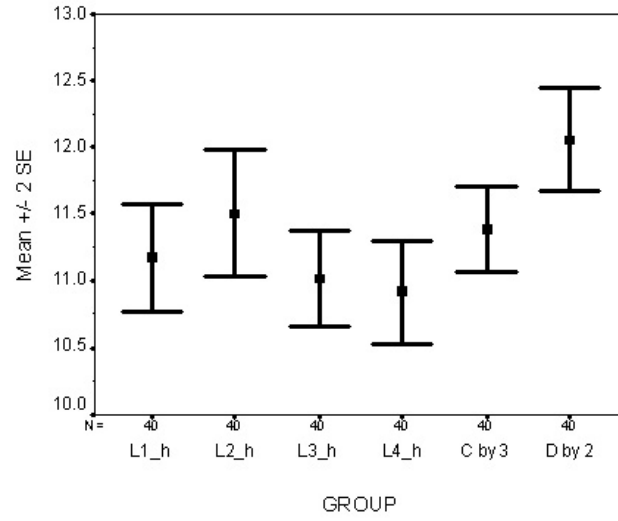
	
--	---

**Table 14.** The mean, standard deviation, and range values for the internal morphology parameters in the selected axial slices of the scapulae specimens (NR# = Not required. *These measurements not required for axial slices 1, and 2 geometry*).

 <b>Slice 1</b>	<b>Glenoid Morphology Parameters</b>	<b>Mean ± S.D. (Range)</b>		
		<b>Slice 1</b>	<b>Slice 2</b>	<b>Slice 3</b>
	<b>D' (mm)</b>	25 ± 3 (20-29)	23 ± 2 (18-26)	18 ± 2 (14-22)
	<b>U (mm)</b>	24 ± 3 (18-29)	20 ± 2 (13-25)	14 ± 2 (11-19)
	<b>V (mm)</b>	13 ± 2 (9-16)	11 ± 1 (9-15)	14 ± 2 (10-20)
	<b>W (mm)</b>	10 ± 2 (6-14)	10 ± 2 (7-14)	8 ± 2 (6-12)
	<b>X (mm)</b>	7 ± 2 (5-10)	9 ± 2 (5-15)	7 ± 2 (4-12)
	<b>Y (mm)</b>	NR#	NR#	8 ± 1 (5-10)
	<b>a (degree)</b>	-1 ± 3 (-11-4)	-1 ± 4 (-9-6)	-6 ± 4 (-15-2)
	<b>m (degree)</b>	-2 ± 4 (-11-7)	-2 ± 5 (-10-7)	-3 ± 5 (-14-5)
	<b>r (degree)</b>	63 ± 4 (52-73)	68 ± 5 (57-80)	91 ± 10 (73-119)
	<b>s (degree)</b>	57 ± 6 (48-70)	48 ± 6 (36-62)	58 ± 6 (48-75)
	<b>p (degree)</b>	NR#	NR#	155 ± 12 (131-177)
	<b>q (degree)</b>	NR#	NR#	158 ± 10 (127-176)

**Table 15. The descriptive values of the selected variables, the p-value of the test of homogeneity of variances, and the one-way ANOVA analysis results.**

<b><u>DESCRIPTIVES</u></b>								
<b>Sample variables</b>	<b>N</b>	<b>Mean (mm)</b>	<b>S.D. (mm)</b>	<b>Std. Error</b>	<b>95% Confidence Interval for Mean</b>		<b>Min</b>	<b>Max</b>
					<b>Lower bound</b>	<b>Upper Bound</b>		
L1_h	40	11.1779	1.2635	.1998	10.7738	11.5820	9.1267	13.9387
L2_h	40	11.5080	1.4841	.2347	11.0333	11.9826	9.1149	15.4636
L3_h	40	11.0178	1.1347	.1794	10.6549	11.3807	8.9715	13.5452
L4_h	40	10.9178	1.2368	.1956	10.5222	11.3133	8.3963	14.5322
C by 3	40	11.3891	1.0042	.1588	11.0679	11.7103	9.3622	13.0923
D by 2	40	12.0615	1.2332	.1950	11.6671	12.4558	9.6030	14.4282
Total	240	11.3453	1.2791	.0826	11.1827	11.5080	8.3963	15.4636
<b><u>TEST OF HOMOGENEITY OF VARIANCES</u></b>								
<b>Levene Statistic</b>		<b>df1</b>	<b>df2</b>		<b>p-value</b>			
1.622		5	234		0.155			
<b><u>ONE-WAY ANOVA</u></b>								
	<b>Sum of Squares</b>	<b>df</b>	<b>Mean Square</b>		<b>F</b>	<b>p-value</b>		
<b>Between Groups</b>	34.373	5	6.875		4.510	.001		
<b>Within Groups</b>	356.675	234	1.524					
<b>Total</b>	391.048	239						



**Figure 49.** The error bar plot showing equal variance between the selected parameters  $L_{1h}$ ,  $L_{2h}$ ,  $L_{3h}$ ,  $L_{4h}$ ,  $C/3$ , and  $D/2$  (y-axis unit is “mm”) (figure by author).

**Table 16. The Post Hoc Tukey's honestly significant difference (HSD) procedure (\*: *The mean difference is significant at the 0.05 level*).**

(I) GROUP	(J) GROUP	Mean Difference (I-J)	Std. Error	p- value	95% Confidence Interval	
					Lower Bound	Upper Bound
<b>L<sub>1h</sub></b>	<b>L<sub>2h</sub></b>	-.3301	.2761	.839	-1.1233	.4632
	<b>L<sub>3h</sub></b>	.1601	.2761	.992	-.6332	.9534
	<b>L<sub>4h</sub></b>	.2601	.2761	.935	-.5332	1.0534
	<b>C by 3</b>	-.2112	.2761	.973	-1.0045	.5821
	<b>D by 2</b>	-.8836*	.2761	.019	-1.6768	-.0903
<b>L<sub>2h</sub></b>	<b>L<sub>1h</sub></b>	.3301	.2761	.839	-.4632	1.1233
	<b>L<sub>3h</sub></b>	.4902	.2761	.484	-.3031	1.2834
	<b>L<sub>4h</sub></b>	.5902	.2761	.272	-.2031	1.3835
	<b>C by 3</b>	.1189	.2761	.998	-.6744	.9121
	<b>D by 2</b>	-.5535	.2761	.343	-1.3468	.2398
<b>L<sub>3h</sub></b>	<b>L<sub>1h</sub></b>	-.1601	.2761	.992	-.9534	.6332
	<b>L<sub>2h</sub></b>	-.4902	.2761	.484	-1.2834	.3031
	<b>L<sub>4h</sub></b>	.1000	.2761	.999	-.6933	.8933
	<b>C by 3</b>	-.3713	.2761	.760	-1.1646	.4220
	<b>D by 2</b>	-1.0437*	.2761	.003	-1.8369	-.2504
<b>L<sub>4h</sub></b>	<b>L<sub>1h</sub></b>	-.2601	.2761	.935	-1.0534	.5332
	<b>L<sub>2h</sub></b>	-.5902	.2761	.272	-1.3835	.2031
	<b>L<sub>3h</sub></b>	-.1000	.2761	.999	-.8933	.6933
	<b>C by 3</b>	-.4713	.2761	.528	-1.2646	.3220
	<b>D by 2</b>	-1.1437*	.2761	.001	-1.9370	-.3504
<b>C by 3</b>	<b>L<sub>1h</sub></b>	.2112	.2761	.973	-.5821	1.0045
	<b>L<sub>2h</sub></b>	-.1189	.2761	.998	-.9121	.6744
	<b>L<sub>3h</sub></b>	.3713	.2761	.760	-.4220	1.1646
	<b>L<sub>4h</sub></b>	.4713	.2761	.528	-.3220	1.2646
	<b>D by 2</b>	-.6724	.2761	.148	-1.4656	.1209
<b>D by 2</b>	<b>L<sub>1h</sub></b>	.8836*	.2761	.019	.0903	1.6768
	<b>L<sub>2h</sub></b>	.5535	.2761	.343	-.2398	1.3468
	<b>L<sub>3h</sub></b>	1.0437*	.2761	.003	.2504	1.8369
	<b>L<sub>4h</sub></b>	1.1437*	.2761	.001	.3504	1.9370
	<b>C by 3</b>	.6724	.2761	.148	-.1209	1.4656

**Table 17.** The homogenous subsets using Tukey's HSD (Means for groups in homogenous subsets are displayed. Harmonic Mean sample size = 40)

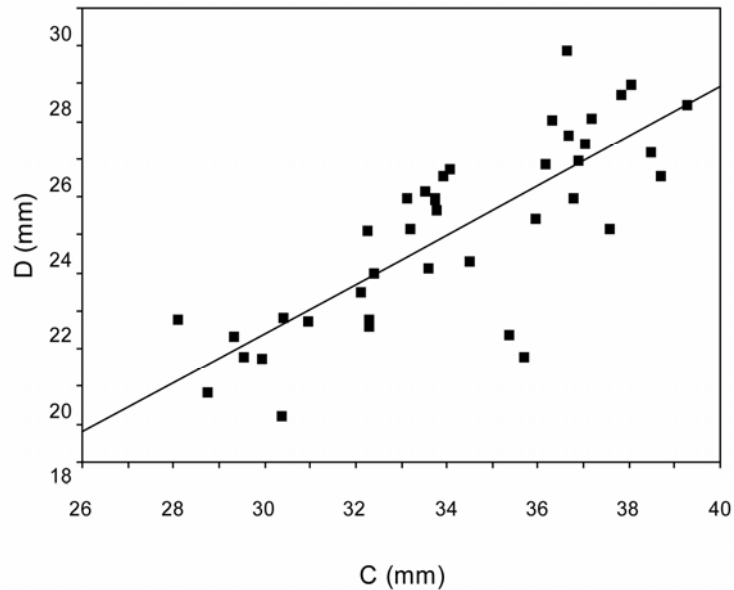
GROUP	N	Subset for alpha = 0.05	
		1	2
L4h	40	10.9178	
L3h	40	11.0178	
L1h	40	11.1779	
C by 3	40	11.3891	11.3891
L2h	40	11.5080	11.5080
D by 2	40		12.0615
Sig.		0.272	0.148

**Table 18.** The mean\*, and standard deviation of the bone density values in the various regions of interest in the three axial slices (\*: These values are not clinically equivalent, #NR = Not required. ROC 5 not present in axial slice 3).

Axial slice	ROI 1	ROI 2	ROI 3	ROI 4	ROI 5
	Mean ± S.D. (HSU)	Mean ± S.D. (HSU)	Mean ± S.D. (HSU)	Mean ± S.D. (HSU)	Mean ± S.D. (HSU)
1	-265 ± 208	-430 ± 152	-326 ± 194	-263 ± 299	-218 ± 327
2	-83 ± 251	-370 ± 159	-336 ± 212	-133 ± 398	-271 ± 309
3	-383 ± 190	-430 ± 210	-412 ± 208	-462 ± 179	NR #

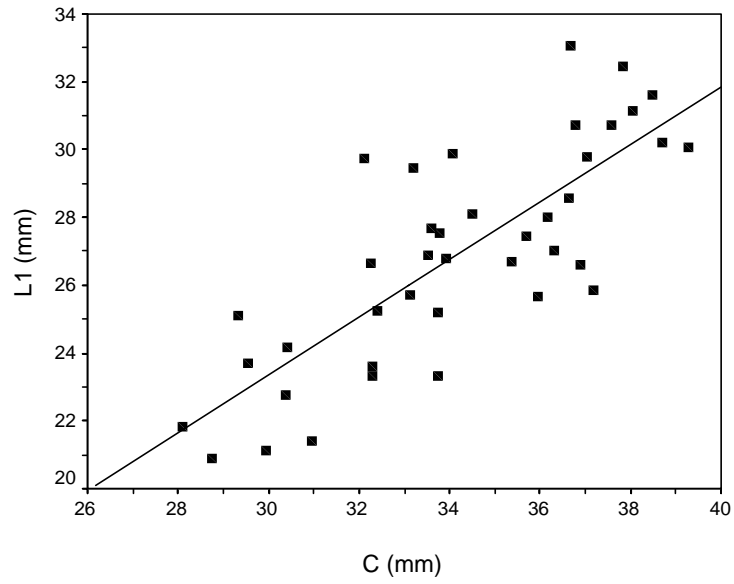
**Table 19.** The correlation coefficients (r) and p-values (in parentheses) from linear regression analysis of selected external and internal bone morphological parameters.

Morphology Parameters	H (mm)	D (mm)	D' (mm)	E (mm)	Δht (mm)	d (mm)	A (mm)	B (mm)
C (mm)	0.92 (0.0)	0.80 (0.0)	0.72 (0.0)	0.51 (0.0)	0.73 (0.0)	0.63 (0.0)	0.62 (0.0)	0.66 (0.0)
H (mm)		0.76 (0.0)	0.64 (0.00)	0.43 (0.0)	0.59 (0.0)	0.53 (0.0)	0.63 (0.0)	0.55 (0.0)
D (mm)			0.74 (0.0)	0.45 (0.0)	0.52 (0.0)	0.54 (0.0)	0.69 (0.0)	0.30 (0.1)
D' (mm)				0.74 (0.0)	0.40 (0.0)	0.45 (0.0)	0.50 (0.0)	0.40 (0.0)
E (mm)					0.23 (0.2)	0.41 (0.0)	0.23 (0.2)	0.43 (0.0)
Δht (mm)						0.73 (0.0)	0.47 (0.0)	0.53 (0.0)
d (mm)							0.39 (0.0)	0.42 (0.0)
A (mm)								0.00 (0.0)

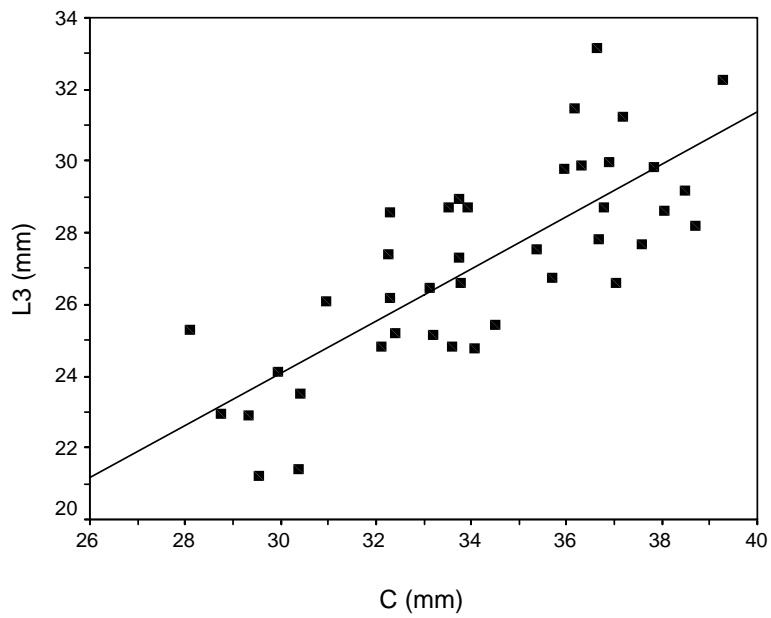


**Figure 50.** Linear regression between C and D ( $p = 0.0$ ,  $r = 0.80$ ,  $D = 1.8653 + 0.6514C$ ) (figure by author).

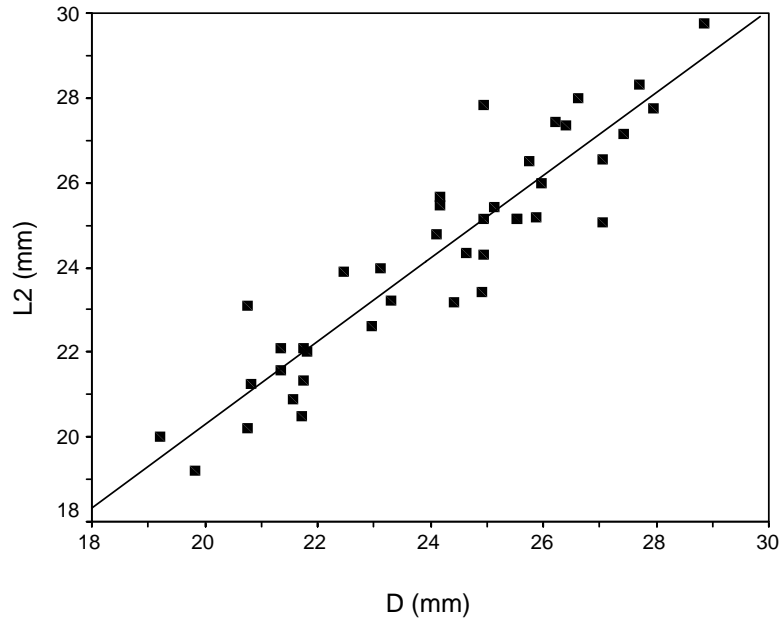




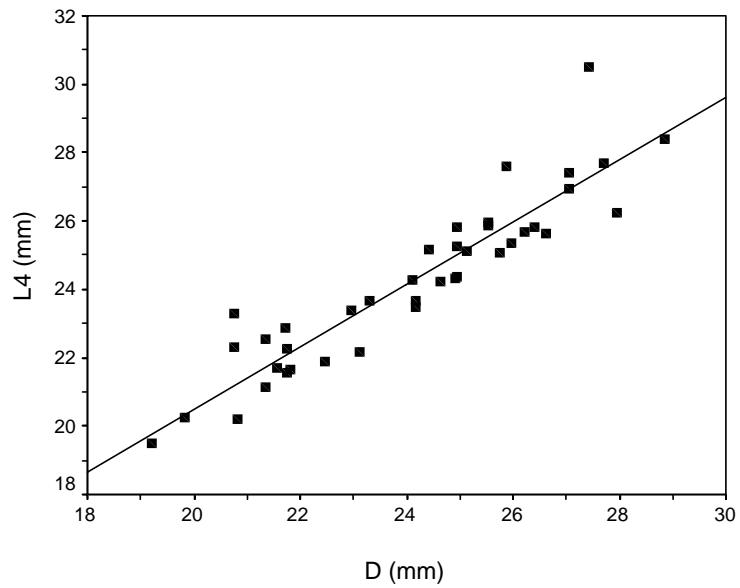
**Figure 51. Linear regression between C and L<sub>1</sub> ( $p = 0.0$ ,  $r = 0.79$ ,  $L_1 = -2.2369 + 0.8526C$ ) (figure by author).**



**Figure 52. Linear regression between C and L<sub>3</sub> ( $p = 0.0$ ,  $r = 0.78$ ,  $L_3 = 2.2699 + 0.7276C$ ) (figure by author).**


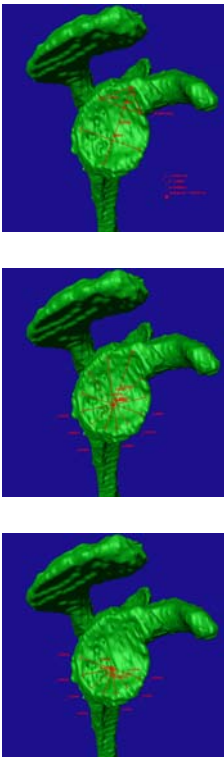


**Figure 53. Linear regression between D and L<sub>2</sub> ( $p = 0.0$ ,  $r = 0.92$ ,  $L_2 = 0.6817 + 0.9799D$ ) (figure by author).**

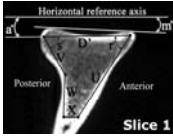
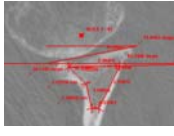

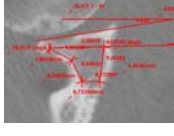

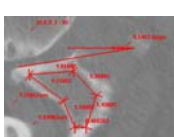


**Figure 54. Linear regression between D and L<sub>4</sub> ( $p = 0.0$ ,  $r = 0.93$ ,  $L_4 = 2.2829 + 0.9108D$ ) (figure by author).**

**Table 20.** The mean and standard deviation of the glenoid external morphology parameters in the normal, and osteoarthritic (OA) scapulae specimen lateral view.

Normal Scapula	OA Scapula	Glenoid morphology parameters	Mean $\pm$ S.D.		P value for Normal Vs. OA difference
			Normal	OA	
		<b>C (mm)</b>	34 $\pm$ 3	38 $\pm$ 4	0.025
		<b>D (mm)</b>	24 $\pm$ 3	29 $\pm$ 5	0.006
		<b>d (mm)</b>	18 $\pm$ 2	21 $\pm$ 3	0.028
		<b>E (mm)</b>	17 $\pm$ 2	21 $\pm$ 5	0.316
		<b>F (mm)</b>	12 $\pm$ 2	16 $\pm$ 3	0.002
		<b>G (mm)</b>	17 $\pm$ 2	18 $\pm$ 1	0.467
		<b>H (mm)</b>	23 $\pm$ 2	25 $\pm$ 4	0.052
		<b>k (degree)</b>	56 $\pm$ 6	44 $\pm$ 7	0.001
		<b>n (degree)</b>	11 $\pm$ 2	15 $\pm$ 2	0.004
		<b>L<sub>1</sub> (mm)</b>	27 $\pm$ 3	34 $\pm$ 3	0.001
		<b>L<sub>2</sub> (mm)</b>	24 $\pm$ 3	30 $\pm$ 5	0.001
		<b>L<sub>3</sub> (mm)</b>	27 $\pm$ 3	32 $\pm$ 3	0.006
		<b>L<sub>4</sub> (mm)</b>	24 $\pm$ 2	30 $\pm$ 2	0.0
		<b>L<sub>1h</sub> (mm)</b>	11 $\pm$ 1	14 $\pm$ 3	0.292
		<b>L<sub>2h</sub> (mm)</b>	12 $\pm$ 2	15 $\pm$ 5	0.391
		<b>L<sub>3h</sub> (mm)</b>	11 $\pm$ 1	13 $\pm$ 2	0.016
		<b>L<sub>4h</sub> (mm)</b>	11 $\pm$ 1	13 $\pm$ 2	0.005
		<b>Δht (mm)</b>	11 $\pm$ 2	10 $\pm$ 1	0.201
		<b>b (degree)</b>	15 $\pm$ 3	14 $\pm$ 3	0.899
		<b>t<sub>1</sub> (degree)</b>	48 $\pm$ 3	41 $\pm$ 3	0.001
		<b>t<sub>2</sub> (degree)</b>	55 $\pm$ 4	46 $\pm$ 8	0.001

**Table 21.** The mean, and standard deviation for the internal morphology parameters in the selected axial slices of the normal (N) and the osteoarthritic (OA) scapulae specimen (NR# = Not required. *These measurements not required for the concerned axial slices*).

Normal	OA	Glenoid Morphology Parameters	Mean ± S.D.					
			Slice 1		Slice 2		Slice 3	
			N	OA	N	OA	N	OA
		<b>D' (mm)</b>	25±3	25±2	23±2	22±1	18±2	18±5
		<b>U (mm)</b>	24±3	20±6	20±2	16±3	14±2	16±5
		<b>V (mm)</b>	13±2	13±2	11±1	10±2	14±2	17±1
		<b>W (mm)</b>	10±2	11±4	10±2	9±0	8±2	11±2
		<b>X (mm)</b>	7±2	4±1	9±2	6±3	7±2	4±1
		<b>Y (mm)</b>	NR#	NR#	NR#	NR#	8±1	10±4
		<b>a (degree)</b>	-1±3	-2±0	-1±4	-2±1	-6±4	-3±2
		<b>m (degree)</b>	-2±4	-16±6	-2±5	-17±9	-3±5	-21±13
		<b>r (degree)</b>	63±4	59±3	68±5	66±21	91±10	90±42
		<b>s (degree)</b>	57±6	32±16	48±6	30±6	58±6	67±52
		<b>p (degree)</b>	NR#	NR#	NR#	NR#	155±12	143±12
		<b>q (degree)</b>	NR#	NR#	NR#	NR#	158±10	144±25
		<b>H17 (mm)</b>	7±0	3±1	4±0	2±0	NR#	NR#
		<b>H34 (mm)</b>	18±1	9±9	14±1	7±5	NR#	NR#
		<b>H50 (mm)</b>	21±0	14±9	19±1	13±3	19±0	11±2
		<b>H68 (mm)</b>	15±0	13±2	16±1	11±5	NR#	NR#
		<b>H85 (mm)</b>	7±0	6±0	9±1	9±6	NR#	NR#

## APPENDIX B

### MATLAB® PROGRAM FOR BONE ELEMENTS MATERIAL PROPERTIES

#### 2D FEA:

```
% Code for creating the Ansys FEA material input file for 2D axial slice of %
% scapula specimen T9R
% The material properties for each element is obtained using the CT number
% from the T9R CT scanning data

% This code has been written by Gulshan Sharma at the Musculoskeletal
% Imaging and Biomechanics Laboratory (MIBL) in the University of
% Pittsburgh, Bioengineering Department.

% Date: 2 March 2005

clear;
close all;
%*****%
%           READ THE ELEMENTS FROM THE CREATED TEXT FILE           %
%*****%

elemfile = input('Enter the BONE ELEMENTS filename with extension .txt:
','s');
elem = load(elemfile);
sprintf('Reading Element Data..... DONE')

%*****%
%           READ THE NODE COORDINATES FROM THE CREATED TEXT FILE   %
%*****%

nodefile = input('Enter the BONE NODES filename with extension .txt: ','s');
nodes = load(nodefile);
sprintf('Reading Node Data.....DONE')

%*****%
%           COMPUTING THE CENTROID FOR EACH ELEMENT                 %
%*****%
```

```

%*****%
sprintf('Begin.....Centroid Calculation for %d Elements',length(elem))

j = 100;

for i=1:length(elem)
    n1 = find(nodes(:,1)==elem(i,2));
    n2 = find(nodes(:,1)==elem(i,3));
    n3 = find(nodes(:,1)==elem(i,4));

    if (i == j)
        sprintf('Completed.....%d of %d ',j,length(elem))
        j = j + 100;
    end

    centroids(i,1:2)=( nodes(n1,2:3)+nodes(n2,2:3)+nodes(n3,2:3) )/3;
end
sprintf('Element Centroid Calculations.....DONE')

centroids = 100 * centroids; % converting from meters to centimeters

%*****%
%           READING THE T9R CT SCAN & SETTING SPATIAL COORDINATES           %
%*****%

% the X-coordinates for all the pixels in the CT space
x(1:271)=(-11.78)+((0:270)*0.0433594);
% the Y-coordinates for all the pixels in the CT space
y(1:415)=(-12.65)+((0:414)*0.0433594);
% the Z-coordinate for the location of slice in the CT space
z= -6.61005 ;

I = dicomread('1.2.840.113619.2.30.1.1762813188.1929.1043417636.200.dcm');
I = double(I);
% 415 rows (in y-direction) by 271 columns (in x-direction)
I = I(1:415,1:271);
CT(1:415,1:271)=I;

maxCT=max(max(CT));
minCT=min(min(CT));
%generating an empty image for the reassigned CT numbers corresponding to the
%element locations
CTreassign(1:415,1:271)=-10;

%*****%
%           EVALUATING THE BONE-DENSITY & MATERIAL PROPERTIES           %
%           FOR EACH ELEMENT IN THE FINITE ELEMENT MODEL           %
%*****%

for count = 1:length(centroids)
    temp_x = centroids(count,1);

```

```

temp_y = centroids(count,2);
% finding the indices for the spatial location of the centroid
xmin = find(x<temp_x);
xmax = find(x>temp_x);

ymin = find(y<temp_y);
ymax = find(y>temp_y);

xp1 = x(xmax(1)); % x plus 1
xm1 = x(xmin(length(xmin))); % x minus 1

if ( (abs(xp1-temp_x)) < (abs(xm1-temp_x)) )
    x_ct=find(x==xp1);
else
    x_ct=find(x==xm1);
end

yp1 = y(ymax(1)); % y plus 1
ym1 = y(ymin(length(ymin))); % y minus 1

if ( (abs(yp1-temp_y)) < (abs(ym1-temp_y)) )
    y_ct=find(y==yp1);
else
    y_ct=find(y==ym1);
end

CTtemp(count)=CT(y_ct,x_ct);
%noting the indices of the elements in the CT space
elem_indices(count,1:2)=[y_ct x_ct];

CTnew = ( (( (1476-CTtemp(count))/2500) * (-10) )+( (1 - (( (1476-
CTtemp(count))/2500)) ) * 1476 );

temp_CT(count)=CTnew;

CTreassign(y_ct,x_ct) = CTnew;

end

figure(1)
subplot(2,1,1);
imagesc(CT,[-10 1476]);
title(['Original CT Nos ( ',elemfile,' )']);
subplot(2,1,2);
imagesc(CTreassign,[-10 1476]);
title(['Discrete CT Nos ( ',elemfile,' )']);

%*****%

```

```

%                SETTING MATERIALS AT EVERY 10 HU                %
%                AND ASSIGNING MATERIAL NUMBERS TO ELEMENTS      %
%*****%

mat_CT=[-10:10:1476];
mat_CT(1 + length(mat_CT))=1476;

elem_CT(1:length(elem))=0;

clear i;

for i = 1:length(temp_CT)

    a = find(mat_CT <= temp_CT(i));
    a = a(length(a));
    b = find(mat_CT > temp_CT(i));
    b = b(1);

    if ( abs(temp_CT(i)-mat_CT(a)) <= abs(temp_CT(i)-mat_CT(b)) )
        mat_num(i) = a;
        elem_CT(i)=mat_CT(a);
    else
        mat_num(i) = b;
        elem_CT(i)=mat_CT(b);
    end

end

%*****%
%                COMPUTING THE MATERIAL PROPERTIES                %
%*****%

% From Taylor Paper - Orthotropic

E1max = 11.6e9;
E2max = 12.2e9;
E3max = 19.9e9;
G12max = 4e9;
G13max = 5e9;
G23max = 5.4e9;
nu12 = 0.42;
nu23 = 0.23;
nu13 = 0.23;

% from Buchler paper - Isotropic

E0 = 15e9;
nu0 = 0.3;

rho_app_max = 1.9;%max bone density in g/cc

clear count;

```



```

for count = 1:length(mat_CT)%for the total number of materials

%calculating the density of bone (g/cc) from CT value using the
%analytically derived relationship
%App_density(count) = ( (1.9*mat_CT(count))+(1024*1.9) )/2915;
App_density(count)= ( (0.9/1476)*mat_CT(count) ) + 1;

E1(count)=E1max*((App_density(count)/rho_app_max)^2);
E2(count)=E2max*((App_density(count)/rho_app_max)^2);
E3(count)=E3max*((App_density(count)/rho_app_max)^2);
G12(count)=G12max*((App_density(count)/rho_app_max)^2);
G13(count)=G13max*((App_density(count)/rho_app_max)^2);
G23(count)=G23max*((App_density(count)/rho_app_max)^2);

E(count)=E0*((App_density(count)/rho_app_max)^2);

end

%*****%
% WRITE OUT THE ANSYS MATERIALS FILE %
%*****%

outfile = input('Enter filename for BONE material file with extension .txt:
','s');
fid = fopen(outfile,'w');

clear count;
%start the Ansys materials ID from 3, since 1 and 2 are for UHMWPE and Ti
count = 3;
check(1:length(mat_CT))=0;%total number of materials
mat_ansys(1:length(mat_CT))=0;

for j = 1:length(mat_num)% for all the elements
n=mat_num(j);%get the material number of the element

young_modulus(j) = E(n);%assigning the young's modulus of each element
bone_density(j) = 1000*App_density(n);%assign the density of each element

if (check(n)==0)%check whether this material has been defined previously
check(n)=1;
mat_ansys(n)=count;%assign the material number ID for Ansys script
fprintf(fid,'MP,EX,%d,%g\t\t!Pa\n',count,E(n));%Young's modulus in Pa
fprintf(fid,'MP,PRXY,%d,%f\t\t!No Units\n',count,nu0);%Poisson Ratio
%density in kg/cubic meter
fprintf(fid,'MP,DENS,%d,%f\t\t!kg/cubic...
meter\n\n',count,1000*App_density(n));
%changing the old element material to this new material
fprintf(fid,'MPCHG,%d,%d\n\n',count,elem(j,1));
count = count + 1;%incrementing the material ID
elseif (check(n)==1)%if the material had previously been defined then
%simply change the old element material to the new material
fprintf(fid,'MPCHG,%d,%d\n\n',mat_ansys(n),elem(j,1));

```

```

end
end

fclose(fid);

%*****
% Plotting the distribution of CT numbers across the elements before and
% after modifying the CT values

figure(2);
subplot(2,1,1)
hist(CTtemp)
axis([-1500 2000 0 4000]);
grid on
title(['Original CT Nos Distribution ( ',elemfile,' )']);
xlabel('CT value (HU)');
ylabel('Number of Elements');
subplot(2,1,2)
hist(temp_CT)
axis([-1500 2000 0 4000]);
grid on
title(['Modified CT Nos Distribution ( ',elemfile,' )']);
xlabel('CT value (HU)');
ylabel('Number of Elements');

%*****

% Plotting the Element material properties - Young's Modulus

elem1 = load('AllPEAnt_Elems.txt');
nodes1 = load('AllPEAnt_Nodes.txt');
young_modulus(1,3970:6969) = 1.2e9;
FEMplotter(elem1,nodes1,young_modulus);
xlabel('X-Axis')
ylabel('Y-Axis')
t1 = input('title:', 's');
title(t1);
FEMplotter(elem,nodes,elem_CT);
FEMplotter(elem,nodes,bone_density);

% Function to plot the material properties, stresses for 2D finite element
% models
% written by: Gulshan Baldev Sharma
% date: 4th March 2005
function [] = FEMplotter(elem,nodes,vals)

%creating patches

figure;

for i = 1:length(elem)

```

```

x1 = nodes(elem(i,2),2);
x2 = nodes(elem(i,3),2);
x3 = nodes(elem(i,4),2);

y1 = nodes(elem(i,2),3);
y2 = nodes(elem(i,3),3);
y3 = nodes(elem(i,4),3);

x = [x1 x2 x3];
y = [y1 y2 y3];

patch(x,y,vals(i));

hold on;

end

hold off;
colorbar;
axis square;

```

### **3D FEA:**

```

% Code for creating the Ansys FEA input file for scapula specimen T9R
% having elements (10 node tetrahedrons) and nodes. The material properties
% for each element is obtained using the CT number from the T9R CT scanning
% data

```

```

% This code has been written by Gulshan Sharma at the Musculoskeletal
% Imaging and Biomechanics Laboratory (MIBL) in the University of
% Pittsburgh, Bioengineering Department under the guidance of Dr. Douglas
% Robertson.

```

```

% Date: 3 Feb 2005 Date Modified: 15 August 2005

```

```

clear;
close all;
%*****%
%          READ THE ELEMENTS FROM THE CREATED TEXT FILE          %
%*****%

```

```

elemfile = input('Enter the Bone elements filename with extension .txt:
','s');
elem = load(elemfile);
sprintf('Reading Element Data..... DONE')

```

```

%*****%
%          READ THE NODE COORDINATES FROM THE CREATED TEXT FILE          %
%*****%

```

```

nodefile = input('Enter the Bone nodes filename with extension .txt: ','s');
nodes = load(nodefile);
sprintf('Reading Node Data.....DONE')

%*****%
%      COMPUTING THE CENTROID FOR EACH ELEMENT      %
%*****%
sprintf('Begin.....Centroid Calculation for %d Elements',length(elem))

Le = length(elem(:,1)); % total no.of elements
centroids(1:Le,1:3)= (
nodes(elem(1:Le,6),2:4)+nodes(elem(1:Le,7),2:4)+nodes(elem(1:Le,8),2:4)+nodes
(elem(1:Le,9),2:4) )/4;

sprintf('Element Centroid Calculations.....DONE')

centroids = 100 * centroids; % converting from meters to centimeters

%*****%
%      READING THE T9R CT SCANS & SETTING SPATIAL COORDINATES      %
%*****%

fid = fopen('filenames.txt','r');

x(1:271)=(-11.78)+((0:270)*0.0433594); % the X-coord voxels in the CT space
y(1:415)=(-12.65)+((0:414)*0.0433594); % the Y-coord voxels in the CT space
z(1:178)=(-18.5101)+(0.1*(0:177)); % the Z-coord voxels in the CT space

for k = 1:178
    file = fscanf(fid,'%s\n',1);
    I = dicomread(file);
    I = double(I);
    I = I(1:415,1:271); % 415 rows(y-direction) by 271 cols(x-direction)
    CT(1:415,1:271,k)=I;
    sprintf('Read %d of 178',k)
end
sprintf('Reading DICOM Data.....DONE')

fclose(fid);

maxCT=max(max(max(CT)));
minCT=min(min(min(CT)));

%generating empty img for reassigned CT corresponding to Element locations
CTreassign(1:415,1:271,1:178)=-10;

%*****%
%      EVALUATING THE BONE-DENSITY & MATERIAL PROPERTIES      %
%      FOR EACH ELEMENT IN THE FINITE ELEMENT MODEL      %
%*****%

```

```

%*****%

for count = 1:length(centroids)%for all elements
    temp_x = centroids(count,1);
    temp_y = centroids(count,2);
    temp_z = centroids(count,3);

    xmin = find(x<temp_x); % find the indices for the spatial loc of centroid
    xmax = find(x>temp_x);

    ymin = find(y<temp_y);
    ymax = find(y>temp_y);

    zmin = find(z<temp_z);
    zmax = find(z>temp_z);

    xp1 = x(xmax(1)); % x plus 1
    xm1 = x(xmin(length(xmin))); % x minus 1

    if ( (abs(xp1-temp_x)) < (abs(xm1-temp_x)) )
        x_ct=find(x==xp1);
    else
        x_ct=find(x==xm1);
    end

    yp1 = y(ymax(1)); % y plus 1
    ym1 = y(ymin(length(ymin))); % y minus 1

    if ( (abs(yp1-temp_y)) < (abs(ym1-temp_y)) )
        y_ct=find(y==yp1);
    else
        y_ct=find(y==ym1);
    end

    zp1 = z(zmax(1)); % z plus 1
    zm1 = z(zmin(length(zmin))); % z minus 1

    if ( (abs(zp1-temp_z)) < (abs(zm1-temp_z)) )
        z_ct=find(z==zp1);
    else
        z_ct=find(z==zm1);
    end

    CTtemp(count)=CT(y_ct,x_ct,z_ct);

    CTnew = ( (( (1891-CTtemp(count))/2915) * (-10) )+( (1 - (( (1891-
    CTtemp(count))/2915)) ) * 1891 );

    temp_CT(count)=CTnew;

    CTreassign(y_ct,x_ct) = CTnew;

end

```

```

%*****%
%           SETTING MATERIALS AT EVERY 10 HU           %
%           AND ASSIGNING MATERIAL NUMBERS TO ELEMENTS           %
%*****%

mat_CT=[-10:10:1891];
mat_CT(1 + length(mat_CT))=1891;

elem_CT(1:length(elem))=0;

clear i;

for i = 1:length(temp_CT)%for all elements

    a = find(mat_CT <= temp_CT(i));
    a = a(length(a));
    b = find(mat_CT > temp_CT(i));
    b = b(1);

    if ( abs(temp_CT(i)-mat_CT(a)) <= abs(temp_CT(i)-mat_CT(b)) )
        mat_num(i) = a;
        elem_CT(i)=mat_CT(a);
    else
        mat_num(i) = b;
        elem_CT(i)=mat_CT(b);
    end

end

%*****%
%           COMPUTING THE MATERIAL PROPERTIES           %
%*****%

% From Taylor Paper - Orthotropic

E1max = 11.6e9;
E2max = 12.2e9;
E3max = 19.9e9;
G12max = 4e9;
G13max = 5e9;
G23max = 5.4e9;
nu12 = 0.42;
nu23 = 0.23;
nu13 = 0.23;

rho_app_max = 1.9;%max bone density in g/cc

% from Buchler paper - Isotropic (i guess)

E0 = 15e9;
nu0 = 0.3;

clear count;

```

```

for count = 1:length(mat_CT)%for the total number of materials

    %calculating the density of bone (g/cc) from CT value using the
    %analytically derived relationship
    % App_density(count) = ( (1.9*mat_CT(count))+(1024*1.9) )/2915;
    App_density(count)= ( (0.9/1891)*mat_CT(count) ) + 1;

    E1(count)=E1max*((App_density(count)/rho_app_max)^2);
    E2(count)=E2max*((App_density(count)/rho_app_max)^2);
    E3(count)=E3max*((App_density(count)/rho_app_max)^2);
    G12(count)=G12max*((App_density(count)/rho_app_max)^2);
    G13(count)=G13max*((App_density(count)/rho_app_max)^2);
    G23(count)=G23max*((App_density(count)/rho_app_max)^2);

    E(count)=E0*((App_density(count)/rho_app_max)^2);

end

%*****%
%   WRITE OUT THE ANSYS MATERIALS FILE   %
%*****%

outfile=input('Enter filename for BONE material file with extension .txt:
','s');
fid = fopen(outfile,'w');

clear count;

count = 3;
%start the Ansys materials ID from 3, since 1 and 2 are for UHMWPE and Ti
check(1:length(mat_CT))=0;%total number of materials
mat_ansys(1:length(mat_CT))=0;
%initializing the young modulus element matrix
young_modulus(1:elem(length(elem))) = 0;

for j = 1:length(mat_num)% for all the elements
    n=mat_num(j);%get the material number of the element

    young_modulus(j) = E(n);%assigning the young's modulus of each element
    bone_density(j) = 1000*App_density(n);%assgn density of each element

    if (check(n)==0)%check whether this material has been defined previously
        check(n)=1;
        mat_ansys(n)=count;%assign the material number ID for Ansys script
        fprintf(fid,'MP,EX,%d,%g\t\t!Pa\n',count,E(n));%Young's mod Pascals
        fprintf(fid,'MP,PRXY,%d,%f\t\t!No Units\n',count,nu0);%Poisson's
        fprintf(fid,'MP,DENS,%d,%f\t\t!kg/cubic
meter\n\n',count,1000*App_density(n));
        %defining the density in kg/cubic meter
        fprintf(fid,'MPCHG,%d,%d\n\n',count,elem(j,1));
        %changing the old element material to this new material
        count = count + 1;%incrementing the material ID
    end
end

```

```

elseif (check(n)==1)%if the material had previously been defined then
    %simply change the old element material to the new material
    fprintf(fid, 'MPCHG,%d,%d\n\n',mat_ansys(n),elem(j,1));
end
end

fclose(fid);

%*****
% Plotting the distribution of CT numbers across the elements before and
% after modifying the CT values

figure
subplot(2,1,1)
hist(CTtemp)
grid on
title(['Original CT Nos Distribution ( ',elemfile,' )']);
xlabel('CT value (HU)');
ylabel('Number of Elements');
subplot(2,1,2)
hist(temp_CT)
grid on
title(['Modified CT Nos Distribution ( ',elemfile,' )']);
xlabel('CT value (HU)');
ylabel('Number of Elements');

```



## APPENDIX C

### VON MISES STRESS PLOTS FOR 2D FEA OF GLENOID PROSTHESES

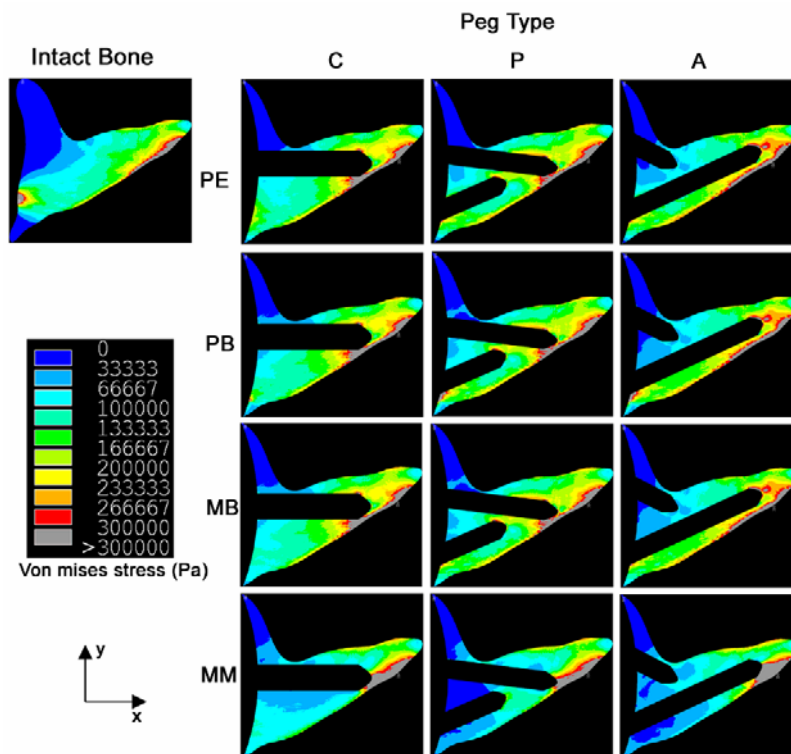


Figure 55. von Mises stress (Pa), for the anterior offset loading case, in the cancellous bone of the intact, and the twelve glenoid prostheses. Rows show the various prostheses backing and the pegs materials (PE: all-PE, PB: Partial Metal Backing with PE pegs, MB: Metal Backing with PE pegs and MM: Metal Backing with Metal pegs). Columns indicate the peg type (C: straight center long, P: angled posterior-long anterior-short, and A: angled anterior-long posterior-short) (figure by author).

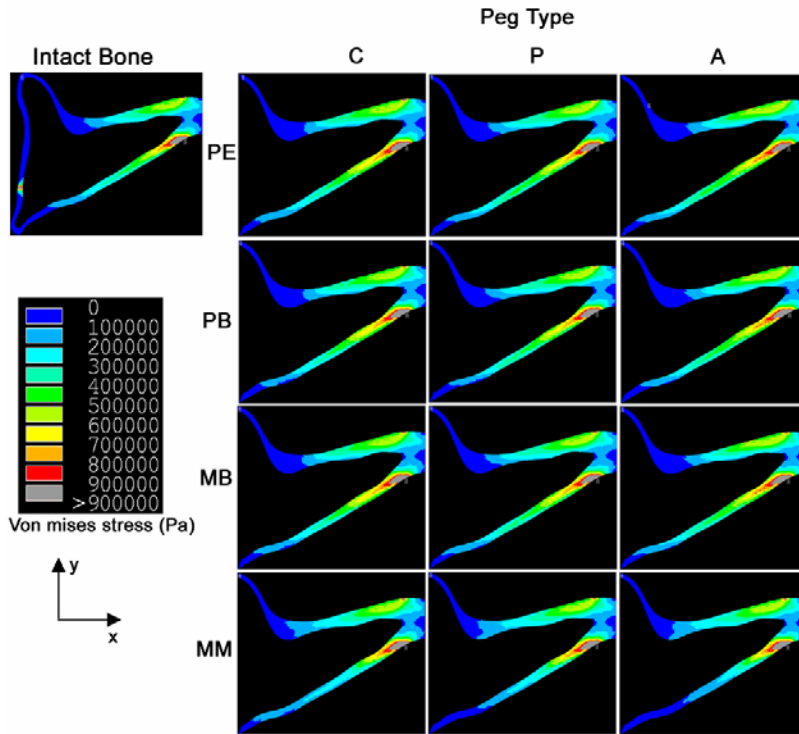
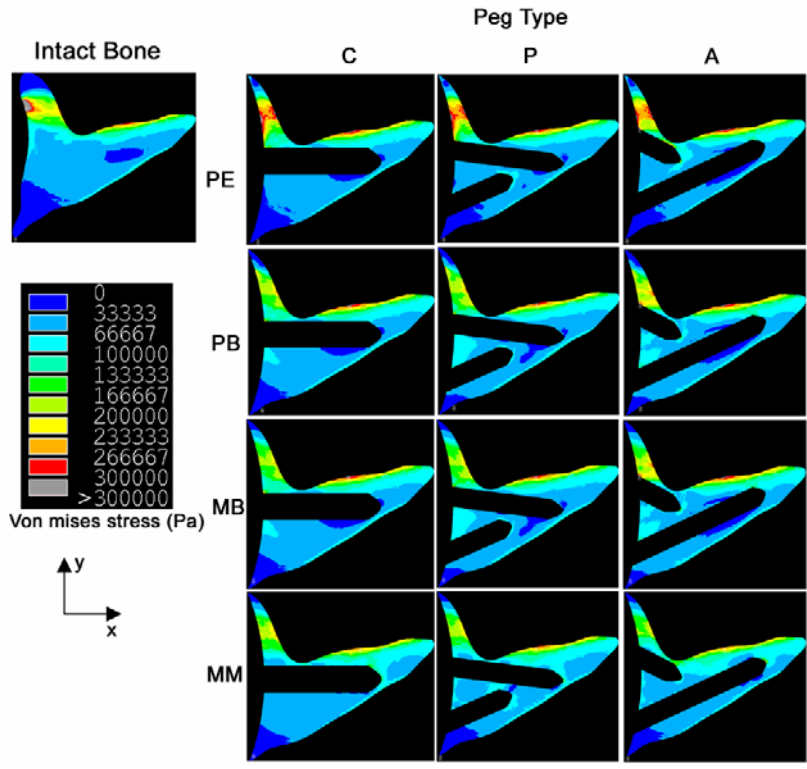


Figure 56. von Mises stress (Pa), for the anterior offset loading case, in the cortical bone of the intact, and the twelve glenoid prostheses. Rows show the various prostheses backing and the pegs materials (PE: all-PE, PB: Partial Metal Backing with PE pegs, MB: Metal Backing with PE pegs and MM: Metal Backing with Metal pegs). Columns indicate the peg type (C: straight center long, P: angled posterior-long anterior-short, and A: angled anterior-long posterior-short) (figure by author).



**Figure 57.** von Mises stress (Pa), for the posterior offset loading case, in the cancellous bone of the intact, and the twelve glenoid prostheses. Rows show the various prostheses backing and the pegs materials (PE: all-PE, PB: Partial Metal Backing with PE pegs, MB: Metal Backing with PE pegs and MM: Metal Backing with Metal pegs). Columns indicate the peg type (C: straight center long, P: angled posterior-long anterior-short, and A: angled anterior-long posterior-short) (figure by author).

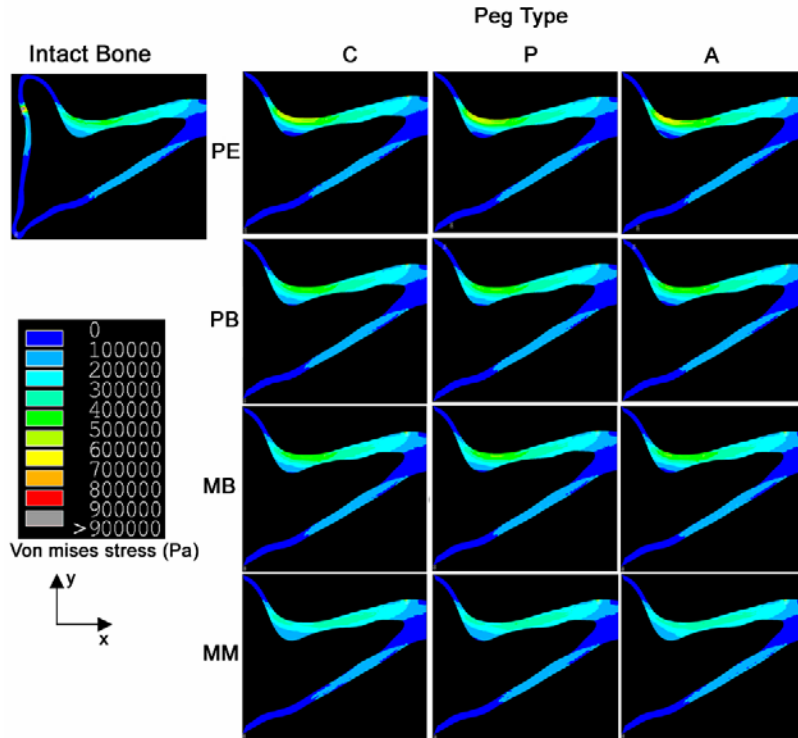


Figure 58. von Mises stress (Pa), for the posterior offset loading case, in the cortical bone of the intact, and the twelve glenoid prostheses. Rows show the various prostheses backing and the pegs materials (PE: all-PE, PB: Partial Metal Backing with PE pegs, MB: Metal Backing with PE pegs and MM: Metal Backing with Metal pegs). Columns indicate the peg type (C: straight center long, P: angled posterior-long anterior-short, and A: angled anterior-long posterior-short) (figure by author).

## APPENDIX D

### ANSYS® PROGRAM FOR FEM-BASED GLENOID BONE REMODELING

#### Element based approach

```
! Written by Gulshan Sharma, Univ Pittsburgh, Bioeng. MIBL, Pittsburgh, PA,  
! USA  
! Date started: 22 June 2006
```

```
! Code for the second part of the bone remodeling project.  
! In this code first the 2D FEM of proximal glenoid axial slice is created,  
! then the Ansys materials are set up, load and boundary conditions are  
! applied, homogeneous bone material properties are assigned,  
! reference nodal stimulus values are imported, problem is solved in  
! iterative process and in each iteration the bone material properties are  
! modified accordingly as well as exported in an appendable text file.
```

```
elemnum = 6606      ! total number of elements  
nodenum = 13495    ! total number of nodes  
Ecols = 7          ! total cols in the elem mat 7 for 2DFEA and 11 for 3DFEA  
Ncols = 3          ! total cols in the node mat 3 for 2DFEA and 4 for 3D FEA
```

```
! Enter details for the loading sequence  
! FL = first load  
! SL = second load  
! TL = third load  
! Load key: Center=1; Anterior=2; Posterior=3
```

```
!case1=CPA=132; case2=CAP=123; case3=ACP=213; case4=APC=231; case5=PCA=312;  
!case6=PAC=321
```

```
FL=1  
SL=3  
TL=2
```

```

!-----Create TEMP arrays for elements and nodes-----
! These arrays will be transposed to correctly orient the matrix since the
! vread command
! reads rows as columns
!-----

*DIM, Etemp, ARRAY, Ecols, elemnum !Temporary element matrix creation
*DIM, Ntemp, ARRAY, Ncols, nodenum !Temporary node matrix creation
*DIM, TEDens, ARRAY, 1, elemnum !Temporary elem density matrix creation
*DIM, TSarea,ARRAY,1,1800 !Temp surf area density matrix creation

!-----Create the arrays for elements and nodes-----
! These arrays will store the data in the correct orientation
!-----

*DIM, Ematrix, ARRAY, elemnum, Ecols !element matrix creation
*DIM, Nmatrix, ARRAY, nodenum, Ncols !node coordinates matrix creation
*DIM, EDens, ARRAY, elemnum, 1 !Elem dens val in each iter mat creation
*DIM, iEDens,ARRAY,elemnum,1 !initial elem original material property
*DIM, Sref, ARRAY, elemnum, 1 !Reference stimulus value matrix creation
*DIM, SrefC, ARRAY, elemnum, 1 !Ref stim val matr creation center load
*DIM, SrefA, ARRAY, elemnum, 1 !Ref stim val matr creation for ant load
*DIM, SrefP, ARRAY, elemnum, 1 !Ref stim val matr creation for post load

*DIM, Selem, ARRAY, elemnum, 1 !Stim val in each iteration matrix creation
*DIM, Sarea, ARRAY, 1800 , 1 !Surf area dens vals for all the dens vals

*DIM, Earea, ARRAY, elemnum, 1 !matrix to store element area

*VREAD, Etemp(1,1), Ax119Elems, txt, , elemnum ! Read element matrix
(7F12.2)

*VREAD, Ntemp(1,1), Ax119Nodes, txt, , nodenum ! Read node matrix
(F10.1,F20.10,F20.10)

*VREAD, TEDens(1,1), Ax119EDens, txt, , elemnum ! Read elem dens matrix
(F20.2)

! Read values of surface area density matrix
*VREAD, TSarea(1,1), SurfaceAreaDensity, txt , , 1800
(F30.15)

*MFUN, Ematrix(1,1), TRAN, Etemp(1,1) ! Transpose element matrix
*MFUN, Nmatrix(1,1), TRAN, Ntemp(1,1) ! Transpose node matrix
*MFUN, iEDens(1,1), TRAN, TEDens(1,1) ! Transpose elem dens matrix
*MFUN, Sarea(1,1), TRAN, TSarea(1,1) ! Transpose surf area dens matrix

/PREP7

!-----

```

```

! Creating the Ansys materials and element material props
!-----

rhomin = 1          ! min apparent bone density in kg/cubic.meter
rhomax = 1800       ! max apparent bone density in kg/cubic.meter
ygmax = 15E9        ! max Young's modulus for scapula bone in Pa
I = 1               ! initialize Ansys material number

*DO, rho, 1, rhomax
  !compute the young modulus (Pa) from bone density
  ygmod = (ygmax*(rho/rhomax))*(rho/rhomax)
  MP, EX, I, ygmod  !assign material young mod value in Pa
  MP, PRXY, I, 0.3  !assign material Poisson ratio value
  MP, DENS, I, rho  !assign material density value in kg/cubic.meter
  I = I+1           !increment the material number
*ENDDO

NUMSTR, NODE, 1     ! Set starting node number = 1
NUMSTR, ELEM, 1     ! Set starting element number = 1

*DO, I, 1, nodenum          ! Define the nodes
  N, Nmatrx(I,1), Nmatrx(I,2), Nmatrx(I,3),0      ! values in meters
*ENDDO

ET,1,PLANE2,,0,,,          !Declaring the element type as 2D 6-node triangle

*DO, J, 1, elemnum         ! Define the elements
  E, Ematrx(J,2), Ematrx(J,3), Ematrx(J,4), Ematrx(J,5), Ematrx(J,6),
  Ematrx(J,7)
*ENDDO

*DO, K, 1, elemnum         !Assign ansys materials to elements

!elem mat number is in column 2 of matrix, and elem number is in column 1
  *IF,iEDens(K,1),LT,1,THEN
    iEDens(K,1)=1
    MPCHG,iEDens(K,1),K
  *ELSEIF,iEDens(K,1),GT,1800,THEN
    iEDens(K,1)=1800
    MPCHG,iEDens(K,1),K
  *ELSE
    MPCHG,iEDens(K,1),K
  *ENDIF
*ENDDO

I=1
vol = 0
*DO,I,1,elemnum           !compute the element area and bone volume
  *GET,Earea(I,1),ELEM,I,AREA
  vol=vol+Earea(I,1)
*ENDDO

```

FINISH

!-----Setup arrays for cosine profile pressure loading-----

!first create the arrays to compute the values

Ccount=155

APcount = 77

\*DIM,Tcent,ARRAY,Ccount,1

\*DIM,Tant,ARRAY,APcount,1

\*DIM,Tpost,ARRAY,APcount,1

!create 1-D arrays that hold the node values

\*DIM,Cnode,ARRAY,Ccount,1

\*DIM,Anode,ARRAY,APcount,1

\*DIM,Pnode,ARRAY,APcount,1

!Enter the nodes for the three loads

Cnode(1,1)=228,229,230,231,232,233,234,235,236,237

Cnode(11,1)=238,239,240,241,242,243,244,245

Cnode(19,1)=32,247,248,249,250,251,252,253,254,255

Cnode(29,1)=256,257,258,259,260,261,262,263,264,265

Cnode(39,1)=266,267,268,269,270,271,272,273,274,275

Cnode(49,1)=276,277,278,279,280,281,282,283,284,285

Cnode(59,1)=286,287,288,289,290,291,292,293,294,295

Cnode(69,1)=296,297,298,299,300,301,302,303,304,305

Cnode(79,1)=246,307,308,309,310,311,312,313,314,315

Cnode(89,1)=316,317,318,319,320,321,322,323,324,325

Cnode(99,1)=326,327,328,329,330,331,332,333,334,335

Cnode(109,1)=336,337,338,339,340,341,342,343,344,345

Cnode(119,1)=346,347,348,349,350,351,352,353,354,355

Cnode(129,1)=356,357,358,359,360,361,362,363,364,365

Cnode(139,1)=366,367,368,369,370,371,372,373,374,375

Cnode(149,1)=306,376,377,378,379,380,381

Anode(1,1)=228,229,230,231,232,233,234,235,236,237

Anode(11,1)=238,239,240,241,242,243,244,245

Anode(19,1)=32,247,248,249,250,251,252,253,254,255

Anode(29,1)=256,257,258,259,260,261,262,263,264,265

Anode(39,1)=266,267,268,269,270,271,272,273,274,275

Anode(49,1)=276,277,278,279,280,281,282,283,284,285

Anode(59,1)=286,287,288,289,290,291,292,293,294,295

Anode(69,1)=296,297,298,299,300,301,302,303,304!,305

!Anode(67,1)=246,307,308

Pnode(1,1)=246,307,308,309,310,311

Pnode(7,1)=312,313,314,315,316,317,318,319,320,321

Pnode(17,1)=322,323,324,325,326,327,328,329,330,331

Pnode(27,1)=332,333,334,335,336,337,338,339,340,341

Pnode(37,1)=342,343,344,345,346,347,348,349,350,351

Pnode(47,1)=352,353,354,355,356,357,358,359,360,361

Pnode(57,1)=362,363,364,365,366,367,368,369,370,371

Pnode(67,1)=372,373,374,375,306,376,377,378,379,380

Pnode(77,1)=381



!create components of the nodes making up the cent, ant, post loads

ALLSEL

```
NSEL,S,NODE,,Cnode(1,1),Cnode(1,1),1
*DO,I,2,Ccount
    NSEL,A,NODE,,Cnode(I,1),Cnode(I,1),1
*ENDDO
CM,centnodes,NODE
```

ALLSEL

```
NSEL,S,NODE,,Anode(1,1),Anode(1,1),1
*DO,I,2,APcount
    NSEL,A,NODE,,Anode(I,1),Anode(I,1),1
*ENDDO
CM,antnodes,NODE
```

ALLSEL

```
NSEL,S,NODE,,Pnode(1,1),Pnode(1,1),1
*DO,I,2,APcount
    NSEL,A,NODE,,Pnode(I,1),Pnode(I,1),1
*ENDDO
CM,postnodes,NODE
```

ALLSEL

!determining the lengths of lines over which the pressure will be applied

!center load

```
Lcent = 0
*DO,I,2,Ccount
    Lcent = Lcent + sqrt(((Nmatrx(Cnode(I-1,1),2)-
Nmatrx(Cnode(I,1),2))* (Nmatrx(Cnode(I-1,1),2)-
Nmatrx(Cnode(I,1),2)))+( (Nmatrx(Cnode(I-1,1),3)-
Nmatrx(Cnode(I,1),3))* (Nmatrx(Cnode(I-1,1),3)-Nmatrx(Cnode(I,1),3))))))
*ENDDO
```

!anterior load

```
Lant = 0
*DO,I,2,APcount
    Lant = Lant + sqrt(((Nmatrx(Anode(I-1,1),2)-
Nmatrx(Anode(I,1),2))* (Nmatrx(Anode(I-1,1),2)-
Nmatrx(Anode(I,1),2)))+( (Nmatrx(Anode(I-1,1),3)-
Nmatrx(Anode(I,1),3))* (Nmatrx(Anode(I-1,1),3)-Nmatrx(Anode(I,1),3))))))
*ENDDO
```

!posterior load

```
Lpost = 0
*DO,I,2,APcount
    Lpost = Lpost + sqrt(((Nmatrx(Pnode(I-1,1),2)-
Nmatrx(Pnode(I,1),2))* (Nmatrx(Pnode(I-1,1),2)-
Nmatrx(Pnode(I,1),2)))+( (Nmatrx(Pnode(I-1,1),3)-
Nmatrx(Pnode(I,1),3))* (Nmatrx(Pnode(I-1,1),3)-Nmatrx(Pnode(I,1),3))))))
*ENDDO
```

```

! then create the arrays that will be used to assign the values
*DIM,cent,ARRAY,nodenum,1
*DIM,ant,ARRAY,nodenum,1
*DIM,post,ARRAY,nodenum,1

!initialize the assigning arrays to zero
*DO,I,1,nodenum
    cent(I,1)=0
    ant(I,1)=0
    post(I,1)=0
*ENDDO

*AFUN,DEG !change angles to degrees

pi = 22/7 !computing PI

!create and assign the values for the arrays
*DO,I,1,Ccount
    Tcent(I,1)=((400*pi)/Lcent)*COS((180/2)-((I-1)*(180/(Ccount-1))))
    cent(Cnode(I,1),1)=Tcent(I,1)
*ENDDO

*DO,I,1,APcount
    Tant(I,1)=((200*pi)/Lant)*COS(90-((I-1)*(180/(APcount-1))))
    Tpost(I,1)=((200*pi)/Lpost)*COS(90-((I-1)*(180/(APcount-1))))
    ant(Anode(I,1),1)=Tant(I,1)
    post(Pnode(I,1),1)=Tpost(I,1)
*ENDDO

ALLSEL

!Determining the reference stimulus for the cent, ant, and post load cond

/SOLU

!----- Boundary Conditions -----

D,1,UX,0,0,31,1,UY

!----- Loading Condition -----

!-----CENTER LOAD-----

NSEL,S,NODE,,centnodes
SFFUN,PRES,cent(1)
SF,ALL,PRES,0
ALLSEL

EQLV,SPARSE !use the sparse solver

SOLVE

```

```

FINISH

!----- Enter Post processor to evaluate Sref values -----

/POST1

I=1
*DO,I,1,elemnum
    *GET,Uelem,ELEM,I,SENE ! get element stiffness energy or strain energy
    SrefC(I,1)=Uelem/iEDens(I,1) !reference stimulus
*ENDDO

FINISH

! reassign specimen mat prop before going to the next loading condition

/PREP7

I=1
*DO,I,1,elemnum
    MPCHG,iEDens(I,1),I
*ENDDO

FINISH

/SOLU

!----ANTERIOR----

SFDELE,ALL,PRES
NSEL,S,NODE,, antnodes
SFFUN,PRES,ant(1)
SF,ALL,PRES,0
ALLSEL

EQLV,SPARSE !use the sparse solver

SOLVE

FINISH

!----- Enter Post processor to evaluate Sref values -----

/POST1

I=1
*DO,I,1,elemnum
    *GET,Uelem,ELEM,I,SENE ! get elem stiffness energy or strain energy
    SrefA(I,1)=Uelem/iEDens(I,1) !ref stimulus
*ENDDO

FINISH

! reassign specimen mat prop before going to the next loading condition

/PREP7

```

```

*DO,I,1,elemnum
      MPCHG,iEDens(I,1),I
*ENDDO

FINISH

/SOLU

!-----POSTERIOR LOAD-----

SFDELE,ALL,PRES
NSEL,S,NODE,,postnodes
SFFUN,PRES,post(1)
SF,ALL,PRES,0
ALLSEL

EQSLV,SPARSE !use the sparse solver

SOLVE

FINISH

!----- Enter Post processor to evaluate Sref values -----

/POST1

I=1
*DO,I,1,elemnum
      *GET,Uelem,ELEM,I,SENE ! get element stiffness energy or strain energy
      SrefP(I,1)=Uelem/iEDens(I,1) !ref stimulus
*ENDDO

FINISH

!-----
!
!
!-----

!-Initialize the bone material as homogeneous density of 600 kg/cubic.meter--

/PREP7

*DO,I,1,elemnum
      MPCHG,600,I
      EDens(I,1)=600
*ENDDO

iternum = 0 !Remod iteration counter

!---- export the initial condition
export

FINISH

```

```

!----- Bone remodeling equation parameters -----
s = 0.4                !Remodeling constant
B = 200                !Remodeling rate coefficient
dt = 864000            !time increment in seconds for 10 days
iters = 100            ! total number of iterations to be done for remodeling

*DIM,objfun,ARRAY,(iters*3),1!stores val of obj func through all iter
*DIM,diff1,ARRAY,elemnum,1
*DIM,dtime,ARRAY,iters,1

*DO,K,1,iters

!----- APPLY THE FIRST LOAD -----

/SOLU

ALLSEL

*IF,FL,EQ,1,THEN

    !-----CENTER LOAD-----
    SFDELE,ALL,PRES
    NSEL,S,NODE,,centnodes
    SFFUN,PRES,cent(1)
    SF,ALL,PRES,0
    ALLSEL

    *DO,I,1,elemnum
        Sref(I,1)=SrefC(I,1)
    *ENDDO

*ELSEIF,FL,EQ,2,THEN

    !-----ANTERIOR-----
    SFDELE,ALL,PRES
    NSEL,S,NODE,,antnodes
    SFFUN,PRES,ant(1)
    SF,ALL,PRES,0
    ALLSEL

    *DO,I,1,elemnum
        Sref(I,1)=SrefA(I,1)
    *ENDDO

*ELSEIF,FL,EQ,3,THEN

    !-----POSTERIOR LOAD-----
    SFDELE,ALL,PRES
    NSEL,S,NODE,,postnodes
    SFFUN,PRES,post(1)
    SF,ALL,PRES,0
    ALLSEL

*DO,I,1,elemnum
    Sref(I,1)=SrefP(I,1)

```

```

*ENDDO

*ENDIF

FINISH

!-----
!Bone remodeling iterative method
!-----

!----- Solve the problem -----
/SOLU
EQSLV,SPARSE
SOLVE
FINISH

!----- Enter post-processor to compute elem stimulus value -----

/POST1

*DO, I, 1, elemnum
  *GET,Uelem,ELEM,I,SENE
  Selem(I,1)=Uelem/EDens(I,1)
*ENDDO

FINISH

!-----Enter pre-processor to re-assign element material props -----

/PREP7

sum = 0!Initializing sum parameter for computing the Objective function

!----Determine the difference in the stimulus values -----
!----Also evaluate the objective function value -----

*DO,J,1,elemnum
  *IF,EDens(J,1),EQ,rhmax,THEN
    diff=0
  *ELSEIF,Selem(J,1),GE,(Sref(J,1)*(1+s)),THEN
    diff = (Selem(J,1)-(Sref(J,1)*(1+s)))*(Sarea(NINT(EDens(J,1)),1))
  *ELSEIF,Selem(J,1),LE,(Sref(J,1)*(1-s)),THEN
    diff = (Selem(J,1)-(Sref(J,1)*(1-s)))*(Sarea(NINT(EDens(J,1)),1))
  *ELSE
    diff = 0
  *ENDIF

  sum=sum+ABS(diff)

  diff1(J,1)=diff
*ENDDO

*DO,I,1,elemnum
  EDens(I,1)=EDens(I,1)+(B*dt*diff1(I,1))
*ENDDO

```



```

*ELSEIF,SL,EQ,3,THEN

    !-----POSTERIOR LOAD-----
    SFDELE,ALL,PRES
    NSEL,S,NODE,,postnodes
    SFFUN,PRES,post(1)
    SF,ALL,PRES,0
    ALLSEL

    *DO,I,1,elemnum
        Sref(I,1)=SrefP(I,1)
    *ENDDO

*ENDIF

FINISH

!-----BONE REMODELING-----

!----- Solve the problem -----
/SOLU
EQSLV,SPARSE
SOLVE
FINISH

!----- Enter post-processor to compute elem stimulus value -----

/POST1

*DO, I, 1, elemnum
    *GET,Uelem,ELEM,I,SENE
    Selem(I,1)=Uelem/EDens(I,1)
*ENDDO

FINISH

!----- Enter pre-processor to re-assign element material props -----

/PREP7

sum = 0!Initializing sum parameter for computing the Objective function

!--Determine the difference in the stimulus values -----
!----- Also evaluate the objective function value -----

*DO,J,1,elemnum
    *IF,EDens(J,1),EQ,rhmax,THEN
        diff=0
    *ELSEIF,Selem(J,1),GE,(Sref(J,1)*(1+s)),THEN
        diff = (Selem(J,1)-(Sref(J,1)*(1+s)))*(Sarea(NINT(EDens(J,1)),1))
    *ELSEIF,Selem(J,1),LE,(Sref(J,1)*(1-s)),THEN
        diff = (Selem(J,1)-(Sref(J,1)*(1-s)))*(Sarea(NINT(EDens(J,1)),1))
    *ELSE
        diff = 0
    *ENDIF

    sum=sum+ABS(diff)

```



```

        diff1(J,1)=diff
*ENDDO

*DO,I,1,elemnum
        EDens(I,1)=EDens(I,1)+(B*dt*diff1(I,1))
*ENDDO

!----- Re-assign material properties -----

*DO,J,1,elemnum
        EDens(J,1) = NINT(EDens(J,1))
        *IF,EDens(J,1),LE,rhomin,THEN
                MPCHG,rhomin,J
                EDens(J,1)=rhomin
        *ELSEIF,EDens(J,1),GE,rhomin,THEN
                MPCHG,rhomin,J
                EDens(J,1)=rhomin
        *ELSE
                MPCHG,EDens(J,1),J
        *ENDIF
*ENDDO

!----- Increment iteration number -----

iternum=iternum+1
objfun(iternum,1)=sum      !storing the value for the objective function

FINISH

!----- export the elem density -----
export

!----- APPLY THE THIRD LOAD -----

/SOLU

ALLSEL

*IF,TL,EQ,1,THEN

        !-----CENTER LOAD-----
        SFDELE,ALL,PRES
        NSEL,S,NODE,,centnodes
        SFFUN,PRES,cent(1)
        SF,ALL,PRES,0
        ALLSEL

        *DO,I,1,elemnum
                Sref(I,1)=SrefC(I,1)
        *ENDDO

*ELSEIF,TL,EQ,2,THEN

        !-----ANTERIOR-----
        SFDELE,ALL,PRES
        NSEL,S,NODE,,antnodes

```

```

SFFUN,PRES,ant(1)
SF,ALL,PRES,0
ALLSEL

*DO,I,1,elemnum
    Sref(I,1)=SrefA(I,1)
*ENDDO

*ELSEIF,TL,EQ,3,THEN

    !-----POSTERIOR LOAD-----
    SFDELE,ALL,PRES
    NSEL,S,NODE,,postnodes
    SFFUN,PRES,post(1)
    SF,ALL,PRES,0
    ALLSEL

    *DO,I,1,elemnum
        Sref(I,1)=SrefP(I,1)
    *ENDDO

*ENDIF

FINISH

!-----BONE REMODELING-----

!----- Solve the problem -----
/SOLU
EQSLV,SPARSE
SOLVE
FINISH

!----- Enter post-processor to compute elem stimulus value -----

/POST1

*DO, I, 1, elemnum
    *GET,Uelem,ELEM,I,SENE
    Selem(I,1)=Uelem/EDens(I,1)
*ENDDO

FINISH

!---- Enter pre-processor to re-assign element material props -----

/PREP7

sum = 0!Initializing sum parameter for computing the Objective function

!----Determine the difference in the stimulus values -----
!---- Also evaluate the objective function value -----

*DO,J,1,elemnum
    *IF,EDens(J,1),EQ,rhmax,THEN
        diff=0
    *ELSEIF,Selem(J,1),GE,(Sref(J,1)*(1+s)),THEN

```

```

        diff = (Selem(J,1)-(Sref(J,1)*(1+s)))*(Sarea(NINT(EDens(J,1)),1))
*ELSEIF,Selem(J,1),LE,(Sref(J,1)*(1-s)),THEN
        diff = (Selem(J,1)-(Sref(J,1)*(1-s)))*(Sarea(NINT(EDens(J,1)),1))
*ELSE
        diff = 0
*ENDIF

sum=sum+ABS(diff)

diff1(J,1)=diff
*ENDDO

*DO,I,1,elemnum
        EDens(I,1)=EDens(I,1)+(B*dt*diff1(I,1))
*ENDDO

!----- Re-assign material properties -----

*DO,J,1,elemnum
        EDens(J,1) = NINT(EDens(J,1))
        *IF,EDens(J,1),LE,rhomin,THEN
                MPCHG,rhomin,J
                EDens(J,1)=rhomin
        *ELSEIF,EDens(J,1),GE,rhobox,THEN
                MPCHG,rhobox,J
                EDens(J,1)=rhobox
        *ELSE
                MPCHG,EDens(J,1),J
        *ENDIF
*ENDDO

!----- Increment iteration number -----

iternum=iternum+1
objfun(iternum,1)=sum!storing the value for the objective function

FINISH

!----- export the elem density -----
export

*ENDDO

!----- export objective function -----
export1

```

## Node based approach

```
! Written by Gulshan Sharma, Univ Pittsburgh, Bioeng. MIBL, Pittsburgh, PA,  
! USA  
! Date started: 22 June 2006
```

```
! Code for the second part of the bone remodeling project.  
! In this code first the 2D FEM of proximal glenoid axial slice is created,  
! then the ansys materials are set up, load and boundary conditions are  
! applied, homogeneous bone material properties are assigned,  
! reference nodal stimulus values are imported, problem is solved in  
! iterative process and in each iteration the bone material proerties are  
! modified accordingly as well as exported in an appendable text file.
```

```
elemnum = 6606 ! total number of elements  
nodenum = 13495 ! total number of nodes  
Ecols = 7 ! total cols in elem mat, 7 for 2DFEA and 11 for 3DFEA  
Ncols = 3 ! total cols in node mat, 3 for 2DFEA and 4 for 3D FEA
```

```
! Enter details for the loading sequence  
! FL = first load  
! SL = second load  
! TL = third load  
! Load key: Center=1; Anterior=2; Posterior=3
```

```
!case1=CPA=132; case2=CAP=123; case3=ACP=213; case4=APC=231; case5=PCA=312;  
case6=PAC=321
```

```
FL=1  
SL=3  
TL=2
```

```
!-----Create TEMP arrays for elements and nodes-----  
! These arrays will be transposed to correctly orient the matrix since the  
! vread command reads rows as columns  
!-----
```

```
*DIM, Etemp, ARRAY, Ecols, elemnum !Temp elem mat  
*DIM, Ntemp, ARRAY, Ncols, nodenum !Temp node mat  
*DIM, TEDens, ARRAY, 1, elemnum !Temp elem dens mat  
*DIM, TNDens, ARRAY, 1, nodenum !Temp nodal dens mat  
*DIM, TSarea,ARRAY,1,1800 !Temp surf area dens mat
```

```
!-----Create the arrays for elements and nodes-----  
! These arrays will store the data in the correct orientation  
!-----
```

```
*DIM, Ematrix, ARRAY, elemnum, Ecols !elem mat  
*DIM, Nmatrix, ARRAY, nodenum, Ncols !node coord mat  
*DIM, EDens, ARRAY, elemnum, 1 !Elem dens in each iter mat  
*DIM, iEDens,ARRAY,elemnum,1 !initial elem original mat prop  
*DIM, NDens, ARRAY, nodenum, 1 !Nodal dens in each iter mat  
*DIM, iNDens, ARRAY, nodenum, 1 !initial Nodal dens val  
*DIM, SrefC, ARRAY, nodenum, 1 !Ref stimulus val center load
```

```

*DIM, SrefA, ARRAY, nodenum, 1      !Ref stimulus val anterior load
*DIM, SrefP, ARRAY, nodenum, 1      !Ref stimulus val posterior load
*DIM, Sref, ARRAY, nodenum, 1       !Ref stimulus val for temp value
*DIM, Snode, ARRAY, nodenum, 2      !Stimulus val in each iter
*DIM, uDens, ARRAY, nodenum, 1      !Nodal Strain Energy Density
*DIM, Sarea, ARRAY, 1800, 1         !Surf area dens values
*DIM, flag, ARRAY, nodenum, 1       !Sentinel array to keep track nodes used
                                     !computing nodal strain energy density

*DIM, Earea, ARRAY, elemnum, 1      !matrix to store element area

*DIM, Selem, ARRAY, elemnum, 1      !stimulus val at elem centroids

*VREAD, Etemp(1,1), Ax119Elems, txt, , elemnum ! Read elements
(7F12.2)

*VREAD, Ntemp(1,1), Ax119Nodes, txt, , nodenum ! Read nodes
(F10.1,F20.10,F20.10)

*VREAD, TEDens(1,1), Ax119EDens, txt, , elemnum ! Read elem dens
(F20.2)

*VREAD, TNDens(1,1), Ax119NDens, txt, , nodenum ! Read node dens
(F20.2)

! Read surface area density
*VREAD, TSarea(1,1), SurfaceAreaDensity, txt, , 1800
(F30.15)

*MFUN, Ematrix(1,1), TRAN, Etemp(1,1) ! Transpose element matrix
*MFUN, Nmatrix(1,1), TRAN, Ntemp(1,1) ! Transpose node matrix
*MFUN, iEDens(1,1), TRAN, TEDens(1,1) ! Transpose elem dens matrix
*MFUN, iNDens(1,1), TRAN, TNDens(1,1) ! Transpose node dens matrix
*MFUN, Sarea(1,1), TRAN, TSarea(1,1) ! Transpose surf area dens

/PREP7

!-----
! Creating the Ansys materials and element material props
!-----

rhomin = 1          ! min apparent bone density in kg/cubic.meter
rhomax = 1800       ! max apparent bone density in kg/cubic.meter
ygmax = 15E9        ! max Young's modulus for scapula bone in Pa
I = 1               ! initialize ansys material number

*DO, rho, 1, rhomax
  !compute Young modulus (Pa) from bone density
  ygmod = (ygmax*(rho/rhomax)*(rho/rhomax))
  MP, EX, I, ygmod  !assign material young mod value in Pa
  MP, PRXY, I, 0.3  !assign material poisson ratio value
  MP, DENS, I, rho  !assign material density value in kg/cubic.meter

```

```

        I = I+1      !increment the material number
*ENDDO

NUMSTR, NODE, 1    ! Set starting node number = 1
NUMSTR, ELEM, 1    ! Set starting element number = 1

*DO, I, 1, nodenum ! Define the nodes
    N, Nmatrx(I,1), Nmatrx(I,2), Nmatrx(I,3),0      ! values in meters
    NDens(I,1)=600                                ! value in kg/cubic.meter
*ENDDO

ET,1,PLANE2,,0,,, !Declaring the element type as 2D 6-node triangle

*DO, J, 1, elemnum ! Define the elements
    E, Ematrx(J,2), Ematrx(J,3), Ematrx(J,4), Ematrx(J,5), Ematrx(J,6),
    Ematrx(J,7)
*ENDDO

!Assign ansys materials to elements
!elem mat number is in column 2 of matrix, and elem number is in column 1
*DO, K, 1, elemnum
    *IF,iEDens(K,1),LT,1,THEN
        iEDens(K,1)=1
        MPCHG,iEDens(K,1),K
    *ELSEIF,iEDens(K,1),GT,1800,THEN
        iEDens(K,1)=1800
        MPCHG,iEDens(K,1),K
    *ELSE
        MPCHG,iEDens(K,1),K
    *ENDIF
*ENDDO

!compute the element area and bone volume
I=1
*DO,I,1,elemnum
    *GET,Earea(I,1),ELEM,I,AREA
*ENDDO

FINISH

!-----Setup arrays for cosine profile pressure loading-----

!first create the arrays to compute the values
Ccount=155
APcount = 77

*DIM,Tcent,ARRAY,Ccount,1
*DIM,Tant,ARRAY,APcount,1
*DIM,Tpost,ARRAY,APcount,1

!create 1-D arrays that hold the node values
*DIM,Cnode,ARRAY,Ccount,1
*DIM,Anode,ARRAY,APcount,1
*DIM,Pnode,ARRAY,APcount,1

```

```

!Enter the nodes for the three loads
Cnode(1,1)=228,229,230,231,232,233,234,235,236,237
Cnode(11,1)=238,239,240,241,242,243,244,245
Cnode(19,1)=32,247,248,249,250,251,252,253,254,255
Cnode(29,1)=256,257,258,259,260,261,262,263,264,265
Cnode(39,1)=266,267,268,269,270,271,272,273,274,275
Cnode(49,1)=276,277,278,279,280,281,282,283,284,285
Cnode(59,1)=286,287,288,289,290,291,292,293,294,295
Cnode(69,1)=296,297,298,299,300,301,302,303,304,305
Cnode(79,1)=246,307,308,309,310,311,312,313,314,315
Cnode(89,1)=316,317,318,319,320,321,322,323,324,325
Cnode(99,1)=326,327,328,329,330,331,332,333,334,335
Cnode(109,1)=336,337,338,339,340,341,342,343,344,345
Cnode(119,1)=346,347,348,349,350,351,352,353,354,355
Cnode(129,1)=356,357,358,359,360,361,362,363,364,365
Cnode(139,1)=366,367,368,369,370,371,372,373,374,375
Cnode(149,1)=306,376,377,378,379,380,381

```

```

Anode(1,1)=228,229,230,231,232,233,234,235,236,237
Anode(11,1)=238,239,240,241,242,243,244,245
Anode(19,1)=32,247,248,249,250,251,252,253,254,255
Anode(29,1)=256,257,258,259,260,261,262,263,264,265
Anode(39,1)=266,267,268,269,270,271,272,273,274,275
Anode(49,1)=276,277,278,279,280,281,282,283,284,285
Anode(59,1)=286,287,288,289,290,291,292,293,294,295
Anode(69,1)=296,297,298,299,300,301,302,303,304!,305
!Anode(67,1)=246,307,308

```

```

Pnode(1,1)=246,307,308,309,310,311
Pnode(7,1)=312,313,314,315,316,317,318,319,320,321
Pnode(17,1)=322,323,324,325,326,327,328,329,330,331
Pnode(27,1)=332,333,334,335,336,337,338,339,340,341
Pnode(37,1)=342,343,344,345,346,347,348,349,350,351
Pnode(47,1)=352,353,354,355,356,357,358,359,360,361
Pnode(57,1)=362,363,364,365,366,367,368,369,370,371
Pnode(67,1)=372,373,374,375,306,376,377,378,379,380
Pnode(77,1)=381

```

```

!create components of the nodes making up the cent, ant, post loads

```

```

ALLSEL

```

```

NSEL,S,NODE,,Cnode(1,1),Cnode(1,1),1
*DO,I,2,Ccount
    NSEL,A,NODE,,Cnode(I,1),Cnode(I,1),1
*ENDDO
CM,centnodes,NODE

```

```

ALLSEL

```

```

NSEL,S,NODE,,Anode(1,1),Anode(1,1),1
*DO,I,2,APcount
    NSEL,A,NODE,,Anode(I,1),Anode(I,1),1
*ENDDO
CM,antnodes,NODE

```

```

ALLSEL

NSEL,S,NODE,,Pnode(1,1),Pnode(1,1),1
*DO,I,2,APcount
    NSEL,A,NODE,,Pnode(I,1),Pnode(I,1),1
*ENDDO
CM,postnodes,NODE

ALLSEL

!determining the lengths of lines over which the pressure will be applied

!center load

Lcent = 0
*DO,I,2,Ccount
    Lcent = Lcent + sqrt(((Nmatrx(Cnode(I-1,1),2)-
        Nmatrx(Cnode(I,1),2))*(Nmatrx(Cnode(I-1,1),2)-
        Nmatrx(Cnode(I,1),2)))+(Nmatrx(Cnode(I-1,1),3)-
        Nmatrx(Cnode(I,1),3))*(Nmatrx(Cnode(I-1,1),3)-Nmatrx(Cnode(I,1),3))))
*ENDDO

!anterior load
Lant = 0
*DO,I,2,APcount
    Lant = Lant + sqrt(((Nmatrx(Anode(I-1,1),2)-
        Nmatrx(Anode(I,1),2))*(Nmatrx(Anode(I-1,1),2)-
        Nmatrx(Anode(I,1),2)))+(Nmatrx(Anode(I-1,1),3)-
        Nmatrx(Anode(I,1),3))*(Nmatrx(Anode(I-1,1),3)-Nmatrx(Anode(I,1),3))))
*ENDDO

!posterior load
Lpost = 0
*DO,I,2,APcount
    Lpost = Lpost + sqrt(((Nmatrx(Pnode(I-1,1),2)-
        Nmatrx(Pnode(I,1),2))*(Nmatrx(Pnode(I-1,1),2)-
        Nmatrx(Pnode(I,1),2)))+(Nmatrx(Pnode(I-1,1),3)-
        Nmatrx(Pnode(I,1),3))*(Nmatrx(Pnode(I-1,1),3)-Nmatrx(Pnode(I,1),3))))
*ENDDO

! then create the arrays that will be used to assign the values
*DIM,cent,ARRAY,nodenum,1
*DIM,ant,ARRAY,nodenum,1
*DIM,post,ARRAY,nodenum,1

!initialize the assigning arrays to zero
*DO,I,1,nodenum
    cent(I,1)=0
    ant(I,1)=0
    post(I,1)=0
*ENDDO

*AFUN,DEG !change angles to degrees

pi = 22/7 !computing PI

```



```

!create and assign the values for the arrays
*DO,I,1,Ccount
  Tcent(I,1)=((400*pi)/Lcent)*COS((180/2)-((I-1)*(180/(Ccount-1))))
  cent(Cnode(I,1),1)=Tcent(I,1)
*ENDDO

*DO,I,1,APcount
  Tant(I,1)=((200*pi)/Lant)*COS(90-((I-1)*(180/(APcount-1))))
  Tpost(I,1)=((200*pi)/Lpost)*COS(90-((I-1)*(180/(APcount-1))))
  ant(Anode(I,1),1)=Tant(I,1)
  post(Pnode(I,1),1)=Tpost(I,1)
*ENDDO

ALLSEL

!Determining the ref stim for the cent, ant, and post load conditions

/SOLU

!----- Boundary Conditions -----

D,1,UX,0,0,31,1,UY

!----- Loading Condition -----

!-----CENTER LOAD-----

NSEL,S,NODE,,centnodes
SFFUN,PRES,cent(1)
SF,ALL,PRES,0
ALLSEL

EQSLV,SPARSE !use the sparse solver

SOLVE

FINISH

!----- Enter Post processor to evaluate Sref values -----

/POST1

!first get the stimulus value at the element centroid

I=1
*DO,I,1,elemnum
  *GET,Uelem,ELEM,I,SENE ! get element stiffness energy or strain energy
  Selem(I,1)=Uelem/iEDens(I,1) !reference stimulus
*ENDDO

!next extrapolate the value at the centroid to the element nodes

! initialization

*DO,I,1,nodenum
  Snode(I,1)=0
  Snode(I,2)=0

```

```

*ENDDO

*DO,I,1,elemnum
  Snode(Ematrx(I,2),1)=Snode(Ematrx(I,2),1)+Selem(I,1)
  Snode(Ematrx(I,3),1)=Snode(Ematrx(I,3),1)+Selem(I,1)
  Snode(Ematrx(I,4),1)=Snode(Ematrx(I,4),1)+Selem(I,1)
  Snode(Ematrx(I,5),1)=Snode(Ematrx(I,5),1)+Selem(I,1)
  Snode(Ematrx(I,6),1)=Snode(Ematrx(I,6),1)+Selem(I,1)
  Snode(Ematrx(I,7),1)=Snode(Ematrx(I,7),1)+Selem(I,1)

  Snode(Ematrx(I,2),2)=Snode(Ematrx(I,2),2)+1
  Snode(Ematrx(I,3),2)=Snode(Ematrx(I,3),2)+1
  Snode(Ematrx(I,4),2)=Snode(Ematrx(I,4),2)+1
  Snode(Ematrx(I,5),2)=Snode(Ematrx(I,5),2)+1
  Snode(Ematrx(I,6),2)=Snode(Ematrx(I,6),2)+1
  Snode(Ematrx(I,7),2)=Snode(Ematrx(I,7),2)+1
*ENDDO

!average to get stimulus value at the node

*DO,I,1,nodenum
  SrefC(I,1)=Snode(I,1)/Snode(I,2)
*ENDDO

FINISH

! reassign specimen mat prop before going to the next loading condition

/PREP7

I=1
*DO,I,1,elemnum
  MPCHG,iEDens(I,1),I
*ENDDO

FINISH

/SOLU

!-----ANTERIOR-----

SFDELE,ALL,PRES
NSEL,S,NODE,,antnodes
SFFUN,PRES,ant(1)
SF,ALL,PRES,0
ALLSEL

EQSLV,SPARSE !use the sparse solver

SOLVE

FINISH

!----- Enter Post processor to evaluate Sref values -----

```

```

/POST1

!first get the stimulus value at the element centroid

I=1
*DO,I,1,elemnum
    *GET,Uelem,ELEM,I,SENE ! get element stiffness energy or strain energy
    Selem(I,1)=Uelem/iEDens(I,1) !ref stimulus
*ENDDO

!next extrapolate the value at the centroid to the element nodes

! initialization

*DO,I,1,nodenum
    Snode(I,1)=0
    Snode(I,2)=0
*ENDDO

*DO,I,1,elemnum
    Snode(Ematrx(I,2),1)=Snode(Ematrx(I,2),1)+Selem(I,1)
    Snode(Ematrx(I,3),1)=Snode(Ematrx(I,3),1)+Selem(I,1)
    Snode(Ematrx(I,4),1)=Snode(Ematrx(I,4),1)+Selem(I,1)
    Snode(Ematrx(I,5),1)=Snode(Ematrx(I,5),1)+Selem(I,1)
    Snode(Ematrx(I,6),1)=Snode(Ematrx(I,6),1)+Selem(I,1)
    Snode(Ematrx(I,7),1)=Snode(Ematrx(I,7),1)+Selem(I,1)

    Snode(Ematrx(I,2),2)=Snode(Ematrx(I,2),2)+1
    Snode(Ematrx(I,3),2)=Snode(Ematrx(I,3),2)+1
    Snode(Ematrx(I,4),2)=Snode(Ematrx(I,4),2)+1
    Snode(Ematrx(I,5),2)=Snode(Ematrx(I,5),2)+1
    Snode(Ematrx(I,6),2)=Snode(Ematrx(I,6),2)+1
    Snode(Ematrx(I,7),2)=Snode(Ematrx(I,7),2)+1
*ENDDO

!average to get stimulus value at the node

*DO,I,1,nodenum
    SrefA(I,1)=Snode(I,1)/Snode(I,2)
*ENDDO

FINISH

! reassign specimen mat prop before going to the next loading condition

/PREP7

*DO,I,1,elemnum
    MPCHG,iEDens(I,1),I
*ENDDO

FINISH

/SOLU

!-----POSTERIOR LOAD-----

```

```

SFDELE,ALL,PRES
NSEL,S,NODE,,postnodes
SFFUN,PRES,post(1)
SF,ALL,PRES,0
ALLSEL

EQSLV,SPARSE !use the sparse solver

SOLVE

FINISH

!----- Enter Post processor to evaluate Sref values -----

/POST1

!first get the stimulus value at the element centroid

I=1
*DO,I,1,elemnum
  *GET,Uelem,ELEM,I,SENE ! get element stiffness energy or strain energy
  Selem(I,1)=Uelem/iEDens(I,1) !ref stimulus
*ENDDO

!next extrapolate the value at the centroid to the element nodes

! initialization

*DO,I,1,nodenum
  Snode(I,1)=0
  Snode(I,2)=0
*ENDDO

*DO,I,1,elemnum
  Snode(Ematrx(I,2),1)=Snode(Ematrx(I,2),1)+Selem(I,1)
  Snode(Ematrx(I,3),1)=Snode(Ematrx(I,3),1)+Selem(I,1)
  Snode(Ematrx(I,4),1)=Snode(Ematrx(I,4),1)+Selem(I,1)
  Snode(Ematrx(I,5),1)=Snode(Ematrx(I,5),1)+Selem(I,1)
  Snode(Ematrx(I,6),1)=Snode(Ematrx(I,6),1)+Selem(I,1)
  Snode(Ematrx(I,7),1)=Snode(Ematrx(I,7),1)+Selem(I,1)

  Snode(Ematrx(I,2),2)=Snode(Ematrx(I,2),2)+1
  Snode(Ematrx(I,3),2)=Snode(Ematrx(I,3),2)+1
  Snode(Ematrx(I,4),2)=Snode(Ematrx(I,4),2)+1
  Snode(Ematrx(I,5),2)=Snode(Ematrx(I,5),2)+1
  Snode(Ematrx(I,6),2)=Snode(Ematrx(I,6),2)+1
  Snode(Ematrx(I,7),2)=Snode(Ematrx(I,7),2)+1
*ENDDO

!average to get stimulus value at the node

*DO,I,1,nodenum
  SrefP(I,1)=Snode(I,1)/Snode(I,2)
*ENDDO

FINISH

```

```

!-----
!                               BONE REMODELING CODE
!-----

! Initialize the bone material as homogeneous density of 600 kg/cubic.meter

/PREP7

*DO,I,1,elemnum
    MPCHG,600,I
    EDens(I,1)=600
*ENDDO

iternum = 0                !Remod iteration counter

!---- export the initial condition
exportN

FINISH

!----- Bone remodeling equation parameters -----
s = 0.4      !Remodeling constant
B = 200     !Remodeling rate coefficient
dt = 864000 !time increment in seconds for 10 days
iters = 100 ! total number of iterations to be done for remodeling

*DIM,objfun,ARRAY,(iters*3),1 !stores objective function all the iters
*DIM,diff1,ARRAY,elemnum,1
*DIM,dtime,ARRAY,iters,1

*DO,K,1,iters

!----- APPLY THE FIRST LOAD -----

/SOLU

ALLSEL

*IF,FL,EQ,1,THEN

    !-----CENTER LOAD-----
    SFDELE,ALL,PRES
    NSEL,S,NODE,,centnodes
    SFFUN,PRES,cent(1)
    SF,ALL,PRES,0
    ALLSEL

    *DO,I,1,elemnum
        Sref(I,1)=SrefC(I,1)
    *ENDDO

*ELSEIF,FL,EQ,2,THEN

    !-----ANTERIOR-----
    SFDELE,ALL,PRES
    NSEL,S,NODE,,antnodes

```

```

SFFUN,PRES,ant(1)
SF,ALL,PRES,0
ALLSEL

*DO,I,1,elemnum
    Sref(I,1)=SrefA(I,1)
*ENDDO

*ELSEIF,FL,EQ,3,THEN

    !-----POSTERIOR LOAD-----
    SFDELE,ALL,PRES
    NSEL,S,NODE,,postnodes
    SFFUN,PRES,post(1)
    SF,ALL,PRES,0
    ALLSEL

    *DO,I,1,elemnum
        Sref(I,1)=SrefP(I,1)
    *ENDDO

*ENDIF

FINISH

!-----
!Bone remodeling iterative method
!-----

!----- Solve the problem -----
/SOLU
EQSLV,SPARSE
SOLVE
FINISH

!----- Enter post-processor to compute elem stimulus value -----

/POST1

!first get the stimulus value at the element centroid

I=1
*DO,I,1,elemnum
    *GET,Uelem,ELEM,I,SENE ! get element stiffness energy or strain energy
    Selem(I,1)=Uelem/EDens(I,1) !reference stimulus
*ENDDO

!next extrapolate the value at the centroid to the element nodes

! initialization

*DO,I,1,nodenum
    Snode(I,1)=0
    Snode(I,2)=0
*ENDDO

*DO,I,1,elemnum

```

```

Snode(Ematrx(I,2),1)=Snode(Ematrx(I,2),1)+Selem(I,1)
Snode(Ematrx(I,3),1)=Snode(Ematrx(I,3),1)+Selem(I,1)
Snode(Ematrx(I,4),1)=Snode(Ematrx(I,4),1)+Selem(I,1)
Snode(Ematrx(I,5),1)=Snode(Ematrx(I,5),1)+Selem(I,1)
Snode(Ematrx(I,6),1)=Snode(Ematrx(I,6),1)+Selem(I,1)
Snode(Ematrx(I,7),1)=Snode(Ematrx(I,7),1)+Selem(I,1)

Snode(Ematrx(I,2),2)=Snode(Ematrx(I,2),2)+1
Snode(Ematrx(I,3),2)=Snode(Ematrx(I,3),2)+1
Snode(Ematrx(I,4),2)=Snode(Ematrx(I,4),2)+1
Snode(Ematrx(I,5),2)=Snode(Ematrx(I,5),2)+1
Snode(Ematrx(I,6),2)=Snode(Ematrx(I,6),2)+1
Snode(Ematrx(I,7),2)=Snode(Ematrx(I,7),2)+1
*ENDDO

!average to get stimulus value at the node

*DO,I,1,nodenum
  Snode(I,1)=Snode(I,1)/Snode(I,2)
*ENDDO

FINISH

!----- Enter pre-processor to re-assign element material props -----

/PREP7

sum = 0 !Initializing the sum parameter for computing the Objective function

! Determine the difference in the stimulus values -----
! Also evaluate the objective function value -----

*DO,J,1,nodenum
  *IF,NDens(J,1),EQ,rhoxmax,THEN
    diff=0
  *ELSEIF,Snode(J,1),GE,(Sref(J,1)*(1+s)),THEN
    diff = (Snode(J,1)-(Sref(J,1)*(1+s)))*(Sarea(NINT(NDens(J,1)),1))
  *ELSEIF,Snode(J,1),LE,(Sref(J,1)*(1-s)),THEN
    diff = (Snode(J,1)-(Sref(J,1)*(1-s)))*(Sarea(NINT(NDens(J,1)),1))
  *ELSE
    diff = 0
  *ENDIF

  sum=sum+ABS(diff)

  NDens(J,1) = NDens(J,1)+(diff*dt*B) !remodeled nodal density value

  *IF,NDens(J,1),LE,rhomin,THEN
    NDens(J,1)=rhomin
  *ELSEIF,NDens(J,1),GE,rhoxmax,THEN
    NDens(J,1)=rhoxmax
  *ELSE
    NDens(J,1)=NDens(J,1)
  *ENDIF
*ENDDO

```

```

!----- Re-assign material properties -----

!For all elems determine the dens at the centroid and change mat props

*DO,J,1,elemnum
  Emat=( (-
    1/9)*(NDens(Ematr(J,2),1)+NDens(Ematr(J,3),1)+NDens(Ematr(J,4),1))+
    ((4/9)*(NDens(Ematr(J,5),1)+NDens(Ematr(J,6),1)+NDens(Ematr(J,7),1))
  )
  Emat = NINT(Emat)
  *IF,Emat,LE,rhomin,THEN
    MPCHG,rhomin,J
    EDens(J,1)=rhomin
  *ELSEIF,Emat,GE,rhmax,THEN
    MPCHG,rhmax,J
    EDens(J,1)=rhmax
  *ELSE
    MPCHG,Emat,J
    EDens(J,1)=Emat
  *ENDIF
*ENDDO

!----- Increment iteration number -----

iternum=iternum+1
objfun(iternum,1)=sum          !storing the value for the ojective function

FINISH

!----- export the node density -----
exportN

!----- APPLY THE SECOND LOAD -----

/SOLU

ALLSEL

*IF,SL,EQ,1,THEN

  !-----CENTER LOAD-----
  SFDELE,ALL,PRES
  NSEL,S,NODE,,centnodes
  SFFUN,PRES,cent(1)
  SF,ALL,PRES,0
  ALLSEL

  *DO,I,1,elemnum
    Sref(I,1)=SrefC(I,1)
  *ENDDO

*ELSEIF,SL,EQ,2,THEN

  !-----ANTERIOR-----
  SFDELE,ALL,PRES
  NSEL,S,NODE,,antnodes

```



```

SFFUN,PRES,ant(1)
SF,ALL,PRES,0
ALLSEL

*DO,I,1,elemnum
    Sref(I,1)=SrefA(I,1)
*ENDDO

*ELSEIF,SL,EQ,3,THEN

    !-----POSTERIOR LOAD-----
    SFDELE,ALL,PRES
    NSEL,S,NODE,,postnodes
    SFFUN,PRES,post(1)
    SF,ALL,PRES,0
    ALLSEL

    *DO,I,1,elemnum
        Sref(I,1)=SrefP(I,1)
    *ENDDO

*ENDIF

FINISH

!-----BONE REMODELING-----

!----- Solve the problem -----
/SOLU
EQSLV,SPARSE
SOLVE
FINISH

!----- Enter post-processor to compute elem stimulus value -----

/POST1

!first get the stimulus value at the element centroid

I=1
*DO,I,1,elemnum
    *GET,Uelem,ELEM,I,SENE ! get element stiffness energy or strain energy
    Selem(I,1)=Uelem/EDens(I,1) !reference stimulus
*ENDDO

!next extrapolate the value at the centroid to the element nodes

! initialization

*DO,I,1,nodenum
    Snode(I,1)=0
    Snode(I,2)=0
*ENDDO

*DO,I,1,elemnum
    Snode(Ematrix(I,2),1)=Snode(Ematrix(I,2),1)+Selem(I,1)
    Snode(Ematrix(I,3),1)=Snode(Ematrix(I,3),1)+Selem(I,1)

```

```

Snode(Ematrx(I,4),1)=Snode(Ematrx(I,4),1)+Selem(I,1)
Snode(Ematrx(I,5),1)=Snode(Ematrx(I,5),1)+Selem(I,1)
Snode(Ematrx(I,6),1)=Snode(Ematrx(I,6),1)+Selem(I,1)
Snode(Ematrx(I,7),1)=Snode(Ematrx(I,7),1)+Selem(I,1)

Snode(Ematrx(I,2),2)=Snode(Ematrx(I,2),2)+1
Snode(Ematrx(I,3),2)=Snode(Ematrx(I,3),2)+1
Snode(Ematrx(I,4),2)=Snode(Ematrx(I,4),2)+1
Snode(Ematrx(I,5),2)=Snode(Ematrx(I,5),2)+1
Snode(Ematrx(I,6),2)=Snode(Ematrx(I,6),2)+1
Snode(Ematrx(I,7),2)=Snode(Ematrx(I,7),2)+1
*ENDDO

!average to get stimulus value at the node

*DO,I,1,nodenum
  Snode(I,1)=Snode(I,1)/Snode(I,2)
*ENDDO

FINISH

!----- Enter pre-processor to re-assign element material props -----

/PREP7

sum = 0      !Initializing the sum param for computing the Objective function

!----- Determine the difference in the stimulus values -----
!----- Also evaluate the objective function value -----

*DO,J,1,nodenum
  *IF,NDens(J,1),EQ,rhymax,THEN
    diff=0
  *ELSEIF,Snode(J,1),GE,(Sref(J,1)*(1+s)),THEN
    diff = (Snode(J,1)-(Sref(J,1)*(1+s)))*(Sarea(NINT(NDens(J,1)),1))
  *ELSEIF,Snode(J,1),LE,(Sref(J,1)*(1-s)),THEN
    diff = (Snode(J,1)-(Sref(J,1)*(1-s)))*(Sarea(NINT(NDens(J,1)),1))
  *ELSE
    diff = 0
  *ENDIF

  sum=sum+ABS(diff)

  NDens(J,1) = NDens(J,1)+(diff*dt*B) !remodeled nodal density value

  *IF,NDens(J,1),LE,rhomin,THEN
    NDens(J,1)=rhomin
  *ELSEIF,NDens(J,1),GE,rhymax,THEN
    NDens(J,1)=rhymax
  *ELSE
    NDens(J,1)=NDens(J,1)
  *ENDIF

*ENDDO

!----- Re-assign material properties -----

```

```

!For all elems determine the dens at the centroid and change mat properties

*DO,J,1,elemnum
  Emat = ((-
    1/9)*(NDens(Ematrx(J,2),1)+NDens(Ematrx(J,3),1)+NDens(Ematrx(J,4),1))+
    (4/9)*(NDens(Ematrx(J,5),1)+NDens(Ematrx(J,6),1)+NDens(Ematrx(J,7),1))
  )
  Emat = NINT(Emat)
  *IF,Emat,LE,rhomin,THEN
    MPCHG,rhomin,J
    EDens(J,1)=rhomin
  *ELSEIF,Emat,GE,rhomax,THEN
    MPCHG,rhomax,J
    EDens(J,1)=rhomax
  *ELSE
    MPCHG,Emat,J
    EDens(J,1)=Emat
  *ENDIF
*ENDDO

!----- Increment iteration number -----

iternum=iternum+1
objfun(iternum,1)=sum          !storing the value for the ojective function

FINISH

!----- export the node density -----
exportN

!----- APPLY THE THIRD LOAD -----

/SOLU

ALLSEL

*IF,TL,EQ,1,THEN

  !-----CENTER LOAD-----
  SFDELE,ALL,PRES
  NSEL,S,NODE,,centnodes
  SFFUN,PRES,cent(1)
  SF,ALL,PRES,0
  ALLSEL

  *DO,I,1,elemnum
    Sref(I,1)=SrefC(I,1)
  *ENDDO

*ELSEIF,TL,EQ,2,THEN

  !-----ANTERIOR-----
  SFDELE,ALL,PRES
  NSEL,S,NODE,,antnodes
  SFFUN,PRES,ant(1)
  SF,ALL,PRES,0

```

```

ALLSEL

*DO,I,1,elemnum
    Sref(I,1)=SrefA(I,1)
*ENDDO

*ELSEIF,TL,EQ,3,THEN

    !-----POSTERIOR LOAD-----
    SFDELE,ALL,PRES
    NSEL,S,NODE,,postnodes
    SFFUN,PRES,post(1)
    SF,ALL,PRES,0
    ALLSEL

    *DO,I,1,elemnum
        Sref(I,1)=SrefP(I,1)
    *ENDDO

*ENDIF

FINISH

!-----BONE REMODELING-----

!----- Solve the problem -----
/SOLU
EQSLV,SPARSE
SOLVE
FINISH

!----- Enter post-processor to compute elem stimulus value -----

/POST1
!first get the stimulus value at the element centroid

I=1
*DO,I,1,elemnum
    *GET,Uelem,ELEM,I,SENE ! get element stiffness energy or strain energy
    Selem(I,1)=Uelem/EDens(I,1) !reference stimulus
*ENDDO

!next extrapolate the value at the centroid to the element nodes

! initialization

*DO,I,1,nodenum
    Snode(I,1)=0
    Snode(I,2)=0
*ENDDO

*DO,I,1,elemnum
    Snode(Ematrx(I,2),1)=Snode(Ematrx(I,2),1)+Selem(I,1)
    Snode(Ematrx(I,3),1)=Snode(Ematrx(I,3),1)+Selem(I,1)
    Snode(Ematrx(I,4),1)=Snode(Ematrx(I,4),1)+Selem(I,1)
    Snode(Ematrx(I,5),1)=Snode(Ematrx(I,5),1)+Selem(I,1)
    Snode(Ematrx(I,6),1)=Snode(Ematrx(I,6),1)+Selem(I,1)

```

```

      Snode(Ematrx(I,7),1)=Snode(Ematrx(I,7),1)+Selem(I,1)

      Snode(Ematrx(I,2),2)=Snode(Ematrx(I,2),2)+1
      Snode(Ematrx(I,3),2)=Snode(Ematrx(I,3),2)+1
      Snode(Ematrx(I,4),2)=Snode(Ematrx(I,4),2)+1
      Snode(Ematrx(I,5),2)=Snode(Ematrx(I,5),2)+1
      Snode(Ematrx(I,6),2)=Snode(Ematrx(I,6),2)+1
      Snode(Ematrx(I,7),2)=Snode(Ematrx(I,7),2)+1
*ENDDO

!average to get stimulus value at the node

*DO,I,1,nodenum
      Snode(I,1)=Snode(I,1)/Snode(I,2)
*ENDDO

FINISH

!----- Enter pre-processor to re-assign element material props -----
/PREP7

sum = 0      !Initializing the sum param for computing the Objective function

!----- Determine the difference in the stimulus values -----
!----- Also evaluate the objective function value -----

*DO,J,1,nodenum
      *IF,NDens(J,1),EQ,rhymax,THEN
            diff=0
      *ELSEIF,Snode(J,1),GE,(Sref(J,1)*(1+s)),THEN
            diff = (Snode(J,1)-(Sref(J,1)*(1+s)))*(Sarea(NINT(NDens(J,1)),1))
      *ELSEIF,Snode(J,1),LE,(Sref(J,1)*(1-s)),THEN
            diff = (Snode(J,1)-(Sref(J,1)*(1-s)))*(Sarea(NINT(NDens(J,1)),1))
      *ELSE
            diff = 0
      *ENDIF

      sum=sum+ABS(diff)

      NDens(J,1) = NDens(J,1)+(diff*dt*B) !remodeled nodal density value

      *IF,NDens(J,1),LE,rhomin,THEN
            NDens(J,1)=rhomin
      *ELSEIF,NDens(J,1),GE,rhymax,THEN
            NDens(J,1)=rhymax
      *ELSE
            NDens(J,1)=NDens(J,1)
      *ENDIF

*ENDDO

!----- Re-assign material properties -----

!For all elems determine the dens at centroid and change mat props

*DO,J,1,elemnum

```

```

Emat = ((-
1/9)*(NDens(Ematrx(J,2),1)+NDens(Ematrx(J,3),1)+NDens(Ematrx(J,4),1))+
((4/9)*(NDens(Ematrx(J,5),1)+NDens(Ematrx(J,6),1)+NDens(Ematrx(J,7),1))
)
Emat = NINT(Emat)
*IF,Emat,LE,rhomin,THEN
    MPCHG,rhomin,J
    EDens(J,1)=rhomin
*ELSEIF,Emat,GE,rhobox,THEN
    MPCHG,rhobox,J
    EDens(J,1)=rhobox
*ELSE
    MPCHG,Emat,J
    EDens(J,1)=Emat
*ENDIF
*ENDDO

```

!----- Increment iteration number -----

```

iternum=iternum+1
objfun(iternum,1)=sum          !storing the value for the objective function

```

FINISH

!----- export the node density -----  
exportN

\*ENDDO

!----- export objective function -----  
export1

### Function "export"

```

*CFOPEN, %iternum%, txt
*VWRITE, EDens(1,1)
(F30.15)
*CFCLOSE

```

### Function "export1"

```

*CFOPEN, ObjFunction, txt
*VWRITE, objfun(1,1)
(F30.15)
*CFCLOSE

```

### Function "exportN"

```

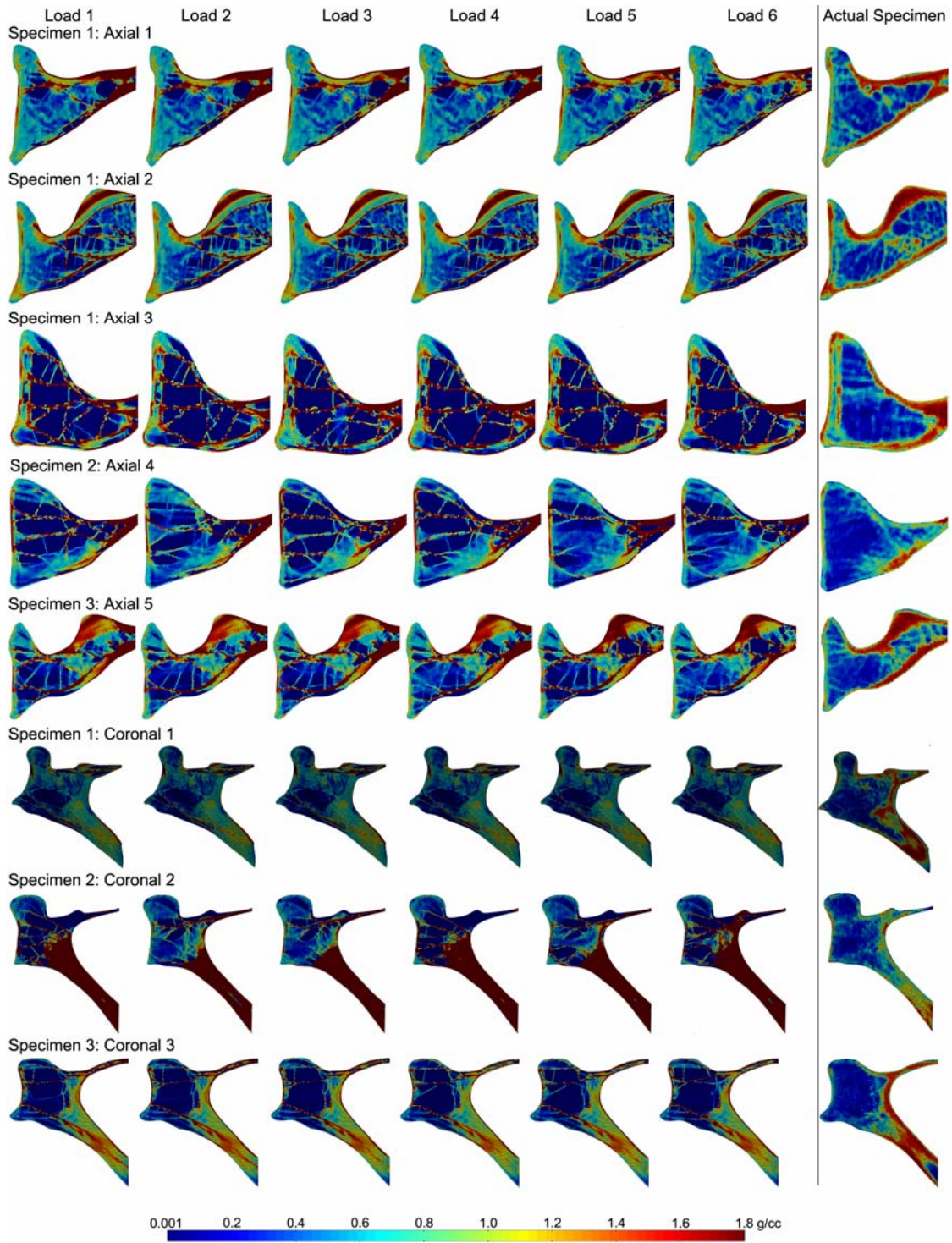
*CFOPEN, %iternum%, txt
*VWRITE, NDens(1,1)
(F30.15)
*CFCLOSE

```

## **APPENDIX E**

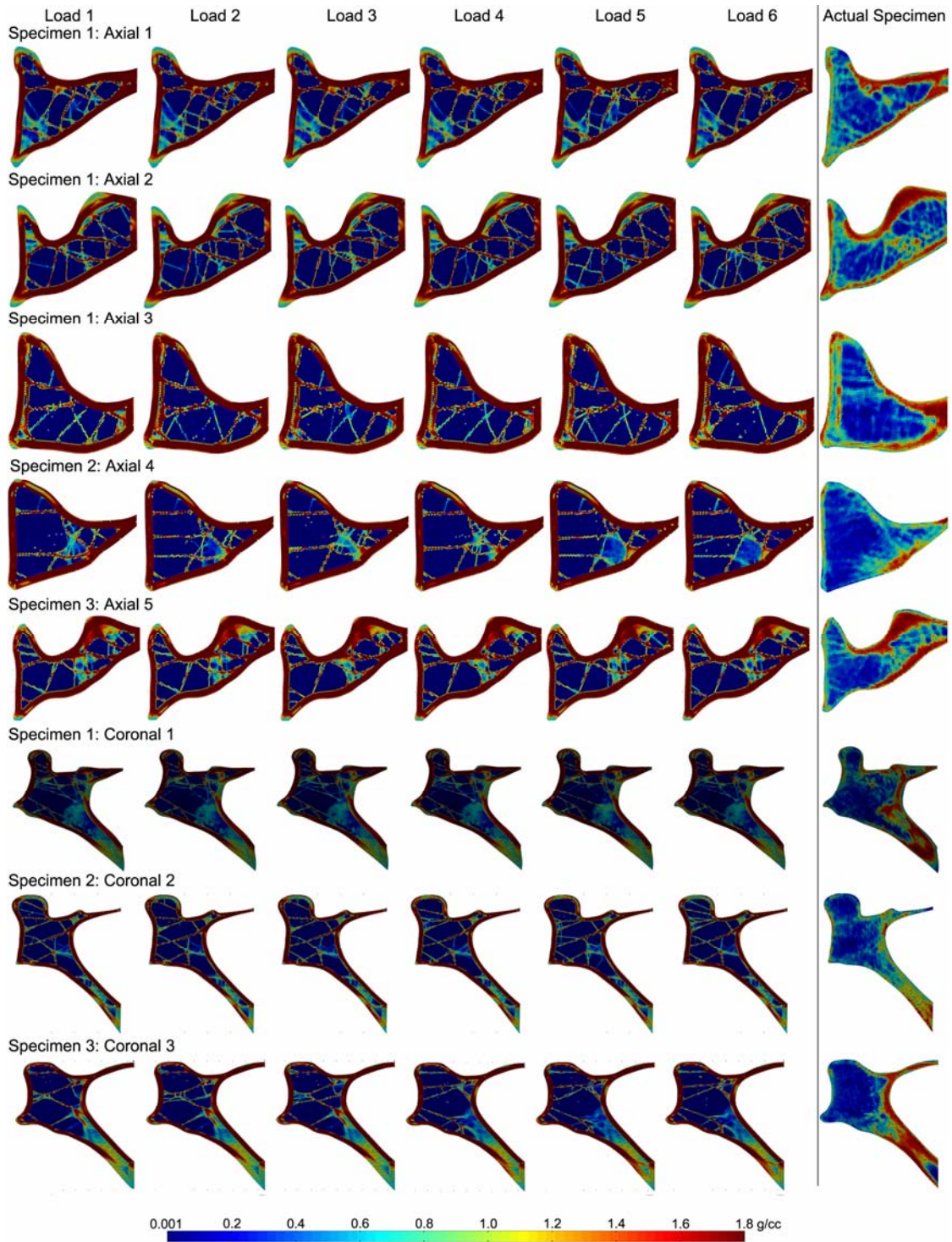
### **GLENOID BONE REMODELING SIMULATION AND VALIDATION RESULTS**

In this section the glenoid bone remodeling simulation and validation are given for all the glenoid finite element models and the six different combinations of multiple loads used in the study. It includes the predicted glenoid bone apparent density distribution at the end of the “element” and the “node” based simulations, the difference of the predicted and actual specimens bone apparent density value in each iteration averaged over all the elements or nodes based on the simulation method, the correlation coefficient of the predicted and actual specimen bone apparent density in each iteration, the absolute bone apparent density difference images at the end of the simulation process, and lastly the linear approximation of the predicted and actual specimen bone apparent density plots.

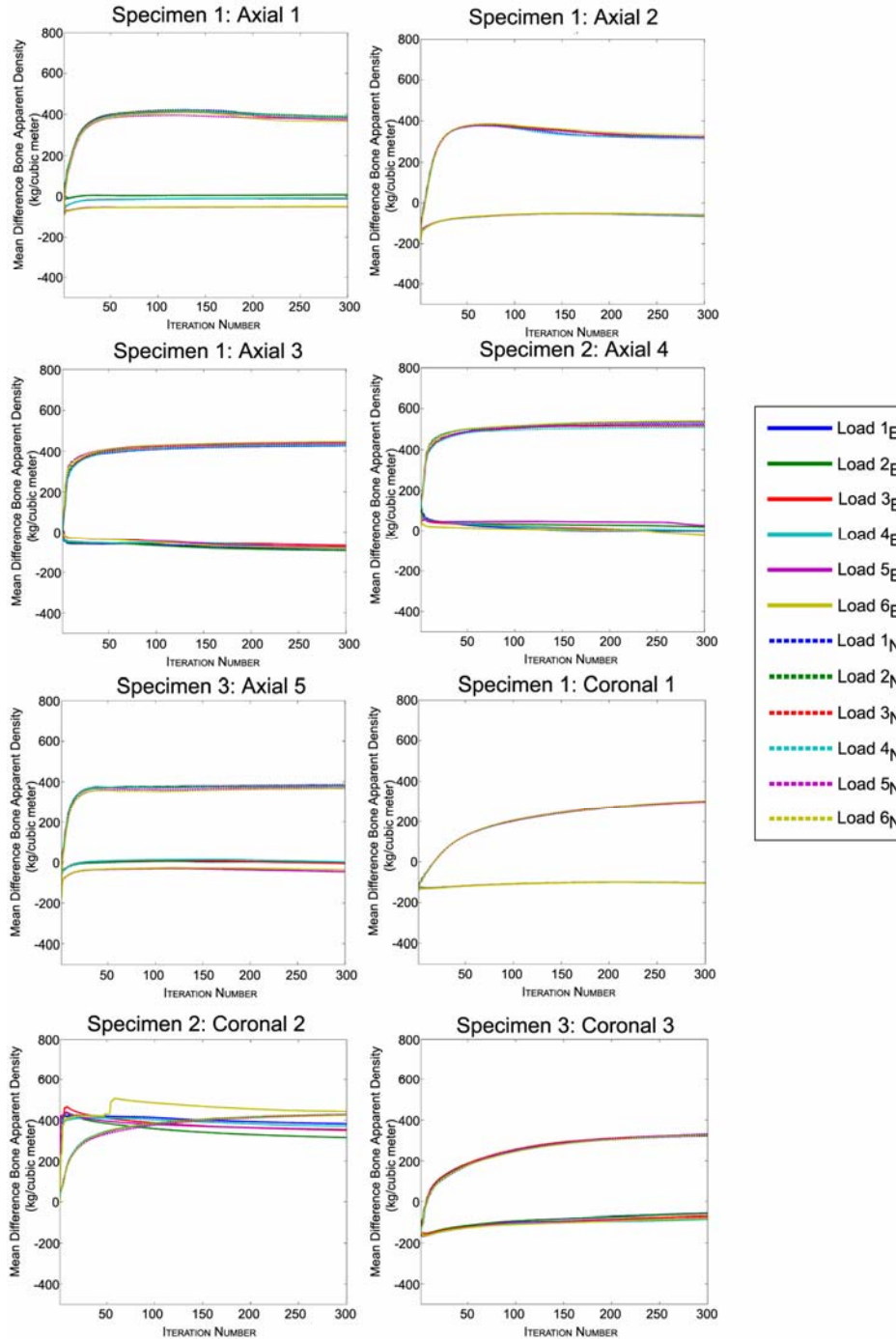


**Figure 59.** The bone apparent density plots at the end of the iterative “element” based remodeling process for all the glenoid finite element models simulated using the six different load combinations (Load 1: ACP/CIS, Load 2: APC/CSI, Load 3: CAP/ICS, Load 4: CPA/ISC, Load 5: PAC/SCI, Load 6: PCA/SIC). Also shown for comparison is the bone apparent density plot for all the actual specimens (figure by author).

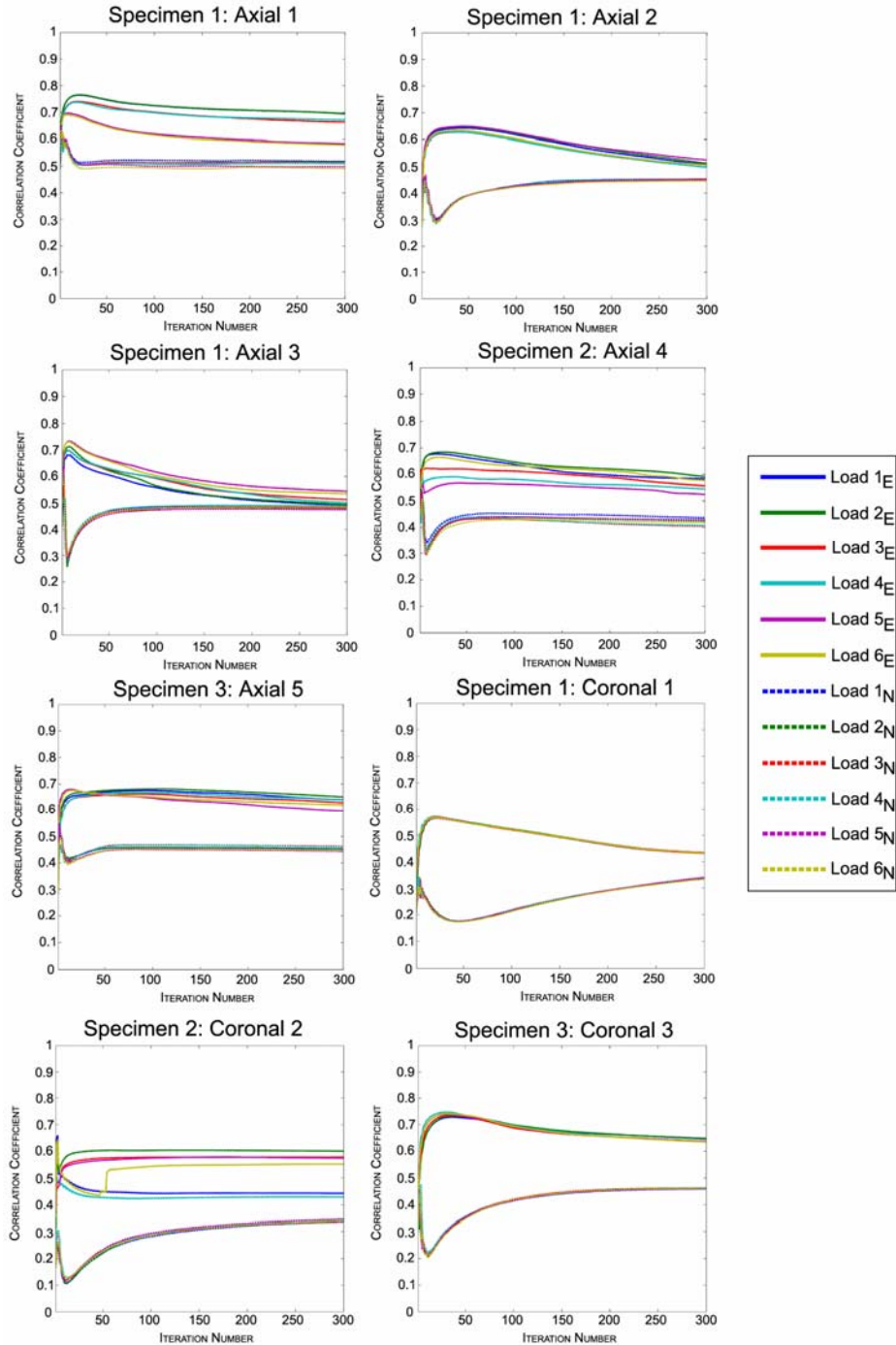




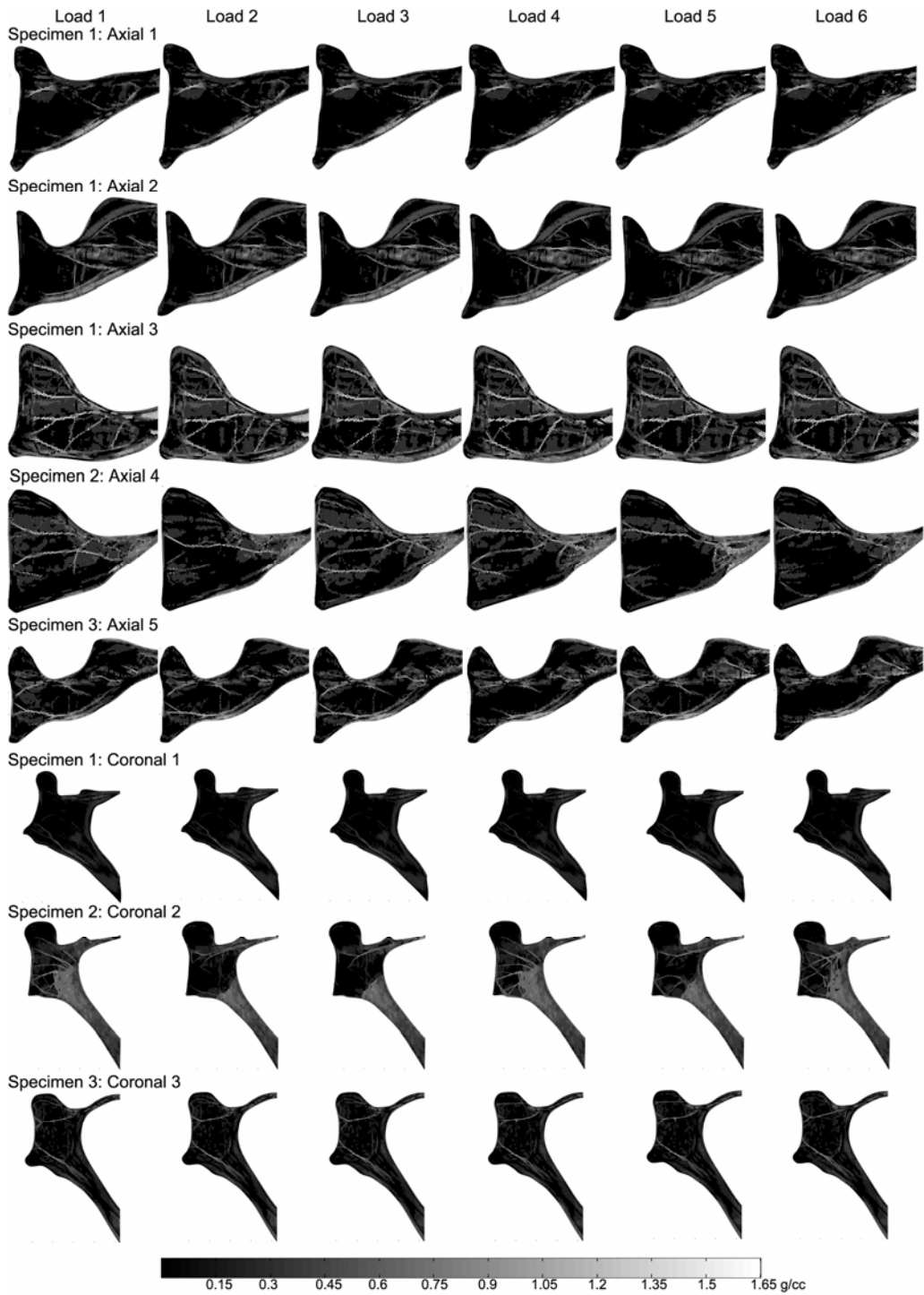
**Figure 60.** The bone apparent density plots at the end of the iterative “node” based remodeling process for all the glenoid finite element models simulated using the six different load combinations (Load 1: ACP/CIS, Load 2: APC/CSI, Load 3: CAP/ICS, Load 4: CPA/ISC, Load 5: PAC/SCI, Load 6: PCA/SIC). Also shown for comparison is the bone apparent density plot for all the actual specimens (figure by author).



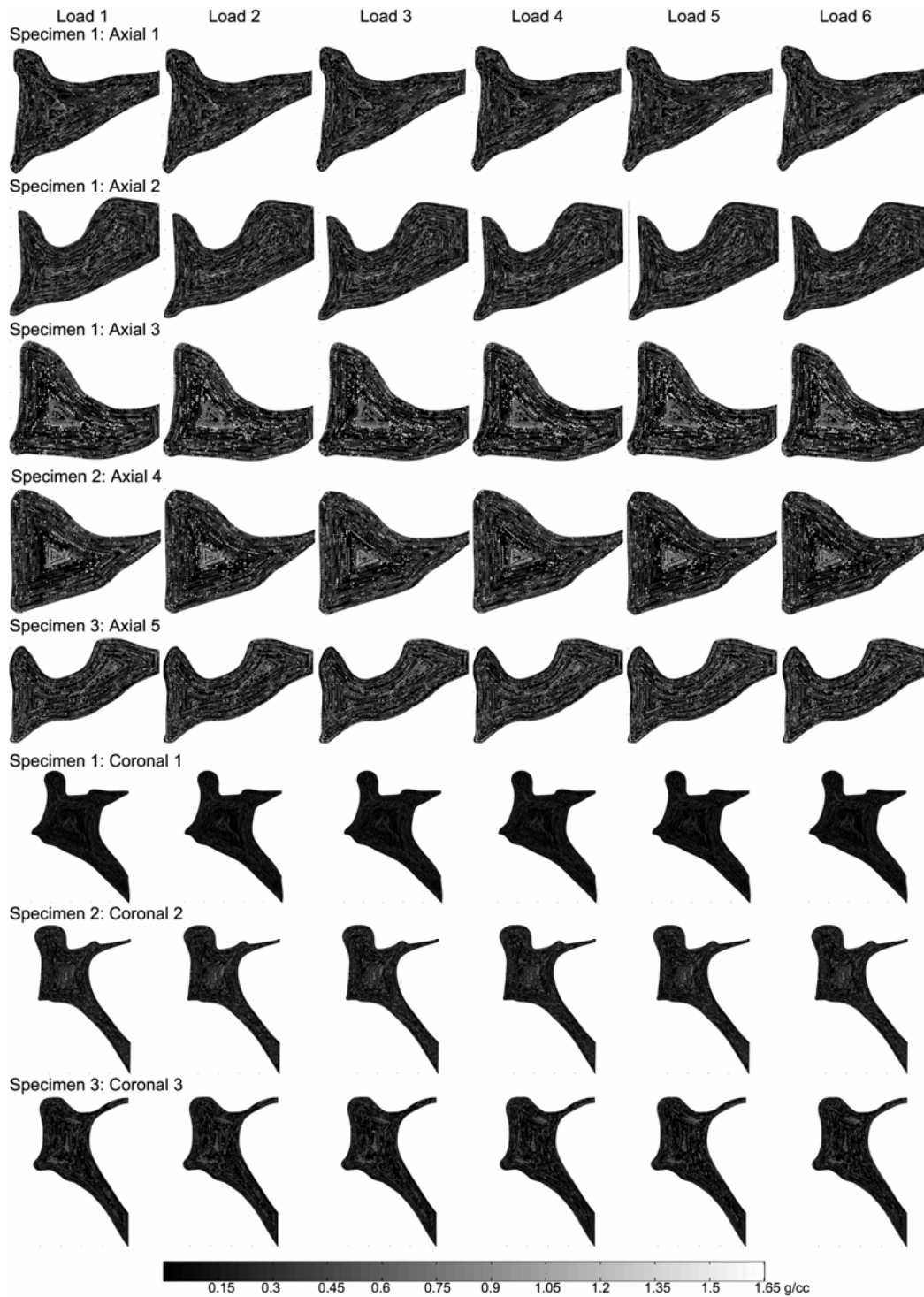
**Figure 61.** The mean of the difference between the predicted and the actual specimens bone apparent density value computed on a location specific basis in each of the iterations over all the elements or nodes depending upon the “element” or the “node” based remodeling process, represented by the subscript ‘E’ and ‘N’ in the legend respectively, used for all the glenoid FEMs with the six different load combinations (Load 1: ACP/CIS, Load 2: APC/CSI, Load 3: CAP/ICS, Load 4: CPA/ISC, Load 5: PAC/SCI, Load 6: PCA/SIC) (figure by author).



**Figure 62.** The correlation coefficient value between the predicted and the actual specimen bone apparent density value in each of the iterations for all the glenoid bone FEMs “element” and “node” based remodeling simulations, represented by subscript ‘E’ and ‘N’ respectively in the legend, with the six different load combinations (Load 1: ACP/CIS, Load 2: APC/CSI, Load 3: CAP/ICS, Load 4: CPA/ISC, Load 5: PAC/SCI, Load 6: PCA/SIC) (figure by author).

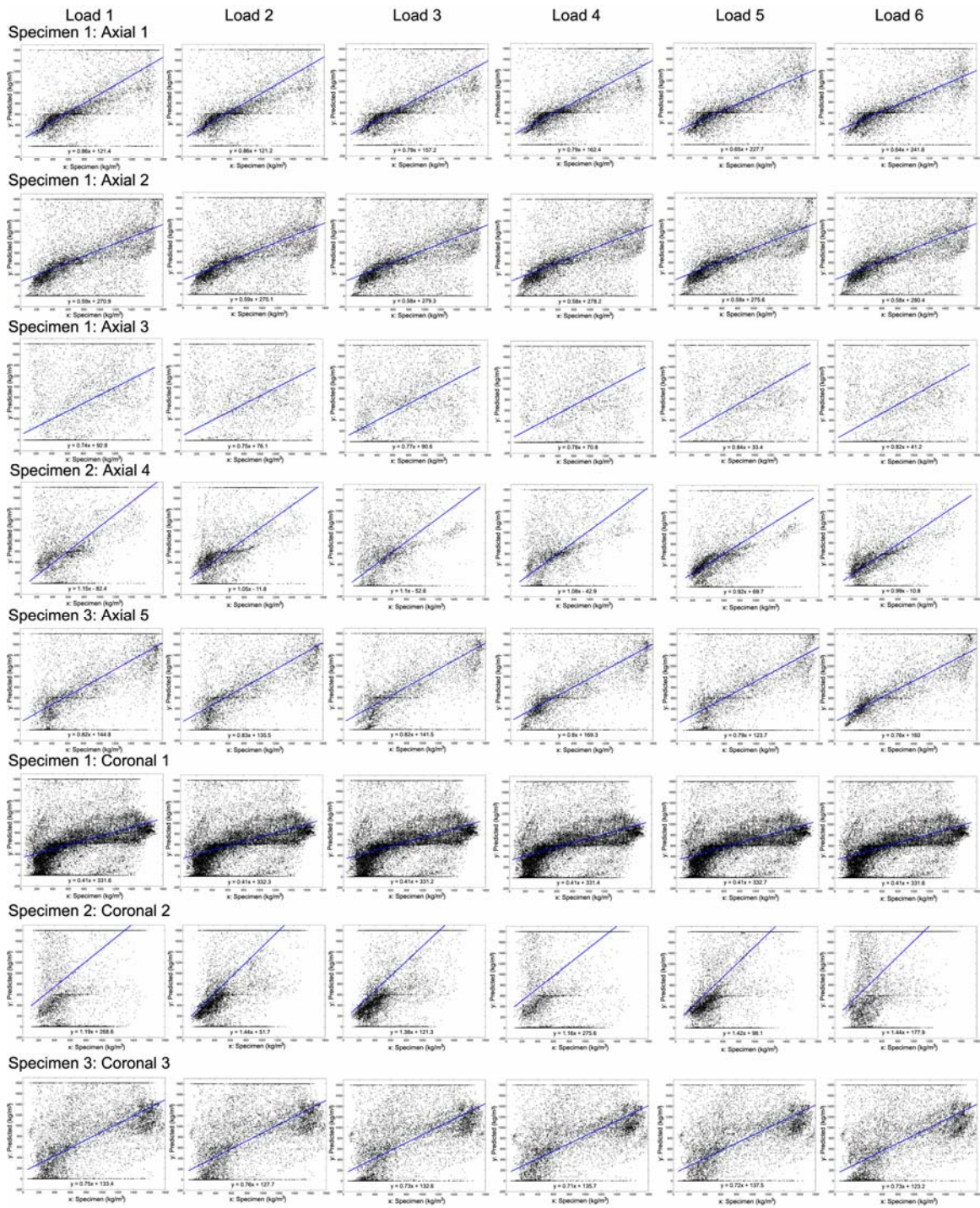


**Figure 63.** The absolute bone apparent density difference images of the glenoid finite element models at the end of the “element” based bone remodeling simulations using the various load combinations (Load 1: ACP/CIS, Load 2: APC/CSI, Load 3: CAP/ICS, Load 4: CPA/ISC, Load 5: PAC/SCI, Load 6: PCA/SIC) and the actual specimen computed on a location-specific basis (figure by author).



**Figure 64.** The absolute bone apparent density difference images of the glenoid finite element models at the end of the “node” based bone remodeling simulations using the various load combinations (Load 1: ACP/CIS, Load 2: APC/CSI, Load 3: CAP/ICS, Load 4: CPA/ISC, Load 5: PAC/SCI, Load 6: PCA/SIC) and the actual specimen computed on a location-specific basis (figure by author).





**Figure 65.** The linear approximation of the predicted bone apparent density value in terms of that in the corresponding specimen for all the glenoid FEMs at the end of “element” based remodeling process for all the load combinations (Load 1: ACP/CIS, Load 2: APC/CSI, Load 3: CAP/ICS, Load 4: CPA/ISC, Load 5: PAC/SCI, Load 6: PCA/SIC) using regression analysis in Matlab® software (figure by author).





## BIBLIOGRAPHY

1. Nordin, M. and V.H. Frankel, *Basic biomechanics of the musculoskeletal system*. 3 ed. 2001, Philadelphia: Lippincott Williams & Wilkins. xvii, 467 p.
2. Prescher, A., *Anatomical basics, variations, and degenerative changes of the shoulder joint and shoulder girdle*. Eur J Radiol, 2000. **35**(2): p. 88-102.
3. Armfield, D.R., et al., *Biomechanical basis of common shoulder problems*. Semin Musculoskelet Radiol, 2003. **7**(1): p. 5-18.
4. Soslowsky, L.J., et al., *Articular geometry of the glenohumeral joint*. Clin Orthop, 1992(285): p. 181-90.
5. Kelly, J.D., Jr. and T.R. Norris, *Decision making in glenohumeral arthroplasty*. J Arthroplasty, 2003. **18**(1): p. 75-82.
6. Edelson, J.G., *Bony changes of the glenoid as a consequence of shoulder instability*. J Shoulder Elbow Surg, 1996. **5**(4): p. 293-8.
7. Craig, E.V., *Total shoulder replacement*. Orthopedics, 1988. **11**(1): p. 125-36.
8. Friedman, R.J., K.B. Hawthorne, and B.M. Genez, *The use of computerized tomography in the measurement of glenoid version*. J Bone Joint Surg Am, 1992. **74**(7): p. 1032-7.
9. Mullaji, A.B., F.H. Beddow, and G.H. Lamb, *CT measurement of glenoid erosion in arthritis*. J Bone Joint Surg Br, 1994. **76**(3): p. 384-8.
10. Walch, G., et al., *Morphologic study of the glenoid in primary glenohumeral osteoarthritis*. J Arthroplasty, 1999. **14**(6): p. 756-60.
11. Edwards, T.B., et al., *A comparison of hemiarthroplasty and total shoulder arthroplasty in the treatment of primary glenohumeral osteoarthritis: results of a multicenter study*. J Shoulder Elbow Surg, 2003. **12**(3): p. 207-13.
12. Felson, D.T., et al., *Osteoarthritis: new insights. Part 2: treatment approaches*. Ann Intern Med, 2000. **133**(9): p. 726-37.
13. Skirving, A.P., *Total shoulder arthroplasty -- current problems and possible solutions*. J Orthop Sci, 1999. **4**(1): p. 42-53.



14. Mileti, J., et al., *Radiographic analysis of polyethylene glenoid components using modern cementing techniques*. J Shoulder Elbow Surg, 2004. **13**(5): p. 492-8.
15. Torchia, M.E., R.H. Cofield, and C.R. Settergren, *Total shoulder arthroplasty with the Neer prosthesis: long-term results*. J Shoulder Elbow Surg, 1997. **6**(6): p. 495-505.
16. Iannotti, J.P., et al., *Prosthetic positioning in total shoulder arthroplasty*. J Shoulder Elbow Surg, 2005. **14**(1 Suppl S): p. 111S-121S.
17. Ibarra, C., D.M. Dines, and J.A. McLaughlin, *Glenoid replacement in total shoulder arthroplasty*. Orthop Clin North Am, 1998. **29**(3): p. 403-13.
18. Oosterom, R., P.M. Rozing, and H.E. Bersee, *Effect of glenoid component inclination on its fixation and humeral head subluxation in total shoulder arthroplasty*. Clin Biomech (Bristol, Avon), 2004. **19**(10): p. 1000-8.
19. Checroun, A.J., et al., *Fit of current glenoid component designs: an anatomic cadaver study*. J Shoulder Elbow Surg, 2002. **11**(6): p. 614-7.
20. Caniggia, M., et al., *Shoulder arthroplasty. Indications, contraindications and complications*. Panminerva Med, 1999. **41**(4): p. 341-9.
21. Cofield, R.H. and B.C. Edgerton, *Total shoulder arthroplasty: complications and revision surgery*. Instr Course Lect, 1990. **39**: p. 449-62.
22. Frich, L.H., et al., *Bone strength and material properties of the glenoid*. J Shoulder Elbow Surg, 1997. **6**(2): p. 97-104.
23. Anglin, C., et al., *Glenoid cancellous bone strength and modulus*. J Biomech, 1999. **32**(10): p. 1091-7.
24. Wirth, M.A. and C.A. Rockwood, Jr., *Complications of total shoulder-replacement arthroplasty*. J Bone Joint Surg Am, 1996. **78**(4): p. 603-16.
25. Hopkins, A.R., et al., *The effects of glenoid component alignment variations on cement mantle stresses in total shoulder arthroplasty*. J Shoulder Elbow Surg, 2004. **13**(6): p. 668-75.
26. Stone, K.D., et al., *Stress analyses of glenoid components in total shoulder arthroplasty*. J Shoulder Elbow Surg, 1999. **8**(2): p. 151-8.
27. Gupta, S., F.C. van der Helm, and F. van Keulen, *Stress analysis of cemented glenoid prostheses in total shoulder arthroplasty*. J Biomech, 2004. **37**(11): p. 1777-86.
28. Lacroix, D., L.A. Murphy, and P.J. Prendergast, *Three-dimensional finite element analysis of glenoid replacement prostheses: a comparison of keeled and pegged anchorage systems*. J Biomech Eng, 2000. **122**(4): p. 430-6.

29. Couteau, B., et al., *Finite element analysis of the mechanical behavior of a scapula implanted with a glenoid prosthesis*. Clin Biomech (Bristol, Avon), 2001. **16**(7): p. 566-75.
30. Terrier, A., P. Buchler, and A. Farron, *Bone-cement interface of the glenoid component: Stress analysis for varying cement thickness*. Clin Biomech (Bristol, Avon), 2005. **20**(7): p. 710-7.
31. Williams, G.R. and J.A. Abboud, *Total shoulder arthroplasty: glenoid component design*. J Shoulder Elbow Surg, 2005. **14**(1 Suppl S): p. 122S-128S.
32. Murphy, L.A., P.J. Prendergast, and H. Resch, *Structural analysis of an offset-keel design glenoid component compared with a center-keel design*. J Shoulder Elbow Surg, 2001. **10**(6): p. 568-79.
33. Orr, T.E., D.R. Carter, and D.J. Schurman, *Stress analyses of glenoid component designs*. Clin Orthop, 1988(232): p. 217-24.
34. Boileau, P., et al., *Arthroplasty of the shoulder*. J Bone Joint Surg Br, 2006. **88**(5): p. 562-75.
35. Orr, T.E., et al., *Computer predictions of bone remodeling around porous-coated implants*. J Arthroplasty, 1990. **5**(3): p. 191-200.
36. Weinans, H., et al., *Adaptive bone remodeling around bonded noncemented total hip arthroplasty: a comparison between animal experiments and computer simulation*. J Orthop Res, 1993. **11**(4): p. 500-13.
37. Smolinski, P. and H.E. Rubash, *Bone remodeling around total hip implants*. Crit Rev Biomed Eng, 1992. **20**(5-6): p. 461-83.
38. Gupta, S., F.C. van der Helm, and F. van Keulen, *The possibilities of uncemented glenoid component--a finite element study*. Clin Biomech (Bristol, Avon), 2004. **19**(3): p. 292-302.
39. Lim, D., et al., *The effect of the loading condition corresponding to functional shoulder activities on trabecular architecture of glenoid*. J Biomech Eng, 2006. **128**(2): p. 250-8.
40. van der Helm, F.C., *Analysis of the kinematic and dynamic behavior of the shoulder mechanism*. J Biomech, 1994. **27**(5): p. 527-50.
41. van der Helm, F.C., *A finite element musculoskeletal model of the shoulder mechanism*. J Biomech, 1994. **27**(5): p. 551-69.
42. Gray, H., 1825-1861, *Anatomy of the human body*. 38th ed, ed. W.H. Lewis. Vol. 2005. 1918, Philadelphia: Lea & Febiger. 1396 p. [www.bartleby.com/107/](http://www.bartleby.com/107/).

43. Gardner, W.D. and W.A. Osburn, *Anatomy of Human Body*. 3 ed. 1978: W. B. Saunders Company. 110-112.
44. Robertson, D.D., et al., *Three-dimensional analysis of the proximal part of the humerus: relevance to arthroplasty*. J Bone Joint Surg Am, 2000. **82-A**(11): p. 1594-602.
45. Carey, J., C.F. Small, and D.R. Pichora, *In situ compressive properties of the glenoid labrum*. J Biomed Mater Res, 2000. **51**(4): p. 711-6.
46. Randelli, M. and P.L. Gambrioli, *Glenohumeral osteometry by computed tomography in normal and unstable shoulders*. Clin Orthop, 1986(208): p. 151-6.
47. Anetzberger, H. and R. Putz, *The scapula: principles of construction and stress*. Acta Anat (Basel), 1996. **156**(1): p. 70-80.
48. Churchill, R.S., J.J. Brems, and H. Kotschi, *Glenoid size, inclination, and version: an anatomic study*. J Shoulder Elbow Surg, 2001. **10**(4): p. 327-32.
49. Gallino, M., E. Santamaria, and T. Doro, *Anthropometry of the scapula: clinical and surgical considerations*. J Shoulder Elbow Surg, 1998. **7**(3): p. 284-91.
50. Hughes, R.E., et al., *Glenoid inclination is associated with full-thickness rotator cuff tears*. Clin Orthop Relat Res, 2003(407): p. 86-91.
51. Iannotti, J.P., et al., *The normal glenohumeral relationships. An anatomical study of one hundred and forty shoulders*. J Bone Joint Surg Am, 1992. **74**(4): p. 491-500.
52. Kwon, Y.W., et al., *Use of three-dimensional computed tomography for the analysis of the glenoid anatomy*. J Shoulder Elbow Surg, 2005. **14**(1): p. 85-90.
53. Lehtinen, J.T., et al., *Anatomy of the superior glenoid rim. Repair of superior labral anterior to posterior tears*. Am J Sports Med, 2003. **31**(2): p. 257-60.
54. McPherson, E.J., et al., *Anthropometric study of normal glenohumeral relationships*. J Shoulder Elbow Surg, 1997. **6**(2): p. 105-12.
55. Prescher, A. and T. Klumpen, *The glenoid notch and its relation to the shape of the glenoid cavity of the scapula*. J Anat, 1997. **190** ( Pt 3): p. 457-60.
56. Welsch, G., et al., *CT-based preoperative analysis of scapula morphology and glenohumeral joint geometry*. Comput Aided Surg, 2003. **8**(5): p. 264-8.
57. Iannotti, J.P., G.R. Williams, and A.R. Karduna, *Factors Affecting the Design of Shoulder Prosthetics*. Seminars in Arthroplasty, 1997. **8**(4): p. 260-267.
58. Burkhart, S.S., et al., *Quantifying glenoid bone loss arthroscopically in shoulder instability*. Arthroscopy, 2002. **18**(5): p. 488-91.

59. De Wilde, L.F., et al., *About the variability of the shape of the glenoid cavity*. Surg Radiol Anat, 2004. **26**(1): p. 54-9.
60. De Wilde, L.F., et al., *Glenohumeral relationship in the transverse plane of the body*. J Shoulder Elbow Surg, 2003. **12**(3): p. 260-7.
61. Inui, H., et al., *Glenoid shape in atraumatic posterior instability of the shoulder*. Clin Orthop, 2002. **403**: p. 87-92.
62. Monk, A.P., et al., *Laser morphometric analysis of the glenoid fossa of the scapula*. Clin Anat, 2001. **14**(5): p. 320-3.
63. Spencer, E.E., Jr., et al., *The effect of humeral component anteversion on shoulder stability with glenoid component retroversion*. J Bone Joint Surg Am, 2005. **87**(4): p. 808-14.
64. Hasan, S.S., et al., *The distribution of shoulder replacement among surgeons and hospitals is significantly different than that of hip or knee replacement*. J Shoulder Elbow Surg, 2003. **12**(2): p. 164-9.
65. Hammond, J.W., et al., *Surgeon experience and clinical and economic outcomes for shoulder arthroplasty*. J Bone Joint Surg Am, 2003. **85-A**(12): p. 2318-24.
66. Jain, N., et al., *The relationship between surgeon and hospital volume and outcomes for shoulder arthroplasty*. J Bone Joint Surg Am, 2004. **86-A**(3): p. 496-505.
67. Couteau, B., et al., *Morphological and mechanical analysis of the glenoid by 3D geometric reconstruction using computed tomography*. Clin Biomech (Bristol, Avon), 2000. **15 Suppl 1**: p. S8-12.
68. Mansat, P., et al., *Anatomic variation of the mechanical properties of the glenoid*. J Shoulder Elbow Surg, 1998. **7**(2): p. 109-15.
69. Frich, L.H., A. Odgaard, and M. Dalstra, *Glenoid bone architecture*. J Shoulder Elbow Surg, 1998. **7**(4): p. 356-61.
70. Couteau, B., et al., *In vivo characterization of glenoid with use of computed tomography*. J Shoulder Elbow Surg, 2001. **10**(2): p. 116-22.
71. Schulz, C.U., et al., *The mineralization patterns at the subchondral bone plate of the glenoid cavity in healthy shoulders*. J Shoulder Elbow Surg, 2002. **11**(2): p. 174-81.
72. Bauer, G.S., A.M. Murthi, and L.U. Bigliani, *Fixation for the millennium: the shoulder*. J Arthroplasty, 2002. **17**(4 Suppl 1): p. 9-10.
73. Hopkins, A.R., et al., *Glenohumeral kinematics following total shoulder arthroplasty: a finite element investigation*. J Orthop Res, 2007. **25**(1): p. 108-15.

74. Severt, R., et al., *The influence of conformity and constraint on translational forces and frictional torque in total shoulder arthroplasty*. Clin Orthop, 1993(292): p. 151-8.
75. Hopkins, A.R., et al., *Finite element modelling of glenohumeral kinematics following total shoulder arthroplasty*. J Biomech, 2006. **39**(13): p. 2476-83.
76. Karduna, A.R., et al., *Glenohumeral joint translations before and after total shoulder arthroplasty. A study in cadavera*. J Bone Joint Surg Am, 1997. **79**(8): p. 1166-74.
77. Anglin, C., U.P. Wyss, and D.R. Pichora, *Shoulder prosthesis subluxation: theory and experiment*. J Shoulder Elbow Surg, 2000. **9**(2): p. 104-14.
78. Klepps, S., et al., *Incidence of early radiolucent glenoid lines in patients having total shoulder replacements*. Clin Orthop Relat Res, 2005(435): p. 118-25.
79. Nagels, J., et al., *Patterns of loosening of the glenoid component*. J Bone Joint Surg Br, 2002. **84**(1): p. 83-7.
80. Lazarus, M.D., et al., *The radiographic evaluation of keeled and pegged glenoid component insertion*. J Bone Joint Surg Am, 2002. **84-A**(7): p. 1174-82.
81. Martin, S.D., D. Zurakowski, and T.S. Thornhill, *Uncemented glenoid component in total shoulder arthroplasty. Survivorship and outcomes*. J Bone Joint Surg Am, 2005. **87**(6): p. 1284-92.
82. Wallace, A.L., et al., *Resurfacing of the glenoid in total shoulder arthroplasty. A comparison, at a mean of five years, of prostheses inserted with and without cement*. J Bone Joint Surg Am, 1999. **81**(4): p. 510-8.
83. Havig, M.T., et al., *Assessment of radiolucent lines about the glenoid. An in vitro radiographic study*. J Bone Joint Surg Am, 1997. **79**(3): p. 428-32.
84. Rahme, H., P. Mattsson, and S. Larsson, *Stability of cemented all-polyethylene keeled glenoid components. A radiostereometric study with a two-year follow-up*. J Bone Joint Surg Br, 2004. **86**(6): p. 856-60.
85. Sanchez-Sotelo, J., et al., *Radiographic assessment of cemented humeral components in shoulder arthroplasty*. J Shoulder Elbow Surg, 2001. **10**(6): p. 526-31.
86. Gartsman, G.M., et al., *Radiographic comparison of pegged and keeled glenoid components*. J Shoulder Elbow Surg, 2005. **14**(3): p. 252-7.
87. Walch, G., et al., *The influence of glenohumeral prosthetic mismatch on glenoid radiolucent lines: results of a multicenter study*. J Bone Joint Surg Am, 2002. **84-A**(12): p. 2186-91.
88. Churchill, R.S., et al., *Glenoid cementing may generate sufficient heat to endanger the surrounding bone*. Clin Orthop, 2004(419): p. 76-9.

89. McElwain, J.P. and E. English, *The early results of porous-coated total shoulder arthroplasty*. Clin Orthop Relat Res, 1987(218): p. 217-24.
90. Cofield, R.H., *Uncemented total shoulder arthroplasty. A review*. Clin Orthop Relat Res, 1994(307): p. 86-93.
91. Boileau, P., et al., *Cemented polyethylene versus uncemented metal-backed glenoid components in total shoulder arthroplasty: a prospective, double-blind, randomized study*. J Shoulder Elbow Surg, 2002. **11**(4): p. 351-9.
92. Sperling, J.W., et al., *Radiographic assessment of ingrowth total shoulder arthroplasty*. J Shoulder Elbow Surg, 2000. **9**(6): p. 507-13.
93. Sperling, J.W., et al., *Ingrowth Total Shoulder Arthroplasty*. J Shoulder Elbow Surg, 1999. **8**: p. 188.
94. Wallace, A.L., W.R. Walsh, and D.H. Sonnabend, *Dissociation of the glenoid component in cementless total shoulder arthroplasty*. J Shoulder Elbow Surg, 1999. **8**(1): p. 81-4.
95. Scarlat, M.M. and F.A. Matsen, 3rd, *Observations on retrieved polyethylene glenoid components*. J Arthroplasty, 2001. **16**(6): p. 795-801.
96. Gunther, S.B., et al., *Retrieved glenoid components: a classification system for surface damage analysis*. J Arthroplasty, 2002. **17**(1): p. 95-100.
97. Feldman, A.Y. and T.D. Bunker, *Rotational dissociation of glenoid components in a total shoulder prosthesis: an indication that sagittal torque forces may be important in glenoid component design*. J Shoulder Elbow Surg, 1999. **8**(3): p. 279-80.
98. Wirth, M.A., et al., *Isolation and characterization of polyethylene wear debris associated with osteolysis following total shoulder arthroplasty*. J Bone Joint Surg Am, 1999. **81**(1): p. 29-37.
99. Friedman, R.J., *Biomechanics of total shoulder arthroplasty: a preoperative and postoperative analysis*. Semin Arthroplasty, 1995. **6**(4): p. 222-32.
100. McCullagh, P.J., *Biomechanics and design of shoulder arthroplasty*. Proc Inst Mech Eng [H], 1995. **209**(4): p. 207-13.
101. Ibarra, C. and E.V. Craig, *Soft-tissue balancing in total shoulder arthroplasty*. Orthop Clin North Am, 1998. **29**(3): p. 415-22.
102. Karduna, A.R., et al., *Total shoulder arthroplasty biomechanics: a study of the forces and strains at the glenoid component*. J Biomech Eng, 1998. **120**(1): p. 92-9.
103. Sanchez-Sotelo, J., et al., *Instability after shoulder arthroplasty: results of surgical treatment*. J Bone Joint Surg Am, 2003. **85-A**(4): p. 622-31.

104. Warren, R.F., S.H. Coleman, and J.S. Dines, *Instability after arthroplasty: the shoulder*. J Arthroplasty, 2002. **17**(4 Suppl 1): p. 28-31.
105. Sperling, J.W., et al., *Shoulder arthroplasty for arthritis after instability surgery*. J Bone Joint Surg Am, 2002. **84-A**(10): p. 1775-81.
106. Hettrich, C.M., et al., *Preoperative factors associated with improvements in shoulder function after humeral hemiarthroplasty*. J Bone Joint Surg Am, 2004. **86-A**(7): p. 1446-51.
107. Parsons, I.M.t., et al., *Glenohumeral arthritis and its management*. Phys Med Rehabil Clin N Am, 2004. **15**(2): p. 447-74.
108. Sperling, J.W., R.H. Cofield, and C.M. Rowland, *Neer hemiarthroplasty and Neer total shoulder arthroplasty in patients fifty years old or less. Long-term results*. J Bone Joint Surg Am, 1998. **80**(4): p. 464-73.
109. Boyd, A.D., Jr., et al., *Total shoulder arthroplasty versus hemiarthroplasty. Indications for glenoid resurfacing*. J Arthroplasty, 1990. **5**(4): p. 329-36.
110. Gartsman, G.M., T.S. Roddey, and S.M. Hammerman, *Shoulder arthroplasty with or without resurfacing of the glenoid in patients who have osteoarthritis*. J Bone Joint Surg Am, 2000. **82**(1): p. 26-34.
111. Sanchez-Sotelo, J., R.H. Cofield, and C.M. Rowland, *Shoulder hemiarthroplasty for glenohumeral arthritis associated with severe rotator cuff deficiency*. J Bone Joint Surg Am, 2001. **83-A**(12): p. 1814-22.
112. Weldon, E.J., 3rd, et al., *Optimizing the glenoid contribution to the stability of a humeral hemiarthroplasty without a prosthetic glenoid*. J Bone Joint Surg Am, 2004. **86-A**(9): p. 2022-9.
113. Bryant, D., et al., *A comparison of pain, strength, range of motion, and functional outcomes after hemiarthroplasty and total shoulder arthroplasty in patients with osteoarthritis of the shoulder. A systematic review and meta-analysis*. J Bone Joint Surg Am, 2005. **87**(9): p. 1947-56.
114. Levy, O. and S.A. Copeland, *Cementless surface replacement arthroplasty (Copeland CSRA) for osteoarthritis of the shoulder*. J Shoulder Elbow Surg, 2004. **13**(3): p. 266-71.
115. Levy, O., et al., *Copeland surface replacement arthroplasty of the shoulder in rheumatoid arthritis*. J Bone Joint Surg Am, 2004. **86-A**(3): p. 512-8.
116. Fink, B., et al., *Surface replacement of the humeral head in rheumatoid arthritis*. Arch Orthop Trauma Surg, 2004. **124**(6): p. 366-73.

117. Levy, O. and S.A. Copeland, *Cementless surface replacement arthroplasty of the shoulder. 5- to 10-year results with the Copeland mark-2 prosthesis*. J Bone Joint Surg Br, 2001. **83**(2): p. 213-21.
118. Pearl, M.L., *Proximal humeral anatomy in shoulder arthroplasty: Implications for prosthetic design and surgical technique*. J Shoulder Elbow Surg, 2005. **14**(1 Suppl S): p. 99S-104S.
119. Pearl, M.L. and S. Kurutz, *Geometric analysis of commonly used prosthetic systems for proximal humeral replacement*. J Bone Joint Surg Am, 1999. **81**(5): p. 660-71.
120. Thomas, S.R., et al., *Geometrical analysis of Copeland surface replacement shoulder arthroplasty in relation to normal anatomy*. J Shoulder Elbow Surg, 2005. **14**(2): p. 186-92.
121. Frankle, M., et al., *The Reverse Shoulder Prosthesis for glenohumeral arthritis associated with severe rotator cuff deficiency. A minimum two-year follow-up study of sixty patients*. J Bone Joint Surg Am, 2005. **87**(8): p. 1697-705.
122. Boileau, P., et al., *Grammont reverse prosthesis: design, rationale, and biomechanics*. J Shoulder Elbow Surg, 2005. **14**(1 Suppl S): p. 147S-161S.
123. Harman, M., et al., *Initial glenoid component fixation in "reverse" total shoulder arthroplasty: a biomechanical evaluation*. J Shoulder Elbow Surg, 2005. **14**(1 Suppl S): p. 162S-167S.
124. Werner, C.M., et al., *Treatment of painful pseudoparesis due to irreparable rotator cuff dysfunction with the Delta III reverse-ball-and-socket total shoulder prosthesis*. J Bone Joint Surg Am, 2005. **87**(7): p. 1476-86.
125. Sirveaux, F., et al., *Grammont inverted total shoulder arthroplasty in the treatment of glenohumeral osteoarthritis with massive rupture of the cuff. Results of a multicentre study of 80 shoulders*. J Bone Joint Surg Br, 2004. **86**(3): p. 388-95.
126. Rittmeister, M. and F. Kerschbaumer, *Grammont reverse total shoulder arthroplasty in patients with rheumatoid arthritis and nonreconstructible rotator cuff lesions*. J Shoulder Elbow Surg, 2001. **10**(1): p. 17-22.
127. Laudicina, L. and R. D'Ambrosia, *Management of irreparable rotator cuff tears and glenohumeral arthritis*. Orthopedics, 2005. **28**(4): p. 382-8; quiz 389-90.
128. Boulahia, A., et al., *Early results of a reverse design prosthesis in the treatment of arthritis of the shoulder in elderly patients with a large rotator cuff tear*. Orthopedics, 2002. **25**(2): p. 129-33.
129. De Wilde, L.F., E.A. Audenaert, and B.M. Berghs, *Shoulder prostheses treating cuff tear arthropathy: a comparative biomechanical study*. J Orthop Res, 2004. **22**(6): p. 1222-30.



130. Vanhove, B. and A. Beugnies, *Grammont's reverse shoulder prosthesis for rotator cuff arthropathy. A retrospective study of 32 cases.* Acta Orthop Belg, 2004. **70**(3): p. 219-25.
131. Seebauer, L., W. Walter, and W. Keyl, *Reverse total shoulder arthroplasty for the treatment of defect arthropathy.* Oper Orthop Traumatol, 2005. **17**(1): p. 1-24.
132. Nyffeler, R.W., et al., *Analysis of a retrieved delta III total shoulder prosthesis.* J Bone Joint Surg Br, 2004. **86**(8): p. 1187-91.
133. Buchler, P., et al., *A finite element model of the shoulder: application to the comparison of normal and osteoarthritic joints.* Clin Biomech (Bristol, Avon), 2002. **17**(9-10): p. 630-9.
134. Gupta, S. and F.C. van der Helm, *Load transfer across the scapula during humeral abduction.* J Biomech, 2004. **37**(7): p. 1001-9.
135. Lacroix, D. and P.J. Prendergast, *Stress analysis of glenoid component designs for shoulder arthroplasty.* Proc Inst Mech Eng [H], 1997. **211**(6): p. 467-74.
136. Wang, V.M., et al., *Biomechanical evaluation of a novel glenoid design in total shoulder arthroplasty.* J Shoulder Elbow Surg, 2005. **14**(1 Suppl S): p. 129S-140S.
137. Maurel, N., et al., *In vitro biomechanical analysis of glenoids before and after implantation of prosthetic components.* J Biomech, 2002. **35**(8): p. 1071-80.
138. Andreykiv, A., et al., *Bone ingrowth simulation for a concept glenoid component design.* J Biomech, 2005. **38**(5): p. 1023-33.
139. Anglin, C., et al., *Loosening performance of cemented glenoid prosthesis design pairs.* Clin Biomech (Bristol, Avon), 2001. **16**(2): p. 144-50.
140. Karduna, A.R., et al., *Joint stability after total shoulder arthroplasty in a cadaver model.* J Shoulder Elbow Surg, 1997. **6**(6): p. 506-11.
141. Anglin, C., U.P. Wyss, and D.R. Pichora, *Mechanical testing of shoulder prostheses and recommendations for glenoid design.* J Shoulder Elbow Surg, 2000. **9**(4): p. 323-31.
142. Nyffeler, R.W., et al., *Influence of peg design and cement mantle thickness on pull-out strength of glenoid component pegs.* J Bone Joint Surg Br, 2003. **85**(5): p. 748-52.
143. Bicknell, R.T., et al., *Does keel size, the use of screws, and the use of bone cement affect fixation of a metal glenoid implant?* J Shoulder Elbow Surg, 2003. **12**(3): p. 268-75.
144. Beaupre, G.S., T.E. Orr, and D.R. Carter, *An approach for time-dependent bone modeling and remodeling--theoretical development.* J Orthop Res, 1990. **8**(5): p. 651-61.
145. Lim, D., et al., *Loading conditions and bone formation in the GH region of the shoulder.* Conf Proc IEEE Eng Med Biol Soc, 2004. **7**: p. 5092-5.

146. Felson, D.T., et al., *Osteoarthritis: new insights. Part 1: the disease and its risk factors*. Ann Intern Med, 2000. **133**(8): p. 635-46.
147. CDC, C.f.D.C.a.P., *Racial/ethnic differences in the prevalence and impact of doctor-diagnosed arthritis--United States, 2002*. MMWR Morb Mortal Wkly Rep, 2005. **54**(5): p. 119-23.
148. CDC, C.f.D.C.a.P., *Public health and aging: projected prevalence of self-reported arthritis or chronic joint symptoms among persons aged >65 years--United States, 2005-2030*. MMWR Morb Mortal Wkly Rep, 2003. **52**(21): p. 489-91.
149. CDC, C.f.D.C.a.P., *Update: direct and indirect costs of arthritis and other rheumatic conditions--United States, 1997*. MMWR Morb Mortal Wkly Rep, 2004. **53**(18): p. 388-9.
150. Lawrence, R.C., et al., *Estimates of the prevalence of arthritis and selected musculoskeletal disorders in the United States*. Arthritis Rheum, 1998. **41**(5): p. 778-99.
151. CDC, C.f.D.C.a.P., *Prevalence of disabilities and associated health conditions among adults--United States, 1999*. MMWR Morb Mortal Wkly Rep, 2001. **50**(7): p. 120-5.
152. U.S. Department of Health and Human Services, Centers for Disease Control and Prevention, National Center for Health Statistics. National Hospital Discharge Survey, 2002.
153. Buckingham, B.P., et al., *Patient functional self-assessment in late glenoid component failure at three to eleven years after total shoulder arthroplasty*. J Shoulder Elbow Surg, 2005. **14**(4): p. 368-74.
154. Murphy, L.A. and P.J. Prendergast, *Acromion-fixation of glenoid components in total shoulder arthroplasty*. J Biomech, 2005. **38**(8): p. 1702-11.
155. Ahir, S.P., et al., *Analysis of glenoid fixation for a reversed anatomy fixed-fulcrum shoulder replacement*. J Biomech, 2004. **37**(11): p. 1699-708.
156. Cattaneo, P.M., M. Dalstra, and L.H. Fric, *A three-dimensional finite element model from computed tomography data: a semi-automated method*. Proc Inst Mech Eng [H], 2001. **215**(2): p. 203-13.
157. Oosterom, R., et al., *Effect of joint conformity on glenoid component fixation in total shoulder arthroplasty*. Proc Inst Mech Eng [H], 2004. **218**(5): p. 339-47.
158. Gupta, R. and T.Q. Lee, *Positional-dependent changes in glenohumeral joint contact pressure and force: possible biomechanical etiology of posterior glenoid wear*. J Shoulder Elbow Surg, 2005. **14**(1 Suppl S): p. 105S-110S.

159. Angst, F., et al., *Comprehensive assessment of clinical outcome and quality of life after total shoulder arthroplasty: usefulness and validity of subjective outcome measures*. Arthritis Rheum, 2004. **51**(5): p. 819-28.
160. U.S. Department of Health and Human Services, Centers for Disease Control and Prevention, National Center for Health Statistics. National Ambulatory Medical Care Survey, 2000.
161. Ebraheim, N.A., et al., *Quantitative anatomy of the scapula*. Am J Orthop, 2000. **29**(4): p. 287-92.
162. Mallon, W.J., et al., *Radiographic and geometric anatomy of the scapula*. Clin Orthop, 1992(277): p. 142-54.
163. von Schroeder, H.P., S.D. Kuiper, and M.J. Botte, *Osseous anatomy of the scapula*. Clin Orthop, 2001(383): p. 131-9.
164. Muller-Gerbl, M., R. Putz, and R. Kenn, *Demonstration of subchondral bone density patterns by three-dimensional CT osteoabsorptiometry as a noninvasive method for in vivo assessment of individual long-term stresses in joints*. J Bone Miner Res, 1992. **7 Suppl 2**: p. S411-8.
165. Inui, H., et al., *Evaluation of three-dimensional glenoid structure using MRI*. J Anat, 2001. **199**(Pt 3): p. 323-8.
166. Wirth, M.A., et al., *Radiologic, mechanical, and histologic evaluation of 2 glenoid prosthesis designs in a canine model*. J Shoulder Elbow Surg, 2001. **10**(2): p. 140-8.
167. Kelkar, R., et al., *Glenohumeral mechanics: a study of articular geometry, contact, and kinematics*. J Shoulder Elbow Surg, 2001. **10**(1): p. 73-84.
168. de Leest, O., et al., *Influence of glenohumeral prosthesis geometry and placement on shoulder muscle forces*. Clin Orthop, 1996(330): p. 222-33.
169. Poppen, N.K. and P.S. Walker, *Forces at the glenohumeral joint in abduction*. Clin Orthop Relat Res, 1978(135): p. 165-70.
170. Chang, Y.S., et al., *Significance of interstitial bone ingrowth under load-bearing conditions: a comparison between solid and porous implant materials*. Biomaterials, 1996. **17**(11): p. 1141-8.
171. Bobyn, J.D., et al., *Characteristics of bone ingrowth and interface mechanics of a new porous tantalum biomaterial*. J Bone Joint Surg Br, 1999. **81**(5): p. 907-14.
172. Hacking, S.A., et al., *Acid-etched microtexture for enhancement of bone growth into porous-coated implants*. J Bone Joint Surg Br, 2003. **85**(8): p. 1182-9.

173. Melican, M.C., et al., *Three-dimensional printing and porous metallic surfaces: a new orthopedic application*. J Biomed Mater Res, 2001. **55**(2): p. 194-202.
174. Ono, I., T. Tateshita, and T. Nakajima, *Evaluation of a high density polyethylene fixing system for hydroxyapatite ceramic implants*. Biomaterials, 2000. **21**(2): p. 143-51.
175. Hayashi, K., T. Mashima, and K. Uenoyama, *The effect of hydroxyapatite coating on bony ingrowth into grooved titanium implants*. Biomaterials, 1999. **20**(2): p. 111-9.
176. Davies, J.P., et al., *Comparison of the mechanical properties of Simplex P, Zimmer Regular, and LVC bone cements*. J Biomed Mater Res, 1987. **21**(6): p. 719-30.
177. Saha, S. and S. Pal, *Mechanical properties of bone cement: a review*. J Biomed Mater Res, 1984. **18**(4): p. 435-62.
178. Hopkins, A.R., U.N. Hansen, and A.A. Amis, *Finite element models of total shoulder replacement: application of boundary conditions*. Comput Methods Biomech Biomed Engin, 2005. **8**(1): p. 39-44.
179. Jacobs, C.R., et al., *Numerical instabilities in bone remodeling simulations: the advantages of a node-based finite element approach*. J Biomech, 1995. **28**(4): p. 449-59.
180. Martin, R.B., *Porosity and specific surface of bone*. Crit Rev Biomed Eng, 1984. **10**(3): p. 179-222.
181. Beaupre, G.S., T.E. Orr, and D.R. Carter, *An approach for time-dependent bone modeling and remodeling-application: a preliminary remodeling simulation*. J Orthop Res, 1990. **8**(5): p. 662-70.
182. Chen, G., et al., *Comparison of two numerical approaches for bone remodelling*. Med Eng Phys, 2007. **29**(1): p. 134-9.